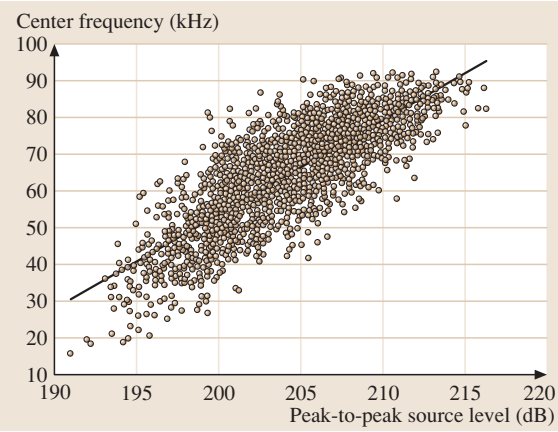


Fig. 20.8 Center frequency of echolocation signals emitted by a *pseudorca* as a function of the peak-to-peak source level (after *Au* et al. [20.52])

creased, the frequency components at higher frequencies also increased in amplitude, suggesting a relationship between source level and center frequency. This relationship can be examined by considering the scatter diagram of Fig. 20.8 showing center frequency plotted against source level. The solid line in the figure is a linear-regression curve fit of the data and has a correlation coefficient of 0.80.

The bimodal property of the echolocation signals of Fig. 20.7 seems to suggest that the response of the sound generator may be determined by the intensity of the driving force that eventually causes an echolocation signal to be produced. When the intensity of the driving force is low, only signals with low amplitudes and low-frequency peak are produced. Therefore, in small tanks, the signals resemble the tank signal of Fig. 20.1, and the bimodal feature is suppressed since the high-frequency portion of the source cannot be used for a low driving force. As the driving force increases to a moderate level, the low-frequency peak also increases in amplitude, and the high-frequency portion of the signal begins to come into use. As the driving force increases further the amplitude of the high-frequency peak becomes larger than that of the low-frequency peak, resulting in type III signals. As the driving force continues to increase to a high level, the amplitude of the high-frequency peak becomes much greater than the amplitude of the low-frequency peak and completely dominates the low-frequency peak causing the bimodal feature to be suppressed. Recent field measurements of free-ranging dolphins [20.55–57] suggest that the majority of echolocation clicks emitted by dolphins are bimodal.

The largest odontocete species is the sperm whale (*Physeter catodon*) and it too emits echolocation signals. Prior to the late 1990s the most prevalent understanding of sperm whale signals is that the clicks were broadband with peak frequencies between 4 and 8 kHz [20.58–61]. There were only two reports on source levels. *Dunn* [20.62] using sonobouys measured 148 sperm whale clicks from a solitary sperm whale and estimated an average peak-to-peak source level of 183 dB re 1 μPa. *Levenson* [20.59] estimated peak-to-peak source level of 180 dB re 1 μPa. The clicks were also thought to be essentially nondirectional and projected in codas [20.63]. Therefore, the notion of sperm whales echolocating was somewhat questionable. Part of the problem was the lack of measurements of sperm whale signaling in conjunction with foraging and the fact that click signals can have more than one function, such as communications and echolocation. In a review paper *Watkins* [20.63] spelled out his rational for not supporting the notion of a sonar function for sperm whale clicks, "Other features of their sounds however, do not so easily fit echolocation:" Watkin's rational included his observations that clicks do not appear to be very directional, the inter-click interval does not varied as if a prey or obstacle is being approached, solitary sperm whales are silent for long periods, the level of their clicks appears to be generally greater than that required for echolocating prey or obstacles and the individual clicks are usually too long for good range resolution. It is important to state that most of Watkins measurements were conducted at low-temperate latitudes where females and calves are found.

Sperm whale echolocation began to be more fully understood with data obtained in ground-breaking work by Bertel Møhl and his students from the University of Aarhus, along with other Danish colleagues. They began to perform large-array aperture measurements of large bull sperm whales foraging along the slope of the continental shelf off Andenes, Norway beginning in the summer of 1977 [20.64]. Up to seven multi-platforms spaced on the order of 1 km apart were used in their study with hydrophones placed at depths varying from 5 to 327 m [20.65]. They also came up with a unique but logistically simple scheme of obtaining global positioning system (GPS) information to localize the position of each platform. Each platform continuously logged its position and time stamps on one track of a digital audio tape (DAT) recorder, the other track being used for measuring sperm whale clicks [20.64]. The GPS signals were converted to an analog signal by frequency-shift keying (FSK) modulation. In this way, each platform can be operated essentially autonomously and yet its lo-

Amazon
EX1010 Page 822

Amazon EX1010 Page 823

cation and time stamps could be related to all the other platforms.

An important finding of *Møhl* et al. [20.64] is the monopulsed nature of on-axis clicks emitted by the sperm whales that were similar in shape and spectrum to dolphin echolocation signals but with peak frequencies between 15 and 25 kHz (this peak frequency range is consistent with the auditory sensitivity observed from evoked potential responses by a young sperm whale to clicks presented by *Ridgway* and *Carder* [20.38]). *Møhl* et al. [20.64] also estimated very high source levels as high as 223 dB re 1 μPa per RMS (root mean square). The per RMS measure is the level of a continuous sine wave having the same peak-to-peak amplitude as the click. This measure is clearly an overestimate of the RMS value of a sperm whale click. Nevertheless, the 223 dB reported by *Møhl* et al. [20.64] can easily be given a peak-to-peak value of 232 dB (adding 9 dB to the per-RMS value). In a follow-on study, *Møhl* et al. [20.65] measured clicks with RMS source levels as high as 236 dB re 1 μPa using the expression

$$p_{\mathrm{RMS}} = \sqrt{\frac{1}{T}\int_0^T p^2(t)\,\mathrm{d}t}\,. \tag{20.5}$$

For this measurement, they used a time interval corresponding to the 3 dB down points of the signal waveform. For this waveform, an RMS source level of 236 dB corresponds to a peak-to-peak source level of 243 dB re 1 μPa. Finally, they found that the clicks were very directional, as directional as dolphin clicks.

20.2.2 Echolocation Signals of Smaller Odontocetes that Do not Whistle

The second class of echolocation signals are produced by dolphins and porpoises that do not emit whistle signals. Not many odontocetes fall into this category and these non-whistling animals tend to be smaller than their whistling cousins. Included in this group of non-whistling odontocetes are the harbor porpoise (*phocoena phocoena*), finless porpoise (*neophocaena phocaenoides*), Dall's porpoise (*phocoenoides dalli*), Commerson's dolphin, *cephalorhynchus commersonii*), Hector's dolphin (*cephalorhynchus hectori*) and pygmy sperm whale (*kogia sp*).

Examples of harbor porpoise and Atlantic bottlenose dolphin echolocation signals presented in a manner for easy comparison are shown in Fig. 20.9. There are four fundamental differences in the two types of echolocation signals. The non-whistling animal emit a signal with longer duration, narrower band, lower amplitude and single mode. The length of the *Phocoena phocoena* signal vary from about 125–150 μs compared to 50–70 μs for the *tursiops truncatus* signal. The bandwidth of the *Phocoena* signal is almost 0.2–0.3 that of the *tursiops* signal. Since the non-whistling dolphins are usually much smaller in length and weight than the whistling dolphins, the smaller animals might be amplitude limited in terms of their echolocation signals and compensate by emitting longer signals to increase the energy output. This issue can be exemplified by characterizing an echolocation click as [20.39]

$$p(t) = As(t)\,, \tag{20.6}$$

where $A = |p|_{\max}$ is the absolute value of the peak amplitude of the signal and $s(t)$ is the normalized wave-

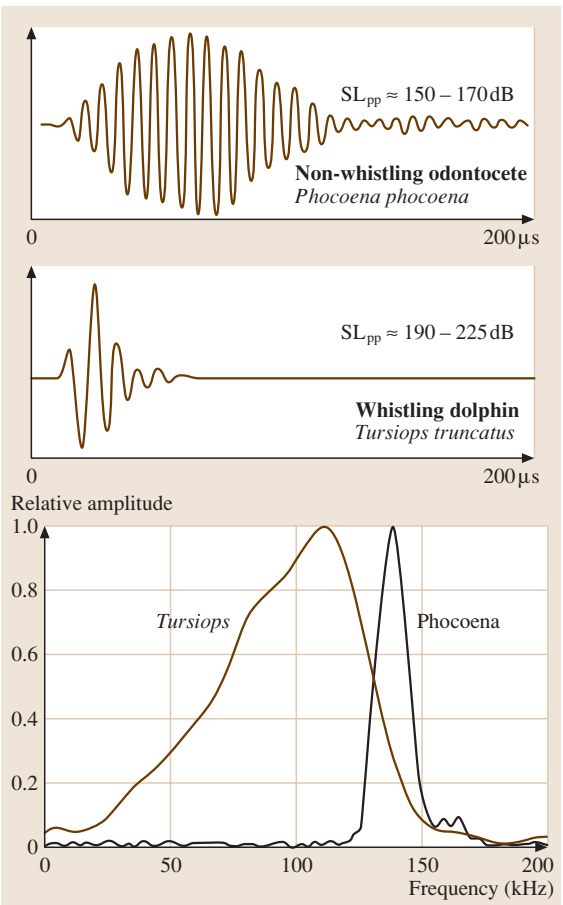


Fig. 20.9 Examples of typical echolocation signals of *phocoena phocoena* and *tursiops truncatus* (after [20.8])

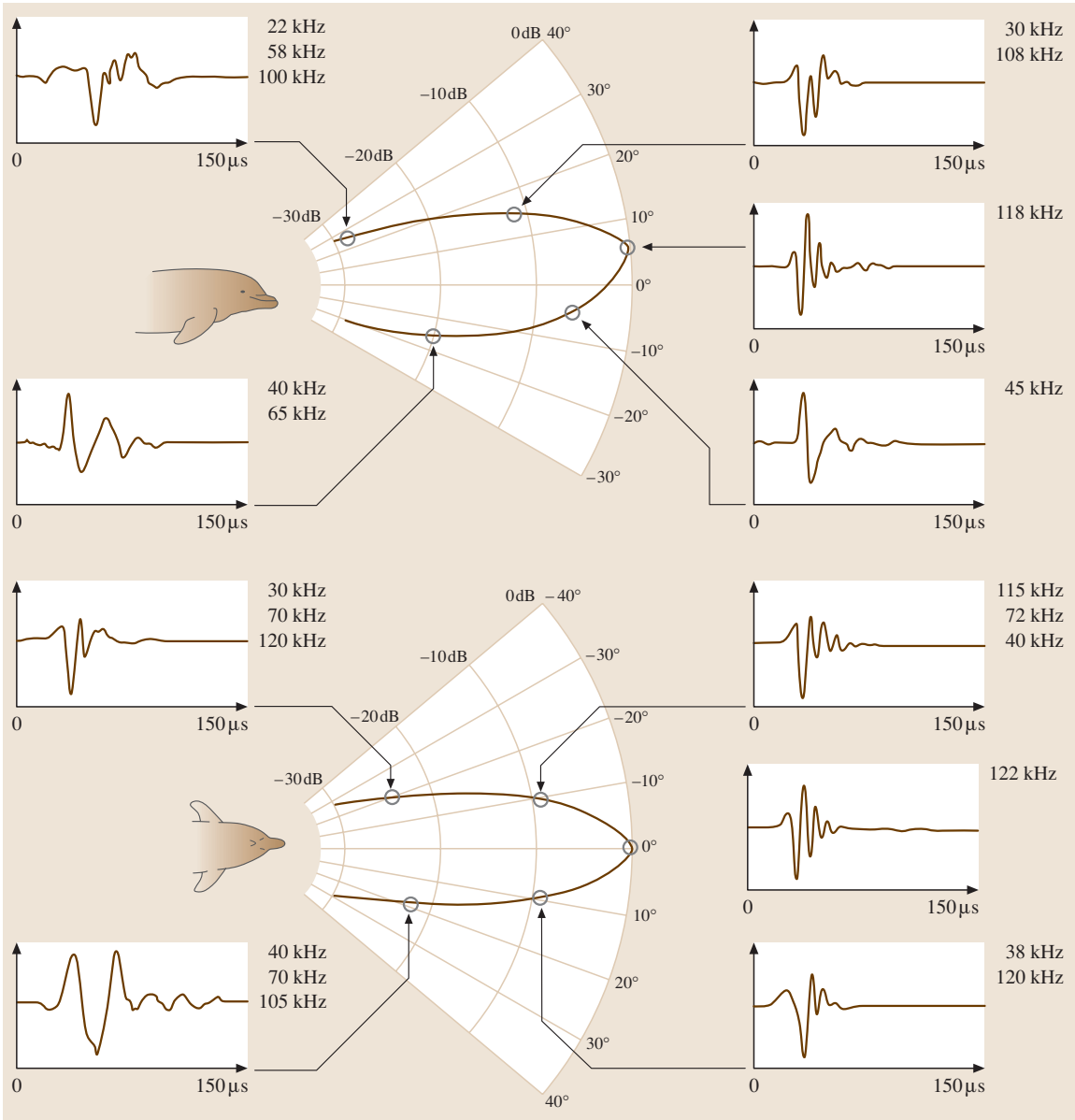


Fig. 20.10 The transmission beam pattern of a *tursiops truncatus* planes with the waveform of a click measured by 5–7 hydrophones (after *Au* [20.39]) in the vertical and horizontal planes

form having a maximum amplitude of unity. The source energy-flux density of the signal in dB can be expressed as

$$\mathrm{SE} = 10\log\left(\int_0^T p(t)^2\,\mathrm{d}t\right)$$

$$= 10\log(A) + 10\log\left(\int_0^T s(t)^2\,\mathrm{d}t\right), \qquad (20.7)$$

where T is the duration of the signal. Letting $2A \approx$ be the peak-to-peak sound pressure level, (20.4) can be

Amazon
EX1010 Page 824

rewritten as

$$\mathrm{SE} = \mathrm{SL} - 6 + 10\log\left(\int_0^T s(t)^2\,\mathrm{d}t\right)\,, \qquad (20.8)$$

where SL is the the peak-to-peak source level and is approximately equal to $10\log(2A)$. From Fig. 20.9, the *Tursiops* can emit signals with peak-to-peak source levels in open water that are greater than 50 dB for *phocoena*. The portion of the source energy that can be attributed to the length of the signal is only about 2–4 dB greater for *phocoena* than *Tursiops* [20.39]. Therefore, one can conclude that the target detection range of *phocoena* is considerably shorter than for *Tursiops*. This has been demonstrated by *Kastelein* et al. [20.67] who measured a target detection threshold range of 26 m for a 7.62 cm water-filled sphere in a quiet environment. The target detection range in a noisy environment and a similar 7.62 cm water-filled sphere was 113 m [20.68].

The echolocation signals of other non-whistling odontocetes are very similar to the *Phocoena phocoena* signal shown in Fig. 20.9. Examples of the echolocation signals of other non-whistling odontocetes can be found in *Au* [20.7, 39, 69]. Unfortunately, reliable source-level data have been collected only for *Phocoena phocoena* [20.70] and *Kogia* [20.69].

20.2.3 Transmission Beam Pattern

The outgoing echolocation signals of dolphins and other odontocetes are projected in a directional beam that have been measured in the vertical and horizontal planes for the bottlenose dolphin [20.39], beluga whale [20.66] and the false killer whale [20.52]. The composite beam pattern from the three measurements on *Tursiops* along with the averaged waveform from a single trial measured by 5 or the 7 hydrophones are shown in Fig. 20.10. The 3 dB beam width for the bottlenose dolphin was approximately 10.2° in the vertical plane and 9.7° in the horizontal plane. The waveforms detected by the various hydrophones in Fig. 20.10 indicate that signals measured away from the beam axis will be distorted with respect to the signals measured on the beam axis. The further away from the beam axis the more distorted the signals will be. This distortion come from the broadband nature of the click signals emitted by whistling dolphins. This characteristics also make it difficult to get good measurements of echolocation signals in the field even with an array of hydrophones since it is extremely difficult to obtain on-axis echolocation signals and also to know the orientation of the animal with respect to the measuring hydrophones. The frequencies shown with each waveform are the fre-

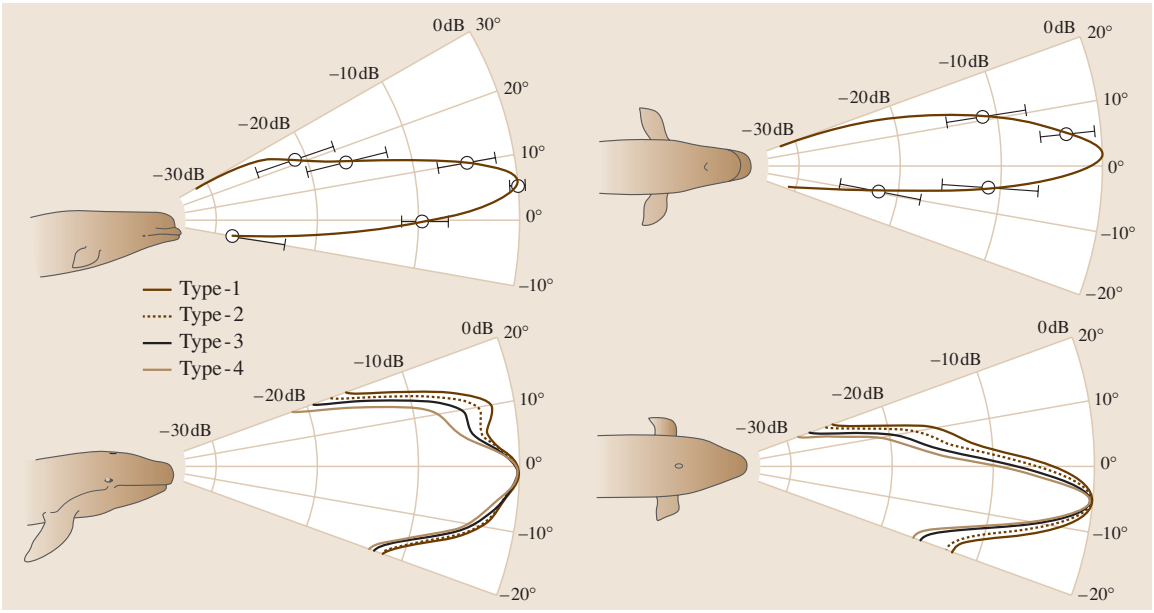


Fig. 20.11 The transmission beam pattern of a *delphinapterus leucas* (after *Au* et al. [20.66]) and a *pseudorca crassidens* (after *Au* et al. [20.52]) in the vertical and horizontal planes

Amazon
EX1010 Page 825

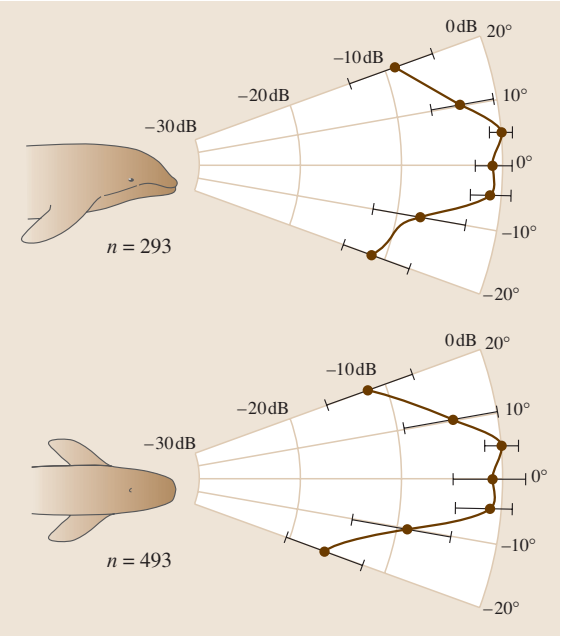


Fig. 20.12 Beam patterns in the vertical and horizontal planes for *phocoena phocoena* (*Au* et al. [20.70])

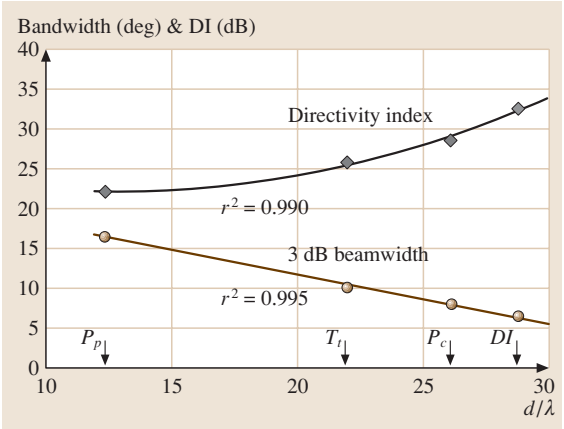


Fig. 20.13 Transmission directivity index and 3 dB beam width for four odontocetes. The directivity index and beam width for *Tursiops truncatus* and *delphinapterus leucas* came from *Au* [20.39] and for *pseudorca crassidens* after *Au* et al. [20.52]. The wavelength λ corresponds to the average peak frequency of the animals' echolocation signals. The directivity index is fitted with a second-order polynomial curve the the beam width is fitted with a linear curve (after *Au* et al. [20.70])

quencies of local maxima in the spectrum. At some angles the averaged signal had multiple peaks in the spectrum and these peaks are listed in order of prominence.

The beam patterns for the beluga and false killer whale are shown in Fig. 20.11. The beam width for the beluga whale was approximately 6.5° in both planes. Four beam patterns corresponding to the four signal types described in Fig. 20.7 are shown for the false killer whale. For the highest frequency (type IV signal) the 3 dB beam width in the vertical plane was approximately 10°, and 7° in the horizontal plane. The beam axis in the vertical plane for the bottlenose dolphin and the beluga whale was +5° above the horizontal plane. For the false killer whale, 49% of the beam axis was at 0° and 32% at −5°. The four beam patterns for the false killer whale indicate that, like a linear transducer, the lower the frequency the wider the beam pattern. The type I signal has a peak frequency of about 30 kHz and has the widest beam. However, even though the peak frequency of the type IV signal is about 3.5 times higher than the type I signal, the beam does not seem to be substantially larger. This property can be used when discussing lower-frequency whistle signals to suggest that whistle signals are also emitted in a beam.

The only transmission beam pattern for a non-whistling odontocete, a *phocoena phocoena*, was measured by *Au* et al. [20.70]. Their results are shown in Fig. 20.12 in both the horizontal and vertical planes. One of the obvious difference between the beam patterns in Fig. 20.12 and those in Figs. 20.10 and 20.11 is the width of the beam. Although the harbor porpoise emitted the highest-frequency signals, its small head size caused the beam to be wider than for the other animals. The beam patterns of Figs. 20.10–20.12 were inserted into (20.1) and numerically evaluated to estimate the corresponding directivity index for *tursiops* and *delphinapterus* [20.39] and for *pseudorca* by *Au* et al. [20.52] and for *phocoena* [20.70], and the results are shown in Fig. 20.13 plotted as a function of the ratio of the head diameter (at the blow hole) of the subject and the average peak frequency of the animals echolocation signal. Also shown in Fig. 20.13 are the 3 dB beam width, where the 3 dB beam width in the vertical and horizontal planes were averaged.

The second-order polynomial fit of the directivity index is given by the equation

$$\mathrm{DI} = 28.89 - 1.04\left(\frac{d}{\lambda}\right) + 0.04\left(\frac{d}{\lambda}\right)^2 . \qquad (20.9)$$

Amazon
EX1010 Page 826

The linear fit of the 3 dB beam width data is given by the equation

$$\mathrm{BW} = 23.90 - 0.60\left(\frac{d}{\lambda}\right) . \qquad (20.10)$$

The results of Fig. 20.13 provides a way of estimating the directivity index and 3 dB beam width of other odontocetes by knowing their head size and the peak frequency of their echolocation signals.

Another interesting characteristics of the beam pattern measurement on the *phocoena phocoena* is that the off-axis signals are not distorted in comparison to the on-axis signal. This is consistent with narrow-band signals whether for a linear technological transducer or a live animal. Therefore, measurements of echolocation signals of non-whistling odontocetes in the field can be performed much easier than for whistling odontocetes.

20.3 Odontocete Acoustic Communication

Members of the *Odontocete* suborder are an intriguing example of the adaptability of social mammalian life to the aquatic habitat. Most odontocetes, particularly marine dolphins, live in groups ranging from several to hundreds of animals in size, forage cooperatively, develop hierarchies, engage in alloparental care and form strong pair bonds and coalitions between both kin and non-kin alike (see [20.71–73] for a review of the literature on dolphin societies). These social traits are analogous to patterns found in many avian and terrestrial mammalian species. It is not surprising, therefore, that odontocetes mediate much social information via communication. Some river dolphins are usually found as solitary individuals or mother–calf pairs although they may occasionally congregate into larger groups.

Odontocetes communicate through a combination of sensory modalities that include the visual, tactile, acoustic and chemosensory channels [20.74]. Visual signals in the form of postural displays are thought to convey levels of aggression, changes in direction of movement, and affiliative states [20.72,75]. Tactile interactions vary in purpose from sexual and affiliative signals to expressions of dominance and aggression [20.76,77]. Although not well documented yet, it is thought that a derivative of chemosensory perception, termed *quasiolfaction* allows dolphins to relay chemical messages about stress and reproductive status [20.78, 79]. However, it is the acoustic communication channel in particular that is believed to be the main communication tool that enables odontocetes to function cohesively as groups in the vast, visually limited environment of the open sea [20.80]. Examining how odontocetes have adapted their use of sound is therefore an important step to understanding how social marine mammal life evolved in the sea and how it has found a way to thrive in a habitat so drastically different from our own.

When compared to all that has been learned about dolphin echolocation over the past several decades, surprisingly little is still known about how dolphins and other odontocetes use acoustic signals for communication. A major reason for this is that it is very difficult to observe the acoustic and behavioral interactions between the producer and the receiver(s) of social signals in the underwater environment. Sound propagation in the sea makes even a simple task like identifying the location of a sound source very challenging for air-adapted listeners. Therefore, matching signals with specific individuals and their behavior in the field is problematic without the use of sophisticated recording arrays [20.57, 76, 81, 82], or directional transducers. In addition, many questions remain unanswered about the nature of social signals themselves. Much still remains unknown about the functional design of dolphin social sounds. This is largely due to the fact that most species specialize in producing and hearing sounds with frequencies well beyond the limits of the human hearing range. Limitations in the technology available to study social signaling in the field have until recently restricted most analyses to the human auditory bandwidth (< 20 kHz). Yet, despite these significant challenges, a great deal of progress has been made in our understanding of odontocete acoustic communication. Rapidly advancing technologies are contributing greatly to our ability to study social signaling both in the field and in the laboratory. The emerging picture reveals that odontocetes have adapted their acoustic signaling to fit the aquatic world in a remarkably elegant way.

20.3.1 Social Acoustic Signals

Odontocetes have evolved in both marine and freshwater habitats for over 50 million years. Over such a long period of adaptive radiation one might expect that a variety of signaling strategies would have evolved among the approximately 65 species of small toothed whales and dolphins. Yet, remarkably, the vast majority of these species have either conserved or converged on the pro-

Amazon
EX1010 Page 827

duction of two types of sounds: whistles and short pulse trains.

Whistles

Whistles are frequency- and amplitude-modulated tones that typically last anywhere from 50 ms to 3 s or more, as illustrated in Fig. 20.14. They are arguably the most variable signals produced by dolphins. Both within and across species they range widely in duration, bandwidth and degree of frequency modulation. How whistles are used in communication is an ongoing topic of debate among researchers, but most agree that they play an important role in maintaining contact between dispersed individuals and are important in social interactions [20.85].

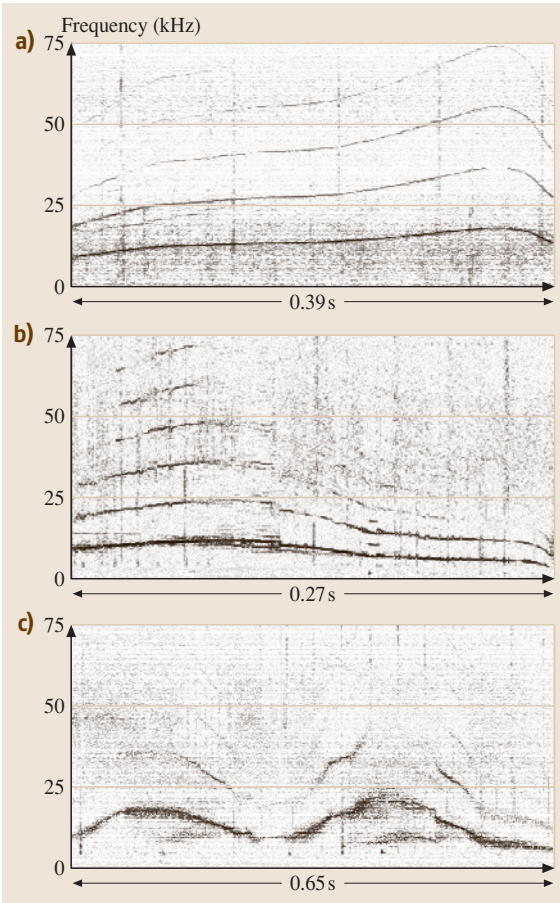


Fig. 20.14a–c Variations in whistle forms produced by Hawaiian spinner dolphins **(a)** and Atlantic spotted dolphins **(b)**, **(c)** exhibiting multiple harmonics (after *Lammers* et al. [20.83, 84])

Dolphin whistles exhibit both species and geographic specificity [20.86–90]. Differences are greatest between distantly related taxa and between species of different size. As a general rule, larger species tend to produce whistles with lower fundamental frequencies than smaller ones [20.88]. Geographic variations within a species are usually smaller than interspecific differences [20.87], but some species do develop regional dialects between populations [20.89, 90]. These dialects tend to become more pronounced with increasing geographic separation. In addition, pelagic species tend to have whistles in a higher-frequency range and with more modulation than coastal and riverine species [20.86, 88]. Such differences have been proposed as species-specific reproductive-isolating characteristics [20.86], as ecological adaptations to different environmental conditions and/or resulting from restrictions imposed by physiology [20.88]. On the other hand, it must also be noted that numerous whistle forms are also shared by both sympatric and allopatric species [20.91]. The communicative function of shared whistle forms is unknown, but it is intriguing as it suggests a further tendency towards a convergence in signal design.

Dolphins produce whistles with fundamental frequencies usually in the human audible range (below 20 kHz). However, whistles typically also have harmonics (Fig. 20.14), which occur at integer multiples of the fundamental and extend well beyond the range of human hearing [20.84]. Harmonics are integral components of tonal signals produced by departures of the waveform from a sinusoidal pattern. Dolphin whistle harmonics have a *mixed directionality* property, which refers to the fact they become more directional with increasing frequency [20.83, 92]. It has been proposed that this signal feature functions as a cue, allowing listening animals to infer the orientation and direction of movement of a signaling dolphin [20.83, 92]. Harmonics may therefore be important in mediating group cohesion and coordination.

Burst Pulses

In addition to whistles, most odontocetes also produce pulsed social sounds known as *burst pulse* signals. Burst pulse signals are broadband click trains similar to those used in echolocation but with inter-click intervals of only 2–10 ms [20.93]. Because these intervals are considerably shorter than the processing period generally associated with echolocation and because they are often recorded during periods of high social activity, burst pulse click trains are thought instead to play an important role in communication.

Amazon
EX1010 Page 828

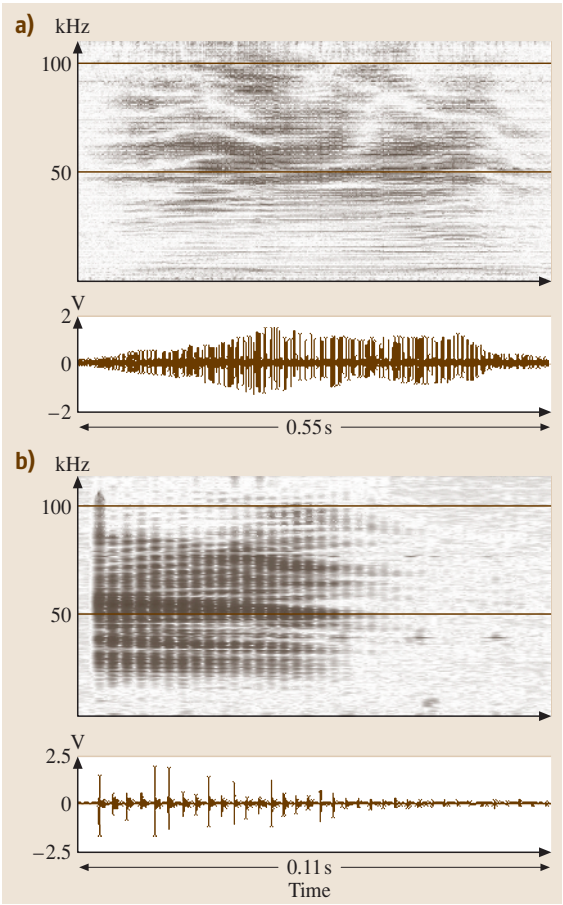


Fig. 20.15a,b Examples of **(a)** high-quantity and **(b)** low-quantity burst pulses produced by Atlantic spotted dolphins (*stenella frontalis*). Click train *a* has 255 clicks with mean ICI (interclick interval) of 1.7 ms. Click train *b* has 35 clicks with a mean ICI of 2.9 ms (after *Lammers* et al. [20.83, 84])

Burst pulses vary greatly in the inter-pulse interval and in the number of clicks that occur in a train, which can number anywhere from three to hundreds of pulses, as depicted in Fig. 20.15. This variation gives them distinctive aural qualities. Consequently, burst pulse sounds have been given many subjective labels, including *yelps* [20.94], *cracks* [20.95], *screams* [20.96] and *squawks* [20.97]. Their production has been reported in a variety of odontocete species including: the Atlantic bottlenose dolphin (*tursiops truncatus*) [20.95], the Hawaiian spinner dolphin (*stenella longirostris*) [20.72], the Atlantic spotted dolphin (*stenella frontalis*) [20.98], the narwhal (*monodon monoceros*) [20.99], Hector's dolphin (*cephalorhynchus hectori*) [20.100], the pilot whale (*globicephala melaena*) [20.101], and the harbor porpoise (*phocoena phocoena*) [20.101]. To date, much remains unknown about how burst pulses function as communication signals. It is generally believed that they play an important role in agonistic encounters because they are commonly observed during confrontational head-to-head behaviors between individuals [20.95, 102–104]. However, some authors have suggested they may represent emotive signals in a broader sense [20.97, 105, 106], possibly functioning as graded signals [20.107].

Given that dolphins have temporal discrimination abilities well within the range required to resolve individual clicks in a burst pulse [20.39, 108], it is possible that the quantity of clicks and their temporal spacing could form an important basis for communication. However, as with whistles, no data presently exist on the classification and discrimination tendencies of dolphins with respect to different burst pulses.

20.3.2 Signal Design Characteristics

Although much remains unknown about how odontocetes use acoustic signals for communication, the communicative potential of their signals can, in part, be inferred by considering the design characteristics that have been uncovered thus far. Signal features such as their detectable range, the production duty cycle, the identification level, the modulation potential and the form–content linkage provide useful clues about how odontocetes might use whistles and burst pulses.

The Active Space of Social Signals

The effective range of signals used for communication is generally termed the *active space*. *Janik* [20.109] investigated the active space of whistles produced by bottlenose dolphins in the Moray Firth, Scotland, using a dispersed hydrophone array to infer geometrically the location of signaling animals and establish the source level of their whistles. The mean source level was calculated to be 158 dB ± 0.6 re 1 µPa, with a maximum recorded level of 169 dB. By factoring in transmission loss, ambient noise levels, the critical ratios and auditory sensitivity of the species involved the active space of an unmodulated whistle between 3.5 and 10 kHz in frequency was estimated to be between 20 and 25 km in a habitat 10 meters deep at sea state 0. At sea state 4 the estimated active space ranged from 14 to 22 km, while for whistles at 12 kHz it dropped to between 1.5 and 4 km. These estimations

Amazon
EX1010 Page 829

were made for dolphins occurring in a relatively shallow, mostly mud-bottom, quiet environment. Presently, no data exist on the active space characteristics of delphinid whistles in pelagic waters and comparatively louder tropical near-shore environments. Similarly, no estimates have yet been made for the active space of burst pulses.

The Duty Cycle of Social Signals

Duty cycle refers to the proportion of time that any given signal or class of signals is *on* versus *off*. Signals can vary in the fine structure of their temporal patterning (e.g. duration), in their temporal spacing within a bout, and in their occurrence within a larger cyclical time frame, such as a 24 hour day. Each of these aspects of the temporal delivery of signals carries its own implication for communication. Fine-scale characteristics can define the nature of the signal itself and provide information about its relationship to other signals as well as constraints associated with its mechanism of production. The occurrence and timing of a signal within a bout can help convey information about the urgency of a situation, the level of arousal, the fitness of an individual and can assist the receiver in the task of localization. Finally, the periodicity of signals over hours or days can be an indicator of variables such as activity levels and reproductive state.

Murray et al. [20.110] investigated the fine-scale duty-cycle characteristics of delphinid social signals. Using a captive false killer whale (*pseudorca crassidens*) as their subject, they examined the temporal relationship between the units of a click train (individual clicks) and tonal signals. Their analysis revealed that false killer whales modulate the temporal occurrence of clicks to the point of grading them into a continuous wave (CW) signal such as a whistle. This finding was interpreted as evidence that *pseudorca* may employ graded signaling for communication (a topic discussed in more detail below), as well as to suggest that clicks and whistles are produced by the same anatomical mechanism.

The timing of signals within a bout has not been investigated with much success among delphinids. The primary obstacle towards this line of work has been the difficulty of identifying the signaler(s) involved for even short periods of time under field conditions. Early work by *Caldwell* and *Caldwell* [20.111] on a group or four naïve captive common dolphins (*delphinus delphis*) suggests that whistle exchanges do have temporal structure. In whistling bouts involving more than one signaler, the onset of a whistle specific to an individual was followed within two seconds by that of another. Furthermore, initiation of a whistle by two animals within 0.3 s of one another always resulted in the inhibition of one of them, with some individuals deferring more than others. Initiations separated by 0.4–0.5 s caused inhibition less frequently while those longer than 0.6 s resulted in almost no inhibition. Repeated whistles produced without an intervening response by another animal were usually delayed by less than one second. Thus, the duty cycle of whistling bouts and chorusing behavior among common dolphins does appear to follow certain temporal rules, but their significance is not clear.

Periodicity in social signaling has been investigated in captive bottlenose dolphins and common dolphins [20.112–114], as well as free-ranging spinner dolphins (*stenella longirostris*) [20.72] and common dolphins [20.115]. In the captive studies, signaling activity was linked to feeding schedules, nearby human activities and responses to different forms of introduced stress [20.113]. For spinner and common dolphins in the wild, the occurrence of social acoustic signals was highest at night, when both species were foraging, and lowest in the middle of the day.

The Identification Level of Social Signals

The role of delphinid whistles as individual-specific signals has been the focus of more scientific attention than any other aspect of their social acoustic signaling. *Caldwell* and *Caldwell* [20.116] were the first to propose that individual dolphins each possess their own distinct *signature* whistle. The idea was borne out of the observation that recently captured dolphins each produce a unique whistle contour that makes up over 90% of the individual's whistle output. Since being proposed, the so-called *signature whistle hypothesis* has emerged as the most widely accepted explanation for whistling behavior among dolphins. The idea has received support from numerous studies involving captive and restrained animals [20.85, 117–121] as well as from field studies of free-ranging animals [20.97, 122, 123]. Some, however, have argued that a simple signature function for dolphin whistling cannot account for the diversity of signals observed in socially interactive dolphin groups [20.124, 125]. While not denying the presence of signature whistles per se, these authors have argued that the large percentage of stereotyped signature signals observed in other studies may be an artifact of the unusual circumstances under which they were obtained (isolation, temporary restraint, separation, captivity). The debate over the prevalence of signature whistles among captive and free-ranging dolphins remains a contested topic in the

Amazon
EX1010 Page 830

literature and at scientific meetings. On the other hand, no evidence or formal discussions presently exist suggesting burst pulse signals carry any individual-specific information.

The Modulation Potential of Social Signals

The modulation potential describes the amount of variation present in any given signal as measured by its position along a scale from stereotyped to graded signaling [20.126]. Stereotyped signals are repeats of structurally identical forms and vary discretely between one another. They are used most often for communication when the prospect of signal distortion is high, such as in noisy or reverberant environments or for communicating over long ranges. Graded signals have more variants than stereotyped ones and are encoded by changing one or more signal dimensions. These can include intensity, repetition rate and/or frequency and amplitude modulation. Graded signals are usually employed when a continuous or relative condition must be communicated in a favorable propagation environment.

Many studies to date have made an a priori assumption that dolphin signaling is categorical in nature, with signals belonging to mutually exclusive classes on the basis of their shared similarities. Some evidence in support of this assumption comes from the signature-whistle hypothesis work, where restrained and isolated individuals are often observed producing highly stereotyped bouts of signaling. However, few data are presently available to suggest how dolphins perceive and distinguish social signals [20.127]. Therefore, it is unclear whether an assumption based on the occurrence of signature whistles is broadly applicable towards other forms of social acoustic signaling (i. e. non-signature whistles and burst pulses).

A few studies have explored the occurrence of graded signaling in the communication of delphinids and the larger whales. *Taruski* [20.128] created a graded model for the whistles produced by North Atlantic pilot whales (*globicephala melaena*). He concluded that these signals could be arranged as a "continuum or matrix (of signals) from simple to complex through a series of intermediates" (*Taruski* [20.128] p. 349). *Murray* et al. [20.110], examining the signals of a captive false killer whale (*Pseudorca crassidens*), came to a similar conclusion and proposed that *Pseudorca* signals were also best represented along a continuum of signal characteristics, rather than categorically. Finally, *Clark* [20.129], examining the "call" signals of southern right whales (a mysticete), made the observation that " ... the total repertoire of calls is best described as a sequence of intergraded types along a continuum" (*Taruski* [20.128] p. 1066). Therefore, graded signaling may well play a role in odontocete communication. Controlled perceptual experiments and a better understanding of the acoustic environment dolphins inhabit are needed to test how odontocetes discriminate and classify social sounds.

The Form–Content Linkage of Social Signals

The degree to which the form of a signal is linked to its content depends on how information is coded and on proximate factors associated with the signal's production. The relationship between a signal's structural form and its message can range from being rather arbitrary to tightly linked to a specific condition [20.126]. Among odontocetes, a clear relationship between signal form and content has only been demonstrated for signature whistles (discussed above). Dolphins have been experimentally shown to be capable of labeling objects acoustically (also known as vocal learning), as well as mimicking model sounds following only a single exposure [20.130]. Additional evidence of vocal learning exists from culturally transmitted signals in the wild [20.131] and in captivity [20.132], as well as from the spontaneous production of acoustic labels in captivity [20.127]. Context-specific variations in signature whistle form have also been demonstrated [20.121]. However, to date, no semantic rules have been identified for naturally occurring social signals among odontocetes.

Geographic Difference and Dialect

There is a distinct difference between geographical difference and dialect. Geographical differences are associated with widely separated populations that do not normally mix. Dialect is best reserved for sound emission differences on a local scale among neighboring populations which can potentially intermix [20.133]. Geographic variations are generally considered to result from acoustic adaptations to different environments, or a functionless byproduct of isolation and genetic divergence caused by isolation [20.134]. The functional significance of dialects is controversial, with some maintaining that dialects are epiphenomena of song learning and social adaptation, whereas others believe that they play a role in assorted mating and are of evolutionary significance [20.134]. Dialects are known to occur in many species of birds [20.135] but appear to be very rare in mammals.

Amazon
EX1010 Page 831

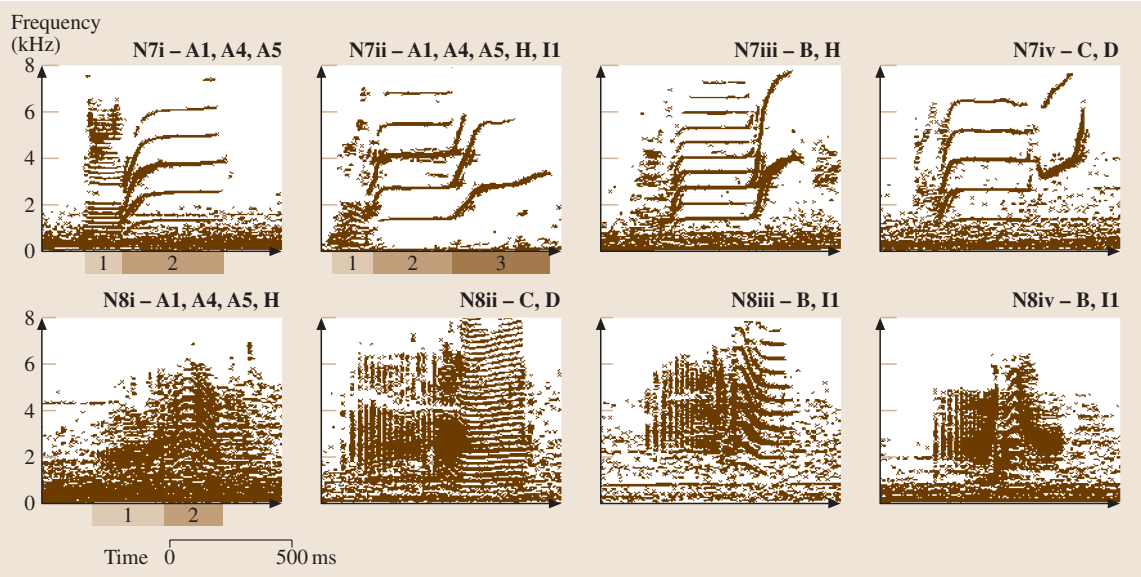


Fig. 20.16 Spectrograms of call types N7 and N8 for clan A. Above each spectrogram is the subtype identification and the pods that produce the variant, and below certain spectrograms are division marks separating calls into their component parts (after *Ford* [20.134]).

Killer Whale

Killer whales (*orcinus orca*) produce a specific type of burst pulse termed the *discrete call*. Discrete calls are thought to serve as contact calls between individuals, much like whistles in other odontocete species [20.136]. Discrete calls are population specific and even pod specific. The dialects of resident killer whales (*Orcinus orca*) in the coastal waters of British Columbia and Washington have been studied over a prolonged period by *Ford* and his colleagues [20.134, 137, 138]. They used photographic identification techniques, keying on unique natural markings on the whales to identify 16 pods or stable kin groups of 232 resident killer whales. Differences in acoustic behavior formed a system of related pod-specific dialects within the call tradition of each clan. *Ford* [20.134] has proposed that each clan is comprised of related pods that have descended from a common ancestral group and pod-specific repertoires probably serve to enhance the efficiency of acoustic communications within the group and act as behavioral indicators of pod affiliation.

Killer whale calls are typically made up of rapidly emitted pulses that to the human ear have a tonal quality [20.134]. Many calls have several abrupt shifts in pulse repetition rate allowing them to be divided into different segments or parts. Although all pods belonging to a clan share a number of calls, these calls were often rendered in consistently different form by different pods. Also, certain pods produced calls that were not used by the rest of the clan. Such variations produced a set of related group-specific dialects within the call tradition of each clan.

Spectrograms of call types N7 and N8 are shown in Fig. 20.16. In this example, we can see that different pods produce similar but different versions of call type N7 and N8. Pods A1, A4 and A5 produced two versions of call type N7 and pod B and I1 produced two versions of call type N8. All of the spectrograms have two parts except for call type N7ii, which had three parts.

Ford [20.134] contended that pod-specific repertories can be retained for periods in excess of 25 years. Discrete calls generally serve as signals for maintaining contact within the pod and that the use of repertoire of pod-specific calls enhances this function by conveying group identity and affiliation [20.134]. Killer whales, like most other small dolphins are able to learn and mimic a wide variety of sounds. Even from a young age, killer whale infants can selectively learn specific calls, especially the calls of their mothers. *Bowles* et al. [20.139] studied the development of calls of a captive-born killer whale calf and found that it learned and reproduced only the calls of its mother and ignored the calls of other killer whales in the same pool. *Ford* [20.134] also observed killer whales imi-

Amazon
EX1010 Page 832

tating the call types of different pods, and even those from other clans. These instances were rare, but it does show a capacity for learning and mimicry of acoustic signals.

Sperm Whales

Sperm whales live in a matrilineal family unit where there exist cooperative behaviors including communal care of the young in ways similar to killer whales. The family units are very stable and females may live as long as 60–70 y [20.140]. One type of signals that sperm whales emit are denoted as codas, which are sequences of click signals that may be the primary means of acoustic communications for these animals [20.58]. *Weilgart* and *Whitehead* [20.141] recorded, for over a year, codas from a number of sperm whales around the South Pacific and in the Caribbean Sea. Photographic identification also allowed them to assign recording sessions to particular groups. They found that the coda repertoire recorded from the same group on the same or different days were much more similar than those recorded from different groups in the same place. Groups recorded in the same place had more similar coda repertoire than those in the same broad area but different places. Groups from the same area were in turn marginally similar to those in the same ocean but different than those in different oceans. Coda class repertoires of groups in different oceans and in different areas within the same ocean were statistically significantly different. They concluded that strong group-specific dialects were apparently overlaid on weaker geographic variation. Sperm whales, killer whales and possibly bottlenose dolphins are the only cetaceans known to have dialects.

20.4 Acoustic Signals of Mysticetes

There are eleven species of mysticetes or baleen whales and sounds have been recorded from all but the pygmy right whale [20.142]. The vocalization of baleen whales can be divided into two general categories: (1) songs and (2) calls [20.142]. The calls can be further subdivided into three categories: (1) simple calls, (2) complex calls and (3) clicks, pulses, knocks and grunts [20.142]. Simple calls are often low-frequency, frequency-modulated signals with narrow instantaneous bandwidth that sound like moans if a recording is speeded up or slowed down, depending on the specific animal. Amplitude modulation and the presence of harmonics are usually part of a simple call, with most of the energy below 1 kHz. Complex calls are pulse-like broadband signals with a variable mixture of amplitude and/or frequency modulation. They sound like screams, roars, and growls, with most of the energy between 500–5000 Hz. Clicks, pulses, knocks and grunts are short-duration (< 0.1 s) signals with little or no frequency modulation. Clicks and pulses are very short (< 2 ms) signals with frequencies between 3–31 kHz, while grunts and knocks are longer (50–100 ms) signals in the 100–1000 Hz range [20.142].

20.4.1 Songs of Mysticete Whales

Songs are defined as "sequences of notes occurring in a regular sequence and patterned in time" [20.142]. Songs are easily discriminated from calls in most instances. Four mysticetes species have been reported to produce songs; the blue whale (*balaenoptera musculus*) [20.143], the fin whale (*balaenoptera physalus*) [20.144, 145], the bowhead whale (*balaena mysticetus*) [20.15], and the humpback whale [20.146]. Songs of humpback whales have without a doubt received the most attention from researchers. Part of the reason for this is the relative ease for investigators to travel and do research in the summer grounds of humpback whales, especially in Hawaii in the Pacific and Puerto Rico in the Atlantic.

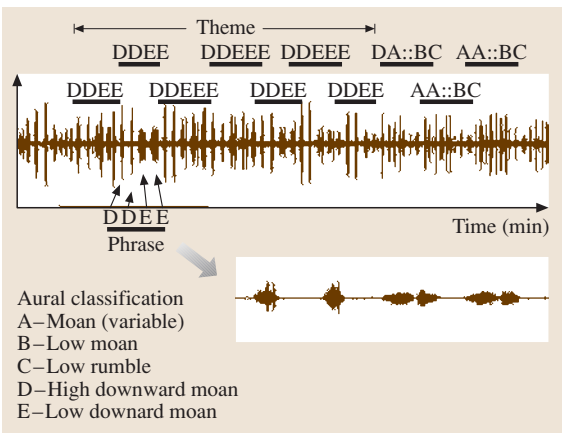


Fig. 20.17 Examples of two themes from a humpback whale song (after *Frankel* [20.36])

Amazon
EX1010 Page 833

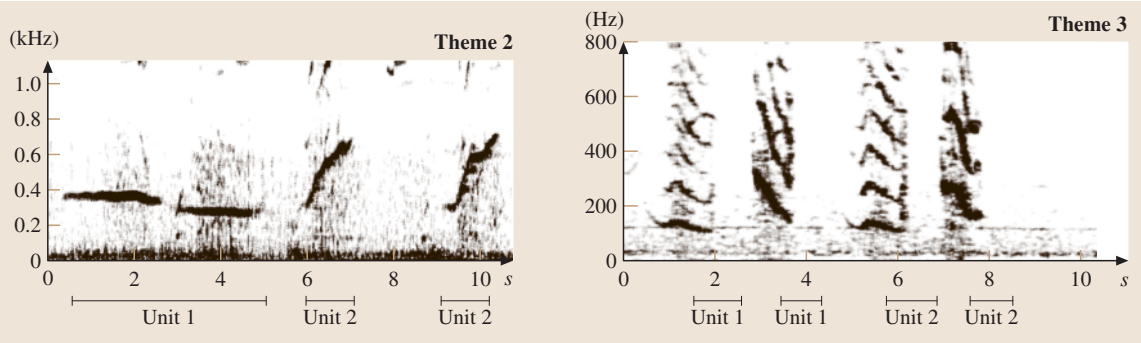


Fig. 20.18 An example of a portion of a humpback whale song. The individual pulse sounds are defined as units and units are aurally categorized based on how they sound. In this example, there are five units. Phrases are formed by a combination of units and themes are formed by a combination of phrases. The whole song consist of a combination of themes that are continuously repeated for the length of the song

Humpback Whale Songs

The list of studies involving humpback whale songs is long and extends from 1971 to the present time, *Helweg* et al. [20.147]. Although some songs may sound almost continuous to human listeners the basic units in a song are pulsed sounds. Songs are sung only by males and consist of distinct units that are produced in some sequence to form a phrase and a repeated set of phrases form a theme and repeated themes form a song. A song can last from minutes to hours depending on the disposition of the singer. An example of a portion of song is shown in Fig. 20.17. Example of two themes of a song in spectrogram format are shown in Fig. 20.18. The variation in frequency as a function of time is clearly shown in the figure.

Some general properties of songs and the whales that are singing are:

1. Songs from the North Pacific, South Pacific and Atlantic populations are different.
2. Singing peaks during the winter months when humpback whales migrate to warmer waters at lower latitudes.
3. Whales within a population sing the same basic song in any one year, although the song may undergo slight changes during a breeding season.
4. Changes in songs are not due to forgetting during the summer months, which are non-singing months, since songs recorded early in the winter breeding season are nearly the same as songs recorded late in the previous breeding season.
5. Songs from consecutive years are very similar but songs across nonconsecutive years will have fewer similarities.
6. Singers are most probably only males, since no females have been observed singing.
7. Some singing also occurs during the summer and fall.
8. Singing whales are often alone, although they have been occasionally observed singing in the presence of other humpback whales.
9. Singers tend to remain stationary. However, they have also been observed singing while swimming.

Other Mysticetes

Bowhead whales emit a variety of different types of simple and complex sounds that sound like moans to the human ear. They also emit sequential sounds that contain repeatable phrases that can be classified as songs during their spring migration [20.15] but not during the summer or autumn [20.148]. The bowhead song had just one theme with basically only two sounds repeated over and over. *Ljungblad* et al. [20.15] reported that songs were very tonal with clear pitch even though they were produced by pulsive moans, whereas *Cummings* and *Holliday* [20.149] described songs as sounding like raucous elephant roars and trumpeting in discrete repetitions or phases that were put together to form longer sequences. Differences in the songs recorded by *Ljungblad* et al. [20.15] and by *Cummings* and *Holliday* [20.149] may be due to bowhead whales changing their songs from year to year.

The sounds from finback whales include single 20 Hz pulses, irregular series of 20 Hz pulses, and stereotyped 20 Hz signal bouts of repetitive sequences of 20 Hz pulses [20.145]. The 20 Hz signals are emitted in bouts that can last for hours. The pulse intervals in a bout were very regular. In general, signals are produced in

Amazon
EX1010 Page 834

Table 20.2 Characteristics of mysticete whales vocalizations

Species of whales	Signal type	Frequency limits(HZ)	Dominat frequency (Hz)	Source level (dB re 1 μPa) at 1 m	References
Blue	FM moans	12.5 – 200	16 – 25	188	*Cummings*, *Thompson* [20.150], *Edds* [20.151]
	Songs	16 – 60	16– 60	–	*McDonald* et al. [20.152]
Bowhead	Tonal moans	25 –900	100 – 400	129 – 178	*Cummings*, *Holliday* [20.149]; *Wursig*, *Clark* [20.148]
	Pulses	25 –3500	152 – 185		
	Songs	20 – 500	158 – 189		*Cummings*, *Holliday* [20.149]; *Ljungblad* et al. [20.15]
Bryde's	FM moans	70 – 245	124 – 132	152 – 174	*Cummings* et al. [20.153]; *Edds* et al. [20.154]
	Pulsed moans	100 - 930	165 – 900	–	*Edds* et al. [20.154]
	Discrete pulses	700- 950	700 – 950	–	*Edds* et al. [20.154]
Finback	FM moans	14 – 118	20	160 – 186	*Watkins* [20.145], *Edds* [20.155], *Cummings*, *Thompson* [20.156]
	Tonals	34 – 150	34 – 150	–	*Edds* [20.155]
	Songs	17 – 25	17 – 25	186	*Watkins* [20.145]
Gray	Pulses	100 – 2000	300 – 825	–	*Dalheim* et al. [20.157]; *Crane* et al. [20.158]
	FM moans	250 – 300	250 – 300	152	*Cummings* et al. [20.159]; *Dalheim* et al. [20.157]
	LF-FM-moans	125 – 1250	< 430	175	*Cummings* et al. [20.159]; *Dalheim* et al. [20.157]
	PM pulses	150 – 1570	225 – 600		*Cummings* et al. [20.159]; *Dalheim* et al. [20.157]
	Complex moans	35 – 360	35 – 360		*Cummings* et al. [20.159]
Humpback	Grunts (pulse & FM)	25 – 1900	25 – 1900	176	*Thompson* et al. [20.160]
	Pulses	25 – 89	25 – 80	144 – 174	*Thompson* et al. [20.160]
	Songs	30 – 8000	120 – 4000	–	*Payne*, *Payne* [20.161]
Minke	FM tones	60 – 130	60 – 130	165	*Schevill*, *Watkins* [20.162],
	Thumps	100 – 200	100 – 200	–	*Winn*, *Perkins* [20.163]
	Grunts	60 – 140	60 – 140	151 – 175	*Winn*, *Perkins* [20.163]
	Ratchets	850 – 6000	850	–	*Winn*, *Perkins* [20.163]
Right-N	Moans	< 400	–	–	*Schevill*, *Watkins* [20.162]
Right-S	Tonal	30 – 1250	160 – 500	–	*Cummings* et al. [20.164], *Clark* [20.129, 165]
	Pulses	30 – 2200	50 – 500	172 – 187	*Cummings* et al. [20.164], *Clark* [20.129, 165]
Sei	FM sweeps	1500 – 3500	1500 – 3500	–	*Knowlton* et al. [20.166]

a relatively regular sequence of repetitions at intervals ranging from about 7–26 s, with bouts that can last as long as 32.5 h. During a bout, periodic rests averaged about 115 s at roughly 15 min intervals and sometimes longer irregular gaps between 20 and 120 min were observed. There was also some variability in the 20 Hz signals in that they were never exactly replicated.

The songs of the blue whales (*balaenoptera musculus*) have been observed by a number of researchers [20.143, 152, 167]. A typical two-part blue whale song time series and corresponding spectrogram is shown in Fig. 20.18. The spectrogram of the first part of the two part song had six spectral lines separated by about 1.5 Hz. This type of spectrogram is typically generated by pulses. *Cummings* and *Thompson* [20.150] previously reported on the pulsive nature of some blue whale moans. The second part of the song was tonal in nature with a slight FM down sweep varying from 19 Hz to 18 Hz in the first 3–4 s. The 18 Hz tone is then carried until the last 5 s when there is an abrupt step down to

Amazon
EX1010 Page 835

17 Hz. The amplitude modulation in the second part of the song was probably caused by multi-path propagation of the signal from the whale to the hydrophones. These two-part songs basically follow a pattern of a 19 s pulsive signal followed by a 24.5 s gap and a 19 s monotonic signal [20.152, 167].

Calls of Mysticete Whales

The calls of mysticete whales have been the subject of much research over the past three decades. As with dolphin sounds, there is also a lack of any standard nomenclature for describing emitted sounds. Similar calls are often given different names by different researchers. A summary of some of the acoustic properties of the different baleen whales is indicated in Table 20.2. Calls and songs are most likely used for some sort of communication, however, at this time the specific meanings of these sounds are not known. It is extremely difficult to study the context and functions of baleen whale vocalization. The sounds of mysticete whales have also been summarized nicely by *Richardson* et al. [20.34]. Instead of discussing the characteristics of various sounds, the properties of calls are summarized in Table 20.2. The calls of mysticete whales are mainly in the low-frequency range, from an infrasonic frequency of about 12.5 Hz for the blue whale to about 3.5 kHz for the sei whale. There are a variety of different types of calls, from FM tones to moans, grunts and discrete pulses. How these sounds are used by whales is still an open question since it is often very difficult to observe behavior associated with different calls.

20.5 Discussion

Cetaceans use a wide variety of sounds from brief echolocation signals used by dolphins having durations less than 100 μs to very long duration songs that can last for hours by are emitted by humpback whales. The range of frequency is also very large, from low-frequency (infrasonic) sounds between 10–20 Hz used by blue and finback whales to high-frequency echolocation signals that extend to 130–140 kHz or perhaps higher (see earlier mention of 180 kHz). It is quite clear that acoustics is important in the natural history of cetaceans since all species regularly emit sounds throughout their daily routine. Yet, it is not at all clear how sounds are used by these animals. The difficulty in observing the behavior of these animals has made it difficult to attach any function to a particular or specific sound. It is nearly impossible to determine a one-to-one relationship between the reception or transmission of a specific sound to specific behavioral response. There are many possible functions of sounds, some of which may include providing contact information in a population of animals, signaling alarm or warning of approaching predators, attracting potential mates, echolocation for prey detection and discrimination while foraging, a way of establishing a hierarchy, providing individual identification, and a method for disciplining juveniles. Although researchers have not been successful in uncovering the role or function of specific sounds in any cetacean species, researchers should not be discouraged but should be innovative and imaginative in designing experiments that can be conducted in the wild to delve deeper into this problem. Even with echolocation sounds, there are many unanswered question. It seems logical that echolocation sounds are used to detect and discriminate prey and to navigate, yet we still know very little about how often they are emitted during a daily routine for dolphins in the field.

In this chapter, we have seen that the characteristics of the sounds emitted by cetaceans depends a lot on the size of the animals. Therefore the active space of different species is indirectly related to the size of the animals since the amount of sound absorption by

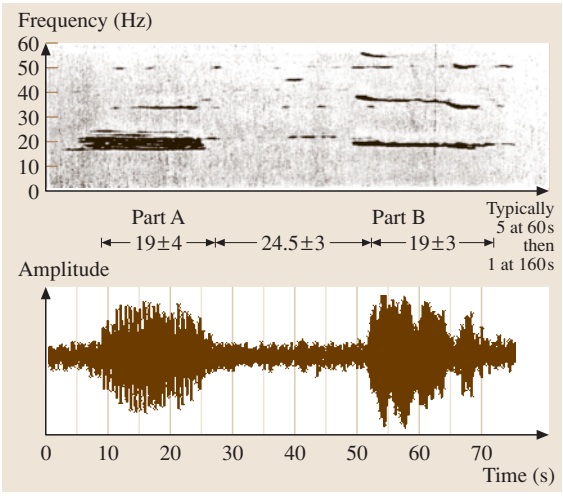


Fig. 20.19 Time series and spectrogram of a typical blue whale song (after [20.152])

Amazon
EX1010 Page 836

sea water increases with frequency. Dolphins and small whales usually emit echolocation signals that can have peak frequencies up to 120–140 kHz and whistles between 10–20 kHz. These signals are not meant to travel large distances so that the active space is rather small, tens of meters for echolocations and burst pulse signals and several hundred meters for whistles. These signals will certainly propagate to much shorter distances than the low-frequency signals used by many of the baleen whales. The sound pressure level (SPL) of an emitted signal at any range from the animal is given by the equation

$$\mathrm{SPL} = \mathrm{SL} - \text{geometric spreading loss} - \alpha R\,, \tag{20.11}$$

where SL is the source level in dB, α is the sound absorption coefficient in dB/m and R is the distance the sound has traveled. The geometric spreading loss does not depend on frequency but is affected by the sound velocity profile, the depth of the source and the receiver. The most severe geometric spreading loss is associated with spherical spreading loss in which the amount of geometric spreading loss is equal to $20 \log R$. The least severe geometric spreading loss is associated with sound channels, such as the sound fixing and ranging (SOFAR) channel. In order to gain an appreciation of the effects of absorption losses for different types of cetacean signals, $-\alpha R$ in (20.9) was calculated as a function of range and the results are shown in Fig. 20.20. The results indicate that the low-frequency sounds used by baleen whales do not suffer as much absorption loss as the sounds of small odontocetes. Therefore, baleen whale signals can propagate long distances if some type of channel is present in the water column.

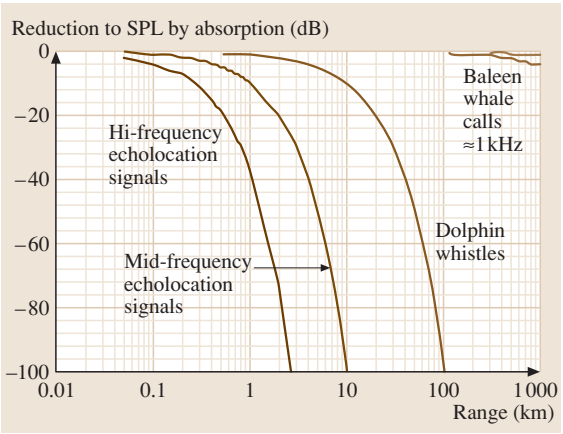


Fig. 20.20 Reduction to sound pressure level caused by sound absorption for different types of cetacean signals. The curve for the high-frequency echolocation signals was calculated at 120 kHz, and for the mid-frequency echolocation signals at 50 kHz. The curve for the dolphin whistle was calculated at 15 kHz. The baleen whale signal curve was determined at 1 kHz.

We have just scraped the top of the iceberg in regards to our understanding of cetacean acoustics. There is much to learn and understand about how these animals produce and receive sounds and how acoustics is used in their daily lives. The future looks extremely promising as new technology arrives on the scene that will allow researchers to delve into the many unanswered questions. As computer chips and satellite transmission tags get smaller and we apply state-of-the-art technologies to the study of cetaceans, our knowledge and understanding can but increase.

References

20.1 S.H. Ridgway: Who are the Whales, Bioacoust. **8**, 3–20 (1997)

20.2 B. Møhl, W.W.L. Au, J. Pawloski, P.E. Nachtigall: Dolphin hearing: Relative sensitivity as a function of point of application of a contact sound source in the jaw and head region, J. Acoust. Soc. Am. **105**, 3421–3424 (1999)

20.3 T.H. Bullock, A.D. Grinnell, E. Ikezono, K. Kameda, Y. Katsuki, M. Nomoto, O. Sato, N. Suga, K. Yanagisawa: Electrophysiological studies of central auditory mechanisms in Cetaceans, Z. Vergl. Phys. **59**, 117–316 (1968)

20.4 J.G. McCormick, E.G. Wever, J. Palin, S.J.H. Ridgway: Sound conduction in the dolphin ear, J. Acoust. Soc. Am. **48**, 1418–1428 (1970)

20.5 K.S. Norris: The evolution of acoustic mechanisms in odontocete cetaceans. In: *Evolution and Environment*, ed. by E.T. Drake (Yale Univ. Press, New Haven 1968) pp. 297–324

20.6 J.L. Aroyan: Three-dimensional modeling of hearing in Delphinus delphis, J. Acoust. Soc. Am. **110**, 3305–3318 (2001)

20.7 W.W.L. Au: Hearing in whales and dolphins: An overview. In: *Hearing by Whales and Dolphins*, ed. by W.W.L. Au, A.N. Popper, R.R. Fay (Springer, Berlin, New York. 2000) pp. 1–42

20.8 W.W.L. Au: Echolocation in dolphins. In: *Hearing by Whales and Dolphins*, ed. by W.W.L. Au, A.N. Popper, R.R. Fay (Springer, Berlin, New York 2000) pp. 364–408

Amazon EX1013 Page 837
EX1010 Page 837

20.9 C.S. Johnson: Sound detection thresholds in marine mammals. In: *Marine Bioacoustics*, ed. by W. Tavolga (Pergamon, New York 1967) pp. 247–260

20.10 S. Andersen: Auditory sensitivity of the harbor porpoise, Phocoena phocoena. Invest. Cetacea **2**, 255–259 (1970)

20.11 R.A. Kastelein, P. Bunskoek, M. Hagedoorn, W.W.L. Au, D. de Haan: Audiogram of a harbor porpoise (Phocoena phocoena) measured with narrow-band frequency modulated signals, J. Acoust. Soc. Am. **112**, 334–344 (2002)

20.12 J.D. Hall, C.S. Johnson: Auditory thresholds of a killer whale, J. Acoust.Soc. Am. **51**, 515–517 (1971)

20.13 M.D. Szymanski, D.E. Bain, K. Kiehi, S. Pennington, S. Wong, K.R. Henry: Killer whale (Orcinus orca) hearing: Auditory brainstem response and behavioral audiograms, J. Acoustic. Soc. Am. **106**, 1134–1141 (1999)

20.14 M.J. White Jr., J. Norris, D. Ljungblad, K. Baron, G. di Sciara: *Auditory thresholds of two beluga whales (Delphinapterus leucas). HSWRI Tech. Rep. No. 78-109* (Hubbs Marine Research Institute, San Diego 1979)

20.15 D.K. Ljungblad, P.D. Scoggins, W.G. Gilmartin: Auditory thresholds of a captive eastern Pacific bottlenose dolphin, Tursiops spp., J. Acoust. Soc. Am. **72**, 1726–1729 (1982)

20.16 J. Thomas, N. Chun, W. Au, K. Pugh: Underwater audiogram of a false killer whale (Pseudorca crassidens), J. Acoust. Soc. Am. **84**, 936–940 (1988)

20.17 D. Wang, K. Wang, Y. Xiao, G. Sheng: Auditory sensitivity of a Chinese River Dolphin, Lipotes vexillifer. In: *Marine Mammal Sensory Systems*, ed. by J.A. Thomas, R.A. Kastelein, Aya Supin (Plenum, New York 1992) pp. 213–221

20.18 P.E. Nachtigall, W.W.L. Au, J.L. Pawloski, P.W.B. Moore: Risso's Dolphin (Grampus griseus) Hearing Thresholds in Kaneohe Bay, Hawaii. In: *Sensory Systems of Aquatic Mammals*, ed. by R.A. Kastelein, J.A. Thomas, P.E. Nachtigall (DeSpiel, Woerden 1995) pp. 49–53

20.19 M. Sauerland, D. Dehnhardt: Underwater Audiogram of a Tucuxi (Sotalia fluviatilis guianensis), J. Acoust. Soc. Am. **103**, 1199–1204 (1998)

20.20 R.A. Kastelein, M. Hagedoorn, W.W.L. Au, D. de Haan: Audiogram of a striped dolphin (Stenella coeruleoalba), J. Acoust. Soc. Am. **113**, 1130–1144 (2003)

20.21 R.R. Fay: *Hearing in Vertebrates: A Psychophysics Databook* (Hill-Fay Associates, Winnetka 1988)

20.22 A.W. Mills: On the Minimum Audible Angle, J. Acoust. Soc. Am. **30**, 237–246 (1958)

20.23 D.L. Renaud, A.N. Popper: Sound localization by the bottlenose porpoise Tursiops truncatus, J. Exp. Biol. **63**, 569–585 (1978)

20.24 A.W. Mills: Auditory localization. In: *Foundations of Modern Auditory Theory*, Vol. 2, ed. by J.V. Tobias (Academic, New York 1972) pp. 303–348

20.25 W.H. van Dudok Heel: Sound and Cetacea, Netherlands J. Sea Res. **1**, 407–507 (1962)

20.26 S. Andersen: Directional hearing in the harbour porpoise, Phocoena phocena. Invest. Cetacea **2**, 261–263 (1970)

20.27 D.L. Renaud, A.N. Popper: Sound localization by the bottlenose porpoise, tursiops truncatus, J. Exp. Biol. **63**, 569–585 (1975)

20.28 W.W.L. Au, P.W.B. Moore: Receiving Beam Patterns and Directivity Indices of the Atlantic Bottlenose Dolphin Tursiops truncates, J. Acoust. Soc. Am. **75**, 255–262 (1984)

20.29 D.S. Houser, J. Finneran, D. Carder, W. Van Bonn, C. Smith, C. Hoh, R. Mattrey, S. Ridgway: Structural and Functional Imaging of BottlenoseDolphin (Tursiops truncatus) Cranial Anatomy, J. Exp. Biol. **207**, 3657–3665 (2004)

20.30 K.A. Zaytseva, A.I. Akopian, V.P. Morozov: Noise resistance of the dolphin auditory analyzer as a function of noise direction, BioFizika **20**, 519–521 (1975)

20.31 R.J. Urick: *Principles of Underwater Sounds for Engineers* (McGraw-Hill, New York 1980)

20.32 J.M. McCormick, M.G. Salvadori: *Numerical Methods in FORTRAN* (Prentice-Hall, Englewood Cliffs 1964),

20.33 D.R. Ketten: The marine mammal ear: specializations for aquatic audition and echolocation. In: *The Evolutionary Biology of Hearing*, ed. by D. Webster, R. Fay, A. Popper (Springer, Berlin, New York 1992) pp. 717–754

20.34 W.J. Richardson, C.R. Greene Jr., C.I. Malme, D.H. Thomson: *Marine Mammals and Noise* (Academic, San Diego 1995)

20.35 W.J. Richardson, B. Würsig, C.R. Greene Jr: Reactions of bowhead whales, Balaena mysticetus, to drilling and dredging noise in the Canadian Beaufort Sea, Mar. Envr. Res. **29**, 135–160 (1990),

20.36 A.S. Frankel: *Acoustic and visual tracking reveals distribution, song variability and social roles of humpback whales in Hawai'ian waters. Ph.D. Dissertation* (Univ. Hawaii, Honolulu, HI 1994)

20.37 C.R. Ridgway: Electrophysiological experiments on hearing in odontocetes. In: *Animal Sonar*, ed. by P.E. Nachtigall, P.W.B. Moore (Plenum, New York 1980) pp. 483–493

20.38 S.H. Ridgway, D.A. Carder: Assessing hearing and sound production in cetaceans not available for behavioral audiograms: Experiences with sperm, pygmy sperm and gray whales, Aquatic Mammals. **27**, 267–276 (2001)

20.39 W.W.L. Au: *The Sonar of Dolphins* (Springer, Berlin, New York 1993)

20.40 S.H. Ridgway, D.A. Carder: Nasal pressure and sound production in an echolocating white whale, Delphinapterus leucas. In: *Animal Sonar: Processes and Performance*, ed. by P.E. Nachtigall,

Amazon
EX1010 Page 838

P.W.B. Moore (Plenum, New York 1988) pp. 53–60,
20.41 F.G. Wood: Discussion. In: *Marine Bio-Acoustics Vol. II*, ed. by W. Tavolga (Pergamon, Oxford 1964) pp. 395–396
20.42 K.S. Norris, G.W. Harvey: Sound transmission in the porpoise head, J. Acoust. Soc. Am. **56**, 659–664 (1974)
20.43 J.L. Aroyan, T.W. Cranford, J. Kent, K.S. Norris: Computer modeling of acoustic beam formation in Delphinus delphis, J. Acoust. Soc. Am. **95**, 2539–2545 (1992)
20.44 T.W. Cranford: In Search of Impulse sound sources in odontocetes. In: *Hearing by Whales and Dolphins*, ed. by W.W.L. Au, A.N. Popper, R.R. Fay (Springer, New York 2000) pp. 109–155
20.45 W.W.L. Au, R.W. Floyd, R.H. Penner, A.E. Murchison: Measurement of echolocation signals of the Atlantic bottlenose dolphin Tursiops truncatus Montagu, in Open Waters, J. Acoust. Soc. Am. **56**, 280–1290 (1974)
20.46 W.E. Evans: Echolocation by marine delphinids and one species of fresh-water dolphin, J. Acoust. Soc. Am. **54**, 191–199 (1973)
20.47 W.W.L. Au, D.A. Carder, R.H. Penner, B.L. Scronce: Demonstration of adaptation in beluga whale echolocation signals, J. Acoust. Soc. Am. **77**, 726–730 (1985)
20.48 B.S. Gurevich, W.E. Evans: Echolocation discrimination of complex planar targets by the beluga whale (Delphinapterus leucas), J. Acoust. Soc. Am. **60**, S5 (1976)
20.49 C. Kamminga, H. Wiersma: Investigations on cetacean sonar V. The true nature of the sonar sound of Cephaloryncus Commersonii, Aqua. Mamm. **9**, 95–104 (1981)
20.50 C.W. Turl, D.J. Skaar, W.W.L. Au: The Echolocation Ability of the Beluga (Delphinapterus leucas) to detect Targets in Clutter, J. Acoust. Soc. Am. **89**, 896–901 (1991)
20.51 P.W.B. Moore, D.A. Pawloski: Investigations on the control of echolocation pulses in the dolphin (Tursiops truncatus). In: *Sensory Abilities of Cetaceans Laboratory and Field Evidence*, ed. by J.A. Thomas, R.A. Kastelein (Plenum, New York 1990) pp. 305–316
20.52 W.W.L. Au, J.L. Pawloski, P.E. Nachtigall: Echolocation signals and transmission beam pattern of a false killer whale (Pseudorc crassidens), J. Acoust. Soc. Am. **98**, 51–59 (1995)
20.53 J. Thomas, M. Stoermer, C. Bowers, L. Anderson, A. Garver: Detection abilities and signal characteristics of echolocating false killer whales (Pseudorca crassidens). In: *Animal Sonar Processing and Performance*, ed. by P.E. Nachtigall, P.W.B. Moore (Plenum, New York 1988) pp. 323–328
20.54 J.A. Thomas, C.W. Turl: Echolocation characteristics and range detection by a false killer whale Pseudorca crassidens. In: *Sensory Abilities of Cateceans: Laboratory and Field Evidence*, ed. by J.A. Thomas, R.A. Kastelein (Plenum, New York 1990) pp. 321–334
20.55 W.W.L. Au, J.K.B. Ford, J.K. Horne, K.A. Newman-Allman: Echolocation signals of free-ranging killer whales (Orcinus orca) and modeling of foraging for chinook salmon (Oncorhynchus tshawytscha), J. Acoust. Soc. Am. **115**, 901–909 (2004)
20.56 W.W.L. Au, B. Würsig: Echolocation signals of dusky dolphins (Lagenorhynchus obscurus) in Kaikoura, New Zealand, J. Acoust. Soc. Am. **115**, 2307–1313 (2004)
20.57 W.W.L. Au, D. Herzing: Echolocation signals of wild Atlantic spotted dolphin (Stenella frontalis), J. Acoust. Soc. Am. **113**, 598–604 (2003)
20.58 W.A. Watkins, W.E. Schevill: Sperm whale codas, J. Acoust. Soc. Am. **62**, 1485–1490 (1977)
20.59 C. Levenson: Source level and bistatic target strength of sperm whale (Physeter catodon) measured from an oceanographic aircraft, J. Acoust. Soc. Am. **55**, 1100–1103 (1974)
20.60 L. Weilgart, H. Whitehead: Distinctive vocalizations from mature male sperm whales (Physter macrocephalus), Can. J. Zool. **66**, 1931–1937 (1988)
20.61 B. Møhl, E. Larsen, M. Amundin: Sperm Whale Size Determination: Outlines of an Acoustic Approach. In: *Mammals in the Seas. Fisheries series No. 5, Mammals of the Seas*, Vol. 3 (FAO (Food and Agriculture Organization of the United Nations) Publications, Rome 1981) pp. 327–331
20.62 J.L. Dunn: Airborne Measurements of the Acoustic Characteristics of a Sperm Whale, J. Acoust. Soc. Am. **46**, 1052–1054 (1969)
20.63 W.A. Watkins: Acoustics and the behavior of sperm whales. In: *Animal Sonar Systems*, ed. by R.G. Busnel, J.F. Fish (Plenum, New York 1980) pp. 291–297
20.64 B. Møhl, M. Wahlberg, A. Heerfordt: A GPS-linked array of independent receiver for bioacoustics, J. Acoust. Am. **109**, 434–437 (2001)
20.65 B. Møhl, M. Wahlberg, P.T. Madsen, A. Heerfordt, A. Lund: The monpulsed natue of sperm whale clicks, J. Acoust. Soc. Am. **114**, 1143–1154 (2003)
20.66 W.W.L. Au, R.H. Penner, C.W. Turl: Propagation of beluga echolocation signal, J. Acoust. Soc. Am. **82**, 807–813 (1987)
20.67 R.A. Kastelein, W.W.L. Au, H.T. Rippe, N.M. Schooneman: Target detection by an echolocating harbor porpoise (Phocoena phocoena), J. Acoustic. Soc. Am. **105**, 2493–2498 (1999)
20.68 W.W.L. Au, K.J. Snyder: Long-range Target Detection in Open Waters by an Echolocating Atlantic Bottlenose Dolphin (Tursiops truncatus), J. Acoust. Soc. Am. **68**, 1077–1084 (1980)
20.69 P.T. Madsen, D.A. Carder, K. Bedholm, S.H. Ridgway: Porpoise clicks from a sperm whale nose –convergent evolution of 130 kHz pulses in toothed whale sonars?, Bioacoustics **15**, 192–206 (2005)
20.70 W.W.L. Au, R.A. Kastelein, T. Ripper, N.M. Schooneman: Transmission beam pattern and echolocation

Amazon
EX1010 Page 839

signals of a harbor porpoise (Phocoena phocoena), J. Acoustic. Soc. Am. **106**, 3699–3705 (1999)
20.71 K.W. Pryor, K.S. Norris: *Dolphin Societies: Discoveries and Puzzles* (Univ. California Press, Berkley 1991)
20.72 K.S. Norris, B. Würsig, R.S. Wells, M. Würsig: *The Hawai'ian Spinner Dolphin* (Univ. California Press, Berkeley 1994) p. 408
20.73 J. Mann, P.L. Tyack, H. Whitehead: *Cetacean societies: field studies of dolphins and whales* (Univ. Chicago Press, Chicago 2000)
20.74 L.M. Herman, W.N. Tavolga: The communications systems of cetaceans. In: *Cetacean Behavior: Mechanisms and Function*, ed. by L.M. Herman (Wiley-Interscience, New York 1980) pp. 149–209
20.75 K.W. Pryor: Non-acoustic communication in small cetaceans: glance touch position gesture and bubbles. In: *Sensory Abilities of Cetaceans*, ed. by J. Thomas, R. Kastelein (Plenum, New York 1990) pp. 537–544
20.76 K.M. Dudzinski: Contact behavior and signal exchange in Atlantic spotted dolphins (Stenella frontalis), Aqua. Mamm. **24**, 129–142 (1998)
20.77 C.M. Johnson, K. Moewe: Pectoral fin preference during contact in Commerson's dolphins (Cephalorhynchus commersonii), Aqua. Mamm. **25**, 73–77 (1999)
20.78 P.E. Nachtigall: Vision, audition and chemoreception in dolphins and other marine mammals. In: *Dolphin Cognition and Behavior: A Comparative Approach*, ed. by R.J. Schusterman, J.A. Thomas, F.G. Wood (Lawrence Erlbaum, Hillsdale 1986) pp. 79–113
20.79 V.B. Kuznetsov: Chemical sense of dolphins: quasi-olfaction. In: *Sensory Abilities of Cetaceans*, ed. by J. Thomas, R. Kastelein (Plenum, New York 1990) pp. 481–503
20.80 K.S. Norris, E.C. Evans III.: On the evolution of acoustic communication systems in vertebrates, Part I: Historical aspects. In: *Animal Sonar: Processes and Performance*, ed. by P.E. Nachtigall, P.W.B. Moore (Plenum, New York 1988) pp. 655–669
20.81 R.E. Thomas, K.M. Fristrup, P.L. Tyack: Linking the sounds of dolphins to their locations and behavior using video and multichannel acoustic recordings, J. Acoust. Soc. Am. **112**, 1692–1701 (2002)
20.82 K.R. Ball, J.R. Buck: A beamforming video recorder for integrated observations of dolphin behavior and vocalizations, J. Acoust. Soc. Am. **117**, 1005–1008 (2005)
20.83 M.O. Lammers, W.W.L. Au, D.L. Herzing: The broadband social acoustic signaling behavior of spinner and spotted dolphins, J. Acoust. Soc. Am. **114**, 1629–1639 (2003)
20.84 M.O. Lammers, W.W.L. Au: Directionality in the whistles of Hawai'ian spinner dolphins (Stenella longirostris): A signal feature to cue direction of movement?, Mar. Mamm. Sci. **19**, 249–264 (2003)
20.85 V.M. Janik, P.J.B. Slater: Context specific use suggests that bottlenose dolphin signature whistles are cohesion calls, Anim. Behav. **56**, 829–838 (1998)
20.86 W.W. Steiner: Species-specific differences in pure-tonal whistle vocalizations of five western north Atlantic dolphin species, Behav. Ecol. Sociobiol. **9**, 241–246 (1981)
20.87 L.E. Rendell, J.N. Matthews, A. Gill, J.C.D. Gordon, D.W. MacDonald: Quantitative analysis of tonal calls from five odontocete species, examining interspecific and intraspecific variation, J. Zool. **249**, 403–410 (1999)
20.88 W. Ding, B. Wursig, W.E. Evans: Comparisons of whistles among seven odontocete species. In: *Sensory Systems of Aquatic Mammals*, ed. by R.A. Kastelein, J.A. Thomas (De Spil, Woerden 1995) pp. 299–323
20.89 W. Ding, B. Wursig, W.E. Evans: Whistles of bottlenose dolphins: comparisons among populations, Aqua. Mamm. **21**, 65–77 (1995)
20.90 C. Bazua-Duran, W.W.L. Au: Geographic variations in the whistles of spinner dolphins (Stenella longirostris) of the Main Hawai'ian Islands, J. Acoust. Soc. Am. **116**, 3757–3769 (2004)
20.91 J.N. Oswald, J. Barlow, T.F. Norris: Acoustic identification of nine delphinid species in the eastern tropical Pacific Ocean, Mar. Mamm. Sci. **19**, 20–37 (2003)
20.92 P.J.O. Miller: Mixed-directionality of killer whale stereotyped calls: a direction-of-movement cue?, Behav. Ecol. Sociobiol. **52**, 262–270 (2002)
20.93 M.O. Lammers, W.W.L. Au, R. Aubauer: A comparative analysis of echolocation and burst-pulse click trains in Stenella longirostris. In: *Echolocation in Bats and Dolphins*, ed. by J. Thomas, C. Moss, M. Vater (Univ. Chicago Press, Chicago 2004) pp. 414–419
20.94 A.E. Puente, D.A. Dewsbury: Courtship and copulatory behavior of bottlenose dolphins (Tursiops truncatus), Cetology **21**, 1–9 (1976)
20.95 M.C. Caldwell, D.K. Caldwell: Intraspecific transfer of information via the pulsed sound in captive Odontocete Cetaceans. In: *Animal Sonar Systems: Biology and Bionics*, ed. by R.G. Busnel (Laboratoire de Physiologie Acoustic: Jouy-en-Josas, France 1967) pp. 879–936
20.96 S.M. Dawson: Clicks and communication: the behavioural and social contexts of Hector's dolphin vocalizations, Ethology **88**, 265–276 (1991)
20.97 D.L. Herzing: Vocalizations and associated underwater behavior of free-ranging Atlantic spotted dolphins, Stenella frontalis and bottlenose dolphin, Tursiops truncatus, Aqua. Mamm. **22**, 61–79 (1996)

Amazon
EX1010 Page 840

20.98 M.C. Caldwell, D.K. Caldwell: Underwater pulsed sounds produced by captive spotted dolphins, Stenella plagiodon, Cetology **1**, 1–7 (1971)

20.99 J.K.B. Ford, H.D. Fisher: Underwater acoustic signals of the narwhal (Monodon monoceros), Can. J. Zool. **56**, 552–560 (1978)

20.100 S.M. Dawson: The high frequency sounds of free-ranging hector's dolphins, Cephalorhynchus hectori, Rep. Int. Whal. Comm. **Spec. Issue 9**, 339–344 (1988)

20.101 R.G. Busnel, A. Dziedzic: Acoustic signals of the Pilot whale Globicephala melaena, Delpinus delphis and Phocoena phocoena. In: *Whales, Dolphins and porpoises*, ed. by K.S. Norris (Univ.California Press, Berkley 1966) pp. 607–648

20.102 N.A. Overstrom: Association between burst-pulse sounds and aggressive behavior in captive Atlantic bottlenose dolphins (Tursiops truncatus), Zoo Biol. **2**, 93–103 (1983)

20.103 B. McCowan, D. Reiss: Maternal aggressive contact vocalizations in captive bottlenose dolphins (Tursiops truncatus): wide-band, low frequency signals during mother/aunt-infant interactions, Zoo Biol. **14**, 293–309 (1995)

20.104 C. Bloomqvist, M. Amundin: High frequency burst-pulse sounds in agonistic/ aggressive interactions in bottlenose dolphins (Tursiops truncatus). In: *Echolocation in Bats and Dolphins*, ed. by J. Thomas, C. Moss, M. Vater (Univ.Chicago Press, Chicago, IL 2004) pp. 425–431

20.105 J.C. Lilly, A.M. Miller: Sounds emitted by the bottlenose dolphin, Science **133**, 1689–1693 (1961),

20.106 D.L. Herzing: *A Quantitative description and behavioral association of a burst-pulsed sound, the squawk, in captive bottlenose dolphins, Tursiops truncatus, Masters Thesis* (San Francisco State University, San Francisco 1988) p. 87

20.107 S.M. Brownlee: *Correlations between sounds and behavior in wild Hawai'ian spinner dolphins (Stenella longirostris). Masters Thesis* (Univ. California, Santa Cruz 1983) p. 26

20.108 V.A. Vel'min, N.A. Dubrovskiy: The critical interval of active hearing in dolphins, Sov. Phys. Acoust. **2**, 351–352 (1976)

20.109 V.M. Janik: Source levels and the estimated active space of bottlenose dolphin (Tursiops truncatus) whistles in the Moray Firth, Scotland, J. Comp. Psych. **186**, 673–680 (2000)

20.110 S.O. Murray, E. Mercado, H.L. Roitblat: Characterizing the graded structure of false killer whale (Pseudorca crassidens) vocalizations, J. Acoust. Soc. Am. **104**, 1679–1688 (1998)

20.111 M.C. Caldwell, D.K. Caldwell: Vocalizations of naïve captive dolphins in small groups, Science **159**, 1121–1123 (1968)

20.112 W.A. Powell: Periodicity of vocal activity of captive Atlantic bottlenose dolphins: Tursiops truncatus, Bull. Soc. Ca. Acad. Sci. **65**, 237–244 (1966),

20.113 I.E. Sidorova, V.I. Markov, V.M. Ostrovskaya: Signalization of the bottlenose dolphin during the adaptation to different stressors. In: *Sensory Abilities of Cetaceans*, ed. by J. Thomas, R. Kastelein (Plenum, New York 1990) pp. 623–638

20.114 S.E. Moore, S.H. Ridgway: Whistles produced by common dolphins from the Southern California Bight, Aqua. Mamm. **21**, 55–63 (1995)

20.115 J.C. Goold: A diel pattern in vocal activity of short-beaked common dolphins, Delphinus delphis, Mar. Mamm. Sci. **16**, 240–244 (2000)

20.116 M.C. Caldwell, D.K. Caldwell: Individualized whistle contours in bottlenosed dolphins (Tursiops truncatus), Nature **207**, 434–435 (1965)

20.117 P.L. Tyack: Whistle repertoires of two bottlenose dolphins, Tursiops truncatus: mimicricy of signature whistles?, Behav. Ecol. Sociobiol. **18**, 251–257 (1986)

20.118 M.C. Caldwell, D.K. Caldwell, P.L. Tyack: A review of the signature whistle hypothesis for the Atlantic bottlenose dolphin. In: *The Bottlenose Dolphin*, ed. by S. Leatherwood, R.R. Reeves (Academic, San Diego 1990) pp. 199–234

20.119 L.S. Sayigh, P.L. Tyack, R.S. Wells, M.D. Scott, A.B. Irvine: Signature differences in signature whistles production of free-ranging bottlenose dolphins Tursiops truncatus, Behav. Ecol. Sociobiol. **36**, 171–177 (1990)

20.120 L.S. Sayigh, P.L. Tyack, R.W. Wells, M.D. Scott, A.B. Irvine: Sex difference in signature whistle production of free-ranging bottlenose dolphins, Tursiops truncatus, Behav. Ecol. Sociobiol. **36**, 171–177 (1995)

20.121 V.M. Janik, G. Denhardt, T. Dietmar: Signature whistle variation in a bottlenosed dolphin, Tursiops truncatus, Behav. Ecol. Sociobiol. **35**, 243–248 (1994)

20.122 R.A. Smolker, J. Mann, B.B. Smuts: Use of signature whistles during separations and reunions by wild bottlenose dolphin mothers and infants, Behav. Ecol. Sociobiol. **33**, 393–402 (1993)

20.123 V.M. Janik: Whistle matching in wild bottlenose dolphins (Tursiops truncatus), Science **289**, 1355–1357 (2000)

20.124 B. McCowan, D. Reiss: Quantitative comparison of whistle repertoires from captive adult bottlenose dolphins (Delphinidae, Tursiops truncatus): A re-evaluation of the signature whistle hypothesis, Ethology **100**, 194–209 (1995)

20.125 B. McCowan, D. Reiss: The fallacy of 'signature whistles' in bottlenose dolphins: a comparative perspective of 'signature information' in animal vocalizations, Anim. Behav. **62**, 1151–1162 (2001)

20.126 J.W. Bradbury, S.L. Vehrencamp: *Principles of Animal Communication* (Sinauer Associates, Sunderland 1998) p. 882

Amazon
EX1010 Page 841

20.127 D. Reiss, B. McCowan: Spontaneous vocal mimicry and production by bottlenose dolphins (Tursiops truncatus): Evidence for vocal learning, J. Comp. Psychol. **101**, 301–312 (1993)

20.128 A.G. Taruski: The whistle repertoire of the North Atlantic pilot whale (Globicephala melaena) and its relationship to behavior and environment. In: *Behavior of Marine Animals: Current Perspectives on Research. Vol. 3: Cetaceans*, ed. by H.E. Winn, B.L. Olla (Plenum, New York 1979) pp. 345–368

20.129 C.W. Clark: The acoustic repertoire of the southern right whale: A quantitative analysis, Anim. Behav. **30**, 1060–1071 (1982)

20.130 D.G. Richards, J.P. Wolz, L.M. Herman: Vocal mimicry of computer-generated sounds and vocal labeling of objects by a bottlenose dolphin, Tursiops truncatus, J. Comp. Psych. **98**, 10–28 (1984)

20.131 V.B. Deecke, J.K.B. Ford, P. Spong: Dialect change in resident killer whales: Implications for vocal learning and cultural transmission, Anim. Behav. **60**, 629–638 (2000)

20.132 B. McCowan, D. Reiss, C. Gubbins: Social familiarity influences whistle acoustic structure in adult female bottlenose dolphins (Tursiops truncatus), Aqua. Mamm. **24**, 27–40 (1998)

20.133 L.G. Grimes: Dialects and geographical variation in the song on the splendid sunbird Nectarinia coccinigaster, Ibis **116**, 314–329 (1974)

20.134 J.K.B. Ford: Vocal traditions among resident killer whales (Orcinus orca) in coastal waters of British Columbia, Can. J. Zool. **69**, 1454–1483 (1991)

20.135 F. Nottebohm: The song of the chingolo, Zonotrichia capensis, in Agentina: description and evaluation of a system of dialect, Condor **71**, 299–315 (1969)

20.136 J.K.B. Ford: Acoustic behaviour of resident killer whales (Orcinus orca) off Vancouver Island, British.Columbia, Can. J. Zool. **67**, 727–745 (1989)

20.137 J.K.B. Ford, H.D. Fisher: Group-specific dialects of killer whales (Orcinus orca) in British Columbia. In: *Communication and Behavior of Whales. AAAS Sel Symp. 76. Boulder* (Westview Press, Boulder, CO 1983) pp. 129–161

20.138 J.K.B. Ford: *Call traditions and dialects of killer whales (Orcinus orca) in British Columbia, Ph.D. Dissertation* (Univ. British Columbia, Vancouver, BC 1984)

20.139 A.E. Bowles, W.G. Young, E.D. Asper: On ontogeny of stereotyped calling of a killer whale calf, orcinus orca, during her first year, Rit Fiskideildar **11**, 251–275 (1988)

20.140 H. Whitehead, S. Waters, L. Weilgart: Social organization in female sperm whales nd their offspring: Constant companions and casual acquaintance, Behav. Ecol. Sociobiol. **29**, 385–389 (1991)

20.141 L. Weilgart, H. Whitehead: Group-Specific Dialects and Geographical Variation in Coda Repertoire in South Pacific Sperm Whale, Behav. Ecol. Sociobiol. **40**, 277–285 (1997)

20.142 C.W. Clark: Acoustic behavior of mysticete whales. In: *Sensory Abilities of Cetaceans*, ed. by J. Thomas, R. Kastelein (Plenum, New York 1990) pp. 571–583

20.143 A.E. Alling, E.M. Dorsey, J.C. Gordon: Blue whales (Balaenoptera musculus) off the northeast coast of Sri Lanka: distribution, feeding, and individual identification. In: *Cetaceans and Cetacean Research in the Indian Ocean Sanctuary*, Mar. Mammal Tech. Rep., Vol. 3, ed. by S. Leaderwood, G.P. Donovan (UNEP, New York, NY 1991) pp. 247–258

20.144 W.A. Watkins, P.L. Tyack, K.E. Moore, J.E. Bird: The 20-Hz signals of finback whales (Balaenoptera physalus), J. Acoust. Soc. Am. **82**, 1901–1912 (1987)

20.145 W.A. Watkins: The activities and underwater sounds of fin whales, Sci. Rep. Whales Res. Inst. **33**, 83–117 (1981)

20.146 R.S. Payne, S. Mcvay: Songs of humpback whales. Humpbacks emit sounds in long, predictable patterns ranging over frequencies audible to humans, Science **173**, 585–597 (1971)

20.147 D.A. Helweg, A.S. Frankel, J.R. Mobley Jr, L.M. Herman: Humpback whale song: our current understanding. In: *Sensory Abilities of Aquatic Mammals*, ed. by J.A. Thomas, R.A. Kastelein, Aya Supin (Plenum, New York 1992) pp. 459–483

20.148 B. Wursig, C. Clark: Behavior. In: *The Bowhead Whale*, Lawrence Soc. Mar. Mammal Spec. Publ., Vol. 2, ed. by J.J. Burns, J.J. Montague, C.J. Cowles (Allen, Lawrence 1993) pp. 157–199

20.149 W.C. Cummings, D.V. Holliday: Sounds and source levels from bowhead whales off Pt. Barrow, Alaska. J. Acoust. Soc. Am. **82**, 814–821 (1987)

20.150 W.C. Cummings, P.O. Thompson: Underwater Sounds from the Blue Whale, Balaenoptera musculus, J. Acoust. Soc. Am. **50**, 1193–1198 (1971)

20.151 P.L. Edds: Characteristics of the blue whale, balaenoptera musculus, in St. Lawrence river, J. Mamm. **63**, 345–347 (1982)

20.152 M.A. McDonald, J.A. Hilderbrand, S.C. Webb: Blue and fin whales observed on a seafloor array in the northeast Pacific, J. Acoust. Soc. Am. **98**, 712–721 (1995)

20.153 W.C. Cummings, P.O. Thompson, S.J. Ha: Sounds from bryde's whale balaenoptera edeni, and finback, b. physalus, whales in the gulf of California: Fishery bulletin, Breviora Mus. Comp. Zool. **84**, 359–370 (1986)

20.154 P.L. Edds, D.K. Odell, B.R. Tershy: Vocalization of a captive juvenile and free-ranging adult-calf pairs of bryde's whales, balaenoptera edeni, Mar. Mamm. Sci. **9**, 269–284 (1993)

20.155 P.L. Edds: Characteristic of finback, balaenoptera physalus, vocalization in the St. Lawrence estuary, Bioacoustics **1**, 131–149 (1988)

Amazon
EX1010 Page 842

20.156 W.C. Cummings, P.O. Thompson: Characteristics and seasons of blue and finback whale sounds along the U.S. west coast as recorded at SOSUS stations, J. Acoust. Soc. Am. **95**, 2853 (1994)
20.157 M.E. Dalheim, D.H. Fisher, J.D. Schempp: Sound Production by the Grey Whale and Ambient Noise Levels in Laguna San Ignacio, Baja California Sur, Mexico. In: *The Grey Whale*, ed. by M. Jones, S. Swartz, S. Leatherwood (Academic Press, S.D. 1984) pp. 511–541
20.158 N.L. Crane: *Sound Production of Gray Whales, Eschrichtius tobustus Along Their Migration Route* (MS Thesis, San Francisco St. Univ., San Francisco, CA 1992)
20.159 W.C. Cummings, P.O. Thompson, R. Cook: Underwater sounds of migrating gray whales, eschrichtius glaucus (cope), J. Acoust. Soc. Am. **44**, 278–1281 (1968)
20.160 P.O. Thompson, W.C. Cummings, S.J. Ha: Sounds, Source Levels, and Associated Behavior of Humpback Whales, Southeast Alaska, J. Acoust. Soc. Am. **80**, 735–740 (1986)
20.161 R.S. Payne, K. Payne: Large scale changes over 19 years in songs of humpback whales in bermuda, Z. Tierpsychol. **68**, 89–114 (1985)
20.162 W.E. Schevill, W.A. Watkins: Intense low-frequency sounds from an antarctic minke whale, balaenoptera acutorostrata, Breviora Mus. Comp. Zool., 1–8 (1972)
20.163 H.E. Winn, P.J. Perkins: Distribution and sounds of the minke whale, with a review of mysticete sounds, Cetology **19**, 1–11 (1976)
20.164 W.C. Cummings, J.F. Fish, P.O. Thompson: Sound production and other behavior of southern right wales, eubalena glacialis, Trans. San Diego Soc. Nat. Hist. **17**, 1–13 (1972)
20.165 C.W. Clark: Acoustic Communication and Behavior of the Southern Right Whale. In: *Behavior and Communication of Whales*, ed. by R.S. Payne (Westview Press, Boulder, CO 1983) pp. 643–653
20.166 A. R. Knowlton, W. W. Clark, S. D. Kraus: Sounds Recorded in the Presence of Sei Whales, Balaenoptera borealis, in Proc. 9th Bienn. Conf. Biol. Mar. Mamm., Chicago, IL, Dec. 1991, p. 40 (1991)
20.167 P.O. Thompson, L.T. Findlay, O. Vidal: Underwater sounds of blue whales, Balaenoptera musculus, in the Gulf of California, Mexico, Mar. Mamm. Sci. **12**, 288–293 (1987)

Amazon
EX1010 Page 843

21. Medical Acoustics

Medical acoustics can be subdivided into diagnostics and therapy. Diagnostics are further separated into auditory and ultrasonic methods, and both employ low amplitudes. Therapy (excluding medical advice) uses ultrasound for heating, cooking, permeablizing, activating and fracturing tissues and structures within the body, usually at much higher amplitudes than in diagnostics. Because ultrasound is a wave, linear wave physics are generally applicable, but recently nonlinear effects have become more important, even in low-intensity diagnostic applications.

This document is designed to provide the nonmedical acoustic scientist or engineer with some insights into acoustic practices in medicine. Auscultation with a stethoscope is the most basic use of acoustics in medicine and is dependent on the fields of incompressible (circulation) and compressible (respiration) fluid mechanics and frictional mechanics. Detailed discussions of tribology, laminar and turbulent hemodynamics, subsonic and supersonic compressional flow, and surfactants and inflation dynamics are beyond the scope of this document. However, some of the basic concepts of auscultation are presented as a starting point for the study of natural body sounds. Ultrasonic engineers have dedicated over half a century of effort to the development of ultrasound beam patterns and beam scanning methods, stretching the current technical and economic limits of analog and digital electronics and signal processing at each stage. The depth of these efforts cannot be covered in these few pages. However, the basic progression of progress in the fields of transducers and signal processing will be covered. The study of the interaction of ultrasound with living tissues is complicated by complex anatomic structures, the high density of scatterers, and the constantly changing nature of the tissues with ongoing life processes including cardiac pulsations, the formation of edema and intrinsic noise sources. A great deal of work remains to be done on the ultrasonic characterization of tissues. Finally, the effect of ultrasound on tissues, both inadvertent and therapeutic will be discussed.

Much of the medical acoustic literature published since 1987 is searchable online, so this document has included key words that will be helpful in performing a search. However, much of the important basic work was done before 1987. In an attempt to help the reader to access that literature, Denis White and associates have compiled a complete bibliography of the medical ultrasound literature prior to 1987. Under Further Reading in this chapter, the reader will find a link to a complete compilation of 99 citations from *Ultrasound in Medicine and Biology* which list the thousands of articles on medical acoustics written prior to 1987.

The academically based authors develop, use and commercialize diagnostic ultrasonic Doppler systems for the benefit of patients with cardiovascular diseases. To translate ultrasonic and acoustic innovation into widespread clinical application requires as much knowledge about the economics of medicine, the training and practices of medical personnel, and the pathology and prevalence of diseases as about the diffraction patterns of ultrasound beams and signal-to-noise ratio of an echo. Although a discussion of these factors is beyond the scope of this chapter, a few comments will help to provide perspective on the likely future contribution of medical acoustics to improved public health.

21.1 **Introduction to Medical Acoustics** 841

21.2 **Medical Diagnosis; Physical Examination** 842
- 21.2.1 Auscultation – Listening for Sounds 842
- 21.2.2 Phonation and Auscultation 847
- 21.2.3 Percussion 847

21.3 **Basic Physics of Ultrasound Propagation in Tissue** 848
- 21.3.1 Reflection of Normal-Angle-Incident Ultrasound 850

Amazon
EX1010 Page 844

21.3.2 Acute-Angle Reflection of Ultrasound 850
21.3.3 Diagnostic Ultrasound Propagation in Tissue 851
21.3.4 Amplitude of Ultrasound Echoes . 851
21.3.5 Fresnel Zone (Near Field), Transition Zone, and Fraunhofer Zone (Far Field) .. 853
21.3.6 Measurement of Ultrasound Wavelength 855
21.3.7 Attenuation of Ultrasound 855

21.4 **Methods of Medical Ultrasound Examination** 857
21.4.1 Continuous-Wave Doppler Systems 857
21.4.2 Pulse-Echo Backscatter Systems .. 859
21.4.3 B-mode Imaging Instruments 862

21.5 **Medical Contrast Agents** 882
21.5.1 Ultrasound Contrast Agents 883
21.5.2 Stability of Large Bubbles 883
21.5.3 Agitated Saline and Patent Foramen Ovale (PFO) . 884
21.5.4 Ultrasound Contrast Agent Motivation 886
21.5.5 Ultrasound Contrast Agent Development 886
21.5.6 Interactions Between Ultrasound and Microbubbles 886
21.5.7 Bubble Destruction 887

21.6 **Ultrasound Hyperthermia in Physical Therapy** 889

21.7 **High-Intensity Focused Ultrasound (HIFU) in Surgery** 890

21.8 **Lithotripsy of Kidney Stones** 891

21.9 **Thrombolysis** 892

21.10 **Lower-Frequency Therapies** 892

21.11 **Ultrasound Safety** 892

References 895

Part F | 21

Standard Symbols

c sound propagation velocity [km/s = mm/μs]
p acoustic pressure fluctuation [d/cm^2; Pa = N/m^2]
t time [s]
Z tissue impedance [Rayles = ρc = kg/(m^{2}s) = 0.1 g/(cm^{2}s)]
λ acoustic wavelength [m]
ρ tissue density [g/cm^3]
$\boldsymbol{\sigma}$ surface tension [d/cm = mN/m]

Special Symbols

d diameter
f frequency [Hz]
f_D Doppler frequency [Hz]
f_{us} ultrasound center frequency [MHz]
fd vibration frequency [Hz]
P total instantaneous pressure [d/cm^2, kPa]
q acoustic molecular displacement [cm]
Q volume flow [cm^3/s]
R reflection coefficient
T transmission coefficient
v_f fluid velocity [cm/s]
v molecular velocity [cm/s]
w transducer element width [cm]
x distance in propagation direction [cm]
κ tissue stiffness [d/cm^2]
θ angle of sound propagation from the normal at a refraction interface
Ψ distance to transition zone
θ_D Doppler angle of sound propagation to vessel axis or velocity vector axis
$\Delta\phi$ ultrasound echo phase shift
$\Delta\boldsymbol{\tau}$ ultrasound echo time shift [ns]
PRF pulse repetition frequency [Hz]
$\boldsymbol{D}$ thermal dose

Subscripts

i incident
r reflected
s shear wave
t transmitted
1 incident material
2 second material

Dimensionless Numbers

St Strouhal number St = $(fD)/V$
Re Reynolds Number $(DV\rho)/\mu = (4Q\rho/\pi D)/\mu$

Units

Np nepers
dB decibels

Amazon
EX1010 Page 845

21.1 Introduction to Medical Acoustics

Medical acoustics covers the use of sub-audio vibration, audible sound and ultrasound for medical diagnostics and treatment. Sound is a popular and powerful tool because of its low cost, noninvasive nature, and wide range of potential applications from passive listening to the application of high-energy pulses used for the destruction of kidney stones.

There are four frequency ranges of sound and three levels of intensity that will be presented in this chapter

Table 21.1 Medical frequencies

Title	Period	Frequency	Power/Intensity
Generation	25 years		
Ovulation	28 days		
Diurnal	1 day		
Respiration	6 s	0.15 Hz	
Heart Rate	1 s	1 Hz	
ECG surface bandwidth	10 ms	100 Hz	
ECG intramyocardial BW	250 μs	4 KHz	
Tremor	100 ms	3–18 Hz	
Electromyography surface	5 ms	200 Hz	
Electromyography intramuscle	100 μs	10 kHz	
Flicker fusion (visual)	60 ms	16 Hz	
Vibration sensation	10 ms	100 Hz	
Sound low	50 ms	20 Hz	
Telephone sound speech	3–0.3 ms	0.3–3 kHz	
Sound high	50 μs	20 kHz	
Electro-encephalography (EEG) surface waves			
Delta waves	300 ms	< 3.5 Hz	
Theta waves	200 ms	3.5–7.5 Hz	
Alpha waves	100 ms	7.5–13 Hz	
Beta waves	50 ms	13–30 Hz	
Intracerebral EEG	100 μs	10 kHz	
Ultrasound cleaners		42 kHz	100 W, 1 W/cm^2
Ultrasound bacteriocidal		22.5 kHz	
Ultrasound therapeutic	0.5 μs	1 3 MHz	15 W, 3 W/cm^2
Ultrasound diagnostic			
Transcranial		1–3 MHz	100 mW/cm^2
Heart, abdomen		2–5 MHz	100 mW/cm^2
Vascular, skeletal		4–10 MHz	100 mW/cm^2
Skin, eye		10–40 MHz	8 mW/cm^2
Ultrasound high intensity focused (HIFU)		2–6 MHz	2000 W/cm^2
Diathermy, shortwave, physiotherapy		13–40 MHz	2–15 W
Diathermy, shortwave, cell destruction		300 kHz	100 W
Diathermy, cancer ablation		500 kHz	500 W
Diathermy microwave		0.4–2.5 GHz	
Light		10^{14} Hz	
X-ray		1×10^{18} Hz 4×10^{18} Hz	

Amazon
EX1010 Page 846

1. Infrasound, acoustic waves with frequencies below the level of human hearing. These vibrations, called *thrills*, are often caused by turbulent blood flow (which is abnormal). At the lowest extreme, the pulse can be considered infrasound with a frequency below 2 Hz. With fingertips, the physician can feel vibrations with amplitudes of 1 μm.
2. Audible sound, acoustic waves with frequencies in the range of human hearing. The audible frequency range for the average human is approximately 20 Hz–20 kHz, with a peak sensitivity around 3–4 kHz. At 1 kHz, the standard reference frequency, the ear is able to detect pressure variations on the order of one billionth of an atmosphere. This corresponds to intensities of about 0.1 fW/cm^2 (10^{-16} W/cm^2 = 10^{-12} W/m^2). The oscillatory velocity of air molecules carrying such sound intensities is $v = 50$ nm/s (1 nm = 10^{-9} m) and the maximum pressure fluctuation is 20 μN/m^2 or 0.2 nanoatmospheres (nanobar). At 1 kHz, the air molecules oscillate back and forth about 0.05 nm. The intensity of conversation is 0.1 nW/cm^2 (1 μW/m^2) causing molecules to oscillate with amplitudes of 50 nm, and oscillatory pressures of 20 mN/m^2.
3. Low-frequency ultrasound, which is used for cleaning and tissue disruption.
4. Radio-frequency ultrasound, acoustic waves with frequencies near 1 MHz and wavelengths in the body near 1 mm.

A list of interesting frequencies in medicine is provided for reference Table 21.1.

21.2 Medical Diagnosis; Physical Examination

The most valuable application of acoustics in medicine is the communication from a patient to their physician. In the modern world of *efficient medicine*, however, physicians are encouraged to avoid wasting time listening to the patient so that objective tests can be ordered without delay. This approach avoids physician frustration from sorting out the complaints and symptoms of the patient, even though the patient initiated the appointment with the physician.

Having gathered background information, the physician can proceed to the physical examination, which includes optical methods, olfaction, palpation, testing the mechanical response of tissues and systems to manipulation, percussion, remote listening and aided auscultation, and acoustic transmission and reflection techniques. Only those techniques related to medical acoustics will be discussed further here. Of future importance in medical practice though, are those methods that can be performed remotely, via the internet.

21.2.1 Auscultation – Listening for Sounds

Sounds in the body are generated through the presence of disturbed flow, such as eddies and turbulence, by frictional rubs, and/or by other sources with high accelerations. There are both normal and abnormal sounds within the body. Auscultation is the act of listening for sounds within the body for diagnostic purposes. This may be conducted on any part of the body from head to toe (Fig. 21.1). Anesthesiologists even use esophageal stethoscopes for convenient acquisition of chest sounds. Information gathered during auscultation includes the frequency, intensity, duration, timing, and quality of the sound.

Lung. Both normal and abnormal sounds can be present in the lungs. The source of normal lung sounds is turbulent flow associated with air movement through orifices along the airways. These are large, low-frequency oscillations that cause the surrounding tissues to vibrate within the audible frequency range. The respiratory system is naturally optimized to minimize the work needed to exchange air, so little energy is converted into acoustic power, resulting in low-amplitude sounds. With constriction of the airways, in such conditions as asthma, the air velocity through the airways increases (conservation of mass). Through conservation of energy and momentum, an increase in flow velocity results in an increase in pressure loss, raising the power needed to drive the system. The energy is of course not lost, but converted, in part, into acoustic power. The increase in flow velocity results in an increase in *turbulent diffusion*, or the transfer of energy from the flow to the surrounding tissues through a growing chain of turbulent eddies. When the passages are smaller, the eddies decrease in size, causing an increase in the frequency of the audible sound. The pressure drop caused by a small lumen is higher, causing an increase in eddy velocity and therefore an increase in acoustic power, and the flow rate is decreased,

Amazon
EX1010 Page 847

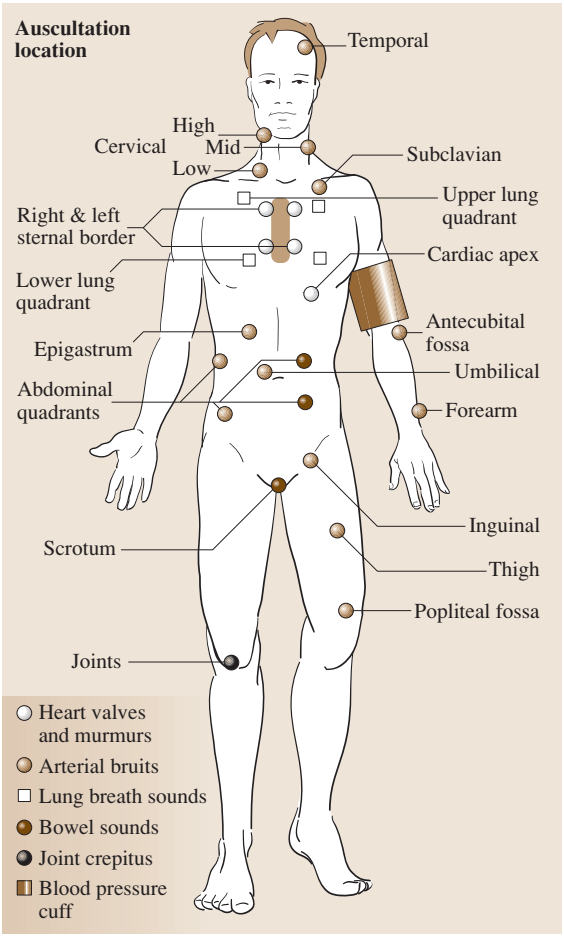


Fig. 21.1 Auscultation sites. Arterial bruits can be heard bilaterally indicating arterial stenoses. Heart valve sounds and heart murmurs are primarily heard in the peristernal intercostal spaces indicating cardiac timing, and valve stenosis and incompetence (insufficiency or regurgitation). Breath sounds in the lung indicate both airway sufficiency, lung inflation, alveolar inflation and pleural friction. Bowel sounds [21.1, 2] indicate normal peristalsis; bowel in the scrotum indicate intestinal hernia. Crepitus on motion indicates air in the tissue, bone fracture or joint [21.3–6] cartilage damage. Auscultation in the antecubital fossa during blood pressure cuff deflation yields Korotkoff sounds [21.7, 8], 1 = a sharp sound each systolic peak when the cuff pressure equals the systolic pressure indicating the momentary separation of the artery walls and the onset of blood flow, 2 = a loud blowing sound due to blood turbulence, 3 = a soft thud when the artery under the cuff is exhibiting maximum change in arterial diameter, 4 = a soft sound indicating slight arterial deformation near diastolic pressure, 5 = silence when the cuff pressure is below the diastolic arterial pressure

causing a longer duration of flow to fill and empty the lungs. Thus the breath sounds are louder, longer, higher-pitched sounds compared with normal lung sounds. In some medical conditions, the flow dynamics may be just right to produce coherent eddy structures, such as one would see in a smoke stack. These signals result in a narrow-band frequency tone.

Abnormal snapping or popping sounds may also be present in the lung. In the normal lung, the alveoli (terminal air sacks, 280 μm in diameter, 3×10^8 in lung) are filled with air. In pneumonia, regions of alveoli are filled with fluid, which prevents a rapid increase in size without the introduction of a gas phase. The rapid introduction of a gas phase when the lung is expanded during the inspiration phase of respiration causes a tiny snapping sound (broadband acoustic impulse) in each alveolus; many snaps together cause the sound of *rales*.

Table 21.2 Diagnosing valve disease from heart murmurs

	Time	Side	Location	Position
Tricuspid stenosis	Diastolic	Parasternal	3rd ICS	Supine
Tricuspid regurgitation	Systolic	Peristernal	3rd ICS	Supine
Pulmonic stenosis	Systolic	Right	Superior	Supine
Pulmonic regurgitation	Diastolic	Right	Superior	Seated
Mitral stenosis	Diastolic	Left	Apex	Supine
Mitral regurgitation	Systolic	Left	Apex-Axilla	Supine
Aortic stenosis	Systolic	Parasternal	Superior	Supine
Aortic regurgitation	Diastolic	Parasternal	Superior	Seated
Side parasternal = in the intercostal spaces on either side of the sternum				
Location 3rd ICS = the space between the 3rd and 4th rib, Erb's point				
Position seated = Seated, leaning forward, breath in expiration				

Amazon
EX1010 Page 848

Because of the lubricant normally present in the pleura located between the lungs and the chest wall, there are normally no sounds generated through a friction rub due to the sliding of the lung along the chest wall. When the pleura are inflamed, coarse rubbing sounds can be heard during breathing.

Cardiac. The cardiovascular system also generates normal and abnormal sounds that can be heard in the chest with a stethoscope [21.9] (Table 21.2). Normal heart sounds [21.10–12] are caused by rapid blood decelerations resulting from the closure of the heart valves. Each of the four heart valves, the tricuspid, pulmonic, mitral and aortic (in order from the venous circulation to the arterial circulation), are flaccid sheets of tissue securely tethered in the closed position to form check (one-way) valves. Like a parachute opening, the valve leaflets move with the reversing blood flow until the tethers become taught, then the leaflets force a rapid deceleration of the blood which generates a sudden (broadband) *thump* with an acoustic power of several watts. No similar rapid acceleration is associated with valve opening. Because the sounds are primarily radiated along the axis of acceleration and conduct better through tissue than the air-filled lungs, the sound of each valve is most prominent at a particular location on the chest wall.

Though four valves are present, usually only two thumps are heard, and they occur at vary precise times in the cardiac cycle. 20 ms after the onset of ventricular contraction, the tricuspid and mitral valves close, causing the first heart sound. 50 ms after closure of the atrioventricular valves, the pulmonic and aortic valves open silently. 320 ms after the onset of ventricular contraction, when ventricular ejection is complete and the ventricular pressures drop below the pulmonary trunk and aortic pressures, the pulmonic and aortic valves snap shut, generating the second heart sound. These times do not vary with heart rate; each cardiac cycle acts like an independent impulse-response system. The systolic ejection volume does vary with the diastolic filling period from the prior cardiac cycle.

Thus, each of the two heart sounds is generated by two valve closures, one in the left heart and one in the right heart. These usually occur simultaneously, however, the sounds do split into two if the inflow valves (tricuspid and mitral) or outflow valves (pulmonic and aortic) close at different times. These *split heart sounds* [21.13] can be indicative of an abnormality. The closure of the tricuspid valve is dependent on contraction of the right ventricle, which in turn is dependent on the electrical conduction system from the pacemaker of the heart. As a result, a delay in conduction or a slow response of the right ventricular muscle (myocardium) will delay the tricuspid sound, causing splitting. Similarly, if there is a delay in the conduction system of the left heart, or the left ventricular myocardium contraction is slow, then the mitral sound is delayed. The closure of the outflow valves is dependent on contraction strength, pressure in the outflow vessels, and ejection volume. A mismatch of any of those factors will cause the pulmonic and aortic valves to close at different times, splitting the second sound. Even the effects of respiration on the filling and emptying of the heart chambers cause some normal heart sound splitting.

Abnormal sounds that occur in the cardiovascular system are called *bruits* and *murmurs* [21.14–17]. A murmur is a sound lasting longer than 10 ms heard by a cardiologist from the heart; a bruit is a similar sound, but heard by an angiologist from an artery. Veins rarely make sounds; venous sounds are called *hums* because they are continuous. A *thrill* is a similar vibration felt by the hand. Because these represent power dissipation from the cardiovascular system, all are considered abnormal. The absence of normal bruits and murmurs results from a biological feedback that forms the shape of the cardiovascular system. The feedback mechanism is not well understood. In fluid mechanics, the transition from laminar flow to turbulent flow occurs near a Reynolds number of 2000. Turbulent flow is highly dissipative while laminar flow is minimally dissipative. Coincidentally, peak flow through the cardiovascular system maintains a condition of Reynolds number less than 2000. If a heart valve or an artery is required to carry higher flow rates, then the conduit will dilate until the Reynolds number (proportional to the flow divided by the diameter) becomes less than 2000. Distal to a stenosis, where turbulence occurs, the conduit dilates, causing post-stenotic dilation. Thus, it appears that sustained turbulence, which dissipates power, is the driving force for remodeling to avoid turbulence and make the hemodynamic system more energy efficient.

The vibrations indicate the presence of disturbed blood flow, caused by deceleration of the blood beyond a narrow stenosis. The vibrations are associated with a pressure drop across the stenosis because of a transfer of hydraulic power to acoustic power through a cascade of eddies. In turbulent flow, the vibrations are broadband. When coherent eddies are present, the vibrations are narrow band, and the frequency of the eddies can be related to the flow velocity (v_f) and vessel diameter (d) through the Strouhal number ($\mathrm{St} = fd/v_f$). In addition to the location and power of a bruit, the frequency of the bruit is also helpful in evaluating its clinical im-

Amazon
EX1010 Page 849

portance. The Strouhal number has been used for the prediction of the residual lumen diameters of carotid stenoses. If the frequency of a bruit is divided into the number 500 [mm Hz], the result is the minimum lumen diameter [21.18–25] in mm. In clinical testing, this method accurately predicted the stenosis in hundreds of cases. However, because cumbersome technology is involved, and because the method fails in tight stenoses, which are most clinically important, this clever method has been abandoned.

Heart murmurs are auscultated at a series of locations on the precordium (the front middle of the chest around the sternum). They are graded from grade 1 (barely audible) to grade 6 (no stethoscope needed). Murmurs may result from leaky (incompetent, regurgitant) valves, stenotic (narrow) valves, or other holes between heart chambers. The differential diagnosis of heart murmurs is based on the timing of the murmur and the locations on the chest wall [21.26, 27] where the murmur is best heard. A murmur can be early systolic, mid-systolic, late systolic, or early diastolic, or mid-diastolic. If a murmur is best heard in the left second intercostal space (the space between the second rib and the third rib along the left boarder of the sternum), it is most probably an aortic stenosis [21.28–30]. Each of the other valve pathologies has a corresponding location where the murmur is likely to be highest. Of course, there is a great deal of variability between patients, and the examiner must apply a full set of detective skills to sort out a proper diagnosis.

There are some common systolic heart murmurs. Athletes, with temporary increased blood flow due to exercise programs have physiologic systolic heart murmurs, as do pregnant women, who have a 30% increase in cardiac output to supply the placenta. Hemodialysis patients also often have systolic heart murmurs because of the increased cardiac output required to supply the dialysis access shunt [21.31] in addition to the supply to the body. In these cases, remodeling of the blood vessels to increase the flow diameter has not had time to occur.

Bruits are almost always associated with stenoses in arteries, which often require treatment. They are classified by their pitch and duration. The occurrence of bruits in the head, in the abdomen after eating and in the legs are all indications of arterial stenoses, or high-velocity blood entering vascular dilations. The presence of a bruit heard in the neck is usually indicative of a carotid stenosis. The carotid arteries are the major vessels located on the left and right side of the neck that supply blood to the brain. The development of an atherosclerotic plaque causes luminal narrowing and the corresponding onset of disturbed flow. This lesion is associated with a 20% risk of stroke in two years from material that can be released by the atherosclerotic plaque and travels to the brain to occlude a branch artery.

Carotid bruits are usually present when the residual lumen (stenotic) diameter is greater than 50% of the original lumen diameter (called a 50% diameter reduction), but less than 90% of the original lumen diameter (90% diameter reduction) In this range, the blood flow rate to the brain through the carotid artery is approximately 5 cm^3/s. If the pressure [21.32] drop across the stenotic region is about 20 mmHg, then the power dissipation at the stenosis is 13 mW, which can appear as sound energy in a bruit. Unfortunately, as the stenosis becomes more severe, the flow rate along the artery decreases, reducing the acoustic power for the bruit, so the bruit is no longer detectable, even though this more severe stenosis carries a higher risk for stroke. The decreased blood flow will not cause symptoms in most people because 95% of the population have collateral connections (the circle of Willis) that can provide the required blood flow that is not delivered by the stenotic artery. In the remaining 5% of the population, a severe carotid stenosis causes impaired mental function.

One of the barriers to new methods in the classification of carotid stenosis is that the first description of the relationship between carotid artery stenosis and apoplexy (stroke) was provided by Egaz Moniz in 1938. Moniz used percent diameter reduction and everyone has followed suit, through a confusing and contentious evolution, even when more-rational and useful alternatives have been developed. Thus, a new method that predicts residual lumen diameter will not be easily adopted by the medical community because of the tradition of using percent diameter reduction.

Bruits may be generated in the abdomen by stenoses in the renal arteries, which supply the kidneys. A renal artery stenosis will cause renovascular hypertension because the kidney is a transducer for detecting low blood pressure. The pressure drop across a renal artery stenosis causes the kidney to measure a low pressure, and deliver the signals to raise blood pressure in the arterial system, causing hypertension in all arteries except those in the affected kidney. The transduction system is called the renin-angiotensin-aldosterone system.

Some cardiovascular sounds are so loud that they cannot be missed. A patient in renal failure, refusing dialysis, had a cardiac friction rub (friction in the pericardial sack from inflammation). The 1 kHz *squeak* occurring with each systole could be heard from the doorway of the patient's room.

Amazon
EX1010 Page 850

A stethoscope can also be used to detect bowel sounds from the abdomen. These sounds are generated by the liquid and gaseous contents of the bowel being forced from one intestinal segment to another through an orifice created by peristaltic action. The same fluid eddies described above are responsible for these sounds. The presence of bowel sounds is an important indicator of a normally functioning gut. It is common, the day after abdominal surgery, to check to be sure that normal bowel sounds are present.

Palpation, though not an acoustic technique, is used to feel, rather than hear, the same vibrations. Hemodialysis patients have a *vascular access* shunt created by tying an artery directly to a vein. This shunt may have a flow rate of 3 liters per minute, half of the cardiac output. The pressure drop is equal to the systolic blood pressure 120 mmHg. So the hemodynamic power dissipated in the shunt is 800 mW of power. This energy is converted to a vibration (thrill) which can be felt with the fingers.

Acoustic Stethoscope

Auscultation may be performed directly, but is most commonly conducted with a stethoscope. The device was invented by Dr. Rene Theophile Hyacinthe Laennec in 1816. While examining a patient, Dr. Laennec rolled up a sheet of paper and placed one end over the patient's heart and the other end over his ear. Dr. Laennec later replaced the rolled paper with a wooden tube (similar in appearance to a candlestick), which was called a stethoscope from the Greek words *stethos* (chest) and *skopein* (to look at). Two modern versions of the stethoscope are notable: the binaural stethoscope and the fetal stethoscope. The common binaural stethoscope consists of a bell connected by flexible tubing to a pair of earpieces. Each earpiece is sealed into the corresponding external auditory meatus. The bell is sometimes covered with a diaphragm, which acts as a high-pass filter. For example, normal heart sounds have frequencies near 50 Hz while heart murmurs have frequencies exceeding 100 Hz. Filtering out the normal heart sounds with the diaphragm of the stethoscope often allows pathologic murmurs to be detected. When using an open bell stethoscope, a diaphragm can be formed by pressing the bell tighter to the skin, stretching the skin and deeper tissue, which attenuates the lower frequencies [21.33–36].

The fetal stethoscope is designed for use in the auscultation of fetal heart sounds, which can be detected during the final half of a 40 week pregnancy. The fetal stethoscope uses a rod connecting the mother's abdominal wall to the examiner's forehead to transmit the sound by bone conduction in the examiner's head to the inner ear where it is converted into nerve impulses. This avoids the impedance changes between tissue and air at the skin surface and then again from air to tissue in the middle ear.

For the last 20 years, small ultrasonic Doppler ultrasound stethoscope systems have been available to detect the fetal heart beat [21.37, 38]. They operate like the ultrasound imaging *phono-angiograph* to easily detect solid tissue vibrations from deep in the body. These continuous-wave instruments allow the pregnant mother to perform easy self-examination. They are available on a rental basis without a medical prescription.

Electronic Stethoscope

Electronic stethoscopes [21.39–41] provide improved amplification and background noise cancelation over traditional stethoscopes. Some also have recording capabilities to provide quantitative, rather than just qualitative, assessment of the sounds heard. For example, by listening to the neck with a phono-angiograph (Fig. 21.2), the location and duration of the bruit can be documented. A phono-angiograph is just an electronic stethoscope with an attached oscilloscope. If applied to the heart, then it is called a phono-cardiograph. This bruit (Fig. 21.2), is a pan-systolic bruit (lasting all of systole) but not a pan-diastolic bruit (lasting all of systole and diastole). Since arterial blood velocities are higher

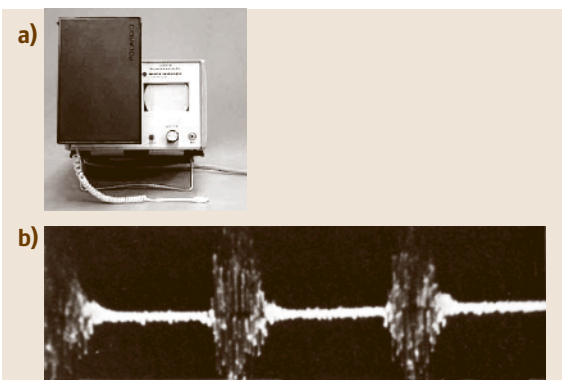


Fig. 21.2a,b Carotid phono-angiography (CPA) **(a)** A microphone fitted with an acoustic coupling to the neck gathers sounds, which are displayed on an oscilloscope and captured with an instant camera. **(b)** The sounds displayed are classified by the location, amplitude, and duration of the bruit. A similar method, phono-cardiography, was used for the heart. A method, quantitative phono-angiography (QCPA) provided an analysis of the frequency content of the bruit

Amazon
EX1010 Page 851

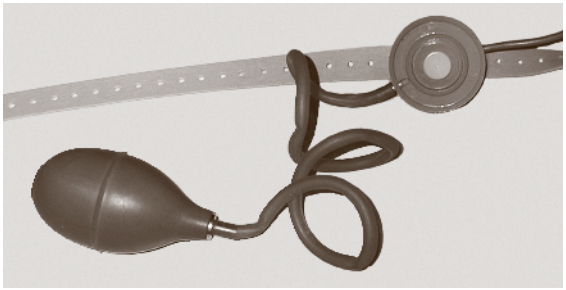


Fig. 21.3 Phono-cardiograph transducer. To avoid sounds and motions introduced by the examiner's hand on the chest, this phonocardiography transducer is fitted with a suction ring and elastic strap to secure the transducer element to the chest. Early echocardiographs had provision for amplifying and displaying the phono-cardiograph signals, which were filtered to display audible frequencies or infrasonic frequencies

during systole than diastole, all arterial bruits include systole. The exceptions, where arterial flow in a collateral pathway is reversed due to a *steal syndrome* are so rare that common names have not been adopted for this condition. To be sure that the bruit is systolic, the examiner can palpate the pulse at the wrist while listening, to associate the bruit timing with systolic arterial motion.

However, if such an image were gathered with a phono-cardiograph (Fig. 21.3) from the heart, it would be impossible to know whether the murmur was coming from aortic or pulmonic stenosis (during systole), aortic or pulmonic regurgitation (during diastole), from tricuspid or mitral regurgitation (during systole), or tricuspid or mitral stenosis (during diastole), unless there were some indication of the timing of the cardiac cycle. A phono-cardiogram displays an associated electro-cardiograph (ECG) tracing to provide that timing information.

Unfortunately, electronic stethoscopes, phono-angiographs and phono-cardiographs are considered too complicated for use in everyday medical practice. Although they do provide a graphical output for the patient chart (required documentation to receive payment for diagnostic procedures), a separate current procedural terminology (CPT) code is not available for phono-angiography, phonocardiography or for stethoscope examination. Like the stethoscope examination, these procedures, if performed, are considered part of a standard office visit. Physicians are reluctant to use technical examination methods if they cannot charge for the extra time involved. Although a few research facilities documented bruits and murmurs detected with these systems between 1965 and 1985, the systems have nearly disappeared from medical practice. Like the first half of the 20th century, physicians today are trained to use acoustic stethoscopes. Of course, as physicians become more experienced and more mature, their hearing deteriorates. Even the most respected cardiologist will fail to correctly diagnose cardiac valve disease in 50% of patients. Bruits with 35 μm, 300 Hz vibrations from the jugular vein (Fig. 21.4) documented by a new ultrasound imaging phono-angiograph were not detected by stethoscopic auscultation. So, in spite of the ubiquitous use of stethoscopes for bruit/murmur detection, their sensitivity may not be adequate for the task.

21.2.2 Phonation and Auscultation

In addition to listening for sounds with a stethoscope, an examiner may cause the generation of sounds to assess transmission or resonance. During auscultation of the lungs, an examiner may ask the patient to phonate (make voice sounds) at different frequencies "Say 'eeeeeee', now say 'aaaaaaaa'". During that period, the examiner will either palpate the chest wall for vibration or listen to the chest wall with a stethoscope. Poor sound transmission may indicate that the airways are obstructed, enhanced sound transmission (enhanced *fremitus*) indicates fluid has filled a space normally occupied by air.

21.2.3 Percussion

Percussion is another method of sound generation by striking the chest or abdomen to assess transmission or resonance. The skin may be struck with the hand or finger, or one hand may be placed on the skin and struck with the other hand. A higher-frequency shorter pulse can be generated by placing a coin on the skin and striking the coin with another coin. The resultant sound can be assessed by listening to the resonance through the air or by using a hand or stethoscope to assess transmission of the impulse. Percussion that results in a dull sound indicates a fluid-filled space below the skin; a resonant sound indicates an air-filled space below the skin. These methods are often used to find the lower boarder of the lungs, to identify fluid-filled consolidation in the lungs, and to find the edge of the liver (fluid-filled) in the abdomen (air-filled intestines).

These acoustic examination techniques have been developed in medical practice over centuries, and although efforts have been made to use electronic aids for

Amazon
EX1010 Page 852

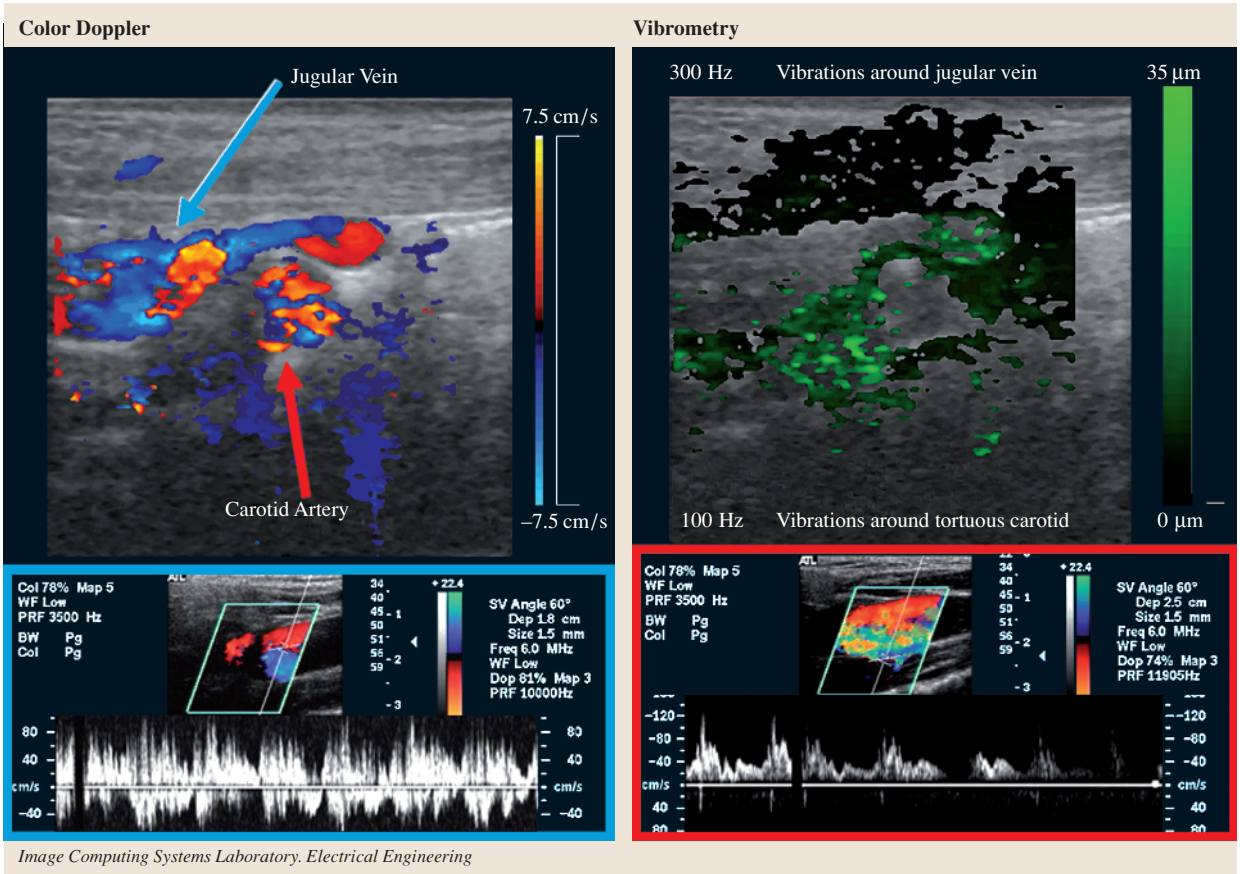


Fig. 21.4 Imaging vibrometry of the neck. Color Doppler image (*upper left*), vibration image (*upper right*), jugular vein Doppler (*lower left*) and carotid artery Doppler (*lower right*) of a patient complaining of "vibrations in the head". The 300 Hz vibrations with an amplitude of 35 µm could not be heard with a stethoscope by either of two experienced examiners (Courtesy M. Paun, S. Sikdar)

diagnosis and for training, still, the common practice is to learn these methods from a mentor. In the last quarter of the 20th century, ultrasound has become adopted in specialty medical practice, but has not made inroads in general practice. It is likely that, if and when ultrasound diagnostic methods become widely used in general medical practice, it will be used with the same level of skill as stethoscope auscultation.

21.3 Basic Physics of Ultrasound Propagation in Tissue

The vibrations of molecules at any location (or time) in a sound wave can be characterized by four parameters: the pressure fluctuation from the mean static pressure (p), the molecular velocity (v), the displacement of the molecules from the resting location (d), and the molecular acceleration (a). The two most basic parameters, pressure deviation and molecular velocity are dependent only on the intensity of the sound. Their ratio, p/v, is determined by the acoustic impedance ($Z = p/v$), a property of the tissue. At the sound level shown in Fig. 21.5, 300 mW/cm^2 (3 kW/m^2), the maximum acoustic pressure fluctuation equals 1 atm. If the sound intensity is increased, then the negative peaks represent a pressure below zero. Most ultrasound examinations are performed at pulse peak intensities 25 times this high, and therefore, peak amplitudes five times atmo-

Amazon
EX1010 Page 853

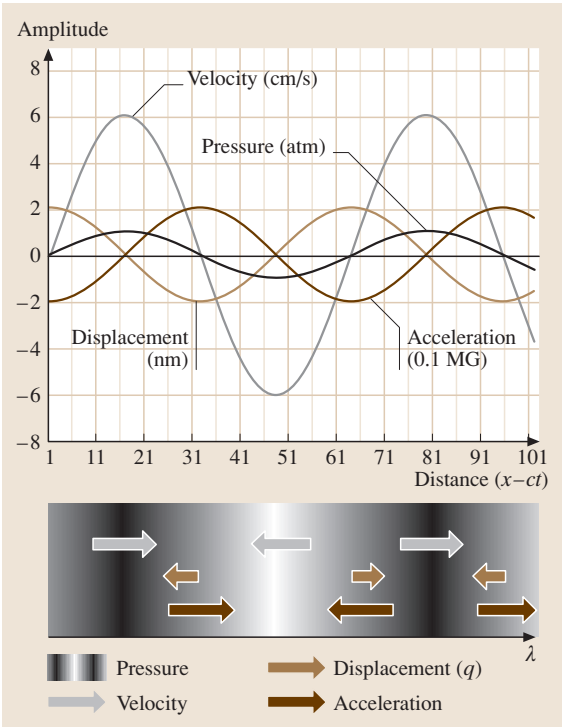


Fig. 21.5 Typical acoustic parameters of a 300 mW/cm^2, 5 MHz ultrasonic wave in tissue impedance. Input parameters: Tissue impedance = $Z = 1.5$ MRayles = 1.5 MN s/m^3 = 1.5×10^6 kg/(m^{2}s), pressure amplitude = $p = 1$ atm (bar) = 101 kPa (kN/m^2) = 760 mmHg (Torr), frequency = 5 MHz; resultant wave parameters: intensity = 0.33 W/cm^2 = $p^2/2Z$, peak molecular velocity = 6 cm/s = p/Z, molecular displacement = 1.9 nm, molecular acceleration of 0.19 million times the acceleration of gravity

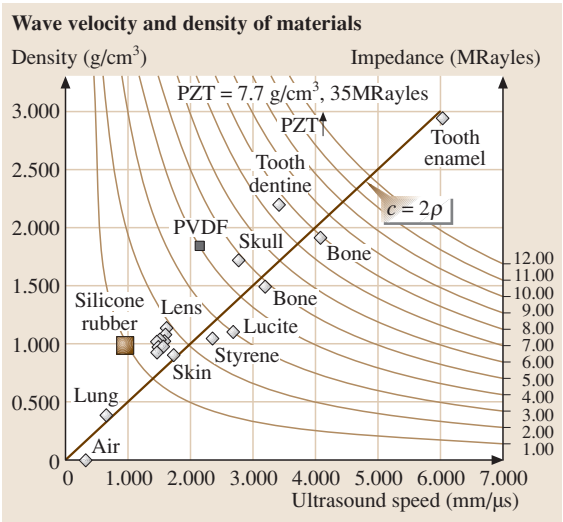


Fig. 21.6 Acoustic properties of materials of medical interest. Empirically, the acoustic properties of tissues fall on a line relating ultrasound speed (c) and tissue density (ρ); $c = 2\rho$. Using the equation for impedance $Z = \rho c$, then $Z = c^2/2 = 2\rho^2$. Polyvinylidene fluoride (PVDF) transducer material has acoustic properties near soft tissue, lead zirconate titanate (PZT) transducer material has much higher density and acoustic impedance

spheric pressure, making the compressions 6 atm and the decompressions −4 atm.

The linear acoustic relationships can be easily derived using a simple linear elastic model of tissue (Fig. 21.5) and Newton's first law of motion on the molecules. The molecules in the tissue will accelerate along the axis of the ultrasound propagation (x) and displace a distance (q) away from equilibrium because of a gradient in pressure ($\mathrm{d}p/\mathrm{d}x$), which is related to the tissue compression ($\mathrm{d}q/\mathrm{d}x$) and the tissue stiffness (κ).

$$p = -\frac{\kappa\,\mathrm{d}q}{\mathrm{d}x} = -\kappa q' \,, \tag{21.1}$$

$$\kappa\frac{\mathrm{d}^2 q}{\mathrm{d}x^2} = -\frac{\mathrm{d}p}{\mathrm{d}x} = \rho\frac{\mathrm{d}q^2}{\mathrm{d}t^2} \,. \tag{21.2}$$

Solving this equation with the variable $q(x - Ct)$ produces

$$\kappa q'' = \rho C^2 q'' \,, \tag{21.3}$$

so

$$C = \sqrt{\frac{\kappa}{\rho}} \,. \tag{21.4}$$

The molecular velocity ($v = \mathrm{d}q/\mathrm{d}t = -Cq'$) and the tissue pressure ($p = -\kappa q'$) form an important ratio

$$Z = \frac{p}{v} = \frac{\kappa}{c} = \sqrt{\kappa\rho} = \rho C \,. \tag{21.5}$$

Although the tissue density (ρ) and stiffness (κ) determine the acoustic impedance (Z) and acoustic wave speed (C), it is more convenient to measure the density and wave speed of a material and compute the impedance.

A good deal of effort has been devoted to measuring the properties of tissues (Figs. 21.6–21.8). Measurement differences between laboratories and differences in tissue preparation contribute to the variability of tissue property values. While living mammalian body tissues

Amazon
EX1010 Page 854

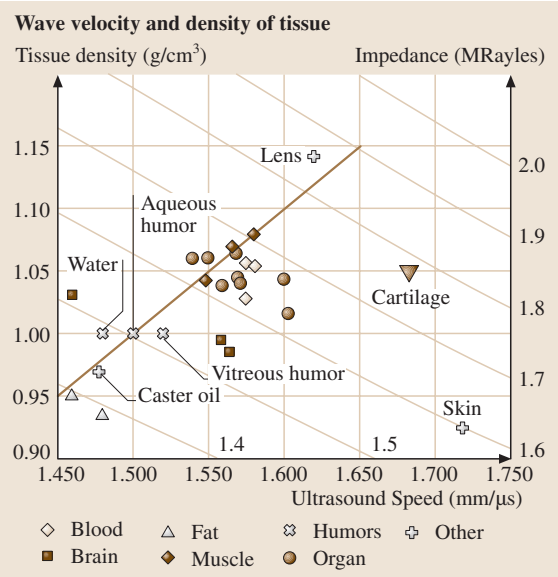


Fig. 21.7 Acoustic properties of soft tissues

are held to a temperature near 37 °C, and have blood flow that swells the tissue and changes the average composition with the heart rate and respiratory rate, it is convenient to measure properties of dead tissue at bench-top temperatures (25 °C). Fortunately, the exact acoustic properties of tissues have not proven very useful in clinical diagnostic applications. Ultrasound imaging methods have not been able to differentiate tissue types in spite of a half century of efforts. The identification of disease with ultrasound imaging uses the shapes of large structures as the primary diagnostic tool.

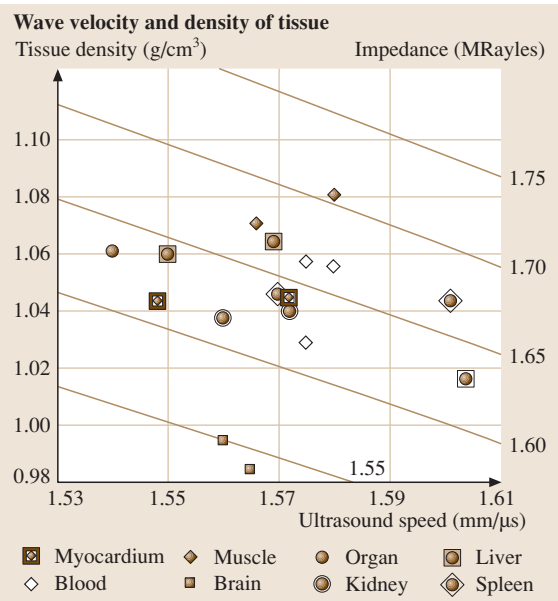


Fig. 21.8 Detailed acoustic properties of soft tissues

21.3.1 Reflection of Normal-Angle-Incident Ultrasound

When ultrasound intersects an interface between two materials with differing acoustic impedances (Z_1 and Z_2), perpendicular to the interface, then the amplitude of the reflection of ultrasound at the interface can be computed from the requirement that the pressure change and molecular velocity of the incident wave (p_i, v_i) must equal sum of the pressure changes and molecular velocities of the transmitted and reflected waves (p_t, p_r, v_t, v_r). The impedances of the materials relate the pressures and molecular velocities ($Z_1 = p_i/v_i = -p_r/v_r$, $Z_2 = p_t/v_t$). The pressure reflection and transmission coefficients are

$$\frac{p_r}{p_i} = R = \frac{Z_2 - Z_1}{Z_2 + Z_1} , \tag{21.6}$$

$$\frac{p_t}{p_i} = T = 2\frac{Z_2}{Z_2 + Z_1} . \tag{21.7}$$

Note that if the acoustic impedance of the second material is lower than the acoustic impedance of the first material, then the reflected wave is inverted. The sum of the transmitted and reflected power equals the incident power.

21.3.2 Acute-Angle Reflection of Ultrasound

If the ultrasound is incident on the interface at an acute angle, the ultrasound that passes into the second tissue is tilted to a new direction according to Snell's law (Fig. 21.9).

$$\frac{C_1}{\sin\theta_1} = \frac{C_2}{\sin\theta_2} . \tag{21.8}$$

Because the component of molecular velocity normal to the surface must be preserved:

$$\frac{p_r}{p_i} = R = \frac{\frac{Z_2}{\cos\theta_2} - \frac{Z_1}{\cos\theta_1}}{\frac{Z_2}{\cos\theta_2} + \frac{Z_1}{\cos\theta_1}} . \tag{21.9}$$

In this case, not all of the ultrasound power is found in the sum of the reflected wave and the transmitted wave. The remaining portion of the power appears as a surface *capillary* wave propagating along the surface of

Amazon
EX1010 Page 855

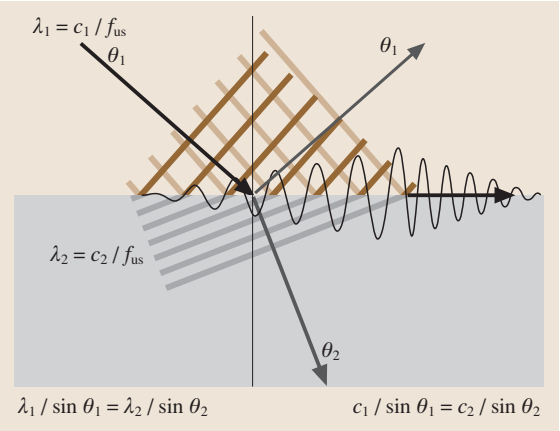


Fig. 21.9 Refraction of ultrasound as it passes from one material to another. *Dark brown*: incident compressional wavefronts and wave vector incident at angle θ_1. *Light brown*: reflected compressional wavefronts and wave vector reflecting at angle θ_1. *Gray*: transmitted compressional wave. The interfacial shear wave increases in intensity as the ultrasound beam cross section coherently contributes to the wave; attenuation of the shear wave causes a rapid decrease in amplitude outside the beam

the interface. This capillary wave is subject to high attenuation. Because tissue has an interface on every cell boundary and every tissue boundary, this mechanism is responsible for some of the conversion of incident ultrasound power into heat as ultrasound propagates into tissue. It is important to notice that the propagation speed of the capillary wave is not the same as that of the component of the compressional wave directed along the interface, so the capillary wave is out of phase with the ultrasound wave, contributing to the transfer of energy into the capillary wave. Outside the ultrasound beam, the capillary wave takes on its conventional wavelength (c_s/f), where f is the ultrasound frequency. The propagation speed of the capillary wave (c_s) is proportional to the interfacial tension.

21.3.3 Diagnostic Ultrasound Propagation in Tissue

Diagnostic ultrasound uses ultrasound frequencies of 1–30 MHz. (MHz = cycles per μs). The speed of ultrasound in most tissues is near 1.5 mm/μs (1500 m/s). There are some notable exceptions. In bone the speed is between 3.5 mm/μs and 4 mm/μs, and in air the speed is 0.3 mm/μs. In cartilage the speed is 1.75 mm/μs which of course varies with composition. In fat the speed is 1.45 mm/μs (Table 21.3). In muscle, the speed of ultrasound varies by about 1.5%, depending on the angle of propagation to fiber orientation.

Although most authors focus attention on ultrasound frequency, ultrasound wavelength may be more convenient for understanding the important issues. There are three issues of importance:

- Ultrasound cannot resolve structures smaller than the wavelength.
- Scattering and attenuation [21.42] both depend on ultrasound wavelength and its relationship to the size of the scatterers.
- The focusing properties of ultrasound beam patterns and the formation of side-lobes depend on the ratio between the wavelength and the width of the transducer.

21.3.4 Amplitude of Ultrasound Echoes

Red blood cells (erythrocytes) are 0.007 mm in diameter and about 0.001 mm thick. The largest cells in the body, nerve axons, may be 1 m long, but their diameter is about 0.001 mm. A liver cell is about 0.04 mm in diameter. The smallest structures imaged by ultrasound in clinical practice are layers less than 1 mm thick, such as the media lining major arteries (the intima-media thickness, IMT) [21.43], corneal layers (with 30 MHz ultrasound) and skin surfaces. However, these structures can only be observed in the range (depth) direction because resolution is best in that direction. Lateral resolution is dependent on the numeric aperture of the ultrasound beam pattern and the relationship between the object of interest and the focus as well as the ultrasound wavelength. Only the ultrasound wavelength affects depth resolution. The result is that ultrasound images are anisotropic, with much better resolution in the depth direction than in the lateral direction. The image is delivered to the examiner as a pictorial map in two dimensions. In our optical experience, resolution is equal in the two dimensions. Therefore, we expect that, if we can see detail in one dimension, we can also see the detail in the other, even when we cannot. This gives the impression that ultrasound has higher resolving power in the lateral direction than it in fact does. This is particularly important in measurements such as the IMT and measuring the thickness of the atherosclerotic cap. Such structures can only be visualized when the ultrasound beam is oriented perpendicular to the structure.

To identify tissues and organs, the lateral dimensions must by at least 10 wavelengths wide. This

Amazon
EX1010 Page 856

Table 21.3 Ultrasound wavelength versus tissue thickness. To resolve the thickness of these structures, the ultrasound frequency must be much higher than listed in this table. Much lower-frequency ultrasound passes through with little interaction. For particles or cells, lower-frequency ultrasound is subject to Rayleigh scattering

Tissue	Property	Dimension (mm)	Ultrasound	
			Speed (mm/μs)	Frequency (MHz)
Trachea	Lumen diameter	25	0.32	0.013
Aorta	Lumen diameter	30	1.57	0.063
Fat layer	Subcutaneous	20	1.45	0.080
Myocardium	Thickness	10	1.6	0.16
Skull	Thickness	10	4	0.4
Brain	Cortex	3	1.5	0.5
Artery	Wall	0.8	1.6	2
Trachea	Wall	0.6	1.75	2.9
Bone	Cortex	1	4	4
Eye	Cornea	0.6	1.64	2.73
Skin	Dermis	0.3	1.73	5.76
Fat	Cell	0.1	1.45	14.5
Brain	Cell, large	0.1	1.5	15
Skin	Epidermis	0.05	1.73	35
Erythrocyte	Cell	0.007	1.57	225
Bacteria	Cell, large	0.005	1.5	300
Brain	Cell, small	0.004	1.5	375

Notes:
1. Trachea lumen: for phonation below 13 kHz, the trachea diameter is smaller than the wavelength so that the trachea acts like a waveguide, bounded by cartilage with acoustic velocity and impedance higher than the luminal air.
2. Bone cortex and thin skull have thicknesses near the wavelength of transcranial ultrasound and a much higher ultrasound impedance, so the skull can act as an interference filter reflecting some wavelengths and passing others.
3. As the upper limit of most medical ultrasound systems is 15 MHz, small animal research instruments image at frequencies as high as 70 MHz, high enough to resolve the epidermis and large brain cells, but not high enough to image most cells.

number varies depending on the numeric aperture of the imaging system and on the acoustic contrast with the surrounding material. Small round structures such as tendons can be imaged using tricks, such as watching for motion, but most objects successfully imaged by ultrasound are larger. It is important to remember that it is possible to see an object that you cannot resolve. For instance, you are able see stars or lights at night, even though you cannot resolve closely spaced pairs of stars. When the signal from a target is strong, the target can be detected and located, even though a pair of targets cannot be resolved as two. If Doppler demodulation is used, rather than amplitude demodulation (used for B-mode), small vessels with

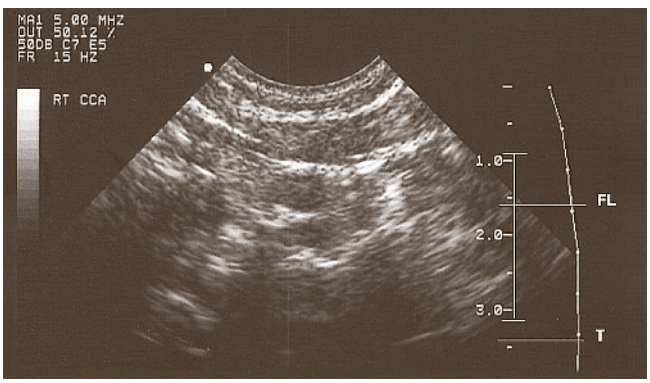


Fig. 21.10 Near-field versus far-field difference in ultrasound image. This is an image taken with a diagnostic scanner using a 5 MHz ultrasound transducer (wavelength = 0.3 mm) with a concavity radius of 16 mm and a transducer diameter of 6.4 mm. The computed *transition zone* is $d^2/4\lambda = 34$ mm. The *focus* must be less than the 34 mm distance to the transition zone to be effective. With a fixed-focus fixed-aperture ultrasound transducer, the transition from the near field to the far field is marked by lateral spreading of the speckle in the far field. There is no effect on the range (depth) speckle dimension

Amazon
EX1010 Page 857

blood flow can be resolved if the signals are strong enough.

Ultrasound imaging is a coherent process that generates speckle in the image. This is often called *tissue texture*, but the spacing of the speckle is about equal to the burst length of the ultrasound pulse, which is up to several wavelengths, and this is much greater than the fine cellular structure of the tissues under observation. Our visual processing is so good that we integrate prior knowledge, and outline shape seamlessly into our recognition process, while believing that we are recognizing texture.

Ultrasound imaging and aeronautical radar imaging are electronically identical. However, in aeronautics, the space between aircraft is very large compared to the size of the aircraft and to the wavelength of the radar wave. In medical ultrasound imaging, the cells are tight packed together, and the cell size (10 μm) is smaller than the wavelength of ultrasound (500 μm) so that the scattering is complex. In addition, ultrasound medical imaging systems often generate images from the complex near field (Fresnel zone) of the ultrasound transducer (Fig. 21.10). This becomes particularly confusing when tissues are moving laterally through an array of ultrasound beams. Because of the Moire effect of this system, tissue motions from left to right can cause speckle patterns to move right to left.

21.3.5 Fresnel Zone (Near Field), Transition Zone, and Fraunhofer Zone (Far Field)

The transition between the Fresnel and Fraunhofer zones can be computed from geometric considerations (Fig. 21.11). As in the computation of the basic wave equations, we assume that ultrasound propagation is a linear process and that superposition holds (pressure fluctuations and molecular velocity fluctuations can be added). Although some authors use Huygens' principle [21.44], dividing the transducer into tiny segments and adding the contribution of each to the wave, the computation is simplified if reciprocity is used (the transmitted ultrasound beam pattern and the received ultrasound beam pattern are the same), and the wave is assumed to be emitted from a test point in the ultrasound beam and received by the transducer.

A wave propagating from a stationary point will expand as a series of concentric spherical surfaces, spaced by the ultrasound wavelength with the source at the center. If the source is close to a planar transducer face, then at every time point some compressional spherical regions and some rarefactional spherical regions will simultaneously be present on the transducer face plane. This provides a mixed signal to the transducer, the compressions and rarefactions destructively inter-

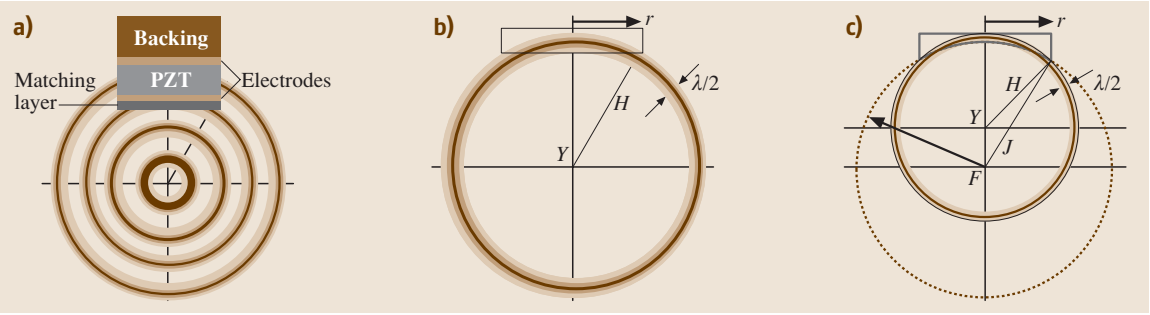
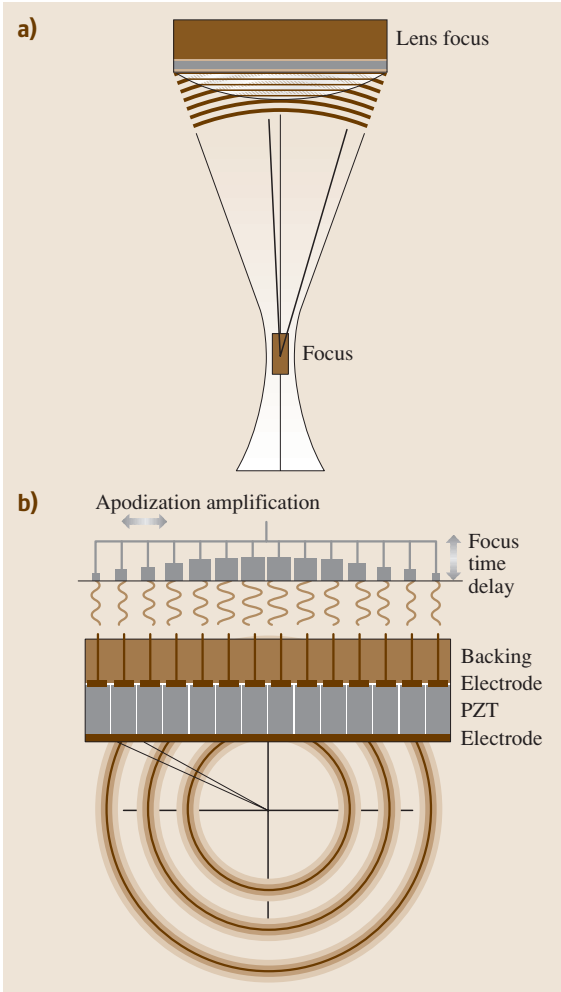


Fig. 21.11a–c Geometry of transition zone between near field (Fresnel zone) and far field (Fraunhofer zone) **(a)** A transducer consists of a piezoelectric element (PZT) with electrodes on the face with an impedance matching layer and on the back with a backing material. For computation, only the wave intersection with the matching layer face needs to be considered. **(b)** By geometry, the distance to the transition zone (Ψ) between the Fresnel zone and the Fraunhofer zone for a flat transducer can be estimated. The transition zone is located at the furthest distance from the transducer that the origin of a compression half-cycle of a wave can completely envelope the transducer face. r = transducer radius, Ψ = distance to transition zone, $\lambda/2$ = half wavelength, H = hypotenuse of transition radius. $H^2 = \Psi^2 + r^2$, $H - \Psi = \lambda/2$. If $\lambda/4 \ll \Psi$, then $\Psi = r^2/\lambda = d^2/4\lambda$, the accepted formula for the transition zone. A wave originating from a closer location (Fresnel zone), will always produce a combination of compressions and decompressions at the transducer surface. **(c)** Drawings can be made for focused transducers whether concave, lens or phased focus array, but the algebra is more complex. The equivalent concave curvature is shown by the *dotted circle*. F = transducer focal radius, J = hypotenuse of focal radius

Amazon
EX1010 Page 858

fering. There are some locations of the source point that result in equal areas of compression and decompression of the transducer surface at all times. These are locations where the transducer has no sensitivity, and are called null points. By reciprocity, if the transducer emitted a wave, a null point will have no sound intensity from the transducer. Ultrasound transducer beam plots often show these null locations along the axis of the ultrasound beam. There may be several of these null points along the beam axis, and at other points in the beam pattern. The *near field* or *Fresnel zone* is the region of the ultrasound beam pattern where these null points are present. In the Fresnel zone, there is always some destructive interference of the ultrasound wave. The Fresnel zone is the region where beam focusing can be achieved.



When the source point is at a greater distance from the transducer plane, these regions of compression and rarefaction become nearly planar. There are times when the planar transducer surface can be completely contained in either a compression zone or a decompression zone. At this range, at least near the axis of the ultrasound beam pattern, there are no regions of destructive interference. This is the *far field* or *Fraunhofer zone*.

There is a transition between the Fresnel and Fraunhofer zones along the ultrasound beam axis, where it is first possible for the ultrasound transducer to be just barely completely contained in a compression half-wave region at some time within the ultrasound wave period. Half a period later, the transducer will be completely contained in a decompression half wave. This location is easily diagrammed geometrically (Fig. 21.11b) and the distance to the transition zone computed. Although the geometry for a similar computation for a concave transducer can be easily drawn (Fig. 21.11c), the algebraic solution for the focused transition, which is now retracted toward the transducer, is more difficult.

In addition to using a concave transducer, focusing of the ultrasound beam pattern can also be achieved by the use of a lens on the front of the transducer (Fig. 21.12a). The lens is often made of silicone rubber because of the low ultrasound propagation speed. Currently, most ultrasound scan heads consist of a linear array of 128 transducer elements; each element is 2 cm long and 0.5 mm wide arranged in a side-by-side row with a footprint of 2 cm by 6.4 cm. Focus is pro-

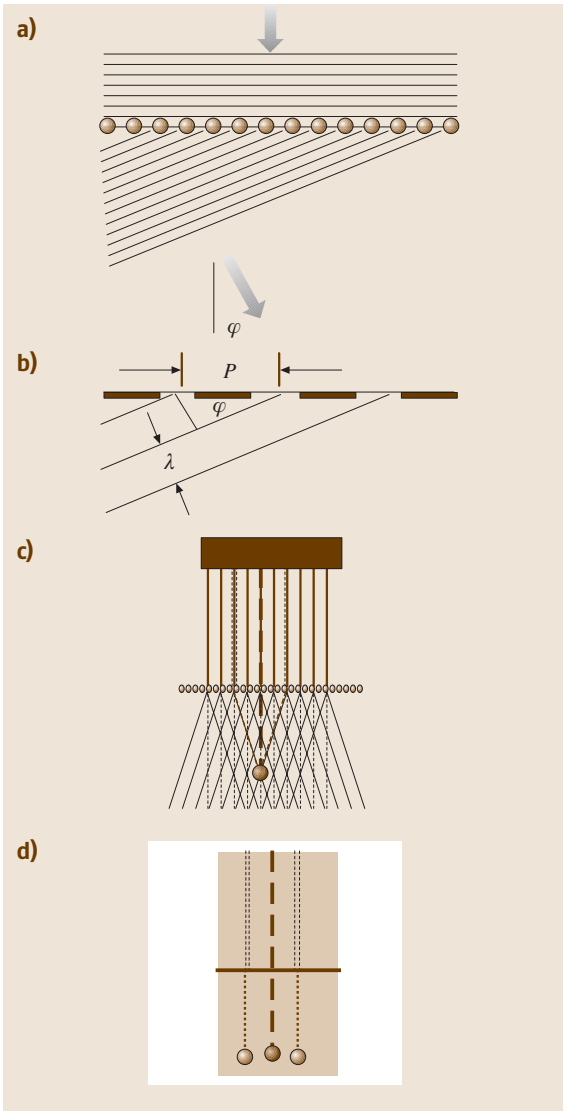
Fig. 21.12a,b Mechanical lens focusing and electronic delay focussing. **(a)** A low acoustic velocity in the lens allows the ultrasound traveling along the shorter central path to be delayed so that the ultrasound along the longer marginal paths can catch up, aligning the compressions and decompressions to provide the highest voltage excursions in the piezoelectric transducer element for ultrasound waves originating from the focal region. **(b)** Electronic delay lines in the signal path after the piezoelectric elements provide the same focusing function as the lens. Apodization *shading* of the sensitivity of the transducers at the edge of the aperture suppresses aperture diffraction side-lobes in the beam. The mechanical focus depth is determined at the time that the ultrasound transducer is manufactured; it cannot be altered by the examiner. The electronic focus depth can be adjusted to a different depth in a microsecond, the time that ultrasound travels 1.5 mm, so that the electronic focus can be adjusted to each depth during the time that the ultrasound is traversing the tissue

Amazon
EX1010 Page 859

vided in the image thickness direction by a cylindrical silicone rubber lens and in the lateral image direction by adjusting the relative phase of the adjacent transducers (Fig. 21.12b).

21.3.6 Measurement of Ultrasound Wavelength

Modern diagnostic ultrasound systems use sophisticated transducers and filters to improve resolution by shifting and broadening the ultrasound frequency band used for imaging, Doppler and other methods. It is possible, however, to use basic wave physics to measure the effective ultrasound wavelength of the system. In addition to refraction, ultrasound waves are also subject to diffraction. By placing a diffraction grating in the ultrasound image path in water, and imaging a point reflector, the diffraction pattern of the wave can be imaged and the wavelengths computed (Figs. 21.13, 21.14).



21.3.7 Attenuation of Ultrasound

As an ultrasound passes through tissue as a pulse or as a *continuous wave* along the beam pattern, some of the ultrasound energy is converted to heat in the tissue and some is reflected or scattered out of the beam pattern. In addition, nonlinear propagation converts some of the energy to higher harmonics ($2f$, $3f$ ...) of the fundamental frequency (f) of the wave. Attenuation increases with frequency, and the harmonic frequencies also may be outside the bandwidth of the detection system. These factors contribute both to actual and apparent attenuation of the ultrasound energy in the pulse and the average power passing through a cross section of the ultrasound beam as a function of depth. Changes in intensity are related to these changes in power, but the intensity is power divided by the cross-sectional area of the beam, so changes in beam cross-sectional area cause intensity changes that are not related to attenuation. Focusing the beam pattern can decrease the area, increasing intensity; diffraction and refraction increase the area, decreasing intensity.

Ultrasound attenuation is usually expressed as a ratio of the output power divided by the input power. In linear systems, this ratio is constant for all ultrasound intensities. In nonlinear systems, the relationship is more complicated. The attenuation rate of ultrasound in tissue

Fig. 21.13a–d Grating diffraction. Like any wave, an ultrasound beam can be tilted by a diffraction grating. The angle of tilt can be computed using Huygens' principle. If the pitch spacing of the grating is P, and the wavelength is λ, then the angle of deflection of the wave is expressed as $\sin\varphi = P/\lambda$. An ultrasound transducer array can act as a diffraction grating. This should be avoided. A diffraction grating in a water tank can be used to measure the wavelength of ultrasound. An image of a reflector deeper than the grating appears three times in the image, once at the true location and once for each of the diffraction orders. **(a)** Plane wave diffracted by grating. **(b)** Computaion of diffraction angle. **(c)** Ultrasound scanhead, diffraction grating and target. **(d)** Expected ultrasound image for a single frequency transducer

Amazon
EX1010 Page 860

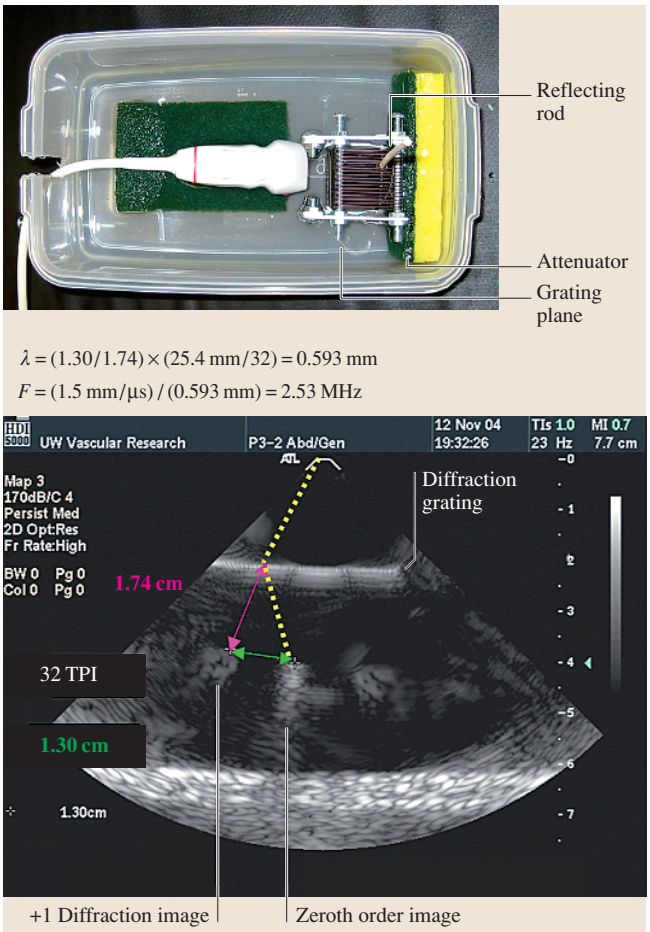


Fig. 21.14 Measuring ultrasound frequency and bandwidth by viewing a reflecting rod through a diffraction grating. The cross section of a rod forms the zeroth-order spot in the image. In addition to passing the ultrasound beam pattern directly (the zeroth image) the diffraction grating forms a +1 branch of the beam pattern (shown in *yellow*), which makes an image of the rod to the left (+1 diffraction image) and a symmetrical −1 image on the right. By measuring the geometric sine of the deflection angle, (1.30/1.74), the ultrasound wavelength can be computed using the spacing of the grating. The grating is made of monofilament fishing line wound on a frame made of 10–32 threaded screws (32 threads per inch, pitch spacing = 0.8 mm)

can be computed using base 10 (dB/cm, for engineers), base "e" (Np/cm, for scientists), compound percentage (% per cm, for physical therapists) or base 2 (half-value layers, for systems designers). The decibel, derived from the bel can be traced to Alexander Graham Bell, and the neper to John Napier. The bel is a factor of 10 in power, the neper is a factor of e (2.718) in amplitude. Ultrasound attenuation in soft tissue is between 3 dB/(MHz cm) and 0.3 dB/(MHz cm). Using intensity as the dependent variable in attenuation computations is complicated by changes in beam area. Some authors apply the bel to intensity. In acoustics the pressure amplitude of the wave, which is proportional to the square root of intensity (assuming constant impedance) is often used. The base 2 system is used to identify the thickness of tissue that attenuates the power by half, the intensity by half or the amplitude by half. The thickness is called the *half-value layer*, often without qualifying whether it is *half power*, *half intensity* or *half amplitude*. Intensity is proportional to the square of the amplitude, which is a multiplier of 2 in logarithms. If the cross-sectional area of the ultrasound beam is constant

$$\begin{aligned} 0.7\ \text{nepers} &= 6\ \text{dB} \\ &= 1\ \text{half-amplitude layer} \\ &= 2\ \text{half-power layers}\ . \end{aligned} \qquad (21.10)$$

Often the attenuation rate is nearly proportional to frequency, and frequency is inversely proportional to wavelength, so the attenuation can be most easily expressed in wavelength (Table 21.4). The use of half-value layers has the advantage that it can be related directly to the number of bits in a digitizer, simplifying computation.

Because of the high instantaneous intensities used in pulse-echo diagnostic ultrasound, all of the ultrasound propagation is nonlinear. The commonly used linear equations do not apply. The beam patterns are

Table 21.4 Ultrasound attenuation

Tissue type	Half amplitude (quarter power) thickness in wavelengths	60 dB pulse-echo attenuation depth in wavelengths (10 bits dynamic range)	Attenuation dB/(cm MHz)
Bone	1	5	30
Cartilage	8	40	10
Tendon	8	40	10
Skin	25	125	3
Muscle	25	125	3
Fat	80	400	1
Liver	80	400	1
Blood	300	1500	0.25

Amazon
EX1010 Page 861

not as predicted, because the wave propagation speed in the higher-pressure regions is faster than in the lower-pressure regions. The waves convert from sinusoidal to sawtooth, introducing a series of harmonic frequencies into the wave. The change in frequency (wavelength) affects the ultrasound beam pattern. The conversion of ultrasound energy into harmonic frequencies also increases the attenuation because the attenuation increases with frequency.

A significant development was the use of tissue-generated harmonic signals for diagnostic imaging. The utility of these harmonics was discovered by accident when investigators were searching for better methods of detecting ultrasound contrast agents. Ultrasound contrast agents consist of microbubbles that have natural oscillation frequencies near diagnostic frequencies. The bubbles therefore oscillate in response to incident ultrasound. The bubble oscillation stores some energy, which is reradiated at the original ultrasound frequency as well as at harmonics of that frequency. Older ultrasound systems were, by nature, insensitive to the second harmonic of the natural transducer frequency. By using a transducer with an increased bandwidth (3 MHz center frequency transducer manufactured with the quality factor reduced spreading the bandwidth to 1.9–4.1 MHz) then lowering the transmit frequency (2 MHz) and raising the receive frequency (4 MHz), a system sensitive to the harmonic emissions from the contrast bubbles can be achieved. Surprisingly, harmonic echoes are generated by tissues even when contrast bubbles are not present.

21.4 Methods of Medical Ultrasound Examination

Over the half century of ultrasonic medical examination, a variety of examination methods have been tried, discarded, with some to be resurrected and honed for use.

A passive method was evaluated to detect local ultrasound emissions above background due to local temperature elevations of cancerous tumors. The emissions of about 10^{-13} W/cm^2 (1 nW/m^2) are present in all warm tissues and provide a minimum intensity for the operation of active ultrasound systems. Transmission ultrasound systems have been developed using an ultrasound transmitter on one side of a body part and a receiver on the other side to detect differences in attenuation (like X-ray imaging). These systems determine ultrasound attenuation and ultrasound speed through the intervening tissues. One version of this system used an acousto-optical holographic system to form the image. Several systems have been explored to insonify tissue from one direction and gather the scattered ultrasound from another direction. Such systems usually require an array of receiving transducers.

The only ultrasound systems that have gained wide acceptance in clinical use are: (1) the continuous-wave (CW) backscatter Doppler system, and (2) common-axis pulse-echo backscatter imaging and Doppler systems. The reason for the failure of the other systems is due to two features of medical ultrasound examination: refraction of ultrasound in tissue and the cost of receiving and processing data from array receivers. The CW methods are used only for Doppler measurements. The first of these systems was constructed before 1960 [21.45, 46]; their application in medical diagnosis was well established by 1970 [21.47–52]. Pulse-echo methods have been under continuous development since 1950. The majority of medical diagnostic imaging examinations in the world are performed with pulse-echo instruments.

21.4.1 Continuous-Wave Doppler Systems

Continuous-wave Doppler was used in one of the earliest ultrasound systems to be commercialized. Developed

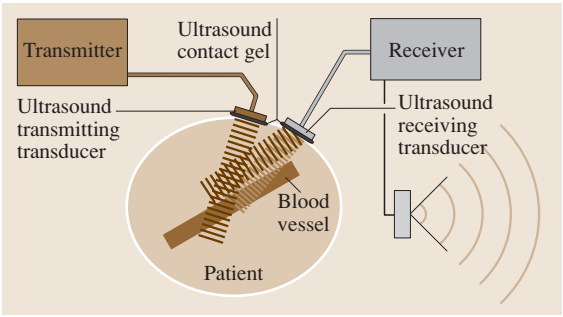


Fig. 21.15 Nondirectional continuous-wave Doppler. In a typical CW 5 MHz nondirectional Doppler, the incident ultrasound beam is scattered by stationary tissue forming a 5 MHz echo and by moving blood forming a 5.0004 MHz echo. The two echoes arrive at the receiving transducer simultaneously. By constructive and destructive interference between these waves, the received 5 MHz signal is amplitude modulated by the 5.0004 MHz echo. The frequency of the amplitude modulation is the difference frequency 5.0004 – 5 MHz or 400 Hz, which is amplitude demodulated, providing a 400 Hz audio signal to the speaker

Amazon
EX1010 Page 862

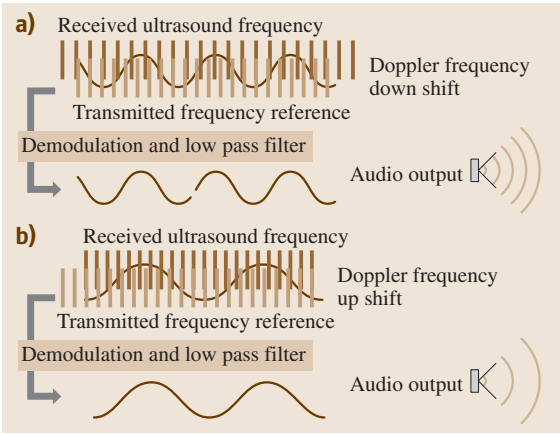


Fig. 21.16a,b Interference between echoes to produce audio frequencies. Constructive interference between the Doppler frequency-shifted echo and the original frequency wave increases the resultant amplitude; destructive interference reduces the amplitude. This occurs whether the Doppler shift is downward **(a)** due to reflections from blood cells receding from the transducer, or is upward **(b)** due to reflections from blood cells advancing toward the transducer. By amplitude demodulating the result, an audio frequency signal results. Amplitude demodulation can be done by multiplying the two ultrasound frequency signals together and low-pass filtering the result or by squaring (rectifying) the sum of the two ultrasound signals and low-pass filtering the result

independently in Japan in 1957 (Satamura and Koneko), and in the US in 1959 (Baker et al.), a system can be constructed from an RF transmitter, transmitting piezoelectric transducer, receiving piezoelectric transducer and amplitude demodulating receiver (Fig. 21.15). In the region of tissue where the transmitting beam pattern overlaps with the receiving beam pattern, the reflected wave from moving tissue will combine to interfere with the reflected wave from stationary tissue. The reflected wave from moving tissue has a Doppler shift. The Doppler-shifted frequency will interfere with the reflected wave from stationary tissue to cause an amplitude modulation in the combined wave. The frequency of that modulation is within the hearing range.

Ultrasonic Doppler examination produced an audible frequency by chance. The best ultrasound frequency to reflect by Rayleigh scattering from blood at a depth of 2 cm is 5 MHz. This frequency is shifted by the ratio of twice the blood speed ($2 \times 0.75\ \text{m/s} = 1.5\ \text{m/s}$) to the ultrasound speed 1500 m/s ($1.5/1500 = 0.001$) to cause a downshift in the ultrasound frequency of 5 kHz. The interference between the unshifted and shifted waves causes a 5 kHz modulation in the amplitude of the 5 MHz wave. This modulation is converted to sound by common amplitude modulation (AM) radio circuitry.

The introduction of the transistor in 1960 allowed this simple circuit to be produced in a palm-size package so that convenient clinical examination could be done. Whether the blood is approaching the transducer or receding from the transducer (Fig. 21.16), the audio signal is the same, with audio frequency proportional to the blood velocity.

These CW Doppler systems allowed the detection of narrow arterial stenosis by the high velocities present in the stenotic lumen. Normal velocities are below 125 cm/s, causing a Doppler shift of 4 kHz if the Doppler angle is 60°. The blood velocity in a stenosis is limited by the blood pressure via the Bernoulli effect; the velocity can be no greater than 500 cm/s for a systolic blood pressure of 100 mmHg. A blood velocity of 500 cm/s causes a Doppler shift of 16 kHz. These CW Doppler systems also allow the detection of venous obstruction by the loss of variations in venous velocity synchronized with respiration, and the testing of venous valve incompetence by the detection of reverse flow resulting from distal compression release or sudden proximal compression. An examiner with one year of

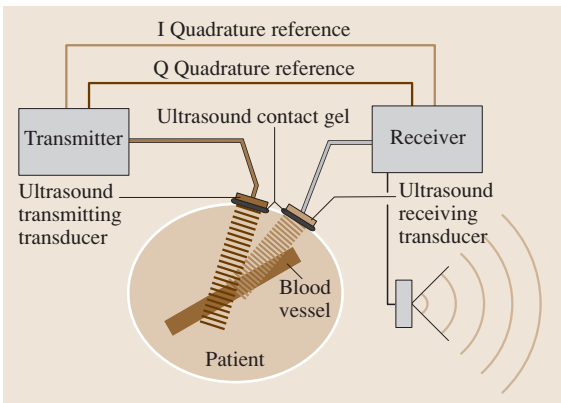


Fig. 21.17 Directional continuous-wave Doppler. By using a pair of reference waves at the transmitted ultrasound frequency, but phase shifted with respect to each other, the receiver Doppler demodulation can be performed against each of the reference waves. This allows the instrument to differentiate Doppler shifted echoes with increased frequency due to blood cells approaching the transducer from those with decreased frequency due to blood cells receding from the transducer

Amazon
EX1010 Page 863

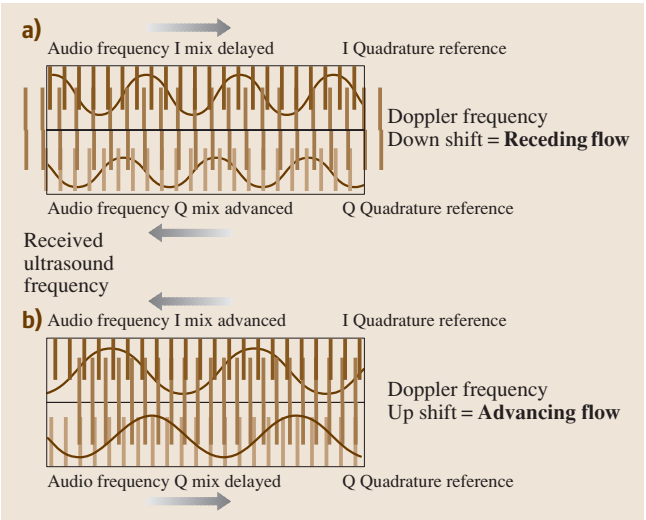


Fig. 21.18a,b Quadrature Doppler demodulation. **(a)** Demodulation of the of a Doppler down shifted echo against an-I reference and Q reference produces a quarter-wave advanced signal (shifted to the right) on the I product compared to the Q product. **(b)** Demodulation of the of a Doppler upshifted echo against an I reference and Q reference produces a quarter wave delayed signal (shifted to the left) on the I product compared to the Q product

training and experience can diagnose all superficial arterial obstructions and venous obstructions and reflux with accuracies exceeding 95% against any gold standard.

The addition of directional detection by Fran McLeod in 1968 simplified the separation of mixed arterial and venous flow, and allowed more-objective evaluation of velocities (Fig. 21.17). Directional detection was accomplished by providing a pair of quadrature signals derived from the transmitted frequency directly to the demodulator in the receiver. Quadrature signals differ only in phase by a quarter cycle. When the Doppler-shifted ultrasound echo is demodulated against each of the quadrature reference signals, the pair of difference waves produced are phase shifted by 90° (Fig. 21.18). If the reflecting blood is advancing toward the transducer then audio frequency (AF) I wave is advanced compared to the AF Q wave, if the reflecting blood is receding, then the AF I wave is delayed with respect to the Q wave. By further delaying the AF Q wave by a quarter cycle (the shift time is dependent on frequency), and adding or subtracting the resultant AF I and AF Q delayed, the sound channels can be separated (Fig. 21.19). After separation, the Doppler signal representing advancing flow can be delivered to one ear and the Doppler signal representing receding flow can be delivered to the other ear. Although these continuous-wave Doppler systems are simple and have not changed substantially since 1970, they still have tremendous clinical utility and are used by angiologists and vascular surgeons in daily practice. A CW Doppler transducer is provided with modern echo-cardiology systems (Fig. 21.20) for the measurement of cardiac output and for accurate velocity measurements of blood flow jets associated with valve disease.

During 1970–1985, several arterial mapping angiographs (Fig. 21.21) were developed to associate high-velocity Doppler signals, indicating stenoses with arterial landmarks such as bifurcations. These angiographs used mechanical or other methods to track the location of the ultrasound beam and display the results on an image that could be compared with an X-ray angiogram. Modern, large-field-of-view three-dimensional ultrasound imaging systems use extensions of this method.

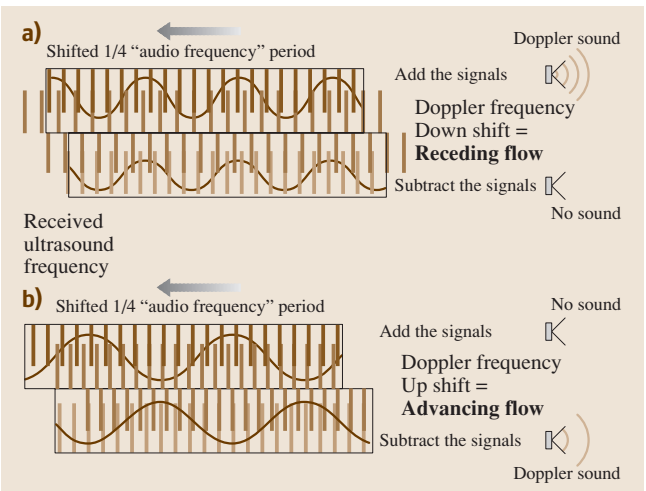


Fig. 21.19a,b Audio direction separation. By retarding the I quadrature channel by 1/4 of the period of the audio frequency, and then adding or subtracting the resultant pairs, the directions of flow can be separated. **(a)** The added pair results in sound for only the downshifted Doppler signals representing receding flow. **(b)** The subtracted pair results in sound for only the upshifted Doppler signals representing advancing flow

Amazon
EX1010 Page 864

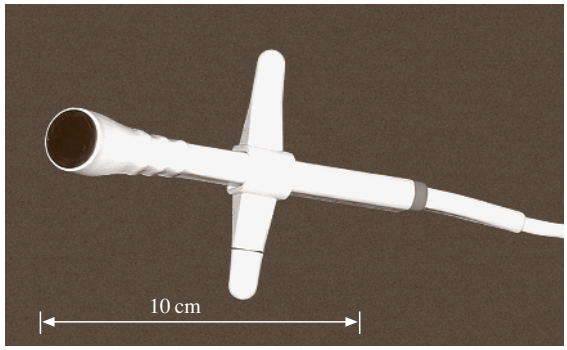


Fig. 21.20 Dual-element continuous-wave Doppler transducer for cardiac output measurements. This transducer is designed to fit in the suprasternal notch between the clavicles at the base of the neck. From this location, the Doppler ultrasound beam patterns can be nearly aligned with the axes of the cardiac valves. The ultrasound avoids the lungs by passing directly down through the mediastinum

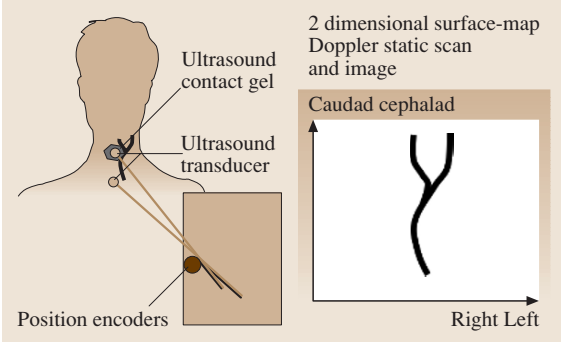


Fig. 21.21 Doppler arteriography. By monitoring the position of a Doppler ultrasound transducer, transferring the position on a storage image screen, and marking the display screen only when the Doppler detects blood flow, an image of the flow can be generated. Most of these systems used continuous-wave Doppler; the Hokanson system used pulsed Doppler

21.4.2 Pulse-Echo Backscatter Systems

Pulse-echo ultrasound consists of sending a pulse of ultrasound into tissue and receiving the echoes from various depths. The length of the transmitted pulse may be as short as 0.5 μs (for B-mode imaging) or as long as 5 μs (for trans-cranial Doppler). Usually the same transducer or transducer aperture is used for both transmitting and receiving. The depth of each reflector is determined by the time of flight between the transmitted pulse and the received echo: a reflector 3 cm deep returns an echo at 40 μs; a reflector 15 cm deep returns an echo at 200 μs. If the system is examining to a depth of 18 cm, then a new pulse can be transmitted after 240 μs. In that case, an echo returning at 40 μs after the later transmit pulse might come from 21 cm deep (280 μs) rather than 3 cm. Tissue attenuation will suppress the echo from deep tissue by about 54 dB (3 MHz ultrasound) compared to the echo from 3 cm.

Table 21.5 Ultrasound examination parameters

Maximum Examination depth (cm)	Ultrasound wavelength (mm)	Ultrasound frequency (MHz)	Pulse repetition Period (μs)	Pulse repetition Frequency (kHz)
3	0.075	20	40	25
5	0.125	12	67	15
6	0.15	10	80	12.5
10	0.250	6	133	7.5
12	0.3	5	160	6.25
15	0.375	4	200	5
20	0.5	3	266	3.75

To perform a pulse-echo examination, an ultrasound transducer (or array of transducers) is positioned to form a beam pattern along an axis, which is assumed to penetrate tissue in a single straight line. A short ultrasound burst is launched along that line. After allowing for the round-trip travel time to the depth of interest (Table 21.5), the ultrasound echo from a segment of tissue in the beam pattern is received, demodulated and prepared for display (Fig. 21.22). The ultrasound transmit pulse can be adjusted for frequency, duration (Fig. 21.23), energy, and aperture size and shape to fine-tune the examination if needed. The ultrasound echo can be demodulated to yield the amplitude (Fig. 21.24) and/or the phase. The results of multiple pulse-echo cycles along a single beam pattern can be combined. The echo is usually amplified with a fast-slew programmed amplifier to increase the gain of later echoes coming from deeper tissues, because they will be attenuated more than shallow echoes. If tissue visualization is desired, the echo strength is displayed in an image along a line representing the direction of the ultrasound beam, with the location along the line (representing depth) determined by the time after transmission that the echo returns. If a measurement of tissue motion is desired, then additional identical pulses are transmitted along the same beam pattern to obtain a series of nearly identical echoes from each depth of interest. These echoes are examined for changes in phase, which is the most sen-

Amazon
EX1010 Page 865

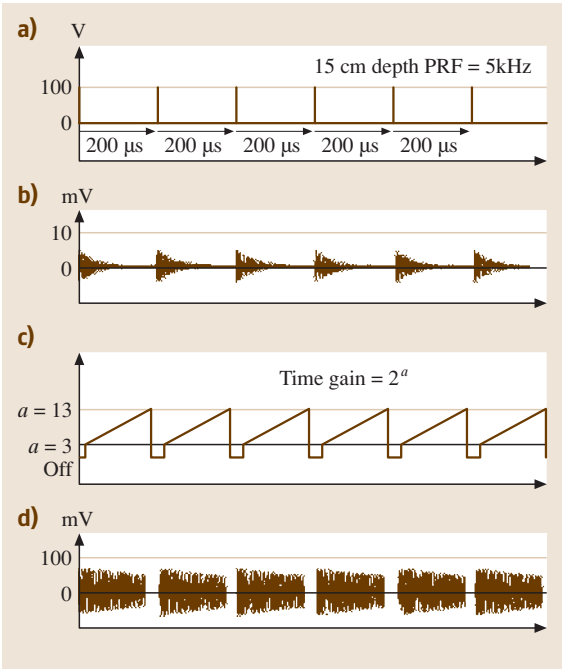


Fig. 21.22a–d Time gain compensation (TGC). **(a)** A new ultrasound pulse is transmitted each pulse repetition period (200 µs in this case). **(b)** Echoes from shallow and deep depths return at known times because of the speed of ultrasound and the expected round-trip travel time. The later echoes received from deeper tissues are weaker than the echoes received from shallow tissues because the echoes from deeper tissues have passed through more-attenuating tissue. **(c)** An amplifier programmed to increase the gain for deep echoes more than for shallow echoes is used to compensate for attenuation. This depth gain compensation (DGC) or time gain compensation (TGC) amplifier is under operator control. **(d)** The echoes, after TGC are ready for demodulation by analog or digital methods

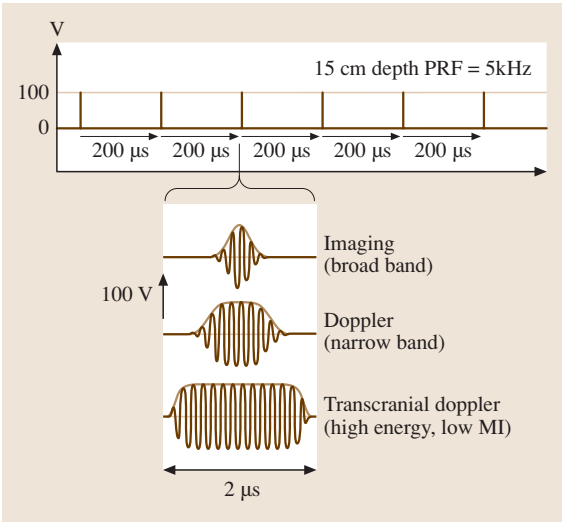


Fig. 21.23 Different ultrasound transmit bursts for imaging and Doppler applications. Short broadband transmit bursts are used for B-mode imaging; long narrow-band transmit bursts are used for Doppler applications. A longer transmit burst contains more energy if the maximum acoustic negative pressure (mechanical index) are limiting factors. A short transmit burst allows better depth resolution and also spreads the diffraction side-lobes of the beam pattern, suppressing lateral ambiguity. A longer transmit burst is preferable for Doppler applications where echoes from blood are weak and coherence length is important for demodulation

sitive indicator of displacement of the tissue reflecting the ultrasound.

This simple model places constraints on the ultrasound examination. First, at any depth, the strongest echoes from a bone or air interface perpendicular to the beam are 10^6 (60 dB) stronger than the weakest echoes from cells in liquid (blood). So, a 10 bit digital echo-processing system is the minimum to handle the range of echo strengths expected in an image. Second, because the speed of ultrasound is about 1.5 mm/µs in most tissues, echoes returning from 15 cm deep arrive 200 µs after ultrasound pulse transmission. A new pulse cannot be sent into the tissue along the same line or along another line until all of the echoes from the first pulse have returned. So, the maximum pulse repetition frequency (PRF) for an examination to a depth of 15 cm is 5 kHz (1/200 µs). Ultrasound energy is attenuated to 1/4 of the incident energy in most body tissues after passing through a depth of 80 wavelengths. So after passing through a depth of 400 wavelengths and returning through 400 wavelengths, the echo strength is only 0.25^{10} or 10^{-6} of the strength of a similar echo from the shallowest tissue. To compensate for this attenuation, an amplifier must amplify the deep echoes 60 dB more than the shallow echoes (Fig. 21.22). An alternative is to digitize the echoes with a 20 bit digitizer, 10 bits for the dynamic range of the echoes from different tissues and 10 bits to account for attenuation. In either case, the maximum depth of an examination is limited to 400 wavelengths of ultrasound. An ultrasound depth resolution cell (a pixel) is equal to about twice the wavelength of ultrasound. So, an ultrasound image can contain 200 pixels in the depth direction (Table 21.5). These con-

Amazon
EX1010 Page 866

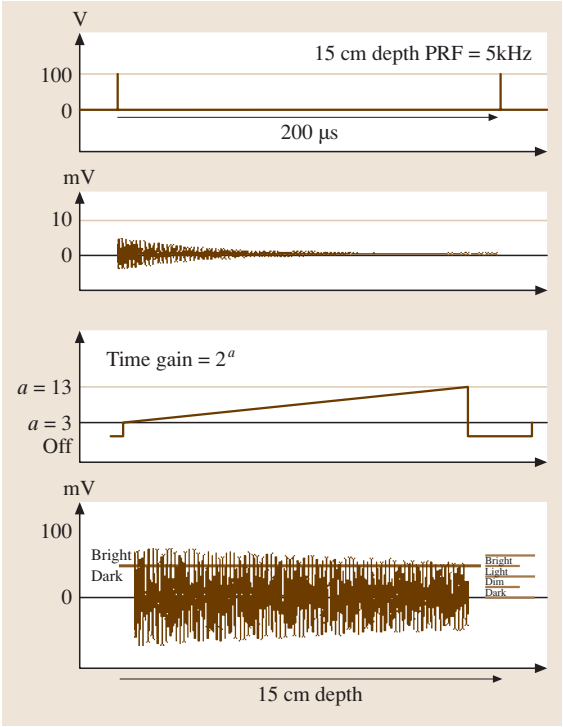


Fig. 21.24 Preparing the amplitude demodulated brightness mode echo for display. The amplitude of the amplified echo can be converted into brightness values by a digitizer. In early B-mode scanners, the display could show bright (echo) or dark (no echo) based on a one bit threshold detector (*dark line*). A two-bit digitizer allows four levels of gray scale (scale on *right*), making the result less sensitive to the setting of the TGC amplifier. Modern ultrasound B-mode imaging systems use an eight-bit digitizer to display 256 levels of gray. Depending on the method of presentation, the eye can distinguish no more than 64 stepped levels of gray or 16 isolated levels of gray

siderations provide a practical relationship between the ultrasound frequency and the PRF, based on the attenuation of tissue. The PRF is 1/800 of the ultrasound frequency in most applications.

21.4.3 B-mode Imaging Instruments

A series of B-mode (brightness mode) ultrasound imaging methods have been developed over the last 40 years. The methods have used the latest electronic technologies to improve the speed, convenience, capability and utility of the systems. The original imaging systems were based on radar technology and analog electronic

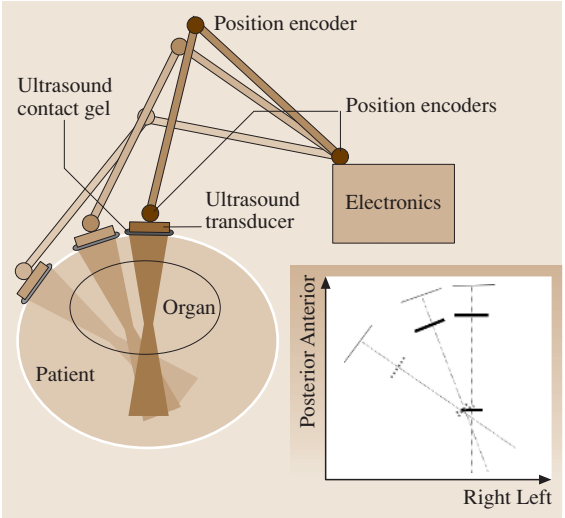


Fig. 21.25 B-mode static scanner. The traditional B-scanner restricted the transducer position and direction to movements in one plane that would form a cross-sectional image through the patient. The position of the transducer was located on the image display, and a line projected from the origin along the display in the direction of sound beam propagation. During the scan a marker was moved along the ultrasound beam direction at a speed of 0.75 mm/µs, representing the time that an echo would return after a round trip to each depth when traveling at 1.5 mm/µs. If a strong echo was detected, then a mark was stored on the screen to contribute to the image. The transducer was scanned across the skin to form an ultrasound scan cross-sectional image of the tissue

parts. Today, ultrasound systems are personal computers using standard operating systems with specialized display software coupled to custom ultrasound circuitry on the front end. A review of the history is useful because the modern instruments keep incorporating older methods.

Two-Dimensional Static B-mode

The original B-scanners (Figs. 21.25, 21.26) consisted of a single ultrasound transducer element coupled to a mechanical system to track the origin and direction of the ultrasound beam. The systems had the advantage that large fields of view could be scanned, such as a plane through a full-term fetus, and the sonographer could return to portions of the image to *paint in* anatomical features by approaching each of the reflecting interfaces from a perpendicular direction. As the image display system showed the brightest echo for

Amazon
EX1010 Page 867

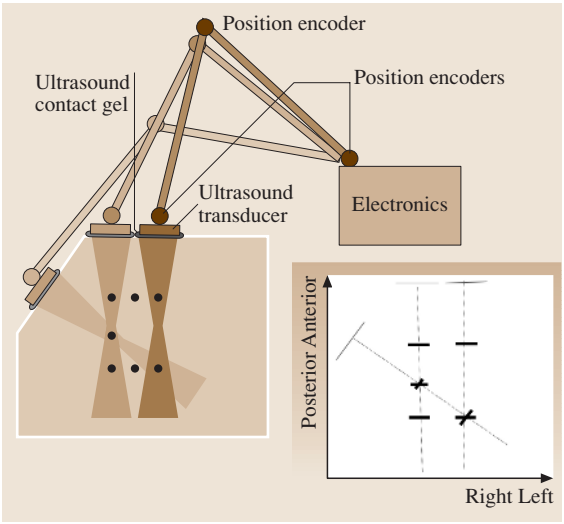


Fig. 21.26 B-mode calibration phantom. Analog electronics were not stable at the time that static B-scanners were constructed. Calibration phantoms were used to assure that a target would appear in the same location when viewed from different locations. Adjustments were provided to align the electronics

each anatomic location, *compound scanning* was used to obtain echoes from a variety of directions at each tissue location to render a useful image. Since a scan might take 5 min, movement of the patient during the scanning period was a problem, rendering the image useless. Because these systems used analog electronic

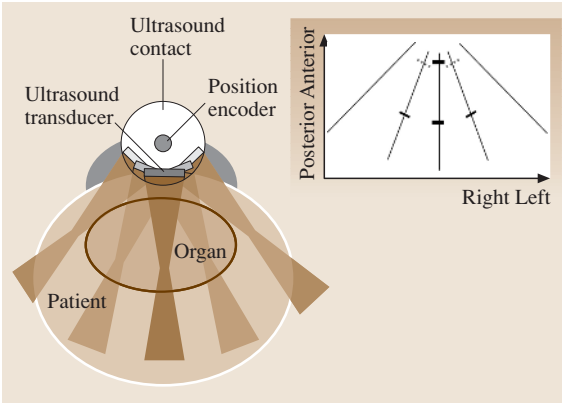


Fig. 21.27 Real-time two-dimensional ultrasound images. Motor-driven ultrasound transducers were able to rapidly tilt to a series of angles obtaining data from a series of lines in a plane of tissue to form a new two-dimensional image 10 times or 30 times per second

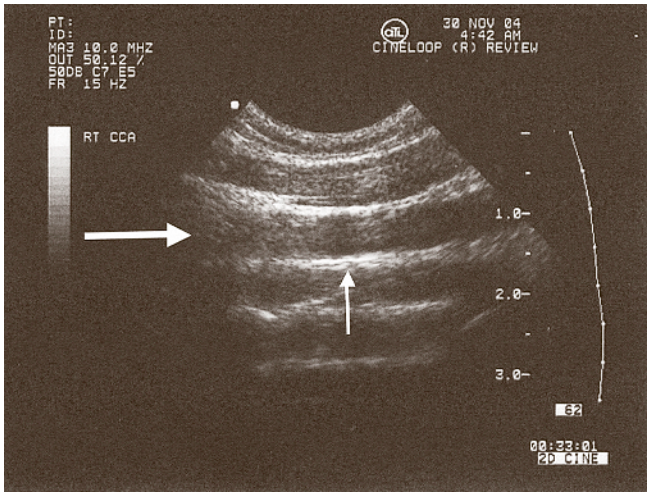


Fig. 21.28 Two-dimensional B-mode (brightness mode) common carotid artery image. The lumen of the common carotid artery in longitudinal section appears as a darker streak (*wide arrow*) bounded by the superficial and deep walls separated by 6 mm. The walls appear brighter where the ultrasound scan lines are perpendicular to the walls (*narrow arrow*) because of the specular backscatter.

devices, which were subject to deterioration over time, the stability and alignment of the instruments was important. In addition, since the same tissue was examined from multiple locations, the co-registered alignment of the tissue voxels (small volumes of tissue) on the image

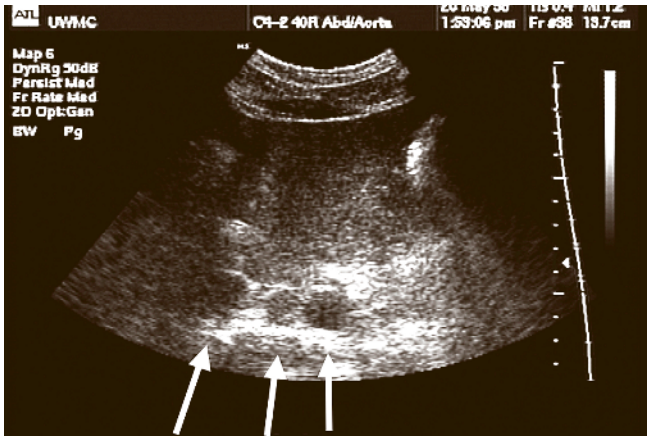


Fig. 21.29 Duplication of aorta [21.53] in the image. Refractive tissues composed of fat ($c = 1.45\,\mathrm{mm/\mu s}$) and muscle ($c = 1.58\,\mathrm{mm/\mu s}$) at the midline of the abdomen form two prisms. Each prism allows the aorta to be viewed resulting in two images of the aorta. This effect has also caused double viewing of a single pregnancy

Amazon
EX1010 Page 868

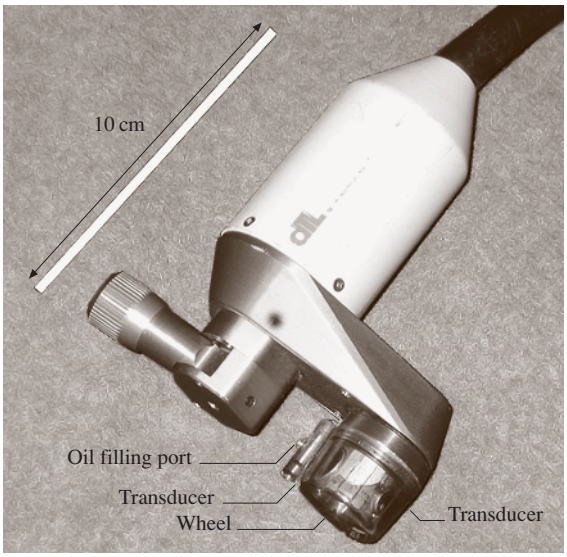


Fig. 21.30 Mechanical scan head. Three transducers are mounted around a rotating wheel encased in a cover filled with oil. Two of the 3 transducers can be seen in the image. Between the transducers is an air bubble in the oil; the air bubble must be removed through the oil filling port before scanning. Under the bubble is a rectangular shape that is the housing for a switch. Each of the transducers has a switch mounted opposite the transducer on the wheel which is activated magnetically to connect the transducer when the transducer is pointed toward the patient. The transducer wheel is driven by a motor in the white housing through a belt. A control knob on a joystick allows adjustment of the Doppler ultrasound beam, when needed; swinging the arm tilts the beam, rotating the knob advances the sample volume along the line. Electrical coupling to the transducer was accomplished by using a transformer aligned on the axle of the wheel with one coil stationary and one rotating. The magnet-activated switches mentioned above selected the proper transducer that was pointing at the patient

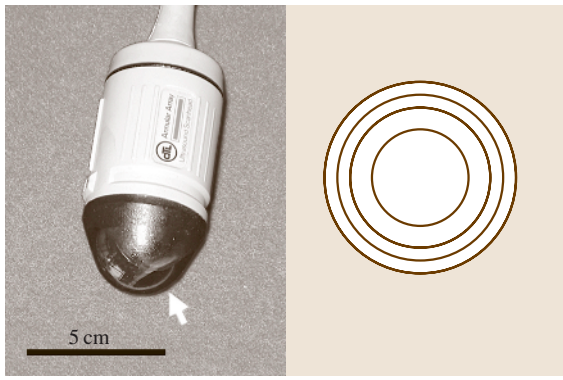


Fig. 21.31 Mechanically steered annular array scan head. The circular transducer is divided into concentric circles with each segment having the same area. By delaying by different amounts, the signals to the more central transducers, the depth of focus can be adjusted. A 10 ns delay between the transducer rings with the central transducer operating last will retract the focus a centimeter. The oil between the transducer and the dome shaped cap provides refractive focus in addition to the focus provided by the delays to the transducer. To point the ultrasound beam along different lines, the transducer wobbled back and forth rather than rotated. A rotating motion was not possible because the four coaxial cables could not cross the rotating axis. The arrow is pointing at the transducer along its axis

was critical. Regular testing of the instrument on alignment phantoms was required. The speed of ultrasound in the phantoms was controlled by the chemical composition of the phantom at the time of fabrication and the temperature of the phantom at the time of use. Of course, because the speed of ultrasound is not the same in different tissues, the success of the phantom in controlling image distortions in the depth direction during actual examination was limited. In addition, because the ultrasound beam can bend due to refraction as it passes from tissue to tissue, a factor ignored in the phantom, preventing lateral image distortions was impossible. However the phantoms did serve to prevent huge errors. Modern real-time ultrasound scanners that complete a scan in 30 ms (Fig. 21.27) form each image without overlapping beams so object co-registration is not tested. Thus, the value of phantoms has diminished. They still retain educational value.

Two-Dimensional Real-Time B-mode Mechanical Scanning

The earliest real-time systems scanned the ultrasound beam by tilting the ultrasound transducer, tracking the position and direction of the ultrasound beam with timing or an optical encoding system. The images had tremendous utility (Fig. 21.28) in spite of the poor lateral resolution compared to the depth resolution. Unfortunately, neither phantoms nor digital tracking of the ultrasound beam direction avoid image distortions due to refraction of the ultrasound beam in tissue (Fig. 21.29). These distortions, which are still a problem in the lateral direction, are ignored.

The ultrasound scan heads were convenient, ergonomic and compact (Fig. 21.30), located at the end of a cable attached to the ultrasound scanner. A variety

Amazon
EX1010 Page 869

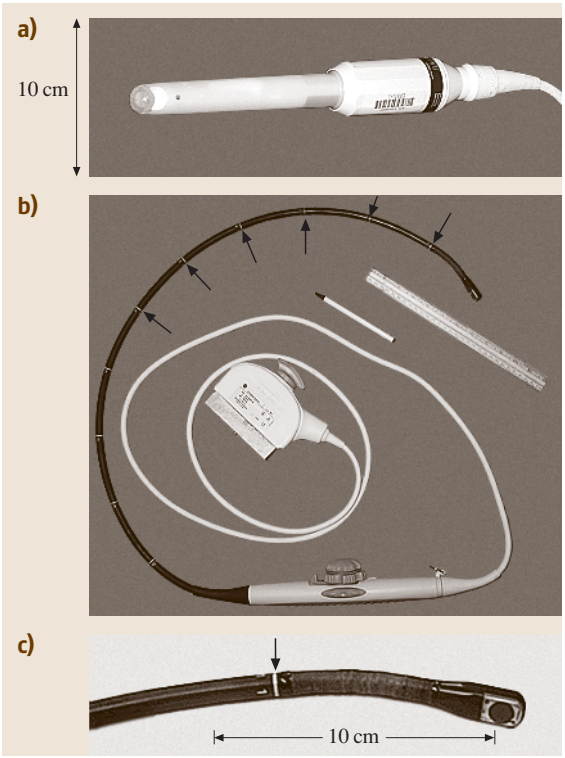


Fig. 21.32a–c Intracavity scan heads. **(a)** Intracavity *wobbler* scan head for transvaginal or transrectal examination. To provide acoustic coupling between the transducer and the housing, the scan head is filled with liquid. The transducer, at the left end of the image, is pointing out of the page. **(b)** Trans-esophageal (TEE) ultrasound scan head. The patient swallows the end with the transducer array (*upper right* in the picture) mounted in the end of the flexible esophageal probe. Marks every 10 cm (*arrows*) allow the cardiologist to monitor the location of the transducer array from the patient's teeth. **(c)** The trans-esophageal ultrasound transducer 5 MHz linear phased array has a circular boarder so that the array can be rotated to rotate the scan plane once the transducer is in the esophagus. A pair of control handles ((**b**) at *bottom*) allows the cardiologist to rotate the transducer array and to tilt the tip housing the array to examine the heart in different planes. Some patients tolerate this procedure well with little anesthesia, others require more sedation

of scan heads were developed including some with electronic focusing (Fig. 21.31) and specialized shapes for placement in the esophagus, rectum, vagina (Fig. 21.32), and some 1 mm in diameter for insertion inside blood vessels.

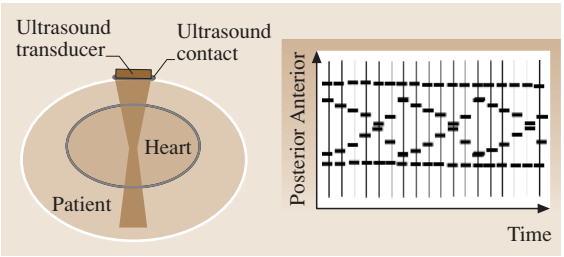


Fig. 21.33 M-mode (motion-mode) examination. For the study of cardiovascular wall motion, a single ultrasound beam is directed through the heart or other tissue. A *horizontal mark* showing the depth of each reflecting tissue in the vertical direction is shown on each vertical image line. By transmitting a new ultrasound pulse every millisecond, the echoes from tissue interfaces can be plotted for each pulse with time on the *horizontal axis*. By placing the lines side by side, the trajectories of tissue motion along the ultrasound beam are displayed. Speed of the reflecting tissue interface along the direction of the ultrasound beam is shown as a tilt or slope of an interface displayed on the image

M-mode Ultrasound

Among the early applications of ultrasound was the study of the motions of the heart using M-mode (motion mode) imaging [21.54, 55] (Fig. 21.33). By holding the ultrasound beam stationary and plotting the image width as a function of time, motions of the heart and other vascular structures could be documented. The velocity of a valve could be determined (Fig. 21.34) by measuring the slope of the trajectory on the M-mode tracing.

Two-Dimensional Real-Time B-mode Electronic Scanning

An alternative to moving the ultrasound transducer to point in different directions, is to have an array of transducers [21.56]. By switching to each transducer in turn to acquire echoes from the corresponding beam pattern, a two-dimensional (2-D) image is formed (Fig. 21.35). Several ultrasound scanners developed between 1970 and 1980 used low-density arrays like this. A scanhead with more transducer elements, spaced closely together (Fig. 21.36), could use groups of transducers to form an aperture. These high-density arrays permit phase focusing to a series of depths (Figs. 21.36–21.38), phase tilting of the ultrasound beam patterns (Fig. 21.39) and apodization of the aperture to smooth the ultrasound beam pattern (Fig. 21.40). The transducer array is usually formed from a single rectangular piezoelectric crystal, cut into a row of thin rectangles to form

Amazon
EX1010 Page 870

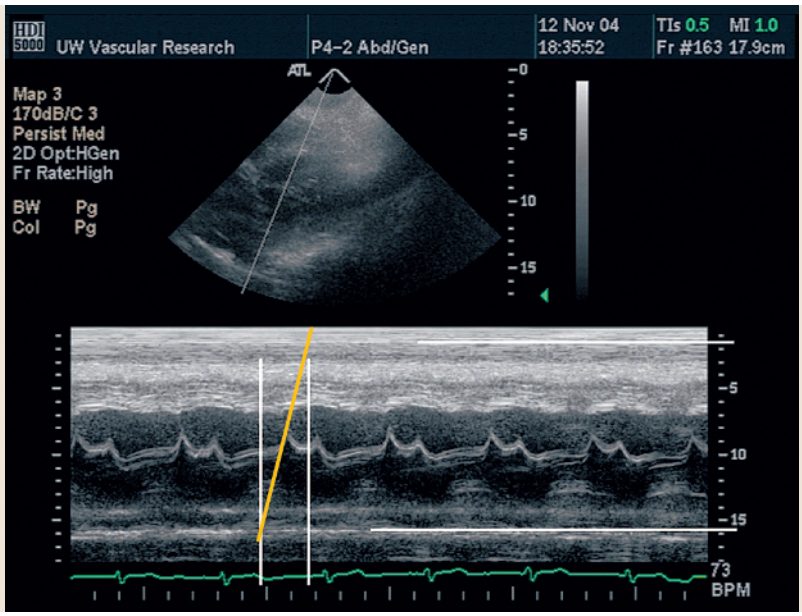


Fig. 21.34 M-mode (motion mode). Motion of a tissue interface along the ultrasound beam line is shown as depth (*vertical*) versus time (*horizontal*). The speed of the heart structure can be computed from the slope of the tracing. In this example, the speed is $158 - 16\,\text{mm}/0.4\,\text{s} = 355\,\text{mm/s}$. The green line across the bottom of the image is the Electrocardiograph (ECG, EKG) timing signal

an array in one direction. Because of the cuts, the array becomes flexible in the long dimension and can be curved (Fig. 21.41) to form a sector scan. Each of the 128 elements is connected via an electrical impedance-matching network to a coaxial cable, which forms part of the scan-head cable running back to the scanner. The plug connecting the 128 coaxial connectors to the ultrasound scanner has separate contacts for all 128 cables. Behind the plug in the scanner are separate ultrasound transmitters and receivers for each transducer element. Often each of the receivers will have a separate digitizer to convert the TGC-amplified signal into digital form.

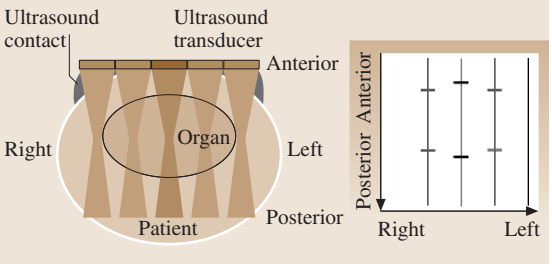


Fig. 21.35 Low-density linear-array two-dimensional B-mode. If the tissue does not move very much during the acquisition of an image, and the ultrasound beam pattern is moved across the tissue by successively activating different transducers and plotting the echoes with depth along the lines of the corresponding beam patterns, a two-dimensional image is formed. By convention in radiologic images, the images are usually displayed as if the patient is facing the physician. There is disagreement between clinics about how images should be oriented

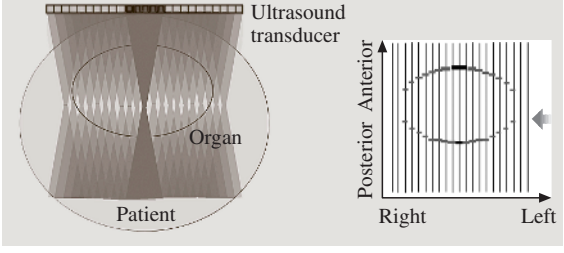


Fig. 21.36 High-density linear-array scan head. The transducers can be spaced more closely than the width of the ultrasound beam. Then each ultrasound aperture is formed by multiple transducers at the scan head face. The beam patterns overlap. The use of multiple transducers in the aperture allows the shaping of the aperture and electronic focusing of the ultrasound beam pattern

Amazon
EX1010 Page 871

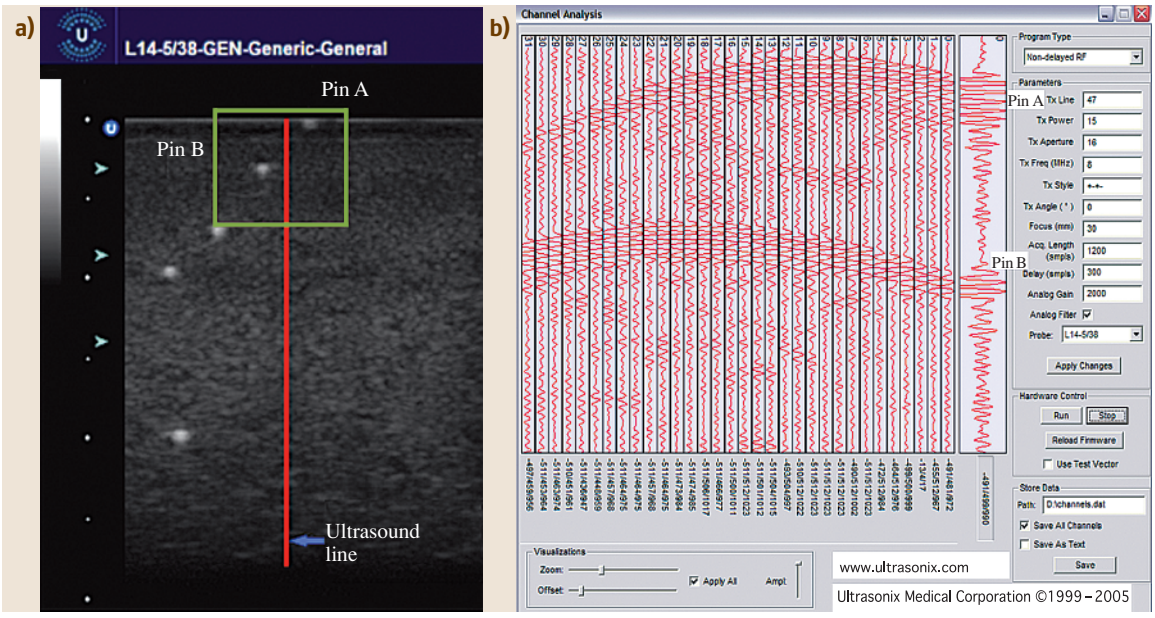


Fig. 21.37a,b Echoes received by each transducer in an array. By imaging highly reflective pins in a phantom, the effect of distance on travel time from a reflector to each transducer element in an array can be appreciated. By applying an appropriate delay on each of the transducer signals so that the echoes from the target align in time, and then adding the transducer signals together, a receiver beam pattern is formed, which is focused on the target. The time delays can be adjusted in 6 ns steps. **(a)** The transmit pulse was launched along the *red ultrasound line*. The echoes are displayed for data gathered from within the *green box*. **(b)** Radio-frequency echoes from each of 32 transducers are displayed for the echoes returning from a single transmit pulse (Courtesy Ultrasonix Medical Corp., Burnaby, www.ultrasonix.com)

The receivers and digitizers together form the ultrasound beam former for receive mode. Early array transducers had 32 elements, and the electronics were located in the scan head. Current instruments have 128 elements, a number limited by the costly cable containing 128 coaxial leads that connects the array to the receivers and transmitters in the console. The number of transducers will increase in the future as higher-capacity cables become available or, alternatively as it becomes possible to house the transmitting and receiving electronics in the ultrasound scan head.

A linear array transducer allows for adjustment of the transmit focus and aperture separate from the receive focus and aperture (Fig. 21.42). Because during the receiving period the relationship between depth and time is 0.75 mm/μs, a system can change receive focus

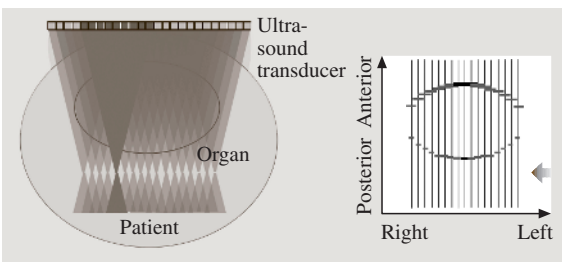


Fig. 21.38 Adjustable focus with large aperture. Using a high-density linear array to generate a large aperture and focus at a deep depth

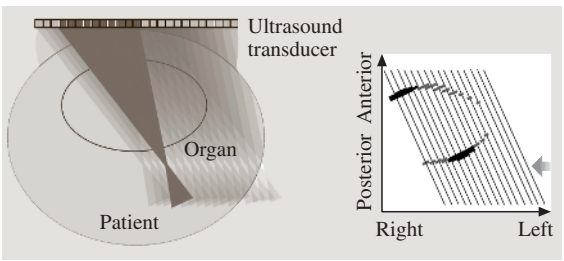


Fig. 21.39 Steering of the ultrasound beam pattern. Multiple transducers in the aperture allows the ultrasound beam to be steered at an angle for either imaging or Doppler by introducing phase delays in the signals to and from the transducers progressively along the transducer array

Amazon
EX1010 Page 872

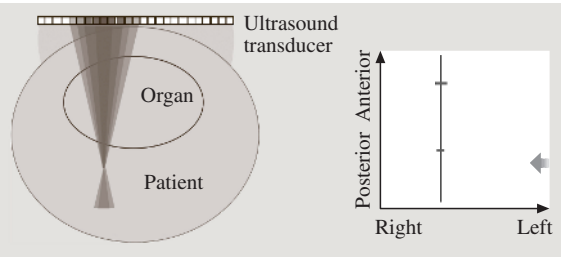


Fig. 21.40 Apodized aperture. Apodization is used to limit the side-lobes of the ultrasound beam pattern. Transducers near the edge of the aperture are excited with a low voltage during transmit compared to the central transducers and are amplified with a lower gain compared to the central transducers during receive. The drawing on the right shows the image line corresponding to the beam pattern with the superficial and deep echoes plus the mark on the right, indicating the focal depth

every 20 μs, advancing the focus 15 mm each time along with the corresponding aperture. This focal adjustment is called dynamic focusing and is similar in concept to time-gain compensation. It is also possible to acquire data along the ultrasound line using several pulse-echo cycles, each with a transmit burst that is focused at a different depth. Although dynamic receive focusing takes no more time than static focusing, using double transmit focusing to further improve the lateral resolution of the image at a greater range of depths does reduce the frame rate by half. The location of the transmit focus is indicated by a carrot on the right of the image.

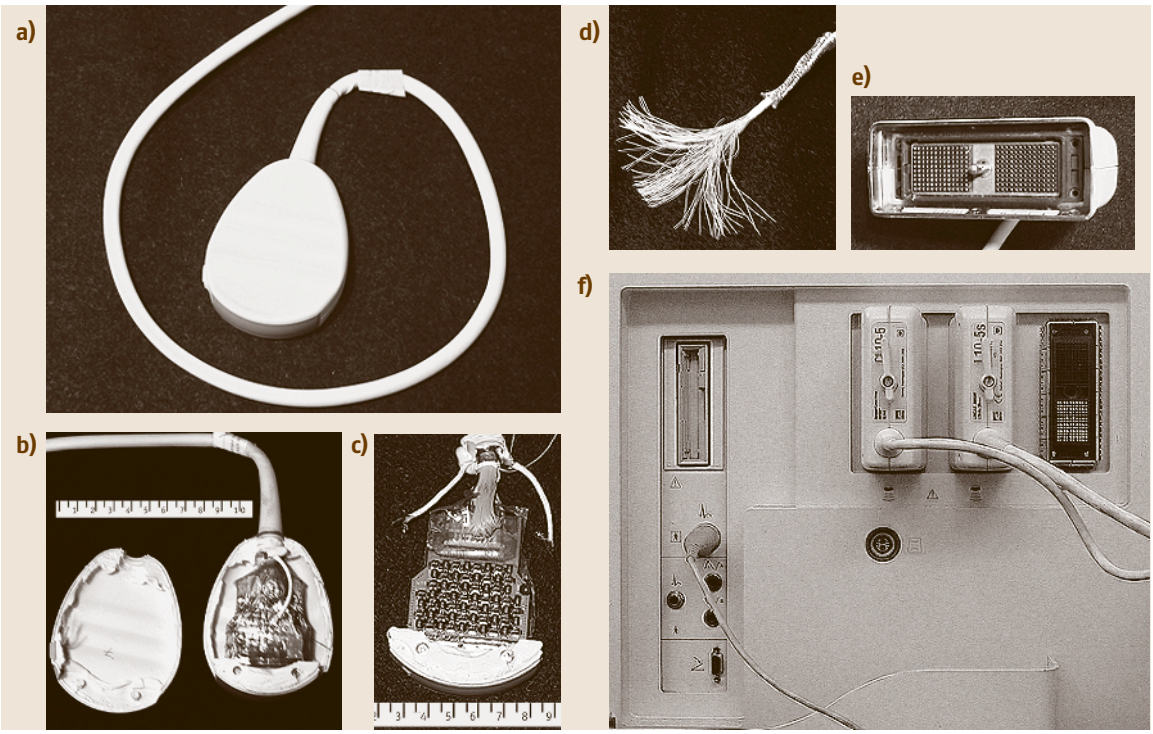


Fig. 21.41a–f Scan head details. This curved linear-array scan head consists of an array of 128 transducer elements cut from a single block of PZT piezoelectric ceramic. The array block is 64 mm long and 5 mm wide, cut into elements 0.4 mm long and 5 mm wide with a 0.1 mm kerf between. The block is curved to form a curved linear array. **(a)** Transducer in housing with cable; **(b)** Transducer housing removed showing the copper foil shielding over the internal electronics; **(c)** Shielding removed to show the 64 electronic matching circuits on this side of the circuit board; **(d)** 128 individual coaxial cables housed in the ultrasound scan head cable; **(e)** Scan head plug showing the connector electrodes for the 128 coaxial cables; **(f)** Front panel of the ultrasound scanner showing the sockets for the scan head connections. The front panel also shows connectors for other instruments including: electrocardiograph, plethysmograph, phonocardiograph microphone and computer disk drive for data exchange

Amazon
EX1010 Page 873

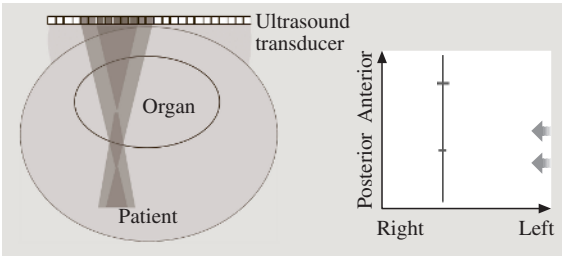


Fig. 21.42 Adjustable focus with large aperture. Using a high = density linear array to generate a large aperture allows electronic adjustment of the focal depth by adjusting the electronic delay of the transmit and receive signals so that the signal at the center transducers is delayed more than the signal at the edge transducers in both transmit and receive. Dual transmit focal depths, indicated by the pair of *arrows* on the right of the image, require that separate transmit pulses be sent into tissue for each of the two focal depths. On receive, the focus can be changed between the time that shallow echoes are received and the time that deep echoes are received

Because a linear array can steer the ultrasound beam, it is possible to form an image of each voxel in the tissue plane from different views, combining the results into a compound image (Fig. 21.43). The algorithm for combining the data from different angles is important in creating a pleasing image.

Phased Array Transducers. By applying a selected time delay to each transducer in an array, the ultrasound beam can be focused or tilted as desired (Fig. 21.39). Phased array transducers (Fig. 21.44) form the ultrasound image by tilting the ultrasound beam using selected delays on each transducer on transmit and receive to achieve the desired tilt. A scanhead with a transducer array of width

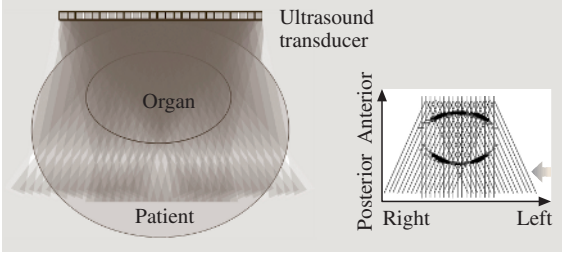


Fig. 21.43 Compound real-time imaging. By tilting the beam patterns to cross during acquisition of the image plane, system can take advantage of the specular backscatter of planar reflectors in the tissue

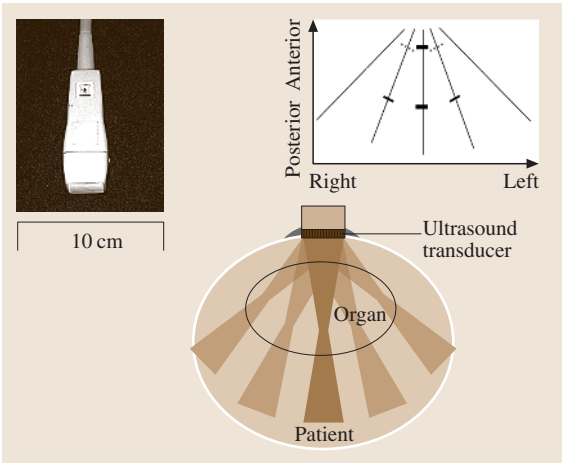


Fig. 21.44 Phased-array scan head. A phased-array scan head is able to use the same aperture for all ultrasound scan line beam patterns, directing the beam along different lines by adjusting the relative phase of the signals to the transducers

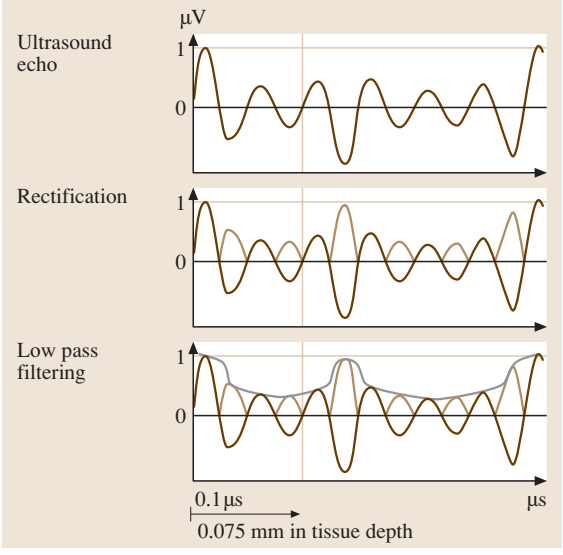


Fig. 21.45 Amplitude demodulation. To create a B-mode image of tissue anatomy, the strength or amplitude of the received ultrasound echo is determined as a function of depth. The RF echo is rectified (converting 5 MHz to 10 MHz) and low-pass-filtered with a 1 MHz cutoff to yield a depth resolution of 0.75 mm. That is effective if the ultrasound transmit burst is shorter than 1 μs. Amplitude demodulation requires one pulse-echo cycle along each ultrasound beam pattern line

Amazon
EX1010 Page 874

D can tilt an ultrasound beam to an angle θ in tissue with an ultrasound velocity of c by applying a time delay gradient along the transducer of

$$\frac{tc}{D} = \sin\theta \,. \tag{21.11}$$

The time t is often represented as a function of the phase of the ultrasound ϕ for the ultrasound frequency f_{us}

$$t = \frac{\frac{\phi}{2\pi}}{f_{us}} \,. \tag{21.12}$$

To allow the ultrasound beam to tilt to θ degrees, the width of each transducer element must be less than $\lambda/2$ but the pitch (w = center to center spacing of the elements) must be $\lambda/4$ in order that, at the maximum deflection angle, a single beam pattern is defined when ultrasound intersects the array at angle θ

$$w < \frac{\lambda}{4\sin\theta} = \frac{c}{4 f_{us}\sin\theta} \,. \tag{21.13}$$

A 3 MHz scan head tilting the ultrasound beam 30° to the left and to the right requires a transducer element pitch of 0.3 mm.

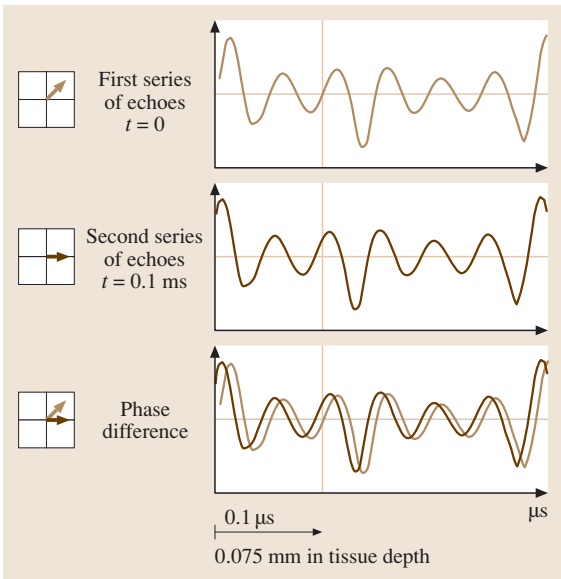


Fig. 21.46 Phase demodulation. To measure blood velocity, or tissue displacement or strain, the change in phase (or echo displacement) between successive pulse-echo cycles at a particular depth must be determined. In this case, a phase change of $\pi/4$ of 5 MHz ultrasound represents an echo time shift of 0.05 μs/8 = 0.006 25 μs, which is equivalent to a displacement of the scatterers toward the transducer of 0.006 25 μs × 0.75 mm/μs = 0.0047 mm in the time between pulse-echo cycles or 0.1 ms, yielding a velocity of 0.047 mm/ms or 0.047 m/s. The Doppler equation, time-domain velocimetry and strain imaging are all based on this computation. In Doppler demodulation, the phase and amplitude of the echo at any depth can be represented as a vector on a phase diagram. These vectors can be represented as complex numbers if the vertical direction is represented as the "imaginary" ($\sqrt{-1}$) direction and the horizontal direction represents the "real" direction

Pulsed Doppler [21.57]

The series of echoes from a single ultrasound transmit pulse provides information about the echogenicity of the tissue along the ultrasound beam pattern at various depths. The echogenicity of the tissue at each depth is determined by amplitude demodulation (Fig. 21.45). The measurement of the velocity of blood or tissue requires pairs of echoes from two (or more) ultrasound transmit pulses along the same beam pattern line, separated by a short time (0.1 ms). By comparing a second echo series from the same transducer beam pattern from a later time to the echo series from the first pulse, motion of the echogenic tissue along the beam pattern can be detected and measured. If the second echo series is identical to the first echo series, then none of the tissue along the ultrasound beam pattern has moved or changed during the period. However, if the second echo series is different, then the tissue has moved or changed. Motion in the direction of ultrasound propagation causes a simple time shift in the echo series, lateral motion or a change in tissue properties results in a loss of coherence between the echoes.

If the tissue has moved toward the ultrasound transducer, then the second echo pattern will arrive earlier after the transmit pulse compared to the first (Fig. 21.46). If the difference is detected by Doppler processing, then the echoes from each region of tissue are characterized by a vector in a complex plane (Fig. 21.46). One rotation of the vector is equivalent to the reflector moving toward the transducer to shorten the round-trip path by one wavelength of the ultrasound. If the ultrasound is 5 MHz, then the wavelength is 320 μm so one rotation represents a shortening of the round trip ultrasound travel distance of 320 μm, or 160 μm each way. A phase rotation of one quarter of a cycle ($\pi/2$ rad) represents 40 μm of motion. Doppler processing cannot tell the difference between 20 and 180 μm of motion because the vector is pointed in the same direction after the 160 μm displacement. This is called aliasing and is responsible for a waveform with the highest forward velocities incorrectly shown as reverse velocities (Fig. 21.47). Doppler

Amazon
EX1010 Page 875

systems cannot tell the difference between displacements of 100 μm toward the transducer and 60 μm away from the transducer, because both are represented by the same phase shift. A motion of 20 μm will result in a rotation of the phase vector by 45° ($\pi/4$ rad). Often the interval between the first echo and the second echo is 0.1 ms. The velocity of the tissue in this case is $20/0.1\,\mu m/ms = 200\,mm/s = 20\,cm/s = 0.2\,m/s$.

The Doppler frequency is the phase change of the echo in cycles during the pulse interval divided by the pulse interval. In this case the phase change is 1/8 cycle, so the Doppler frequency is $0.125/0.1\,ms = 1250\,cy/s = 1.25\,kHz$.

Usually, pulsed Doppler systems are used to measure blood velocity. Unfortunately, it is rarely convenient to align the ultrasound beam pattern along the axis of a blood vessel so typically the angle between the ultrasound beam pattern and the vessel axis is 60°. This is called the Doppler angle. The ultrasound system can only measure the projection of the blood velocity vector along the ultrasound beam. That projection is the cosine of the angle between the velocity vector and the ultrasound beam. The Doppler equation relating velocity to the ultrasound echo is:

$$f = \frac{2 v_f f_{us} \cos\theta_D}{c} \quad \text{or} \quad v_f = c\frac{\frac{f}{f_{us}}}{2\cos\theta_D} . \qquad (21.14)$$

where f is the Doppler frequency that you hear, the factor of 2 accounts for the round-trip of the ultrasound, v_f is the velocity of the blood, f_{us} is the ultrasound frequency, θ_D is the angle between the blood velocity and the ultrasound beam, and c is the speed of ultrasound in tissue. The form

$$\frac{v_f}{c} = \frac{\frac{f}{f_{us}}}{2\cos\theta_D} \qquad (21.15)$$

emphasizes the relationship between the ratio of the blood velocity to the ultrasound velocity and the Doppler frequency to the ultrasound frequency. Since the ultrasound wavelength $\lambda = c/f_{us}$,

$$v_f = \frac{f\lambda}{2\cos\theta_D} . \qquad (21.16)$$

To provide a measurement of blood velocity, ultrasound instruments have a cursor on the screen to align with the axis of the vessel under examination (Fig. 21.48). The associated Doppler data, here represented as a spectral waveform, is provided with a scale showing the angle-adjusted velocity based on the projection of the measured velocity onto the vessel axis. Although this adjustment is theoretically justified by the geometry, unfortunately, it does not provide a useful velocity value. If a Doppler angle of zero degrees is used, then the value is correct, however, if other angles between the ultrasound beam and the presumed velocity vector are used, then the value of the velocity is not correct. The reason is that blood velocity vectors are rarely aligned with the axis of the artery. Instead, blood velocities form helical patterns along the artery [21.58–60]. Angle-adjusted Doppler velocity measurements are systematically higher as the Doppler angle increases from zero to 70 degrees or more. Although at a Doppler angle of zero, velocities are accurately used to determine both the volume flow rate and the Bernoulli pressure drop, neither result is correct when Doppler angles other than zero are used [21.61–63].

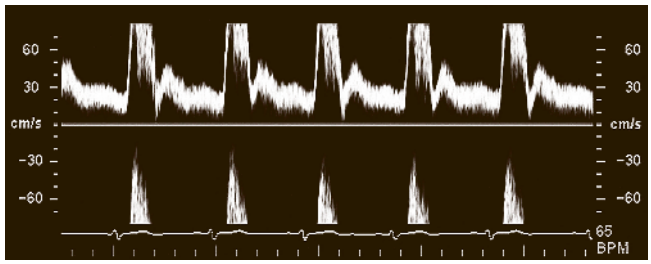


Fig. 21.47 Aliasing. Blood velocities that cause high phase shifts (greater than 180° or π radians) between pairs of pulsed Doppler echoes cause the Doppler system to mistake high-velocity forward flow for reverse flow. Continuity in blood flow allows the examiner to detect this error

Pulsed Doppler Range of Measurement. The highest Doppler frequency shift that can be measured with pulsed Doppler occurs when the phase change of the echoes during the interval between echo acquisitions [pulse repetition interval (PRI)] is 180° (half a cycle). The Doppler frequency at that condition is half of the pulse repetition frequency (PRF, the Doppler sampling frequency). This is called the Nyquist limit, after Harry Nyquist. This establishes the highest velocity that the Doppler can detect, although since the signal is analyzed as a complex number with twice the data (half as a "real" number and half as an "imaginary" number) Doppler frequencies between + 0.5 PRF and − 0.5 PRF are reported. As long as there is no reverse flow the range of Doppler frequencies available is equal to the PRF. If the phase vector is characterized by a 2 bit complex number into four values, then the smallest phase change that can be classified is 1/4 cycle. So, a 5 MHz Doppler system with the data recorded as 2 bits, and a PRF of 10 kHz, can only report four Doppler frequency ranges,

Amazon
EX1010 Page 876

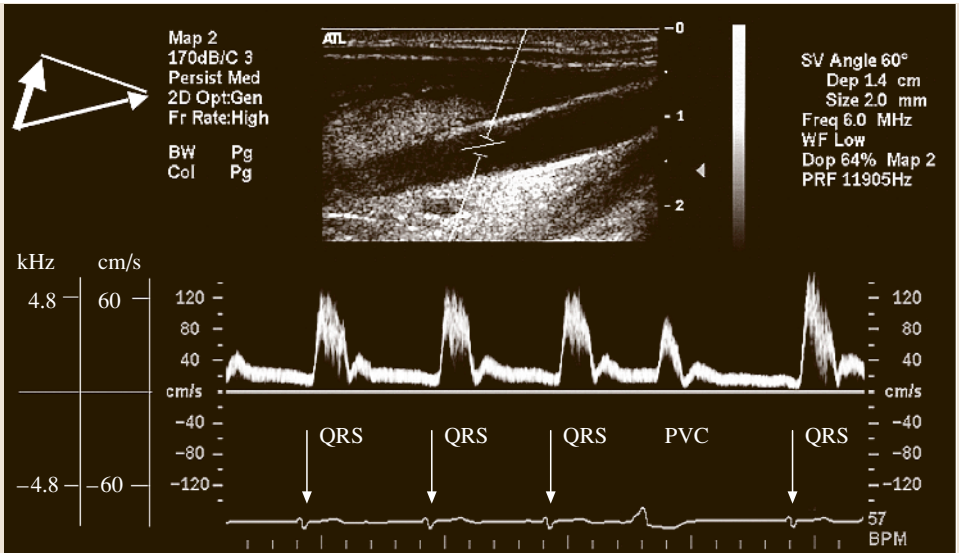


Fig. 21.48 Duplex Doppler image and waveform of a carotid artery. The axis of the ultrasound beam pattern used for Doppler is shown crossing the artery at an angle of 60° to the vessel axis. A cursor is aligned parallel to the vessel axis to provide θ_D for the Doppler equation. The Doppler frequency, which is produced by the speakers of the instrument, is shown by a scale drawn on the *left*. The scale showing the speed at which the blood is approaching the transducer is drawn adjacent to the frequency scale. The instrument computes the scale on the screen by dividing the cosine of the Doppler angle into the approach speed. Along the lower edge of the image is the electrocardiograph tracing (ECG) showing the "QRS complex" (small up and down) indicating the onset of ventricular contraction in each cardiac cycle. The lump in the trace 200 ms later is the T wave indication the end of ventricular contraction. The fourth beat is too early and the QRS has an odd shape. This is a premature ventricular contraction (PVC) originating from an abnormal spot on the ventricle. The PVC causes the ventricle to contract before filling is complete, producing a low-volume contraction, and low systolic blood velocities. The ventricle overfills before the next normal contraction, causing elevated systolic velocities

-1.25 to $+1.25$ kHz, $+1.25$ to $+3.75$ kHz, $+3.75$ to $+6.25$ kHz, and $+6.25$ to $+8.75$ kHz. -1.25 kHz is equal to $+8.75$ kHz. Such a Doppler system would probably classify -1.25 to $+1.25$ kHz as no motion. By increasing the number of bits in the digitizers representing the phase vector, the resolution of the phase shift is increased, and the number of possible measured velocities is increased. This does not increase the Nyquist limit.

Another way to increase the number of velocities that can be measured is to increase the number of pulse-echo cycles or Doppler phase samples that are gathered. The number of samples used to resolve the velocity is called the ensemble length or packet length. In a typical spectral waveform pulsed Doppler system, Doppler samples will be gathered from a voxel at a PRF of 12.8 kHz for 10 ms to provide 128 Doppler samples for frequency analysis. The Nyquist limit (upper frequency limit) is 6.4 kHz. The lowest frequency that can be detected is 100 Hz, one full Doppler cycle in the 10 ms acquisition period. If the signals are digitized into 2 bit complex numbers, then each of the 128 possible frequencies can be tested to see whether each is present or absent, but no information is available about the strength of each frequency signal. To determine the strength of each frequency, the signals must be digitized into numbers with more binary bits. Spectral waveform analysis assumes that there are many Doppler frequencies present in the Doppler signal from the voxel of interest.

Pulsed Doppler Pulse-Pair analysis. The Doppler frequency shift can be measured from just two echo samples separated by a known time. The assumption is that only a single Doppler frequency is present in the signal. The phase change divided by the sample interval time provides the Doppler frequency. The upper limit of the Doppler frequency is the Nyquist limit. To resolve the Doppler frequency, the phase angle change must be resolved. Representing the phase angle by a two bit complex number only resolves the phase angle into four divisions. For 5 MHz ultrasound, displacements of

Amazon
EX1010 Page 877

40 μm can be resolved. For a 10 kHz PRF sample frequency, this allows a velocity of ±40 cm/s (±0.4 m/s) to be detected. However, if the phases are represented by 10 bit complex numbers, the phase angles can be resolved into 1000 divisions and the displacement and velocities can also be resolved. With 10 bit quadrature digitizers, velocities between plus and minus 80 cm/s can be measured with a resolution of 0.8 cm/s, equivalent to displacements of 80 nm during the pulse interval.

Pulsed Doppler Wall/Clutter Filtering. The measurement of blood velocity with ultrasound is complicated by the containment in vascular walls. The echogenicity of the blood is 60 dB less than the echogenicity of the walls at 5 MHz. The blood cells are Rayleigh scatterers because they are smaller (7 μm) than the wavelength of ultrasound (300 μm for 5 MHz). The strength of the echo from blood increases with the fourth power of the frequency. However, frequency-dependent attenuation of the ultrasound by overlying tissues limits most Doppler ultrasound studies to frequencies of 2–6 MHz. 5 MHz produces the strongest echoes for vessels under 2 cm of tissue, deeper vessels, and those behind the skull require 2 MHz ultrasound waves to penetrate these tissues [21.64–66].

In many examinations, Doppler measurements from blood adjacent to the wall are desired, so Doppler echoes from the voxel next to the wall will include strong wall echoes as well as weak echoes from the adjacent blood. Unfortunately, vascular walls move with velocities near 2 mm/10 ms or 0.2 m/s (20 cm/s). The strong echoes from these moving walls must be rejected to reveal the adjacent blood velocity, which may be only slightly higher than 20 cm/s. The strong echoes from the wall are called clutter. 10 bits of the system dynamic range are required to handle the clutter and the blood echoes must be resolved above that, so most ultrasound systems now utilize a 14–16 bit dynamic range, which is achieved by combining the outputs of separate digitizers (one for each transducer) and digitizing faster than the required four times the ultrasound center frequency, then filtering the result for processing.

Pulsed Doppler Spectral Analysis. To measure the Doppler frequency shift, any method of frequency analysis can be used. Zero-crossing rate meters and zero-crossing time interval histograms have been replaced with real-time spectrum analyzers. Although the time-compression analyzer produces identical results, the popular fast Fourier transform (FFT) analyzer is used to produce spectral waveforms of Doppler signals

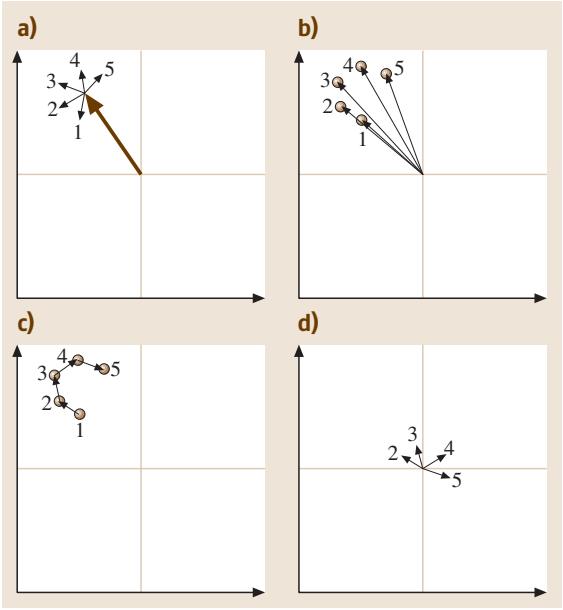


Fig. 21.49a–d Autocorrelation clutter (high-pass) filter. By representing each pulse-echo from a particular depth as a point on a phase diagram, the trajectory of the echo phase in time can be plotted. **(a)** The Doppler echo comes from two types of reflectors, strong reflecting stationary structures (*clutter*) and weak reflecting moving blood cells. In each of the five pulse-echo cycles (ensemble or packet of 5), the contribution from the strong reflectors is the same. The moving blood cells reflect the same amplitude (vector length) but a different phase during each pulse-echo cycle. **(b)** The ultrasound receiver cannot differentiate the clutter contributed by the stationary structures from the signal contributed by the moving blood cells. High-pass filter. **(c)** By taking the difference between successive results, the effect of the clutter is eliminated. **(d)** By centering the resultant vectors on a new phase diagram, the phase angle change between each pulse-echo cycle can be used to compute the blood velocity

(Figs. 21.47, 21.48). The FFT analyzer is coupled to the pulsed Doppler so that the FFT analyzer receives a quadrature pair of data from the depth of interest for each pulse-echo cycle. The advantage of the spectral analysis is that if the voxel contains several flow velocities, the FFT spectrum will display the Doppler frequency for each velocity. Unfortunately, in blood flow, eddy oscillation frequencies up to 500 Hz occur; the typical FFT length of 10 ms (100 spectra per second) is only capable of resolving eddies of 50 Hz or lower. When a voxel contains higher-frequency eddies, the re-

Amazon
EX1010 Page 878

sult appears as spectral broadening or as harmonics on the spectral waveform.

Pulsed Doppler Autocorrelation. Autocorrelation is a frequency analysis method which is an extension of pulse-pair analysis. Autocorrelation analysis assumes that there is only one valid Doppler frequency in the blood flow. Autocorrelation analysis identifies that frequency. However, to reject the stationary and slow moving strong echoes of the wall, a clutter filter must be applied. Clutter is a stationary echo superimposed on the changing Doppler echo. The analysis is based on an ensemble of N echoes, usually eight echoes. The difference between adjacent pairs of echoes n and $n-1$ (for $n=2,\ N$) creates a new group of $N-1$ vectors (Fig. 21.49). By taking the average of the change in angles, a Doppler velocity can be obtained. Sometimes two filtering steps are required rather than one. Such filters are called finite impulse response (FIR) and infinite impulse response (IIR) filters.

Time–Domain Velocimetry. The Doppler equation contains the Doppler frequency and the phase angle. Doppler signals are subject to aliasing when the between-pulse phase angle change ($\Delta\phi$, a circular variable) has a value greater than π. In addition, echoes from deep tissues have a lower center frequency than echoes from shallow tissues, causing confusion about the correct value of the ultrasound frequency f_{us} to use in the equation.

$$\frac{v_f}{c} = \frac{\frac{\Delta\phi}{\Delta t}}{f_{us}\, 2\cos\theta_D}\,. \tag{21.17}$$

Of course, the center frequency of deep echoes is still within the bandwidth of the transmitted ultrasound; the center frequency is depressed because of the greater attenuation of the higher-frequency portions of the transmitted bandwidth.

Since bandwidth is inversely proportional to pulse duration and pulse duration is related to spatial resolution, it is desirable to have a short pulse duration so that spatial resolution is as small as possible. This means broadband pulses, permitting depression of the center frequency of the echo. The desire for improved resolution and the desire to avoid aliasing combine in the use of time-domain velocimetry as an alternative to Doppler.

$$\frac{v_f}{c} = \frac{\frac{\Delta\tau}{\Delta t}}{2\cos\theta_D}\,. \tag{21.18}$$

In time-domain velocimetry, two successive ultrasound echoes are compared to see if a time shift ($\Delta\tau$) has occurred in the echo in the intervening time (Δt), which indicates tissue motion. By measuring the time shift, the velocity can be calculated. Of course, clutter from solid tissue in the voxel may provide a substantial stationary echo superimposed on the small shifted echo. To remove the clutter echo, subtraction of adjacent pairs

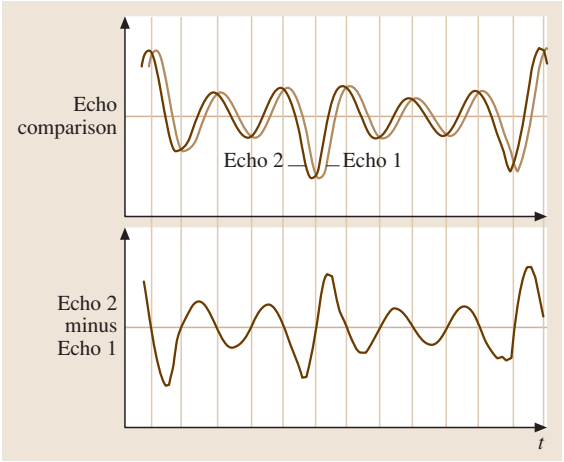


Fig. 21.50 Time-domain demodulation removing clutter. To remove clutter in time-domain demodulation, the RF echo signal from each pulse-echo cycle is subtracted from the preceding RF echo signal to yield the residual due to tissue motion

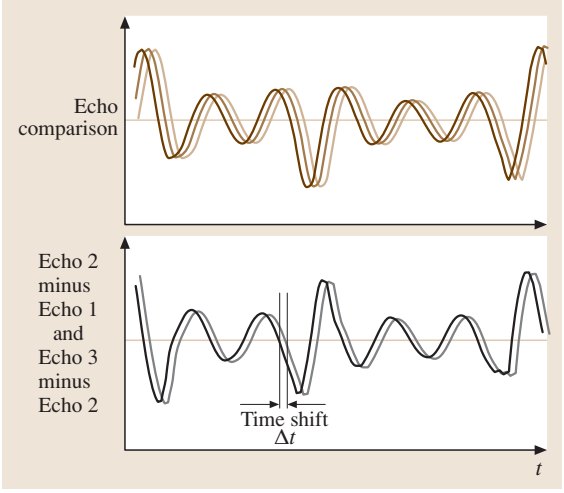


Fig. 21.51 Time-domain demodulation measuring the velocity component. By measuring the time shift between successive echo pairs, multiplying by half the ultrasound velocity and dividing by the pulse repetition interval time, the velocity of the tissue along the ultrasound beam results

Amazon
EX1010 Page 879

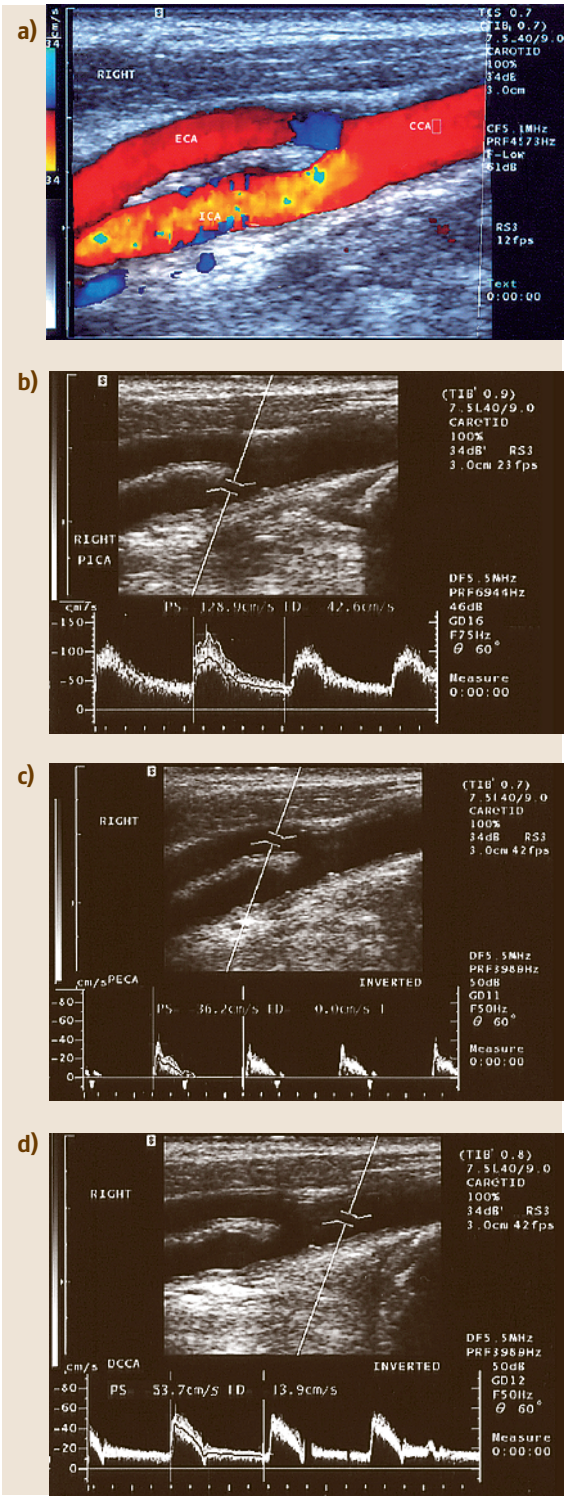


Fig. 21.52a–d Ultrasound images from a conventional carotid artery Doppler examination in the neck [21.67]. *Orientation*: a linear array transducer located at the top of each image acquires the 128 vertical scan lines in sequence across the 35 mm-wide image. Two of the monochrome B-mode images **(c)** and **(d)** were acquired in 24 ms (42 frames per second) so the scan lines progress across the image at a speed of (35/24) 1.46 m/s, a speed similar to blood velocity. The color flow image **(a)** was acquired at 12 fps; the other monochrome image **(b)** was acquired at 23 fps. *Anatomy*: **(a)** ECA external carotid artery supplying the face, ICA internal carotid artery supplying the brain, CCA common carotid artery from the heart via the Brachiocephalic trunk. **(a)** Color Doppler image of the carotid bifurcation. The color scale on the left of the image shows that forward flow is shown as *red* and reverse flow is shown as *blue*. The flow directions are with respect to the transducer array at the top of the image rather than with respect to the heart to the right of the image. The blue region at the origin of the external carotid artery shows that the vertical component of the velocity vector is pointing toward the ultrasound transducer rather than showing that flow is reversed toward the heart. Notice that this region is bounded by black bands indicating *zero* velocity toward the transducer. The *blue spots* in the lumen of the internal carotid artery are aliasing (Fig. 21.47). Notice that each of those regions is surrounded by an *orange* color indicating high blood velocity components with respect to the transducer. *Doppler waveform orientation*: each of the three Doppler waveforms is acquired from an ultrasound beam pattern that is tilted at an angle with respect to the transducer, selected by the examiner to form an angle of 60° with respect to the artery axis. **(b)** *lower* Normal Doppler spectral waveform from the internal carotid artery with high diastolic flow. Because the brain continuously requires 10% (10 ml/s) of the cardiac output (100 ml/s), the peripheral resistance is low so blood flows to the brain during systole and diastole. **(c)** *lower* Normal Doppler spectral waveform from the external carotid artery with low diastolic flow. Because the face at rest requires little blood flow but when active (chewing, blushing) requires more blood flow, at rest the arteriolar sphincters are constricted, only accepting blood flow during systole. When the arteriolar resistance decreases, the external carotid also has flow during diastole. **(d)** *lower* Normal Doppler spectral waveform from the common carotid artery which has the combined internal and external flow waveform. A pulsatility index showing the ratio between the diastolic and systolic velocities is sometimes used to classify waveforms

Amazon
EX1010 Page 880

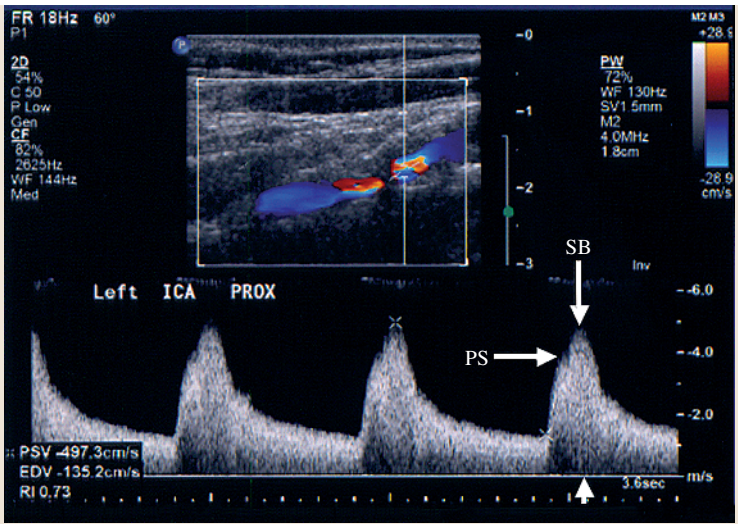


Fig. 21.53 Stenotic internal carotid artery. Even after 25 years of exploring the meaning of carotid artery spectral waveforms, there is no agreement on how the data should be interpreted. Although this color Doppler image shows an interruption in the color flow image of the lumen, the interruption is not due to an arterial occlusion, but to a local region of high ultrasound attenuation which causes the color Doppler signal to drop out. Thus, the diameter of the color Doppler streak cannot be used to assess the lumen. In this case, the vessel walls cannot be easily seen. A stenosis is present at the Doppler sample volume as indicated by the high velocity. The spectral waveform is confusing. The highest Doppler frequency shift which was measured by the examiner 220 ms after the onset of systole at 497.3 cm/s is probably not accurate because the measurement is at the time of greatest spectral broadening (SB), indicating eddies in the flow. Use of the Doppler equation is not appropriate for these eddy velocities because the heading of the vectors is not known. The true peak systolic (PS) velocity probably occurs 100 ms after the onset of systole where the measurement is near 4 m/s and the Doppler equation is probably accurate if the velocity vector is assumed to be parallel to the artery axis. An appreciating of the difference between the believed accuracy of 497.3 cm/s versus 'about 4 m/s' is important because of the clinical decisions that result. The PSV is used to decide whether a patient with symptoms of mini-stroke should have surgery. In this case, the end diastolic velocity (EDV) is measured at 135.2 cm/s. An EDV value exceeding 140 cm/s in a single measurement would cause a vascular surgeon to schedule the patient for carotid endarterectomy surgery even if the patient has no symptoms

of echoes (Fig. 21.50) provides the difference waveform containing the motion information. Then the time shift between difference waveforms can be measured (Fig. 21.51).

A comparison between the time-domain equation and the Doppler equation shows that $\Delta\tau = \Delta\phi / f_{us}$. This indicates that it is the demodulator frequency, not the frequency of the echo, that is relevant for the Doppler equation; the former must be close (and is usually equal) to the transmitted center frequency, i. e., the frequency required in the Doppler equation. There are substantial differences between the Doppler and time-domain systems. First the time-domain system usually transmits a broadband, short ultrasound pulse. The signal-to-noise ratio of the echo is determined by the transmit pulse energy. To achieve the same energy in a short pulse, the temporal peak power must be high, leading to a high acoustic pressure. When analyzing the time shift between the echoes, it is easiest to test for the time-lagged correlation by stepping one digitizing interval at a time. So, if the echo is digitized at a rate of 20 MHz, the digitizing interval is 50 ns ($\Delta\tau$), equivalent to a tissue displacement of 0.0375 mm. If the pulse repetition frequency is 10 kHz, so the inter-pulse interval is 100 µs (Δt), the velocity resolution is 38 cm/s (0.4 m/s). Time-domain systems usually digitize at a higher frequency and usually interpolate the wave between the measurements to improve velocity resolution. For large time shifts, when noise is present, the time domain system usually has trouble with peak hopping, associating the wrong cycles in the wave when determining the time shift. This results in a measurement error identical to

Amazon
EX1010 Page 881

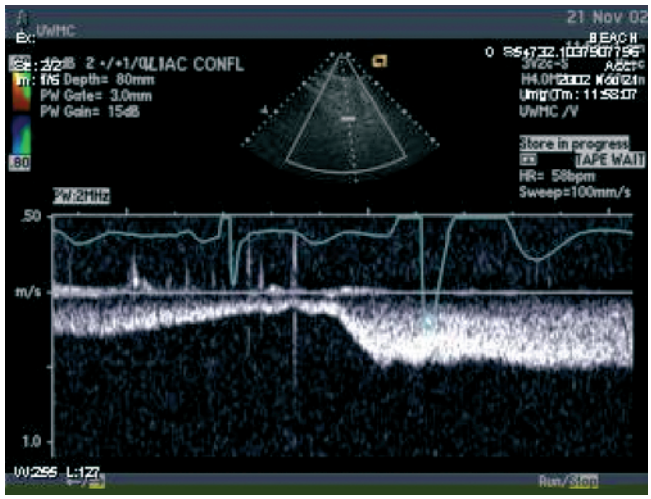


Fig. 21.54 Doppler spectral waveform signals from the inferior vena cava showing augmented flow. Doppler spectral waveforms show velocity (*vertical axis*) versus time (*horizontal axis*). In addition to the difference in flow direction, venous flow is differentiated from cardiac flow because the venous flow varies with respiration and with manual compressions of the tissues. Here the sudden increase in venous flow in the distal inferior vena cava was created by releasing an occlusion of the venous outflow from the legs. ECG tracing (*green*) shows cardiac timing. The heart beat to the right of center is due to a premature ventricular contraction, an abnormal heart rhythm which does not affect the venous flow

aliasing. So, the advantages of time-domain processing over Doppler processing, while promising, have not been fulfilled.

Clinical Applications of Ultrasound Velocimetry

The most common application of pulse Doppler ultrasound spectral waveform analysis is the examination of the carotid arteries [21.68] for stenoses that might lead to stroke (Figs. 21.52, 21.53). The measurement of high systolic (> 125 cm/s) carotid blood velocity is associated with a 20% chance of stroke in two years in a patient reporting stroke-like symptoms

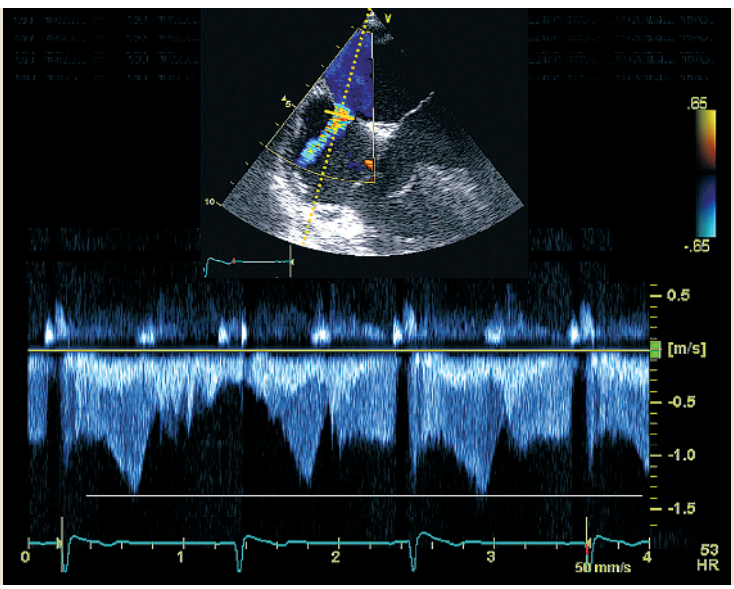


Fig. 21.55 Duplex echocardiogram of a heart with an atrial septal defect. The jet of blood from the left atrium to the right atrium can easily be seen on the color flow image. The Doppler spectral waveform taken at the center of the jet orifice at a Doppler angle of 25° to the jet shows velocities as high as 1.4 m/s when the inter-atrial pressure difference is the greatest. Correcting the velocity for the Doppler angle ($\cos 25 = 0.906$) increases the velocity value to 1.54 m/s. Cardiologists usually attempt to orient the Doppler transducer to align the jet with the Doppler ultrasound beam to achieve a *zero* Doppler angle. The pressure difference between the chambers can be computed using the Bernoulli equation for blood velocity $\Delta p[\text{mmHg}] = 4\,[\text{mmHg}/(\text{m/s})^2]\,\text{V}^2$. The pressure difference here is near 9 mmHg (courtesy Frances DeRook and Keith Comess)

Amazon
EX1010 Page 882

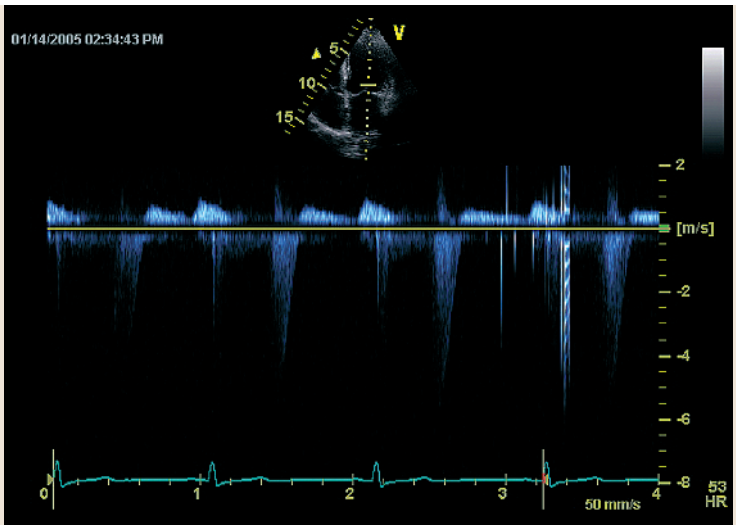


Fig. 21.56 Vibration from the mitral valve. Signals from blood flow are mixed with signals from solid tissue motion. Here, the signal of solid tissue motion is suppressed by the wall filter, which suppresses clutter at frequencies below 400 Hz. However, in this case with the Doppler sample volume in the mitral orifice, as the mitral valve closes for the fourth time, the valve vibrates at a frequency of 2 kHz for a period of 8 ms causing the harmonic (Bessel function) spectral pattern with seven harmonic terms, indicating that the amplitude of the vibration is high (courtesy Frances DeRook and Keith Comess)

(TIA = transient ischemic attack, RIND = reversible ischemic neurological deficit). The measurement of a high-end diastolic velocity (> 140 cm/s) in any patient is associated with a 20% chance of stroke in two years from emboli released from the carotid stenosis. Such findings, by themselves, can direct a patient to treatment that will prevent devastating disability.

Examination of the veins of the legs with Doppler for the detection of deep venous thrombosis (DVT) is another popular examination that can lead to life sav-

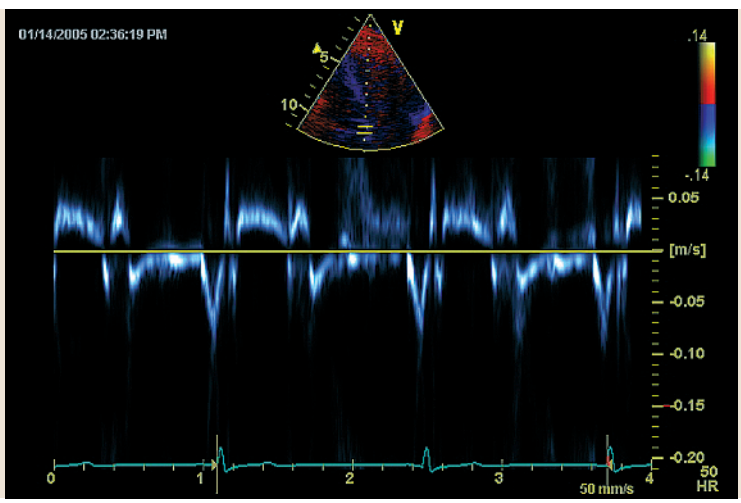


Fig. 21.57 Duplex echocardiogram tissue Doppler of myocardium. Like velocity measurements from blood flow, velocities of solid tissues can also be measured. Low velocities of the intra-ventricular septum of the heart indicates abnormal muscle contraction (courtesy Frances DeRook and Keith Comess)

Amazon
EX1010 Page 883

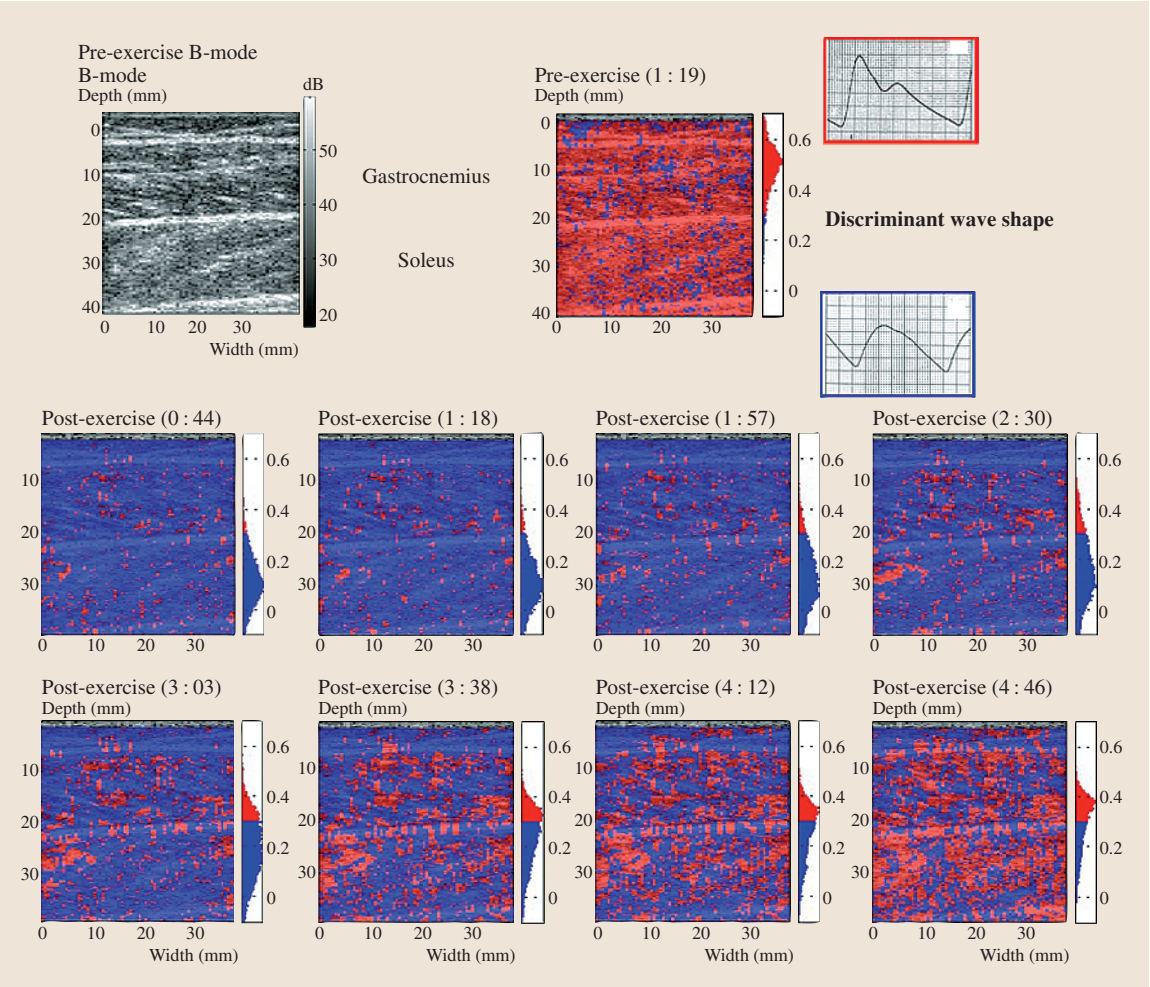


Fig. 21.58 Tissue strain in calf muscles. During tissue perfusion, different strain waveforms indicate resting perfusion (red) with high peripheral (arteriolar) resistance or hyperemic perfusion (blue) with low peripheral resistance. In this case, the calf muscle was imaged at rest, and then at intervals for a period of 5 min following a toe stand exercise. Immediately after exercise, the peripheral resistance is low to make up for the metabolic oxygen deficit after exercise. Five minutes after exercise, most of the muscle tissue has returned to the resting state (Courtesy John Kucewicz)

ing therapy. Because venous pressures are near 5 mmHg in the supine patient, normal venous flow is associated with respiration and minor local compression rather than pulsatile with the cardiac cycle (Fig. 21.54). Pulmonary embolus from venous emboli released from a DVT may account for one-third of sudden cardiac death cases [21.69]. A venous Doppler examination failing to show spontaneous venous flow with respiration indicates a venous obstruction that may be a DVT that could progress to threaten life if not treated with anticoagulation.

Cardiac Doppler examinations for blood flow are perfectly suited to characterize narrow holes between the cardiovascular structures in the chest (Fig. 21.55). By measuring the velocity of blood flow jets and applying the Bernoulli equation, the instantaneous pressure difference between the associated chambers of the heart can be measured. This works for all heart valves and wall defects so the method can be used to identify pulmonary artery hypertension as well as cardiac valve failure.

Although blood velocity through valves can be measured (Fig. 21.56), the dynamics of solid structures such

Amazon
EX1010 Page 884

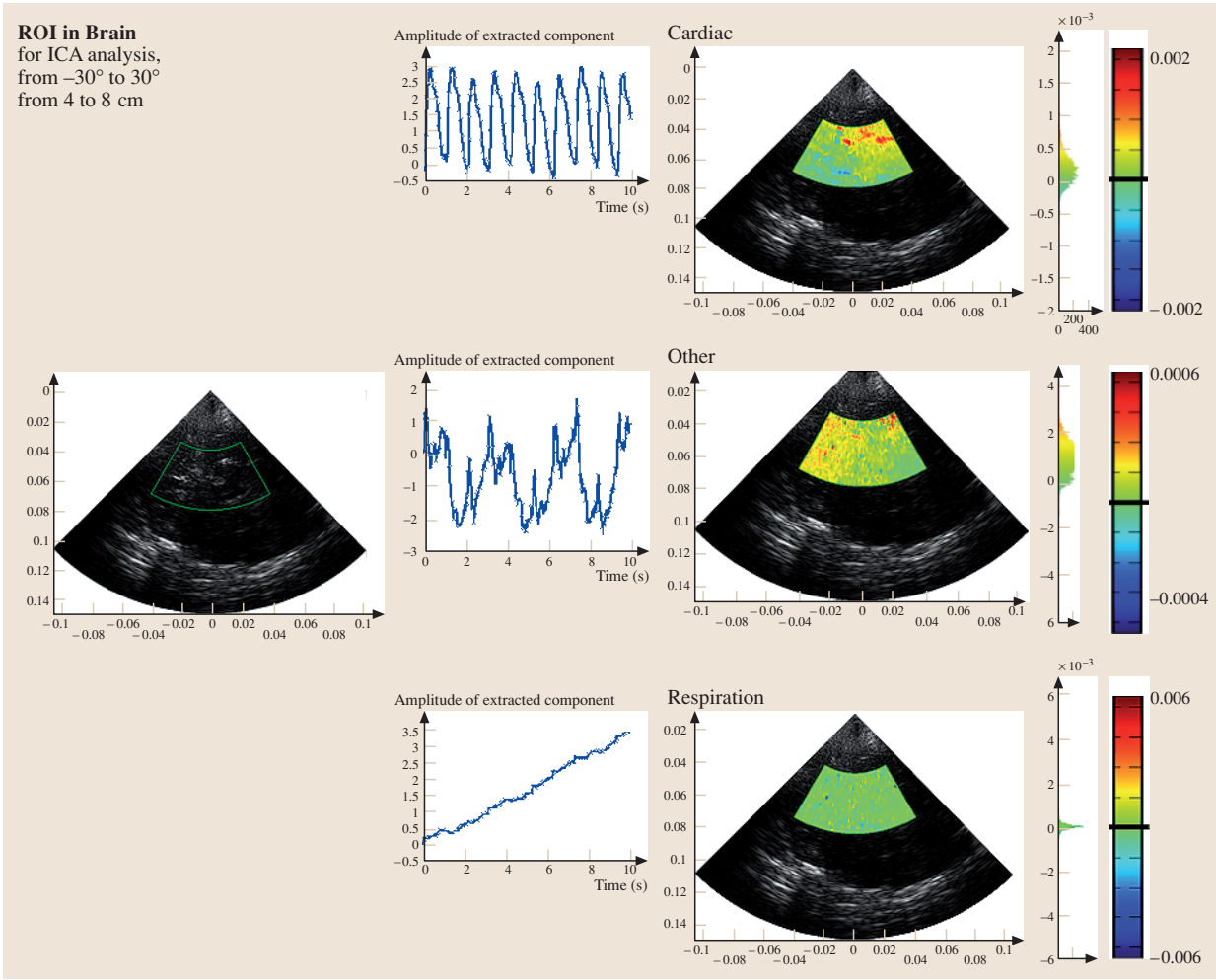


Fig. 21.59 Tissue pulsations in brain measured with ultrasonic phase gradient demodulation. Using ultrasound to measure tissue displacement over time with a resolution of 0.05 μm and differentiating motion with depth to measure strain, perfusion waveforms can be obtained. Independent component analysis of the brain perfusion signal reveals the cardiac and respiration contributions to the natural tissue strain (Courtesy Lingyun Huang)

as valve vibration, can also be characterized. By measuring the velocity of the cardiac wall, regions of poor myocardial function can be identified (Fig. 21.57).

Tissue Strain Imaging

A number of laboratories are exploring the ultrasound measurement of tissue strain [21.70] for diagnostic purposes. The most popular examinations involve the measurement of tissue response to externally applied vibration or pressure. These methods are called elastography or elastometry. During ultrasound examination, the ultrasound scan head or a nearby device is pressed on the tissue to induce a strain of several percent, either static or vibrating. By monitoring the relative motions of the tissues in response to the applied strain using Doppler or time-domain methods, the relative elastic properties of the tissues can be determined. The computation simply takes the derivative of the motion as a function of depth. To achieve 10% resolution on a 1% applied strain in 1 mm voxels requires that the ultrasound motion detection system resolve 1 μm tissue displacements. This requires a 1 GHz digitizing rate for a time-domain system without interpolation. A Doppler system with 6 bits

Amazon
EX1001 Page 8835

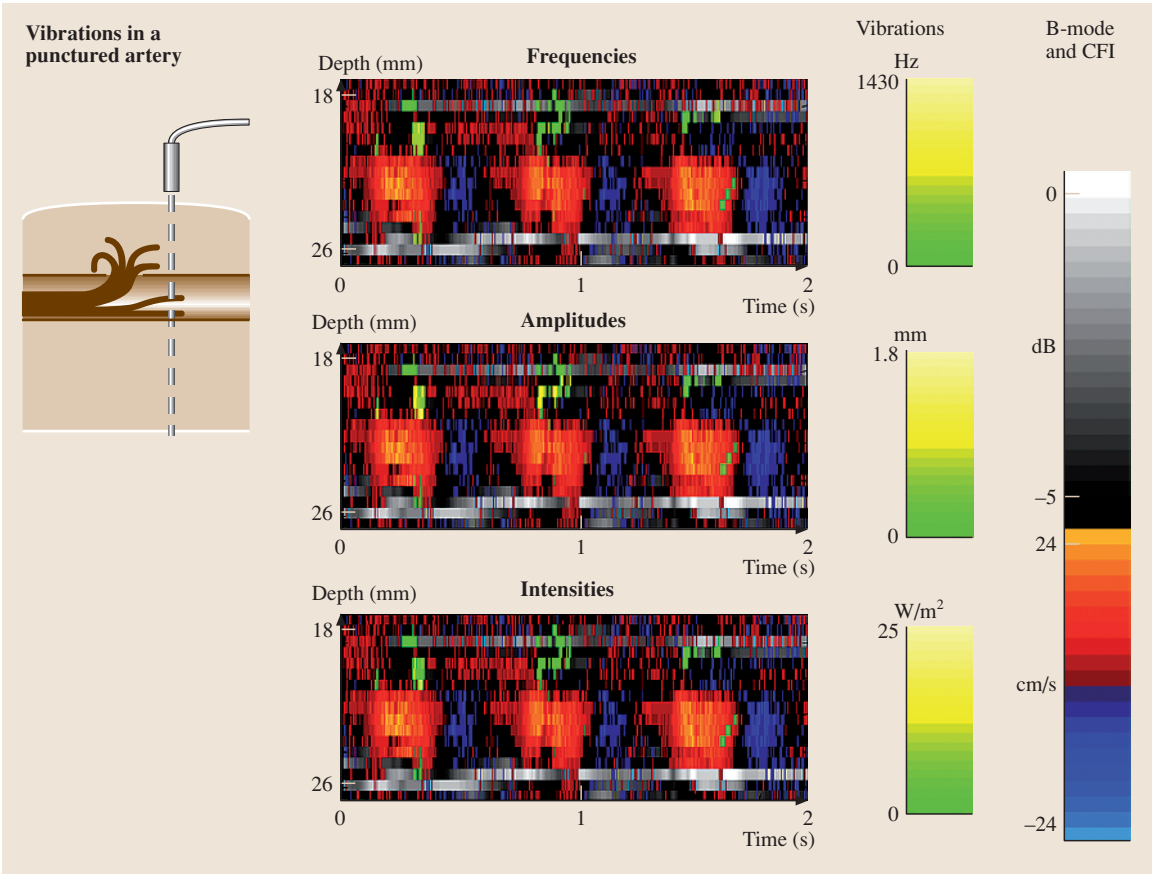


Fig. 21.60 Tissue vibrations of a punctured artery. Flow through any small orifice which results in a pressure drop can cause vibrations. Arterial bleeding can be detected by searching Doppler signals for such vibrations. (Courtesy M. Paun, M. Plett)

of dynamic range can achieve a 1 μm displacement resolution.

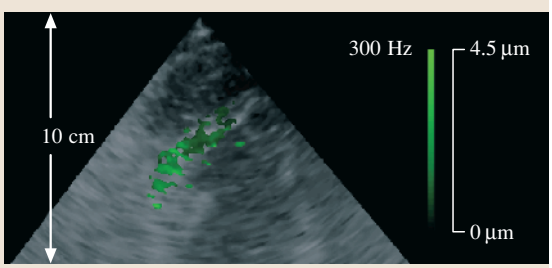


Fig. 21.61 Vibration of a coronary artery stenosis. Flow through any small orifice which results in a pressure drop can cause vibrations. Flow though a stenosis causes a bruit (Fig. 21.2), or murmur which can be detected and measured with ultrasound. These 4.5 μm-amplitude 300 Hz vibrations on the surface of the heart at the location of a stenosis in the right coronary artery occur only in diastole when the coronary flow rates are the highest. (Courtesy S. Sikdar, T. Zwink, S. Goldberg)

More challenging is to examine the natural tissue strain that occurs as the tissue fills and empties of blood each cardiac contraction and each respiratory cycle. Normal tissue strain for arteriolar filling is 0.1%. To resolve 0.1% strain with 10% resolution in 1 mm voxels requires the resolution of 0.1 μm displacements. This requires Doppler demodulation of a 5 MHz echo with at least 9 bits of dynamic range. Ultrasound pulsatil-

Amazon
EX1001 Page 886

ity images can be made of most body tissues including muscle (Fig. 21.58) showing physiological responses to stresses, and brain [21.71] (Fig. 21.59) showing the separate effects of pulse and respiration.

Tissue Vibration Imaging

Several pathological conditions are associated with the presence of tissue vibrations. These were discussed at the beginning of the chapter where the detection of the vibrations with a stethoscope was described. Of particular interest are vibrations associated with arterial stenosis and vibrations and motions associated with internal bleeding [21.72]. Using the same Doppler demodulation methods, but filtering for the cyclic motions of the highly echogenic solid tissues rather than the continuous motions of the poorly echogenic blood, vibrations can be detected and rendered as an image showing pathologies such as arterial bleeding (Fig. 21.60). The amplitude and frequency of the vibrations are characteristic of the rate of bleeding. Arterial stenoses including stenoses of the coronary arteries (Fig. 21.61) can be demonstrated in vibration images.

Modern Ultrasound Scanners

Real-time diagnostic ultrasound scanners changed little on the outside between 1975 and 2000; they are narrow enough to fit through a doorway (Fig. 21.62) and draw less than 1.5 kW of electrical power from a standard power outlet in the hospital wall. However, inside the systems have evolved from analogue devices to digital devices (Fig. 21.63), with the conversion to digital processing determined by cutting-edge computer technology. Now an ultrasound scanner with a full array of functions is constructed from software, using a Windows laptop computer (Fig. 21.64) or a custom box. Ultrasound systems can be produced inexpensively and can obtain the diagnostic results automatically, so that a patient can use the system for self-management of some conditions (Fig. 21.64).



Fig. 21.62 Modern ultrasound imaging system. During the quarter century between 1975 and 2000, ultrasound systems retained the same exterior design, mounted on wheels, narrow enough to fit through a doorway, light enough that a sonographer could push the system, short enough so that a sonographer could see over the top and powered by a 1.5 kW outlet. To the right is the key to good ultrasound diagnosis, the well-trained, certified, experienced ultrasound examiner

21.5 Medical Contrast Agents

Contrast agents are used in medical imaging to make invisible structures visible. Contrast agents can be classified by anatomic/application: intraluminal/intracavity, excretory, diffusional, and chemotactic. Contrast mechanisms include reflection, absorption, fluorescence, emission and nuclear resonance frequency shift.

Intraluminal/intracavity agents are used to visualize the cardiovascular system, gastrointestinal system, reproductive system, body cavities, and other spaces. The contrast agent is injected into the space, where it spreads throughout the structure of interest. Excretory systems are used to visualize the renal system [excretory urogram or intravenous pyelogram (IVP)] or gall bladder and bile duct (cholangiopancreaticogram). The contrast agent is injected into the venous system and is excreted in concentrated form by the target organ. Because of the concentrating action of the kidney, a contrast agent in the urine will be 100 times more concentrated than in the blood. Diffusional agents are injected into the venous system and diffuse into the interstitial space through leaky capillaries. Newly formed capillaries are leaky, and such diffusion may mark local angiogenic factors secreted by tumors or retinopathy. Contrast magnetic resonance imaging (MRI) for breast tumor detection and fluorescene angiography of the retina are examples of diffusional agents. Chemotactic agents are injected into

Amazon
EX1010 Page 887

the veins and diffuse into the interstitial space through normal capillaries, where they bind to tissues of interest such as tumor cells. The time between the injection of a chemotactic contrast agent and the imaging study is several hours. This method is common in nuclear medicine imaging.

Ultrasound contrast agents cause increased backscatter of ultrasound and often cause the generation of harmonics. X-ray contrast agents contain heavy nuclei which absorb X-rays to provide contrast. Fluorescene, indocyanine green and other dyes are activated by high-energy (short-wavelength) photons and emit longer-wavelength photons, which are detected by optical camera systems. Chemotactic chemicals prepared with short-half-life (hours) nuclear isotopes are prepared and injected within a few hours. After allowing time for the agents to accumulate in the tissues of interest, the sources of radiation are imaged with pinhole or collimation nuclear radiation cameras. Gadolinium is used as a contrast agent in nuclear magnetic resonance imaging. The paramagnetism of gadolinium decreases the T_1 and T_2 relaxation times, which are displayed in the MR image.

21.5.1 Ultrasound Contrast Agents

The first intravenous ultrasound contrast agents [21.73] were large bubbles generated by intravenous injection of indocyanine green [21.74], other injectable liquids including saline and blood [21.75–77], and finally agitated saline [21.78]. These bubbles were so large that they would not pass through capillaries, so appearance in the left heart or arteries was proof of a shunt bypassing the lungs. These bubbles were generated inadvertently or deliberately by flow-induced cavitation. The bubbles contained air that was dissolved in the blood. These bubbles generated strong ultrasound reflections because of the large difference in ultrasound impedance between the body (water) and the air in the bubbles. Small bubbles were not stable, so only large bubbles survived.

Currently, most commercial ultrasound contrast agents are small bubbles or particles, which are able to pass through the capillaries of the lungs but are confined to the vascular system. Some ultrasound contrast agents are solid particles smaller than a micron in diameter. These are Rayleigh scatters of ultrasound at the fundamental frequency. Most ultrasound contrast agents are bubbles about 3 μm in diameter (Fig. 21.65) so that they will pass through pulmonary capillaries and recirculate in the cardiovascular system. They are also Rayleigh scatters, but because they oscillate, they convert the fundamental ultrasound frequency into harmonics because of the nonlinear properties of their oscillation.

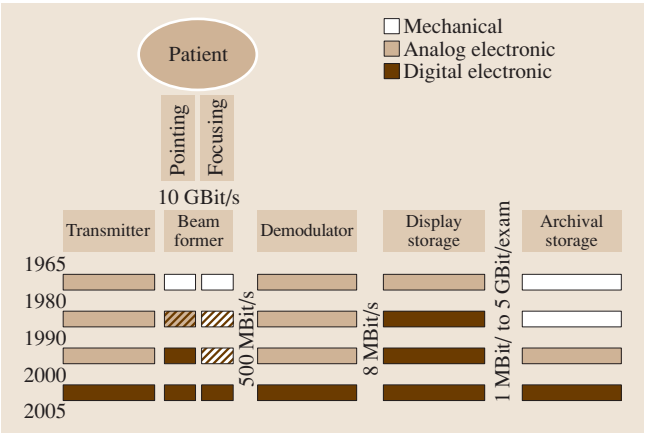


Fig. 21.63 Diagnostic ultrasound signal processing history. The amount of data transferred between the stages of the ultrasound signal-processing chain is a minimum around the display, the display systems were converted to digital processing during the early years of digital technology development. Beam forming occurs in two directions: in the plane of the image, where the evolution from mechanical to analog to digital proceeded with time, and perpendicular to the plane of the image, where mechanical focusing was replaced by digital electronic focusing and then steering with the advent of transducers segmented into two-dimensional arrays. Pointing of the ultrasound beam between 1980 and 1990 was done digitally in linear array raster scans by switching on selected transducers in the array, but in phased-array sector scans the direction of the beam was determined by adjusting the phase delay with nanosecond resolution on each transducer. Because analog signals have a continuum of possible signal levels, small differences in analog signals can be extracted as long as the differences are greater than the noise in the signal. Once a signal is digitized, no noise is added to the signal by processing. The 10 GBit/s data rate on the receiving path is based on the assumption that the transducer is divided into an array

21.5.2 Stability of Large Bubbles

The size of stable bubbles can be estimated from physical principles. The gas inside a stable bubble of radius r (Fig. 21.65) is under a pressure equal to the sum of the ambient atmospheric pressure plus the fluid pressure (1 atm = 10 m of water), and the pressure generated by the surface tension of the interface between the contained gas and the external fluid (water). In the body and in carbonated beverages, the depth of the bubbles is

Amazon
EX1010 Page 888

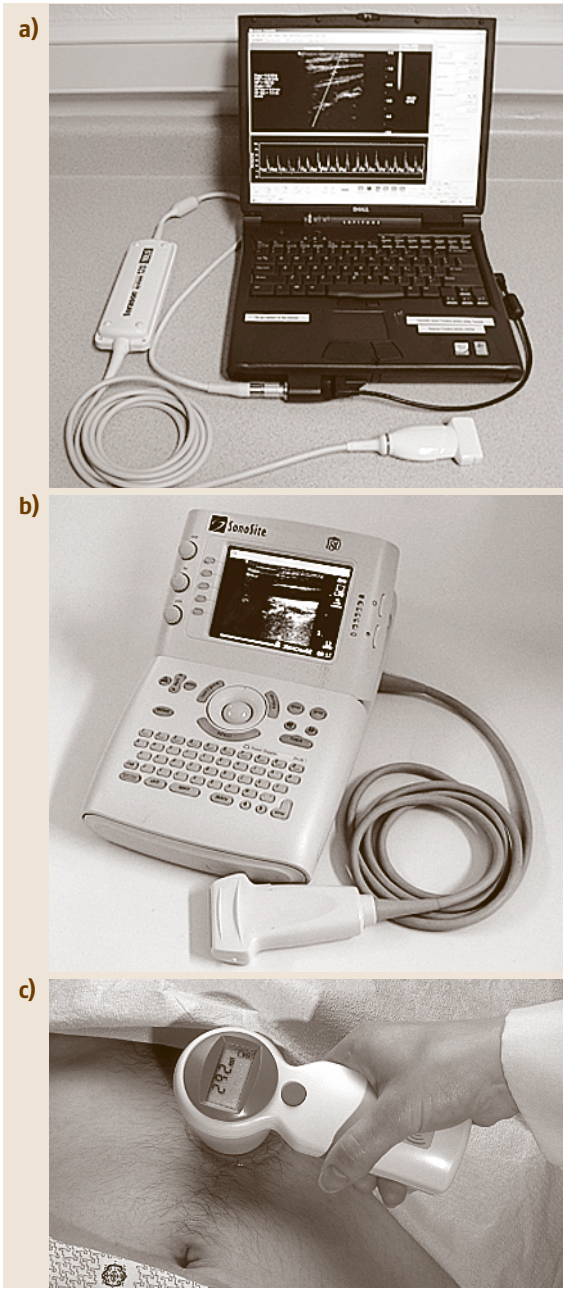


Fig. 21.64a–c Two small ultrasound imaging systems, based on the request of the Defense Advanced Research Project Administration for general-purpose handheld systems with full function **(a)** and **(b)** and an application-specific imaging system. **(a)** Terason scanner using a laptop computer; **(b)** SonoSite scanner using custom electronics; **(c)** Application-specific ultrasound scanners (BladderScan) are palm-sized and fully automatic. This instrument shows no image, but displays the volume of urine in the bladder as a number or an alarm, depending on the application

small compared to 10 m of water, so the pressure added because of the depth of the fluid can be ignored compared to atmospheric pressure. A force balance on the equator of the bubble equates the pressure force $P\pi r^2$ to the surface tension force $\sigma 2\pi r$. Thus the pressure in the bubble above the ambient pressure is $P = 2\sigma/r$. In the absence of a surfactant, the surface tension of water is 70 d/cm. When $r = 1.4\,\mu$m, $P = 1$ atm; this is a huge chemical potential to drive the contained gas into solution. If a bubble is 0.14 mm in diameter, too large to pass through a capillary (red blood cells are 8 μm in diameter), then the pressure elevation in the bubble caused by surface tension is 0.01 atm and the gas contained in the bubble has a low driving force to diffuse into solution. So, large bubbles are more stable than small bubbles. If the surface tension is reduced by applying a surfactant (shell) to the bubble, then small bubbles become stable. If the gas contained in the bubble is less soluble in blood and/or has a low diffusion constant, then the bubble has a longer life.

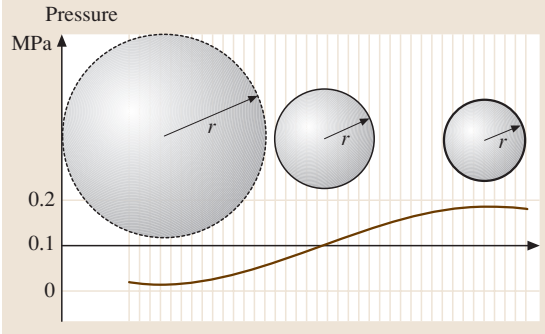


Fig. 21.65 Contrast agent bubble. An ultrasound contrast bubble is a system consisting of a gas inside the bubble, a surfactant, a surrounding liquid, and solutes including gases and surfactants in the liquid solvent. Thermodynamics and the transport of heat and of the dissolved gasses and dissolved surfactant materials all contribute to the response of a bubble to ultrasound exposure. Interactions between bubbles are also important factors in contrast agent dynamics. Here are the expected sizes for a bubble based on an isothermal ideal gas model without considering surface tension for an ultrasound intensity of 87.5 kPa

Amazon
EX1010 Page 889

21.5.3 Agitated Saline and Patent Foramen Ovale (PFO)

Agitated saline contrast bubbles are generated by forcing fluid rapidly through a small orifice, such as an injection needle. They have an important diagnostic application: to determine whether there is a shunt from the right heart to the left heart, bypassing the lungs. The most common of these shunts is the *patent foramen ovale* (PFO). PFO may be a cardiovascular defect of considerable medical importance. If a person under the age of 50 has a stroke due to occluded vessels in the brain (ischemic stroke), the most likely cause is a PFO. One affected group is divers, who return from great depths with large amounts of gas dissolved in their body tissues, especially in fat. Bubbles which form in the low-pressure venous system as the gas is transported toward the lungs, might pass through a PFO during a cough, releasing these large bubbles into the arterial system where they cause occlusion of arteries and ischemia of the tissues that were supplied by the arteries. Ischemia of some tissues might be unnoticed. Ischemia of other tissues might cause pain that is ignored. Ischemia of some portions of the brain might result in undetected changes in personality or memory. Only ischemia of the motor and sensory cortices of the brain causes loss of sensory and motor function that are recognized as stroke symptoms. In divers, these symptoms are called neurological symptoms of the bends, in others they are called transient ischemic attacks (TIA) or stroke, depending on whether the symptoms last less than 24 h or longer than 24 h, respectively.

The foramen ovale is a normal structure before birth, along with the ductus arteriosus, allowing the blood to circulate in parallel through the fetal body, lungs and placenta. At birth, with the muscular constriction of the ductus arteriosus to obliterate the lumen, pressure shifts cause the flap valve of the foramen ovale to close and over time it will seal in most people. However, in some people the foramen ovale does not seal, opening occasionally when the person coughs or strains. The prevalence of PFO in the general population is 30% at age 20 and 10% at age 70. The reason for the decline in prevalence is either because in some people the foramen seals after age 20 or because these people suffer repeated embolic events from the venous to the arterial circulation, which progressively damage body organs leading to failure and death. In the absence of PFO, such venous emboli pass to the lungs where they temporarily occlude portions of the lung, but resolve over time.

The importance of the diagnosis of PFO is currently disputed, but two factors may make testing for PFO a part of every physical examination:

1. the cost of the contrast agent is only the 2 min that it takes to handle off-the-shelf saline and
2. recently catheter methods of sealing a PFO have been released for testing, avoiding the need for open-chest heart surgery to seal the defect. If 2/3 of the

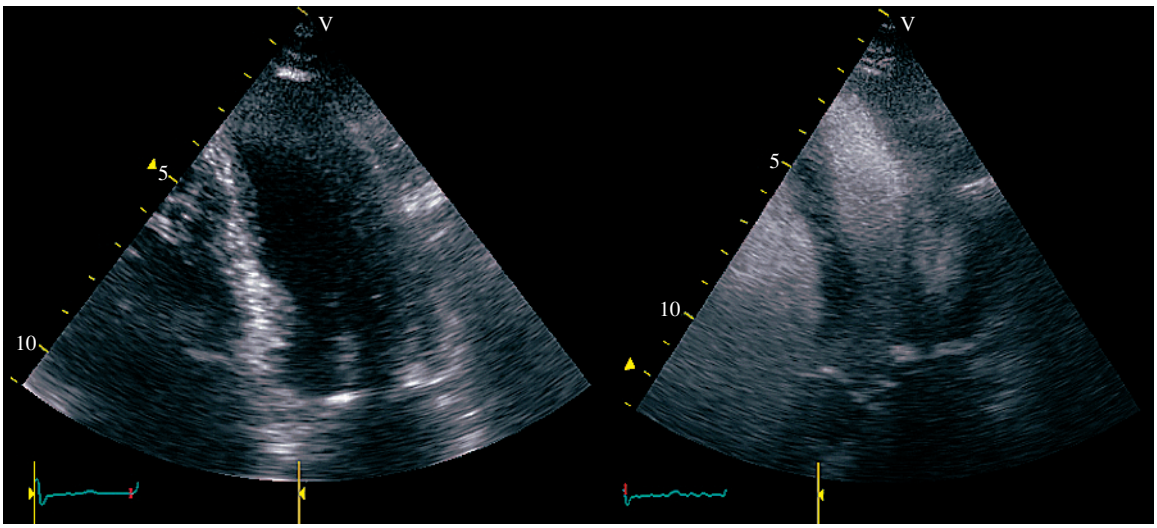


Fig. 21.66 Two-dimensional B-mode real-time echocardiogram of the left ventricle. *Left*: left ventricle without ultrasound contrast agent. *Right*: left ventricle with intravenously infused Optison ultrasound contrast agent (courtesy Frances DeRook and Keith Comess)

Amazon
EX1010 Page 890

people with PFO at age 20 die before the age of 70, this diagnosis would be an issue of considerable importance.

21.5.4 Ultrasound Contrast Agent Motivation

The case for the development of stable ultrasound contrast bubbles small enough to pass through the capillaries of the lungs and appear in the systemic arteries is based on the wide use of ultrasound in medical imaging. Over half of all medical imaging is done with ultrasound, so there are many potential applications for contrast agents. Because these mechanical agents are confined to the vascular space, they cannot provide contrast in excretory, diffusional or extravascular chemotactic applications. Blood is a poor reflector of ultrasound, generating echoes 60 dB below the echoes from vascular walls. Contrast agents increase the backscatter. In most cases, the detection of blood flow is easy by Doppler methods which can reject the high-intensity stationary echoes from vascular walls and detect the moving echoes of blood using Doppler methods. However, in cases where the blood is moving slowly, these methods are more difficult and there is an advantage from the increased echo signals produced by contrast agents. Thus, in identifying the exact location of endocardium (Fig. 21.66), in regions deep within strong attenuators (such as skull) and for blood flow in capillaries, contrast agents promise to provide important additional diagnostic information.

21.5.5 Ultrasound Contrast Agent Development

Ultrasound microbubble contrast agents have been under development for a quarter century [21.79]. The first task in the development of microbubble contrast agents was to make stable bubbles small enough so that they could pass through the capillaries of the lungs (about 3 μm in diameter) after injection into the venous system, and stable enough to survive long enough to be useful (more than 1 min, preferably 30 min). Three strategies are available to stabilize the microbubbles:

1. lower the surface tension,
2. form bubbles of a gas with low solubility or diffusivity in water/blood and
3. produce a gas-impermeable barrier at the gas–liquid interface.

Surfactants lower surface tension; fluorocarbons have low solubility in water/blood; polymeric shells can be impermeable to gas diffusion. A series of contrast agents have been developed based on various combinations of surfactant, contained gas and method of formation.

The behavior of ultrasound contrast agent microbubbles is complicated and can easily consume an entire career. Only a few factors will be mentioned here. A microbubble consists of three phases: the contained gas, the surfactant, and the surrounding fluid. The size distribution of the bubbles is determined by the method of formation. Air-filled albumin-coated microspheres can be formed by whipping a mixture of albumin and water in a blender. This forms a broad distribution of microspheres. The desired size can be selected by centrifugation or flotation. A more nearly uniform microbubble size can be achieved by metering the relative volume of surfactant and gas through a calibrated nozzle orifice. The relative amounts of gas and surfactant are determined by the desired surface to volume ratio. The speed of bubble extrusion is crucial to the formation of bubbles of stable size. If prepared for medical use, in addition to a sterile preparation, formed using Food and Drug Administration (FDA)-approved good manufacturing practice, the agent must have sufficient stability and shelf life to permit distribution, storage and timely preparation for use.

When released into blood, the contained gas is usually not at equilibrium with the dissolved gases in the blood. A microbubble filled with fluorocarbon will take up nitrogen, oxygen and carbon dioxide without releasing much fluorocarbon, so the microbubble will swell after injection. The amount of swelling will depend, in part, on the amount and properties of the surfactant. If the bubble swells so that the surface area begins to exceed the available surfactant, the surface tension rises. This may favor bubble coalescence. As the microbubble passes through the lungs, some of the contained fluorocarbon will be released. Gas exchange between the microbubble and the dissolved gas in the blood is continuous during the life of the bubble. Some surfactants and some contained gases have chemical or physical affinities for the interior surfaces of the cardiovascular system of the lungs, arteries, capillaries or veins. The bubbles may become specifically adsorbed to the endoluminal surfaces of these vessels. This can be accidental or deliberate, and can become part of the functionality of the contrast agent. When specifically adsorbed, the surfactant may migrate to the vascular surface or may take on molecules from the vascular surface or surroundings. Of course, the contrast agent might be taken up by cells,

Amazon
EX1010 Page 891

transported by those cells and/or retained in particular tissues or organs.

21.5.6 Interactions Between Ultrasound and Microbubbles

When exposed to ultrasound at diagnostic frequencies (1–20 MHz), the contrast bubbles will oscillate at the driving frequency of the ultrasound, emitting the fundamental frequency as well as harmonics of the fundamental frequency. Microbubbles have a natural resonance frequency, primarily determined by their size, surface tension, shell rigidity (if any) and the density of surrounding material. If stimulated at a frequency near the resonant frequency, the amplitude of oscillations will be greater. The pressure of the interior gas varies with volume according to the rules of adiabatic compression and expansion, at least to the extent that the process is too fast for heat transfer. Although the waveform of the oscillation is primarily determined by the waveform of the driving ultrasound, the surfactant forces also play a great role in this process. When the ultrasound pressure is high (for 0.3 μs) the gas compresses, the temperature raises, the water vapor pressure increases as does the pressure of other gases. The gas pressures rise above the surrounding partial pressures of gas, providing a driving force to move gas out of the bubble into solution. Because the bubble is small, the surface area available for heat and mass transfer is small, and the amount of loss of heat and gas is small. Alternatively, when the ultrasound pressure is low (the subsequent 0.3 μs), the pressures and temperature drops, providing driving forces for heat and gas to enter the bubble. Now the surface area is large and it is easy for transport into the bubble, leading to rectified diffusion of gas and heat into the bubble.

At the body temperature of 37 °C, the vapor pressure of water is 6.2 kPa, 6% of atmospheric pressure. An acoustic wave of 285 mW/cm^2 SPTP (spatial peak temporal peak) intensity drops the pressure in a bubble below the vapor pressure of water (ignoring surface tension) which will cause the water to vaporize, filling the bubble with water vapor in addition to the other contained gasses. The latent heat of evaporation lowers the temperature of the bubble. On compression, the recondensing of the water adds heat to the bubble. When the ultrasound is compressing the bubble, the surfactant acts as a stable skin. The skin may even exhibit negative surface tension. Like the hull of a submarine deep in the ocean, the surfactant may hold the bubble gas pressure lower than the surrounding pressure. Similarly, when the ultrasound pressure has dropped below ambient, and the bubble expands to form a larger surface area, the surfactant, which is often a monolayer of molecules on the surface, will change in configuration, become patchy and result in increased surface tension, holding the internal gas pressure higher than expected from the surrounding pressure. As there is a driving force for the gaseous contents of the microbubble to experience rectified diffusion, there is also a driving force for the surface phase to experience rectified diffusion, changing the composition of the surface. A stable molecular monolayer on the surface of the bubble at one bubble volume will become compressed when the bubble becomes small, providing a driving chemical potential to both change the phase of the monolayer to a multilayer and to drive some of the surfactant into solution. The monolayer will be expanded when the bubble becomes large, providing a driving chemical potential to draw surfactant from solution. The solution my provide surfactant materials that are similar to or different from the original surfactant on the microbubble. Unless the concentration of potential surfactants in solution is high, this process is too slow to affect bubble behavior. In experimental solutions, such concentrations may be low, but the complex mixture of complex molecules in blood may favor such a process.

21.5.7 Bubble Destruction

The first experiments with microbubble contrast agents were disappointing. Contrast agents did not produce reflections as bright as expected. Increasing the transmit intensity did not improve the strength of the echoes coming from the agents. In an effort to improve the signal strength, broadband ultrasound transducers were used to form harmonic images. An ultrasound transducer oscillates at a resonant fundamental frequency determined by the thickness. The transducer has no efficiency or sensitivity at double the frequency, although it does have one-third the efficiency and sensitivity at triple the frequency. By damping the transducer, a transducer with a center resonant frequency of 3 MHz can be made to operate at frequenciesof 1.9–4.1 MHz. In harmonic imaging to detect contrast bubbles, a 2 MHz transmit burst is applied to this broadband transducer and the receiver is tuned to 4 MHz. Echoes from tissue are expected at 2 MHz, echoes from contrast microbubbles are expected at 2 MHz and 4 MHz. By selecting only echoes at 4 MHz, clear visualization of the contrast bubbles was expected. Unfortunately, for this application, because ultrasound transmit intensities are so high, ultrasound transmission in tissue is nonlinear, generating

Amazon
EX1010 Page 892

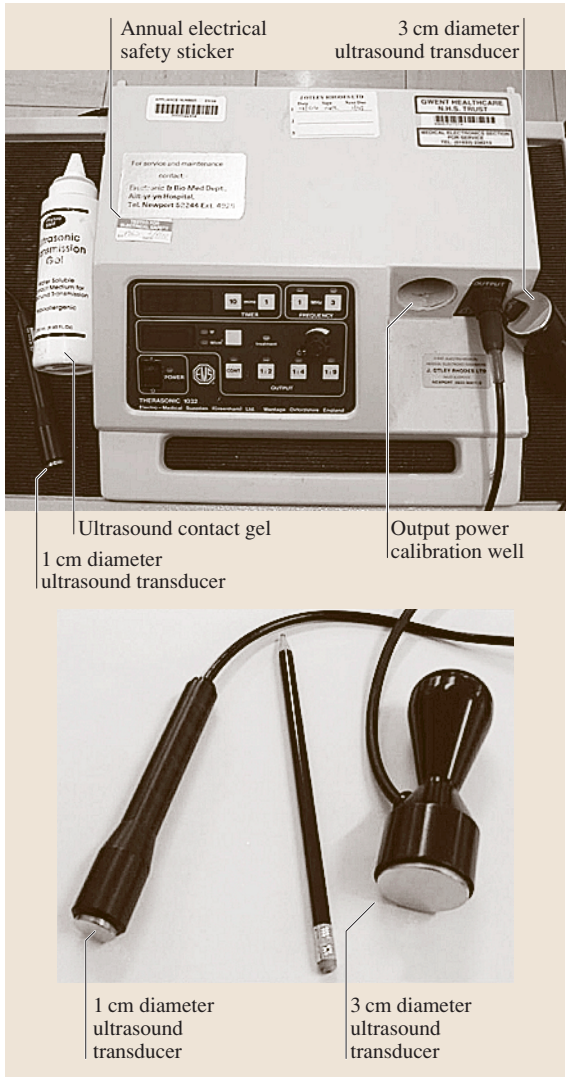


Fig. 21.67 Ultrasound therapy system

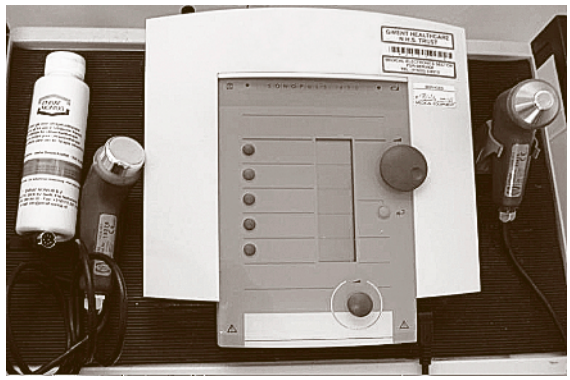


Fig. 21.68 Combined ultrasound diathermy and electrotherapy system. Deep heating of tissue can be achieved by using ultrasound or by using radio-frequency electric currents. This system is capable of delivering both kinds of heating. The two transducers shown are for ultrasound, but since the metallic surface is in contact with the patient, either can also apply RF diathermy when used with a counter-electrode

harmonics in the transmit beam on the way to the reflectors. So even without contrast microbubbles, tissue echoes contain 4 MHz, 6 MHz and 8 MHz components when exposed to 2 MHz transmit pulses. Even more disturbing, real-time B-mode images still did not show brighter echoes from contrast-filled blood spaces than from the same spaces before the introduction of the contrast agent. The reason for this puzzling result is that the transmitted ultrasound pulse destroys the echogenic bubbles, bleaching the contrast effect. Only bubbles of a particular size are bleached by the particular incident ultrasound frequency used, some becoming larger by coalescence and some dividing into smaller sizes, so they are not strongly echogenic at the incident frequency. The process of bubble destruction takes several milliseconds after exposure to a single ultrasound transmit burst. This provided the basis for two new methods of imaging with ultrasound contrast microbubbles: interrupted imaging and color Doppler imaging. If 2-D real-time B-mode imaging is used at a typical frame rate of 30 images per second, the interval between one pulse-echo cycle along an image line and the next is 33 ms, so the echogenic bubbles are gone after the first frame, and any new echogenic bubbles that enter the image field are destroyed as the imaging continues. This led to interrupted imaging of the heart muscle. In interrupted imaging, a series of ECG-triggered images is recorded for later analysis. Each image is acquired at the same time during the cardiac cycle so that successive images are separated by at least one cycle. During the sequence of ECG-triggered acquisition of images from a single plane, an initial image is obtained (i0), after an interval of five cardiac cycles a second image is obtained (i5), after the next interval of four cardiac cycles the next image is obtained (i4), then after three cycles (i3) and after two cycles (i2) and finally after an interval of one cycle the final image is obtained (i1). In theory, the prior image bleaches all of the contrast while acquiring the image. For contrast to appear in the next image, perfusion must carry the contrast bubbles into the image. By subtracting i5 from i0, all regions with significant

Amazon
EX1010 Page 893

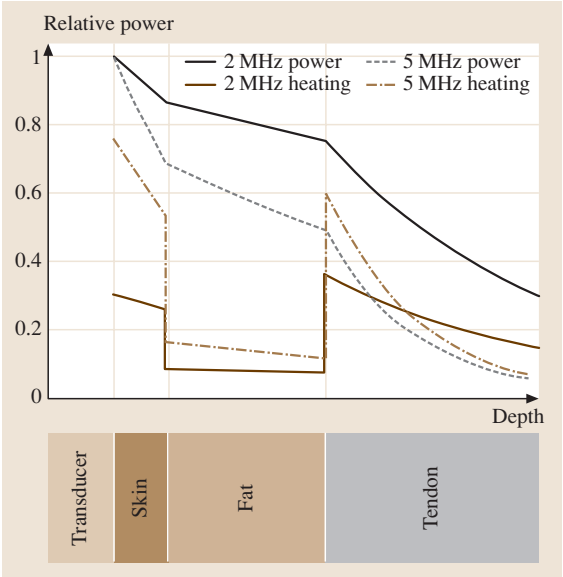


Fig. 21.69 5 MHz ultrasound is attenuated more in a short distance than 2 MHz ultrasound (*upper lines*). At shallow depths 5 MHz ultrasound delivers more heat because of greater absorption (*lower interrupted line*), but at the deepest depths, 2 MHz ultrasound provides greater heating (*lower solid line*). Because of the low absorption of ultrasound by fat, little heating occurs in fat

perfusion are dark. By subtracting i1 from i2, only the regions that are filled with contrast within a second are dark, those that fill during the time between 1 and 2 s are bright. By subtracting i4 from i5, the bright regions showing contrast bubbles in the image i5 that are not present in i4 show the regions that are filling slowly with blood.

During a color Doppler or color power angiography ultrasound examination, the ultrasound system sends an ensemble of eight transmit bursts at intervals of 0.2 ms along the ultrasound beam pattern to measure the changes in phase of the ultrasound echoes. In that 1.6 ms period, the contrast bubbles will begin and complete the process of vanishing. Thus there will be a large change in the echoes received from each depth during the period of the ensemble. This will be interpreted by the ultrasound system as a Doppler signal and displayed as color in the image.

The exact role of ultrasound contrast agents in medical diagnosis remains to be developed. However, there are a number of efforts to develop nanoparticles for useful applications. These nanoparticles are the same size as ultrasound contrast agents and may contain gas as well as liquid. The National Cancer Institute Unconventional Innovations Program supports some of this work for the diagnosis, treatment and monitoring of cancer. Nanoparticles can act as machines, using ultrasound energy as the supply to do useful work. This can be achieved using protein mechanics. Protein folding confirmations can change in nanoseconds, the molecular volume is different for each conformation and the energy states of folding change under high and low pressure, so ultrasound can be used to drive proteins from one conformational state to another. Nanoparticles can be used to deliver drugs [21.80] to target tissues, with ultrasound serving to trigger the release of the drug at desired times.

21.6 Ultrasound Hyperthermia in Physical Therapy

One of the earliest medical applications of ultrasound was the therapeutic heating of deep tissue because absorption of ultrasound by tissue results in the conversion of ultrasound energy into heat. In common practice, an ultrasound transducer 3 cm in diameter transmitting 20 W at a frequency of 3 MHz is applied to the skin (Figs. 21.67, 21.68).

As a rule, the size of the treatment area should be less than twice the surface area of the transducer. Because of diffraction effects, the ultrasound field has a complex pattern of peaks and valleys. The best transducers have a beam nonuniformity ratio (BNR) of 2 : 1 in intensity. A BNR of 6 : 1 is clinically acceptable. Some instruments have a BNR of 8 : 1.

The ultrasound passes through skin and subcutaneous fat to the muscles and connective tissues below. Because the attenuation of ultrasound in tendon is 10 times the attenuation in fat, the majority of the heating is in the tendon (Fig. 21.69). Heating is more superficial when a higher ultrasound frequency is used.

The attenuation in muscle and tendon is higher than in fat, favoring the heating of these tissues even when they are covered by fat. However, the attenuation of skin is quite variable; some reports show skin attenuation higher than tendon. The variability of the attenuation in skin results from two factors, the thin and nonuniform character of skin, and the variable air content of

Amazon
EX1010 Page 894

the stratum corneum, the outermost layer of skin. With careful application of ultrasonic gel, the air can be removed from the stratum corneum layer, lowering the attenuation.

Although ultrasound diathermy as well as other diathermy methods are often used in physical therapy, the effectiveness of the treatments beyond the placebo effect is questioned by some.

21.7 High-Intensity Focused Ultrasound (HIFU) in Surgery

Starting in 1950, William J. Fry and colleagues at the University of Illinois, Urbana, developed an ultrasound method to heat small volumes of deep tissue to high temperatures. Using a 10 cm-diameter transducer operating at 2 MHz focused at a depth of 10 cm, tissue the size of a grain of rice can be heated at 25 °C per second, causing the tissue to boil in 2.5 s. This method allowed Fry to create thermal lesions in the brain for the treatment of brain tumors and other neurological conditions.

The technology is still in evolution, but holds promise of allowing the cautery of deep tissue without damaging the overlying superficial tissue. A 35 mm-diameter 5 MHz concave ultrasound transducer focused at a depth of 35 mm (Fig. 21.70) delivering 30 W of acoustic power to a treatment volume 1 mm in diameter and 10 mm long can deliver an intensity of 3 kW/cm^2 (30 MW/m^2) to form a lesion (Fig. 21.71). At such intensities the nonlinearity of the tissue causes much of the ultrasound to be converted to higher harmonics (Fig. 21.72), increasing the fraction of the incident power absorbed in the treatment volume. During HIFU treatment, ultrasound images of the treatment volume show a spot of increased echogenicity caused by bubbles filled with water vapor (boiling) or with gas coming out of solution. When the HIFU treatment stops, the hyper-echogenic zone quickly becomes anechoic. During treatment, the bubbles may act as a shield, restricting the delivery of ultrasound to deeper tissues (Figs. 21.73, 21.74).

HIFU treatment can coagulate blood to stop bleeding or to render tissue ischemic, causing necrosis. The method holds promise for:

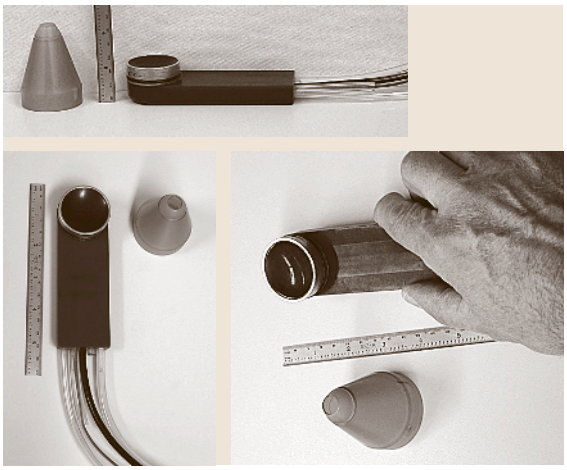


Fig. 21.70 3.5 MHz HIFU transducer used in abdominal surgery research. Notice that the black transducer face is concave (the reflection of the fluorescent light fixture is curved). The transducer is fitted with a signal cable (*black*), a pair of tubes to deliver and return cooling water (*clear*), and a thermocouple cable (*thin*) to monitor the temperature of the transducer. A plastic cone filled with water fits on the front of the transducer to conduct the sound to the tissue

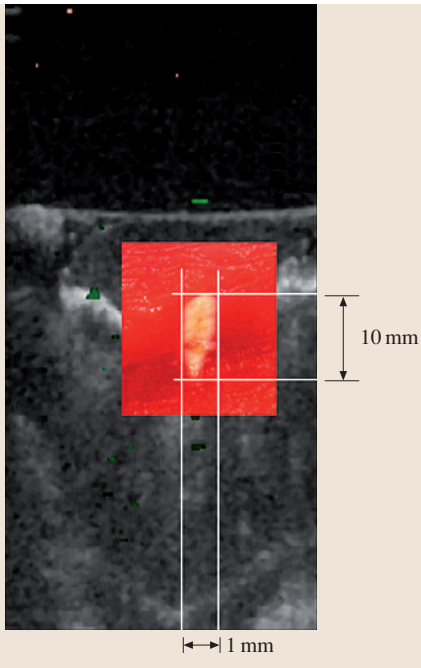


Fig. 21.71 Histology of a HIFU lesion overlaid onto the ultrasound image. 5 s high-intensity focused ultrasound cautry at a depth of 5 cm under tissue in porcine spleen. Typical lesions are 10 mm long (in depth from the transducer) and 1 mm in diameter

Amazon
Amazon EX1013 Page 895
EX1010 Page 895

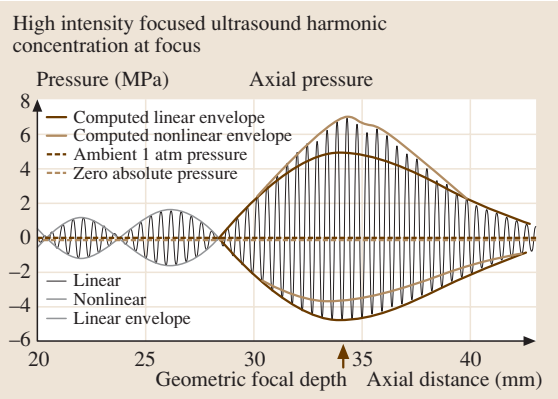


Fig. 21.72 Computed central beam instantaneous pressures from a HIFU transducer. The high acoustic pressures in the focal zone create nonlinear effects that generate harmonics in the transmitted ultrasound beam (courtesy F. Curra)

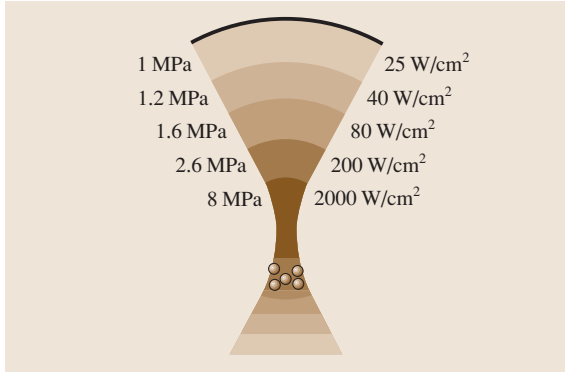


Fig. 21.73 Typical HIFU ultrasound beam profile. High-intensity focused ultrasound beam profile showing increase in beam intensity, not accounting for attenuation. The small circles post focus represent bubbles formed by a combination of mechanical-index-induced cavitation boiling. They are pushed into the post-focus zone by radiation pressure. As the exposure continues, more bubbles will be formed at shallower depths. Post-focal bubbles may provide a safety shield, preventing HIFU exposure of deeper, healthy tissue

1. stopping internal bleeding of the liver or spleen,
2. stopping bleeding due to catheter procedures,
3. reducing the size of tissues such as uterine fibroids and prostate hypertrophy,
4. destroying cancer cells and tumors,
5. birth-control procedures such as vasectomy and tubal ligation,
6. tissue welding, and
7. pushing tissues using radiation force to stretch or compress them.

Thermal dose is one way to summarize hyperthermia treatment conditions. Thermal dose implies that tissue changes occur above 43 °C, and that the effect is increased with increasing time and increasing temperature. One empirical formula for thermal dose has been given [21.81] as:

$$D = \int_{t_1}^{t_2} n(T)^{(T-43)}\,\mathrm{d}t\,,$$

where t_1 and t_2 are the initial and final times of the heating profile, respectively, and $n(T)$ is 4 for $T < 43\,^{\circ}\mathrm{C}$ and 2 for $T > 43\,^{\circ}\mathrm{C}$. The temperature is determined by the rate of heat delivery per tissue volume, which is the product of the intensity times the attenuation minus the rate at which heat is removed from the tissue by conduction through tissues, and convection via the blood.

The most difficult issue with HIFU is the small treatment volume versus the relatively large access window. Under ideal conditions, the treatment of a single volume of tissue 10 mm^3 takes about 2 s. A cubic region 50 mm on a side has a volume of 125 000 mm^3 and requires nearly 4 h to treat. These long treatment times present a considerable economic problem for the adoption of the technology.

21.8 Lithotripsy of Kidney Stones

Explosive ultrasound can be used to fracture kidney stones in the renal pelvis where the urine is collected from the kidney and directed down the ureter to the bladder. Stones which form in the renal pelvis from solutes in the urine are very painful. The pain occurs because urine is moved down the ureter by peristaltic action, and the peristalsis cannot handle a bolus the size of a stone. One type of ultrasound lithotripter uses a 10 cm-diameter concave reflector with a spark gap at the source focus. The elliptical curvature forms a target focus 12 cm from the face of the reflector. Equally intense ultrasound pulses can be formed using focused piezoelectric transducers or electromagnetically driven membranes with the ultrasound focused using an acoustic lens.

Amazon
EX1010 Page 896

A water path is used to couple the reflector to the skin nearest the affected kidney so that the target focus can be positioned on the kidney stone. By firing the spark gap in the water at the source focus, pressures of +100 MPa followed by −10 MPa are achieved at the target focus. Treatment of a kidney stone may require 3000 shocks delivered over an hour. The object of the treatment is to break a large stone (≥ 1 cm in diameter) into smaller pieces (≤ 2 mm diameter) that the ureter can carry to the bladder. The mechanism of stone destruction includes erosion, spallation, fatigue, shear and circumferential compression associated with the primary shock wave or resulting cavitation. Erosion is caused by cavitation. Spallation is the ejection of the distal portion of the stone, resulting from a decompression wave reflected from the distal portion of the stone. Unfortunately, lithotripsy is often associated with injury to the kidney parenchyma [21.82].

21.9 Thrombolysis

A new therapeutic application of ultrasound is the destruction of blood clots occluding vessels. Two mechanical methods may contribute to clot destruction [21.83–85]: the formation of microbubbles in the clot (cavitation) and differential radiation force on the clot squeezing and expanding the clot like a sponge to take up thrombolytic drugs. There are research reports of successful thrombolysis in coronary arteries [21.86], intracranial arteries [21.87, 88] and vascular access shunts for dialysis. The ultrasound intensities required for thrombolysis are similar to those used in diagnostic ultrasound. The mechanisms include streaming and disaggregation of the clot [21.89].

21.10 Lower-Frequency Therapies

Lower-frequency ultrasound is used for tissue disruption and cleaning purposes. To remove an opacified lens (cataract) from the eye through a small incision, a needle oscillating at 25–60 kHz is used to emulsify the lens (phacoemulsification), which is then removed by aspiration (suction).

Dental scaling is performed with a similar instrument operating at frequencies of 18–30 kHz and applied power of 30 W. Cavitation is an important mechanism in the cleaning process. Chemical additives such as toothpaste can suppress cavitation and degrade the cleaning efficiency.

21.11 Ultrasound Safety

Undoubtedly, ultrasound is safe. In over a half century of widespread use of diagnostic ultrasound, there are no currently accepted reports of harm to patients or examiners from the use of diagnostic ultrasound. However, in 1950, unamplified X-ray fluoroscopic imaging was considered so safe that it was used for shoe fitting in nearly all shoe stores, and for the entertainment of children waiting to be served. In 1950, smoking was considered to be so beneficial to health that nearly all doctors smoked. Although there are reports that ultrasound examination in pregnancy is associated with increased birth complications in retrospective studies where ultrasound was applied to high-risk pregnancies, a causative effect is unlikely. Fewer complications were found in pregnancies randomized to ultrasound examination compared to those with conventional care [21.90] because of the increased knowledge of physicians about the expected date of delivery. In one discussion of the safety of Doppler ultrasound examination of the ophthalmic artery through the eye, an experienced investigator stated “If the patient doesn’t see flashes of light, I figure that the exam is safe”. Still today, diagnostic ultrasound is considered so safe that, although there are occasional disclaimers such as “to be used only under the supervision of a physician”, ultrasound examinations are performed for educational purposes on students, demonstrated on hired actors at trade shows, available for home use, and advertised

Amazon
EX1010 Page 897

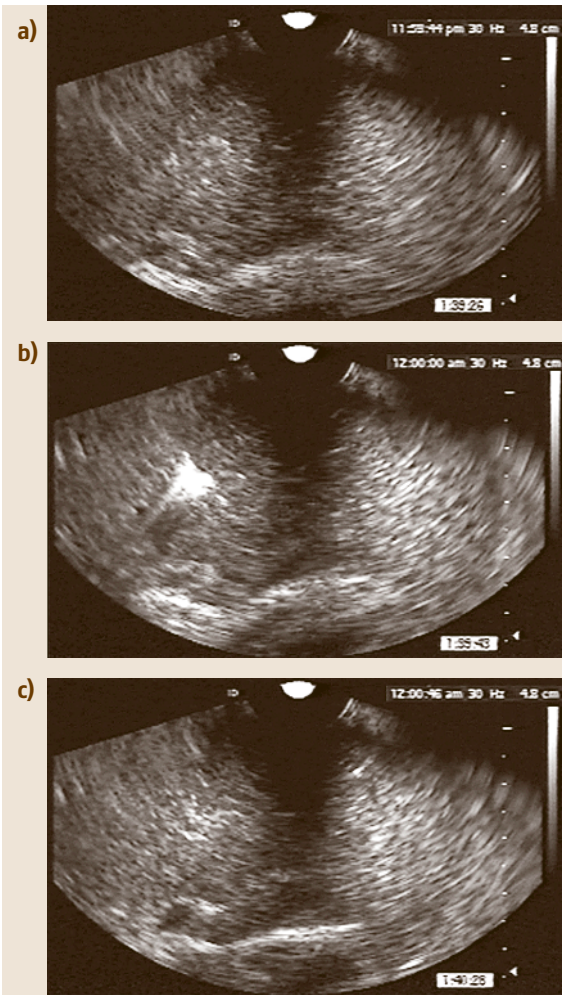


Fig. 21.74a–c B-mode imaging of high-intensity focused ultrasound lesion formation. Focal intensity 1000 W/cm2. **(a)** B-mode image of tissue before HIFU therapy. **(b)** Echogenic region at HIFU treatment zone after 15 s of exposure. **(c)** Echogenicity vanishes with time after cessation of HIFU exposure

for entertainment purposes. One prominent ultrasound safety expert warned that driving to the examination carried more risk than the risk associated with ultrasound examination.

In 1976, the United States congress passed the Medical Device Amendments providing that the Food and Drug Administration should have authority over medical devices [21.91]. At that time, any medical device in clinical use, in the absence of evidence of hazard, was considered safe. Any new medical device that was substantially equivalent to a pre-enactment device could be approved for distribution in interstate commerce and use by filing a 510k application showing equivalence. Devices that were not substantially equivalent required pre-market approval (PMA) as an investigational device. This started a search for existing ultrasound systems that had been sold across state lines so that the ultrasound output levels could be measured. These old systems are called pre-enactment systems. New ultrasound devices that had similar or lower acoustic outputs were considered equivalent and could be approved by the FDA under a 510k application, which was simpler and far less costly than the PMA process.

In 1976, continuous-wave (CW) Doppler systems were in use, pulsed Doppler systems were in use, M-mode, 2-D static B-mode and 2-D real-time B-mode systems were also in use. One CW Doppler system at the time caused red spots on the skin that were called *Doppler hickies*, but were still considered safe because there were no complaints.

The task was to characterize the equivalent acoustic output. Over the quarter century since enactment, various methods have been developed to describe the effect of ultrasound on tissue, to establish equivalence. Because of the common use of therapeutic ultrasound to create tissue hyperthermia, the first consideration was the heating effect of the ultrasound; later mechanical effects were included in the analysis.

The heating of tissue is governed by the bioheat equation. This equation relates the increase in tissue temperature to the rate of heat deposit minus the rate of heat removal divided by the heat capacity of the tissue. The rate of heat deposit is proportional to the incoming ultrasound power minus the outgoing ultrasound power, per unit mass. In a simple computation, the heat capacity of tissue is the same as water, 1 cal/gm or $4.2\,\mathrm{J/gm\,^{\circ}C} = 4.2\,\mathrm{J/cm^3\,^{\circ}C} = 4.2\,\mathrm{W\,s/cm^3\,^{\circ}C}$. So, if ultrasound at an intensity of $4.2\,\mathrm{W/cm^2}$ is completely absorbed by a layer of tissue (water) that is 1 cm thick, the temperature will rise 1 °C per second, if no heat is carried away. $42\,\mathrm{mW/cm^2}$ ($420\,\mathrm{W/m^2}$) will raise the temperature by only 0.01 °C per second, allowing 100 s of exposure to raise the temperature from the normal body temperature of 37 °C to 38 °C, well below fever temperature considered safe by most people. Since at 4 MHz, only half of the ultrasound power is converted to heat in one cm, the heating rate is half of the values above.

Until 1985, ultrasound exposure levels were quoted in terms of $\mathrm{W/cm^2}$ related to tissue heating. Based on pre-enactment levels, diagnostic ultrasound systems had

Amazon
EX1010 Page 898

a temporal average (TA) acoustic intensity at the transducer focal zone measured in a water-filled test tank of 100 mW/cm^2 (1 kW/m^2) or less. The major exception was ultrasound systems for the examination of the eye, which had pre-enactment intensities of 7 mW/cm^2 (70 W/m^2). So, the generally accepted temporal average allowable intensities became: 7 mW/cm^2 (70 W/m^2) for the eye and 100 mW/cm^2 (1 kW/m^2) for all other diagnostic applications. The maximum intensity of sunlight is about 50 mW/cm^2 (500 W/m^2), but the attenuation of sunlight at the skin is near 100%. Acceptable physical therapy ultrasound intensities were about 30 times higher: 3 W/cm^2 (30 kW/m^2).

Ultrasound beam patterns are not uniform, especially in the Fresnel zone (near field). The intensities at the focus in diagnostic ultrasound beams are often three times higher than the average intensities. Because of this, ultrasound intensities were reported as spatial peak (SP) intensities, to indicate the variations, or spatial average (SA) intensities.

With pulsed-echo ultrasound imaging, the transmitted ultrasound is on for less than 0.5 μs every millisecond along the same ultrasound beam pattern in M-mode examination; thus the ultrasound was on only 1/2000 of the time (duty factor or duty cycle of 0.05%). For a spatial peak temporal average intensity of 100 mW/cm^2, (1 kW/m^2) the pulse average (PA) was 2000 times as great or 200 W/cm^2 (2 kW/m^2) (SP PA) and the temporal peak (TP) intensity was twice that value (SPTP, Fig. 21.23, broadband pulse). A conventional pulsed Doppler examination with a 1 μs transmit burst every 50 μs has a duty factor of 2% and an SPTP intensity of 5 W/cm^2 (50 kW/m^2). In both M-mode and Doppler examinations, the ultrasound beam pattern is held stationary for several seconds. But in real-time 2-D B-mode imaging, each successive beam axis is along a different line. Typically, the ultrasound is directed along the same line at the frame rate, about 30 times per second.

Over the next decade, the guidelines for ultrasound intensities in different applications became more sophisticated, separating application-specific output levels into four categories: general, cardiac, vascular, and ophthalmic. The motivation was to allow higher intensity levels to be used for Doppler blood velocity measurements because the echoes returned by blood were 0.000 001 (60 dB) lower than those from tissue. Rather than accepting the intensities measured at the focal zone in a water tank, the intensities were derated by computing the expected intensity if the water were replaced by attenuating tissue with an attenuation rate of 0.3 dB/(MHz cm). Derating allows a 3 MHz cardiac Doppler system focused at a depth of 11 cm to derate the intensity by 10 dB, thus allowing a tenfold increase in transmit power. The derated SPTA limits were: fetal, neonatal and other general-purpose applications −94 mW/cm^2; cardiac −430 mW/cm^2; peripheral vascular −720 mW/cm^2; ophthalmic −17 mW/cm^2; the SPPA limits were 190 W/cm^2 for the first three categories and 28 W/cm^2 for ophthalmic exams.

Working together, the US Food and Drug Administration (FDA), National Electronic Manufacturers Association (NEMA) and the American Institute of Ultrasound in Medicine (AIUM) began to agreed on output display standards (ODS) for ultrasound instruments, including the thermal index (TI, the intensity required to raise the temperature of tissue by 1 °C) predictive of tissue heating, and the mechanical index (MI) predictive of cavitation and interactions with ultrasound contrast agents. The TI was further divided into subcategories for soft tissue (TIS), bone near the focus (TIB) and cranial bone near the skin (TIC) based on the expected absorption of ultrasound in the tissue. These values also include the fact that the ultrasound beam is scanning across the tissue in 2-D imaging. The computation of MI is based on the SPTP intensity values, includes attenuation derating but not the scanning of the ultrasound beam.

To better understand the MI values, refer to Fig. 21.5 which indicates that the amplitude of the pressure fluctuation for a 0.3 W/cm^2 wave is 1 atm, or 100 kPa = 100 kN/m^2. The pressure increases by the square root of intensity, for a linear system (which this cannot be). So, for the M-mode SPTP intensity of 200 W/cm^2, (2 MW/m^2) the pressure amplitude is 26 atm, making the peak positive pressure 27 atm (2.7 MPa) and the peak negative pressure (below zero) −25 atm (−2.5 MPa). The MI is defined as the negative pressure amplitude [MPa] divided by the square root of the ultrasound frequency [MHz]. This provides a basis for the estimation of the chance of an adverse nonthermal event. At 3 MHz, the MI for this case is 1.5. An MI less than 1.9 is acceptable for obstetrical examinations in the absence of ultrasound contrast agents our other sources of gas bubbles.

In 1991, the FDA released its 510k guidance [21.92], establishing a new track for approval of non-PMA devices, regulatory track 3. This permitted increased outputs for devices implementing the output display standard developed jointly by the AIUM and NEMA [21.93]. This standard recognized two general classes of mechanisms by ultrasound could adversely affect biological tissue, thermal and mechanical, and

Amazon
EX1010 Page 899

provided simple metrics for the likelihood of such effects, the thermal index (TI) and mechanical index (MI).

Similar standards have been addressed in other countries by organizations and agencies including Health Canada, the European Committee for Medical Ultrasound Safety (ECMUS), the British Medical Ultrasound Society (BMUS), the European Federation of Societies for Ultrasound in Medicine and Biology (EFSUMB), the Australasian Society for Ultrasound in Medicine (ASUM), the Asian Federation for Societies of Ultrasound in Medicine and Biology (AFSUMB), the Latin American Federation of Ultrasound in Medicine and Biology (FLAUS), the Mediterranean and African Society of Ultrasound (MASU), and the World Federation for Ultrasound in Medicine and Biology (WFUMB).

In spite of the confidence that ultrasound is absolutely safe, all ultrasound agencies subscribe to the policy of using ultrasound exposure levels that are as low as reasonably achievable (ALARA) for diagnostic ultrasound examinations.

In the presence of ultrasound contrast agents or gas in the lungs or gut, there is a risk of damaging capillaries and creating interstitial hemorrhaging in tissues when high-MI examinations are performed.

However, there are some other considerations. In addition to heating tissue and the compression/decompression mechanical factors related to mechanical index, an ultrasound wave exerts radiation pressure on tissue as it passes through. The radiation pressure is proportional to intensity. Radiation force is used in the measurement of acoustic output. The body force is equal to the [power entering a region minus the power transmitted through and exiting the region] divided by the speed of sound. At a pulsed Doppler focus in the examination of the fetus, a temporal peak radiation pressure of 1700 Pa can be generated at a frequency equal to the pulse repetition frequency (PRF) of 5 kHz, which is well within the hearing range. If the ultrasound beam pattern is directed to intersect the ear, the radiation pressure oscillation can be heard by the fetus and cause increased fetal activity [21.94].

Of more serious concern is the increase in permeability in cell membranes and other biologic barriers to small and large molecules that can be induced by ultrasound [21.95]. This may prove useful for the delivery of therapeutic drugs through the skin (sonoporation) and genes across membranes including the placental barrier and the blood–brain barrier, but it might also allow the inadvertent transfer of pathogens. The effect is enhanced in the presence of gas and ultrasound contrast agents. It is possible that such effects have escaped detection by current monitoring methods.

The conceptual simplicity of the pulse-echo system has allowed instrument engineers to devote all efforts toward lowering the cost and improving the diagnostic utility of these instruments. Unlike most other medical imaging methods, ultrasound is low-cost, portable, real-time, and considered safe in most applications.

Further Reading

Please find a complete compilation of citations from Ultrasound in Medicine and Biology which list the thousands of articles on medical acoustics written prior to 1987: http://www.ncbi.nlm.nih.gov/entrez/query.fcgi?CMD=Display&DB=pubmed

References

21.1 G.E. Horn, J.M. Mynors: Recording the bowel sounds, Med. Biol. Eng. **4**(2), 205–208 (1966)

21.2 T. Tomomasa, A. Morikawa, R.H. Sandler, H.A. Mansy, H. Koneko, T. Masahiko, P.E. Hyman, Z. Itoh: Gastrointestinal sounds and migrating motor complex in fasted humans, Am. J. Gastroenterol. **94**(2), 374–381 (1999)

21.3 C. Leknius, B.J. Kenyon: Simple instrument for auscultation of temporomandibular joint sounds, J. Prosthet. Dent. **92**(6), 604 (2004)

21.4 S.E. Widmalm, W.J. Williams, D. Djurdjanovic, D.C. McKay: The frequency range of TMJ sounds, J. Oral. Rehabil. **30**(4), 335–346 (2003)

21.5 C. Oster, R.W. Katzberg, R.H. Tallents, T.W. Morris, J. Bartholomew, T.L. Miller, K. Hayakawa: Characterization of temporomandibular joint sounds. A preliminary investigation with arthrographic correlation, Oral Surg. Oral Med. Oral Pathol. **58**(1), 10–16 (1984)

21.6 A. Peylan: Direct auscultation of the joints; Preliminary clinical observations, Rheumatism **9**(4), 77–81 (1953)

21.7 E.P. McCutcheon, R.F. Rushmer: Korotkoff sounds. An experimental critique, Circ. Res. **20**(2), 149–161 (1967)

21.8 J.E. Meisner, R.F. Rushmer: Production of sounds in distensible tubes, Circ. Res. **12**, 651–658 (1963)

21.9 S. Jarcho: The young stethoscopist (H. I. Bowditch, 1846), Am. J. Cardiol. **13**, 808–819 (1964)

21.10 R.F. Rushmer, R.S. Bark, R.M. Ellis: Direct-writing heart-sound recorder (The sonvelograph), Ama. Am. J. Dis. Child **83**(6), 733–739 (1952)

Amazon
EX1010 Page 900

21.11 M.A. Chizner: The diagnosis of heart disease by clinical assessment alone, Curr. Probl. Cardiol. **26**(5), 285–379 (2001)

21.12 M.A. Chizner: The diagnosis of heart disease by clinical assessment alone, Dis. Mon. **48**(1), 7–98 (2002)

21.13 A.E. Aubert, B.G. Denys, F. Meno, P.S. Reddy: Investigation of genesis of gallop sounds in dogs by quantitative phonocardiography and digital frequency analysis, Circulation **71**, 987–993 (1985)

21.14 R.F. Rushmer, C. Morgan: Meaning of murmurs, Am. J. Cardiol. **21**(5), 722–730 (1968)

21.15 J.E. Foreman, K.J. Hutchison: Arterial wall vibration distal to stenoses in isolated arteries, J. Physiol. **205**(2), 30–31 (1969)

21.16 J.E. Foreman, K.J. Hutchison: Arterial wall vibration distal to stenoses in isolated arteries of dog and man, Circ. Res. **26**(5), 583–590 (1970)

21.17 A.M. Khalifa, D.P. Giddens: Characterization and evolution poststenotic flow disturbances, J. Biomech. **14**(5), 279–296 (1981)

21.18 G.W. Duncan, J.O. Gruber, C.F. Dewey, G.S. Myers, R.S. Lees: Evaluation of carotid stenosis by phonoangiography, N. Engl. J. Med. **293**(22), 1124–1128 (1975)

21.19 J.P. Kistler, R.S. Lees, J. Friedman, M. Pressin, J.P. Mohr, G.S. Roberson, R.G. Ojemann: The bruit of carotid stenosis versus radiated basal heart murmurs. Differentiation by phonoangiography, Circulation **57**(5), 975–981 (1978)

21.20 J.P. Kistler, R.S. Lees, A. Miller, R.M. Crowell, G. Roberson: Correlation of spectral phonoangiography and carotid angiography with gross pathology in carotid stenosis, N. Engl. J. Med. **305**(8), 417–419 (1981)

21.21 R. Knox, P. Breslau, D.E. Strandness Jr.: Quantitative carotid phonoangiography, Stroke **12**, 798–803 (1981)

21.22 R.S. Lees: Phonoangiography: qualitative and quantitative, Ann. Biomed. Eng. **12**(1), 55–62 (1984)

21.23 R.S. Lees, C.F. Dewey Jr.: Phonoangiography: a new noninvasive diagnostic method for studying arterial disease, Proc. Natl. Acad. Sci. USA **67**, 935–942 (1970)

21.24 A. Miller, R.S. Lees, J.P. Kistler, W.M. Abbott: Spectral analysis of arterial bruits (phonoangiography): Experimental validation, Circulation **61**(3), 515–520 (1980)

21.25 A. Miller, R.S. Lees, J.P. Kistler, W.M. Abbott: Effects of surrounding tissue on the sound spectrum of arterial bruits in vivo, Stroke **11**(4), 394–398 (1980)

21.26 D. Smith, T. Ishimitsu, E. Craige: Mechanical vibration transmission characteristics of the left ventricle: implications with regard to auscultation and phonocardiography, J. Am. Coll. Cardiol. **4**, 517–521 (1984)

21.27 D. Smith, T. Ishimitsu, E. Craige: Abnormal diastolic mechanical vibration transmission characteristics of the left ventricle, J. Cardiogr. **15**, 507–512 (1985)

21.28 J.P. Murgo: Systolic ejection murmurs in the era of modern cardiology: What do we really know?, J. Am. Coll. Cardiol. **32**, 1596–1602 (1998)

21.29 H. Nygaard, L. Thuesen, J.M. Hasenkam, E.M. Pedersen, P.K. Paulsen: Assessing the severity of aortic valve stenosis by spectral analysis of cardiac murmurs (spectral vibrocardiography). Part I: Technical aspects, J. Heart Valve Dis. **2**, 454–467 (1993)

21.30 Z. Sun, K.K. Poh, L.H. Ling, G.S. Hong, C.H. Chew: Acoustic diagnosis of aortic stenosis, J. Heart Valve Dis. **14**, 186–194 (2005)

21.31 D.J. Doyle, D.M. Mandell, R.M. Richardson: Monitoring hemodialysis vascular access by digital phonoangiography, Ann. Biomed. Eng. **30**(7), 982 (2002)

21.32 C. Clark: Turbulent wall pressure measurements in a model of aortic stenosis, J. Biomech. **10**(8), 461–472 (1977)

21.33 M.B. Rappoport, H.B. Sprague: Physiologic and physical laws that govern auscultation and their clinical application, Am. Heart J. **21**, 257 (1941)

21.34 R. Tidwell, R. Rushmer, R. Polley: The office diagnosis of operable congenital heart lesions, Northwest Med. **52**(7), 546 (1953)

21.35 R. Tidwell, R. Rushmer, R. Polley: The office diagnosis of operable congenital heart lesions, Northwest Med. **52**(8), 635 (1953)

21.36 R. Tidwell, R. Rushmer, R. Polley: The office diagnosis of operable congenital heart lesions; coarctation of the aorta, Northwest Med. **52**(11), 927 (1953)

21.37 F.D. Fielder, P. Pocock: Foetal blood flow detector, Ultrasonics **6**(4), 240–241 (1968)

21.38 W.L. Johnson, H.F. Stegall, J.N. Lein, R.F. Rushmer: Detection of fetal life in early pregnancy with an ultrasonic doppler flowmeter, Obstet. Gynecol. **26**, 305–307 (1965)

21.39 R.F. Rushmer, C.L. Morgan, D.C. Harding: Electronic aids to auscultation, Med. Res. Eng. **7**(4), 28–36 (1968)

21.40 R.F. Rushmer, D.R. Sparkman, R.F. Polley, E.E. Bryan, R.R. Bruce, G.B. Welch, W.C. Bridges: Variability in detection and interpretation of heart murmurs; A comparison of auscultation and stethography, AMA Am. J. Dis. Child **83**(6), 740–754 (1952)

21.41 R.F. Rushmer, R.A. Tidwell, R.M. Ellis: Sonvelographic recording of murmurs during acute myocarditis, Am. Heart J. **48**(6), 835–846 (1954)

21.42 P.N.T. Wells: Review, absorption and dispersion of ultrasound in biological tissue, Ultrasound Med. Biol. **1**, 369–376 (1975)

21.43 M.A. Allison, J. Tiefenbrun, R.D. Langer, C.M. Wright: Atherosclerotic calcification and intimal medial

Amazon
EX1010 Page 901

thickness of the carotid arteries, Int. J. Cardiol. **103**(1), 98–104 (2005)
21.44 J.A. Jensen: FIELD (1997) http://www.es.oersted.dtu.dk/staff/jaj/field/index.html; http://www.es.oersted.dtu.dk/staff/jaj/old_field/
21.45 R.F. Rushmer, D.W. Baker, H.F. Stegall: Transcutaneous doppler flow detection as a nondestructive technique, J. Appl. Physiol. **21**(2), 554–566 (1966)
21.46 D.L. Franklin, W. Schlegel, R.F. Rushmer: Blood flow measured by doppler frequency shift of back-scattered ultrasound, Science **134**, 564–565 (1961)
21.47 H.F. Stegall, R.F. Rushmer, D.W. Baker: A transcutaneous ultrasonic blood-velocity meter, J. Appl. Physiol. **21**(2), 707–711 (1966)
21.48 D.E. Strandness Jr., E.P. McCutcheon, R.F. Rushmer: Application of a transcutaneous doppler flowmeter in evaluation of occlusive arterial disease, Surg. Gynecol. Obstet. **122**(5), 1039–1045 (1966)
21.49 D.E. Strandness Jr., R.D. Schultz, D.S. Sumner, R.F. Rushmer: Ultrasonic flow detection. A useful technic in the evaluation of peripheral vascular disease, Am. J. Surg. **113**(3), 311–320 (1967)
21.50 R.F. Rushmer, D.W. Baker, W.L. Johnson, D.E. Strandness: Clinical applications of a transcutaneous ultrasonic flow detector, JAMA **199**(5), 326–328 (1967)
21.51 C.R. Hill: Medical ultrasonics: an historical review, Br. J. Radiol. **46**(550), 899–905 (1973)
21.52 A.H. Crawford: Ultrasonic medical equipment, Ultrasonics **8**(2), 105–111 (1970)
21.53 B. Buttery, G. Davison: The ghost artifact, J. Ultras. Med. **3**, 49–52 (1984)
21.54 R.M. Ellis, D.L. Franklin, R.F. Rushmer: Left ventricular dimensions recorded by sonocardiometry, Circ. Res. **4**(6), 684–688 (1956)
21.55 R.F. Rushmer: Continuous measurements of left ventricular dimensions in intact, unanesthetized dogs, Circ. Res. **2**(1), 14–21 (1954)
21.56 J.C. Somer: Electronic Sector Scanning fo Ultrasonic Diagnosis, Ultrasonics **6**(3), 153–159 (1968)
21.57 F.E. Barber, D.W. Baker, A.W. Nation, D.E. Strandness Jr., J.M. Reid: Ultrasonic duplex-echo doppler scanner, IEEE Trans. Biomed. Eng. vBME **21**(2), 109–113 (1974)
21.58 D.N. Ku, D.P. Giddens: Pulsatile flow in a model carotid bifurcation, Arteriosclerosis **3**(1), 31–39 (1983)
21.59 T.L. Yearwood, K.B. Chandran: Experimental investigation of steady flow through a model of the human aortic arch, J. Biomech. **13**(12), 1075–1088 (1980)
21.60 T.L. Yearwood, K.B. Chandran: Physiological pulsatile flow experiments in a model of the human aortic arch, J. Biomech. **15**(9), 683–704 (1982)
21.61 D.E. Strandness Jr.: *Duplex Scanning in Vascular Disorders*, 3rd edn. (Lippincott Williams Wilkins, Philadelphia 2002)
21.62 G. Papanicolaou, K.W. Beach, R.E. Zierler, D.E. Strandness Jr.: The relationship between arm-ankle pressure difference and peak systolic velocity in patients with stenotic lower extremity vein grafts, Ann. Vasc. Surg. **9**(6), 554–560 (1995)
21.63 T.R. Kohler, S.C. Nicholls, R.E. Zierler, K.W. Beach, P.J. Schubert, D.E. Strandness Jr.: Assessment of pressure gradient by Doppler ultrasound: experimental and clinical observations, J. Vasc. Surg. **6**(5), 460–469 (1987)
21.64 D.N. White, J.M. Clark, M.N. White: Studies in ultrasonic echoencephalography. 7. General principles of recording information in ultrasonic B- and C-scanning and the effects of scatter, reflection and refraction by cadaver skull on this information, Med. Biol. Eng. **5**(1), 3–14 (1967)
21.65 D.N. White, J.M. Clark, M.N. White: Studies in ultrasonic echoencephalography. 8. The effects on resolution of irregularities in attenuation of an ultrasonic beam traversing cadaver skull, Med. Biol. Eng. **5**(1), 15–23 (1967)
21.66 D.N. White: Ultrasonic encephalography, Acta Radiol. Diagn.(Stockh.) **9**, 671–674 (1969)
21.67 D.N. Ku, D.P. Giddens, D.J. Phillips, D.E. Strandness Jr.: Hemodynamics of the normal human carotid bifurcation: in vitro and in vivo studies, Ultrasound Med. Biol. **11**(1), 13–26 (1985)
21.68 W.M. Blackshear Jr., D.J. Phillips, B.L. Thiele, J.H. Hirsch, P.M. Chikos, M.R. Marinelli, K.J. Ward, D.E. Strandness Jr.: Detection of carotid occlusive disease by ultrasonic imaging and pulsed doppler spectrum analysis, Surgery **86**(5), 698–706 (1979)
21.69 K.A. Comess, F.A. DeRook, M.L. Russell, T.A. Tognazzi-Evans, K.W. Beach: The incidence of pulmonary embolism in unexplained sudden cardiac arrest with pulseless electrical activity, Am. J. Med. **109**(5), 351–356 (2000)
21.70 R.C. Bahler, T. Mohyuddin, R.S. Finkelhor, I.B. Jacobs: Contribution of doppler tissue imaging and myocardial performance index to assessment of left ventricular function in patients with duchenne's muscular dystrophy, J. Am. Soc. Echocardiogr. **18**(6), 666–673 (2005)
21.71 J.K. Campbell, J.M. Clark, C.O. Jenkins, D.N. White: Ultrasonic studies of brain movements, Neurology **20**(4), 418 (1970)
21.72 S. Sikdar, K.W. Beach, S. Vaezy, Y. Kim: Ultrasonic technique for imaging tissue vibrations: preliminary results, Ultrasound Med. Biol. **31**, 221–232 (2005)
21.73 A. Evans, D.N. Walder: Detection of circulating bubbles in the intact mammal, Ultrasonics **8**(4), 216–217 (1970)
21.74 C. Shub, A.J. Tajik, J.B. Seward, D.E. Dines: Detecting intrapulmonary right-to-left shunt with contrast echocardiography. Observations in a pa-

Amazon
EX1010 Page 902

tient with diffuse pulmonary arteriovenous fistulas, Mayo Clin. Proc. **51**(2), 81–84 (1976)
21.75 E. Grube, H. Simon, M. Zywietz, G. Bodem, G. Neumann, A. Schaede: Echocardiographic contrast studies for the delineation of the heart cavities using peripheral venous sodium chloride injections. A contribution to shunt diagnosis, Verh. Dtsch. Ges. Inn. Med. **83**, 366–367 (1977)
21.76 P.W. Serruys, W.B. Vletter, F. Hagemeijer, C.M. Ligtvoet: Bidimensional real-time echocardiological visualization of a ventricular right-to-left shunt following peripheral vein injection, Eur. J. Cardiol. **6**(2), 99–107 (1977)
21.77 D. Danilowicz, I. Kronzon: Use of contrast echocardiography in the diagnosis of partial anomalous pulmonary venous connection, Am. J. Cardiol. **43**(2), 248–252 (1979)
21.78 C. Tei, T. Sakamaki, P.M. Shah, S. Meerbaum, K. Shimoura, S. Kondo, E. Corday: Myocardial contrast echocardiography: a reproducible technique of myocardial opacification for identifying regional perfusion deficits, Circulation **67**(3), 585–593 (1983)
21.79 J.S. Rasor, E.G. Tickner: Microbubble precursors and methods for their production and use. US Patent 4 442 843 (1984)
21.80 J.L. Nelson, B.L. Roeder, J.C. Carinen, F. Roloff, W.G. Pitt: Ultrasonically activated chemotherapeutic drug delivery in a rat model, Cancer Res. **62**, 7280–7283 (2002)
21.81 S.A. Sapareto, W.C. Dewey: Thermal dose determination in cancer therapy, Int. J. Radiat. Oncol. Biol. Phys. **10**, 787–800 (1984)
21.82 M.R. Bailey, L.A. Crum, A.P. Evan, J.A. McAteer, J.C. Williams, O.A. Sapozhinikov, R.O. Cleveland, T. Colonius: *Cavitation in Shock Wave Lithotripsy (Cav03-0s-2-1-006)* (Fifth Int. Symp. Cavitation (CAV2003), Osaka 2003), http://cav2003.me.es.osaka-u.ac.jp/Cav2003/Papers/Cav03-OS-2-1-006.pdf
21.83 E.A. Noser, H.M. Shaltoni, C.E. Hall, A.V. Alexandrov, Z. Garami, E.D. Cacayorin, J.K. Song, J.C. Grotta, M.S. Campbell: Aggressive mechanical clot disruption. A safe adjunct to thrombolytic therapy in acute stroke?, Stroke **36**(2), 292–296 (2005)
21.84 S. Pfaffenberger, B. Devcic-Kuhar, C. Kollmann, S.P. Kastl, C. Kaun, W.S. Speidl, T.W. Weiss, S. Demyanets, R. Ullrich, H. Sochor, C. Wober, J. Zeitlhofer, K. Huber, M. Groschl, E. Benes, G. Maurer, J. Wojta, M. Gottsauner-Wolf: Can a commercial diagnostic ultrasound device accelerate thrombolysis? An in vitro skull model, Stroke **36**(1), 124–128 (2005)
21.85 S. Schafer, S. Kliner, L. Klinghammer, H. Kaarmann, I. Lucic, U. Nixdorff, U. Rosenschein, W.G. Daniel, F.A. Flachskampf: Influence of ultrasound operating parameters on ultrasound-induced thrombolysis in vitro, Ultrasound Med. Biol. **31**(6), 841–847 (2005)
21.86 D.S. Jeon, H. Luo, M.C. Fishbein, T. Miyamoto, M. Horzewski, T. Iwami, J.M. Mirocha, F. Ikeno, Y. Honda, R.J. Siegel: Noninvasive transcutaneous ultrasound augments thrombolysis in the left circumflex coronary artery – An in vivo canine study, Thromb. Res. **110**(2–3), 149–158 (2003)
21.87 A.V. Alexandrov, C.A. Molina, J.C. Grotta, Z. Garami, S.R. Ford, J. Alvarez-Sabin, J. Montaner, M. Saqqur, A.M. Demchuk, L.A. Moye, M.D. Hill, A.W. Wojner, CLOTBUST Investigators: Ultrasound-enhanced systemic thrombolysis for acute ischemic stroke, N. Engl. J. Med. **351**(21), 2170–2178 (2004)
21.88 J. Eggers, G. Seidel, B. Koch, I.R. Konig: Sonothrombolysis in acute ischemic stroke for patients ineligible for rt-PA, Neurology **64**(6), 1052–1054 (2005)
21.89 D. Harpaz: Ultrasound enhancement of thrombolytic therapy: observations and mechanisms, Int. J. Cardiovasc. Intervent. **3**(2), 81–89 (2000)
21.90 S.H. Eik-Nes, O. Okland, J.C. Aure, M. Ulstein: Ultrasound screening in pregnancy: A randomised controlled trial, Lancet **1**(8390), 1347 (1984)
21.91 FDA, U.S. Food and Drug Administration: *Information for Manufacturers Seeking Marketing Clearance of Diagnostic Ultrasound Systems and Transducers* (Center for Devices and Radiological Health U.S. Food and Drug Administration, Rockville 1997)
21.92 FDA: *510(k) Guide for Measuring and Reporting Output of Diagnostic Ultrasound Medical Devices* (Center for Devices and Radiological Health, U.S. Food and Drug Administration, Rockville 1991)
21.93 AIUM/NEMA: *Standard for Real-Time Display of Thermal and Mechanical Acoustic Output Indices on Diagnostic Ultrasound Equipment* (Am. Inst. Ultrasound Medicine, Laurel 1992)
21.94 M. Fatemi, P.L. Ogburn, J.F. Greenleaf: Fetal stimulation by pulsed diagnostic ultrasound, J. Ultrasound Med. **20**, 883–889 (2001)
21.95 M.A. Dinno, M. Dyson, S.R. Young, A.J. Mortimer, J. Hart, L.A. Crum: The significance of membrane changes in the safe and effective use of therapeutic and diagnostic ultrasound, Phys. Med. Biol. **34**(11), 1543–1552 (1989)

Amazon
EX1010 Page 903

Part G Structural Acoustics and Noise

22 Structural Acoustics and Vibrations
Antoine Chaigne, Palaiseau, France

23 Noise
George C. Maling, Jr., Harpswell, USA

Amazon
EX1010 Page 904

22. Structural Acoustics and Vibrations

This chapter is devoted to vibrations of structures and to their coupling with the acoustic field. Depending on the context, the radiated sound can be judged as desirable, as is mostly the case for musical instruments, or undesirable, like noise generated by machinery. In architectural acoustics, one main goal is to limit the transmission of sound through walls. In the automobile industry, the engineers have to control the noise generated inside and outside the passenger compartment. This can be achieved by means of passive or active damping. In general, there is a strong need for quieter products and better sound quality generated by the structures in our daily environment.

Structural acoustics and vibration is an interdisciplinary area, with many different potential applications. Depending on the specific problem under investigation, one has to deal with material properties, structural modifications, signal processing and measurements, active control, modal analysis, identification and localization of sources or nonlinear vibrations, among other hot topics.

In this chapter, the fundamental methods for the analysis of vibrations and sound radiation of structures are presented. It mainly focuses on general physical concepts rather than on specific applications such as those encountered in ships, planes, automobiles or buildings. The fluid–structure coupling is restricted to the case of light compressible fluids (such as air). Practical examples are given at the end of each section.

After a brief presentation of the properties of the basic linear single-degree-of-freedom oscillator, the linear vibrations of strings, beams, membranes, plates and shells are reviewed. Then, the structural–acoustic coupling of some elementary systems is presented, followed by a presentation of the main dissipation mechanisms in structures. The last section is devoted to nonlinear vibrations. In conclusion, a brief overview of some advanced topics in structural acoustics and vibrations is given.

22.1 **Dynamics of the Linear Single-Degree-of-Freedom (1-DOF) Oscillator** 903
22.1.1 General Solution 903
22.1.2 Free Vibrations 903
22.1.3 Impulse Response and Green's Function 904
22.1.4 Harmonic Excitation 904
22.1.5 Energetic Approach 905
22.1.6 Mechanical Power 905
22.1.7 Single-DOF Structural–Acoustic System 906
22.1.8 Application: Accelerometer 907

22.2 **Discrete Systems** 907
22.2.1 Lagrange Equations 907
22.2.2 Eigenmodes and Eigenfrequencies 909
22.2.3 Admittances 909
22.2.4 Example:2-DOF Plate–Cavity Coupling 911
22.2.5 Statistical Energy Analysis 912

22.3 **Strings and Membranes** 913
22.3.1 Equations of Motion 913
22.3.2 Heterogeneous String. Modal Approach 914
22.3.3 Ideal String 916
22.3.4 Circular Membrane in Vacuo 919

22.4 **Bars, Plates and Shells** 920
22.4.1 Longitudinal Vibrations of Bars ... 920
22.4.2 Flexural Vibrations of Beams 920
22.4.3 Flexural Vibrations of Thin Plates 923
22.4.4 Vibrations of Thin Shallow Spherical Shells 925
22.4.5 Combinations of Elementary Structures 926

22.5 **Structural–Acoustic Coupling** 926
22.5.1 Longitudinally Vibrating Bar Coupled to an External Fluid 927
22.5.2 Energetic Approach to Structural–Acoustic Systems 932
22.5.3 Oscillator Coupled to a Tube of Finite Length 934
22.5.4 Two-Dimensional Elasto–Acoustic Coupling 936

Amazon
EX1010 Page 905

22.6 **Damping** 940
22.6.1 Modal Projection in Damped Systems 940
22.6.2 Damping Mechanisms in Plates ... 943
22.6.3 Friction 945
22.6.4 Hysteretic Damping 947
22.7 **Nonlinear Vibrations** 947
22.7.1 Example of a Nonlinear Oscillator 947
22.7.2 Duffing Equation 949
22.7.3 Coupled Nonlinear Oscillators 951
22.7.4 Nonlinear Vibrations of Strings ... 955
22.7.5 Review of Nonlinear Equations for Other Continuous Systems 956
22.8 **Conclusion. Advanced Topics** 957
References 958

In this chapter, the fundamental methods for the analysis of vibrations and sound radiation of structures are presented. It mainly focuses on general physical concepts rather than on specific applications such as those encountered in ships, planes, automobiles or buildings. The fluid–structure coupling is restricted to the case of light compressible fluid (such as air). The case of strong coupling with heavy fluid (water) is not treated.

If the magnitude of the vibratory and acoustical quantities of interest can be considered as sufficiently small, then the equations that govern the structural–acoustics phenomena can be linearized. The linear theory of vibrations applied to simple continuous elastic structures, such as bars, membranes, shells and plates, forms a reference framework for numerous studies involving more-complex geometries. In some practical situations, it is not necessary to know the exact vibratory shape at each point of a given system: to take advantage of this, a continuous structure can often be represented as a discrete system built with rigid masses connected to springs and dampers. The main results of the linear theory for the vibration of discrete and continuous systems are presented in Sects. 22.1–22.4. Section 22.1 is devoted to the linear single-degree-of-freedom (DOF) oscillator for which the fundamental results are derived with the help of the Laplace transform. In Sect. 22.2, the case of discrete systems with multiple DOFs is used to introduce the concepts of eigenmodes, eigenfrequencies, the admittance and modal analysis. As an illustration, one example of coupled oscillators is solved in detail. Also the fundamental energy equation of statistical energy analysis (SEA) that governs the mean power flow between coupled oscillators is summarized. Section 22.3 deals with the transverse vibrations of strings and membranes, which can be viewed as limiting cases of prestressed structures with negligible stiffness. In Sect. 22.4, longitudinal and transverse vibrations of bars are presented. The case of flexural vibrations is extended to two-dimensional (2-D) structures such as plates and shallow shells. In this latter case, the influence of curvature is emphasized using the example of a spherical cap for which analytical results can be obtained.

The three remaining sections focus on specific problems of great significance in structural acoustics. The case of vibroacoustic coupling is treated in Sect. 22.5 through examples of increasing complexity. Starting from the simple case of a longitudinally vibrating bar coupled to a semi-infinite tube, it is shown that modes of the structure are coupled to the radiated field, and that eigenfrequencies and modal shapes of the in vacuo structure are modified by this coupling. An energetic approach to the structural–acoustic coupling allows the introduction of radiation filters and radiation efficiencies. A state-space formulation of the phenomena is presented, which is of particular interest for the control of radiated sound. The example of a single-DOF oscillator coupled to a tube illustrates the coupling between a structure and a cavity. Finally, attention is paid to fluid–plate coupling, with the introduction of the concept of the critical frequency. Section 22.6 is devoted to the presentation of important causes of damping in structures. Also some indications are given with regard to the validity of the modal approach for damped discrete and continuous systems.

For structures subjected to motion with large amplitude, most of the concepts and methods developed for linear vibrations no longer apply. Specific methods must be used to account for the observed phenomena of distortion, amplitude-dependent resonance, jump, hysteresis, instability and chaos. Section 22.7 introduces the basic concepts of nonlinear vibrations with some examples. The Duffing equation and the example of two nonlinearly coupled oscillators are analyzed in detail. These examples illustrate the use of perturbation methods for solving nonlinear equations of motion for vibrating systems. Finally, some equations for the vibrations of nonlinear continuous systems (strings, beams, shells and plates) are briefly reviewed.

Amazon
EX1010 Page 906

22.1 Dynamics of the Linear Single-Degree-of-Freedom (1-DOF) Oscillator

In the low-frequency range, the linear motion of an electrodynamical loudspeaker, for example, can be described by a single-degree-of-freedom oscillator. This is also the case for any complex structure considered as a rigid body for which the equivalent stiffness is represented by a unique spring, and where all the dissipation mechanisms are approximated by a unique dashpot or *fluid damping* constant; one can think of the rigid-body mode of vibration of an automobile. Also the 1-DOF oscillator has fundamental mathematical properties of great interest in the field of vibrations, since linear vibrations of discrete and continuous structures can be represented by a set of oscillators, as will be shown in the following sections.

The motion of a standard 1-DOF oscillator is governed by a second-order differential equation involving an excitation force $F(t)$ and the response of the structure. Using a formulation with the velocity $v(t)$, we get

$$F = M\frac{\mathrm{d}v}{\mathrm{d}t} + Rv + K\int v\,\mathrm{d}t\,. \tag{22.1}$$

This equation accounts for the motion of a mass M subjected to a restoring force due to a linear spring of stiffness K and a dashpot R which represents a linear viscous fluid damping (Fig. 22.1).

Equation (22.1) can be written alternatively, using the mass displacement $\xi(t)$ and the usual reduced parameters:

$$F = M\left(\frac{\mathrm{d}^2\xi}{\mathrm{d}t^2} + 2\zeta_0\omega_0\frac{\mathrm{d}\xi}{\mathrm{d}t} + \omega_0^2\xi\right)\,, \tag{22.2}$$

where $\omega_0 = \sqrt{M/K}$ is the eigenfrequency of the lossless system and $\zeta_0 = R/2M\omega_0$ is the nondimensional damping coefficient.

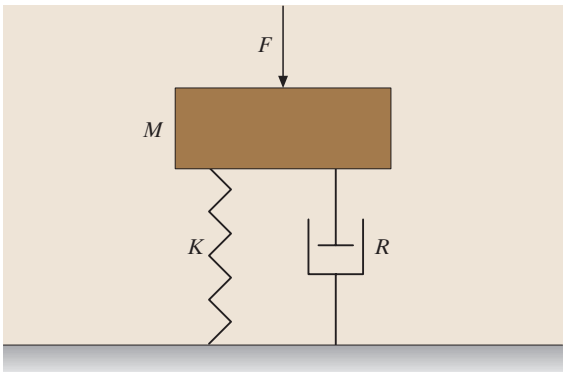


Fig. 22.1 Single-DOF oscillator

22.1.1 General Solution

One strategy for solving a linear equation such as (22.2) is to make use of the Laplace transform [22.1]. Using this transform, (22.2) becomes

$$s^2\mathcal{X}(s) - s\xi(0) - \dot{\xi}(0) + 2\zeta_0\omega_0\left[s\mathcal{X}(s) - \xi(0)\right] + \omega_0^2\mathcal{X}(s) = \frac{\mathcal{F}(s)}{M}\,, \tag{22.3}$$

where $\mathcal{X}(s)$ and $\mathcal{F}(s)$ are the Laplace transforms of $\xi(t)$ and $F(t)$, respectively. Using the tables and properties of the Laplace transforms, we obtain the general solution

$$\xi(t) = \frac{1}{M}\int_0^t F(\theta)G(t-\theta)\,\mathrm{d}\theta + \left[2\zeta_0\omega_0\xi(0) + \dot{\xi}(0)\right]G(t) + \xi(0)\dot{G}(t)\,, \tag{22.4}$$

where $G(t)$ can take different forms, depending on the value of the damping coefficient ζ_0:

- if $\zeta_0 < 1$, which corresponds to the so-called *underdamped* case, then

$$G(t) = \mathrm{e}^{-\zeta_0\omega_0 t}\frac{\sin\omega_0\sqrt{1-\zeta_0^2}\,t}{\omega_0\sqrt{1-\zeta_0^2}}\,; \tag{22.5}$$

- if $\zeta_0 = 1$, which corresponds to the *critical* case, we obtain

$$G(t) = t\,\mathrm{e}^{-\omega_0 t}\,; \tag{22.6}$$

- finally, if $\zeta_0 > 1$, which corresponds to the *overdamped* case, we get

$$G(t) = \mathrm{e}^{-\zeta_0\omega_0 t}\frac{\sinh\omega_0\sqrt{\zeta_0^2-1}\,t}{\omega_0\sqrt{\zeta_0^2-1}}\,. \tag{22.7}$$

22.1.2 Free Vibrations

Free vibrations are characterized by the absence of an external force. With $F(t) = 0$ in (22.4), we get

$$\xi(t) = \left[2\zeta_0\omega_0\xi(0) + \dot{\xi}(0)\right]G(t) + \xi(0)\dot{G}(t)\,, \tag{22.8}$$

Amazon
EX1010 Page 907

- if $\zeta_0 < 1$, the displacement $\xi(t)$ is given by

$$\xi(t) = \mathrm{e}^{-\zeta_0\omega_0 t}\left\{\xi(0)\cos\omega_0\sqrt{1-\zeta_0^2}\,t + \left[\xi(0)\frac{\zeta_0}{\sqrt{1-\zeta_0^2}} + \dot{\xi}(0)\frac{1}{\omega_0\sqrt{1-\zeta_0^2}}\right] \times \sin\omega_0\sqrt{1-\zeta_0^2}\,t\right\} . \tag{22.9}$$

  In this case, the free regime is characterized by a damped sinusoid with oscillation frequency $\omega_0\sqrt{1-\zeta_0^2}$ and decay time $\tau = 1/\zeta_0\omega_0$. The total energy of the system decreases with time.
- if $\zeta_0 = 1$, we obtain

$$\xi(t) = \mathrm{e}^{-\omega_0 t}\left[\xi(0)(1+\omega_0 t) + \dot{\xi}(0)t\right] . \tag{22.10}$$

  The motion exhibits no oscillation. This critical case corresponds to the situation where we get the fastest non-oscillatory motion toward equilibrium;
- if $\zeta_0 > 1$ the displacement $\xi(t)$ becomes

$$\xi(t) = \mathrm{e}^{-\zeta_0\omega_0 t}\left\{\xi(0)\cosh\omega_0\sqrt{\zeta_0^2-1}t + \left[\xi(0)\frac{\zeta_0}{\sqrt{\zeta_0^2-1}} + \dot{\xi}(0)\frac{1}{\omega_0\sqrt{\zeta_0^2-1}}\right] \times \sinh\omega_0\sqrt{\zeta_0^2-1}\,t\right\} . \tag{22.11}$$

  Here again, no oscillation exists. The decay is governed by the combination of two exponentials with decay time τ such that $1/\tau = \omega_0\left(\zeta_0 \pm \sqrt{\zeta_0^2-1}\right)$.

22.1.3 Impulse Response and Green's Function

Consider now the case where $\xi(0) = \dot{\xi}(0) = 0$ and where $F(t)$ is the Dirac delta function $\delta(t)$ whose fundamental property is

$$\int_{-\infty}^{\infty} u(t)\delta(t-a)\,\mathrm{d}t = u(a) , \tag{22.12}$$

where $u(t)$ is a test function. The response $\xi(t)$ can therefore be written as

$$\xi(t) = \frac{1}{M}\int_0^t \delta(\theta)G(t-\theta)\,\mathrm{d}\theta = \frac{1}{M}\int_0^t \delta(t-\theta)G(\theta)\,\mathrm{d}\theta = \frac{G(t)}{M} . \tag{22.13}$$

The function $G(t)$ defined in Sect. 22.1.1 can therefore be defined as the impulse response of the oscillator with mass equal to unity. This function is also referred to as the *Green's function* of the oscillator. For an oscillator initially at rest and excited by an arbitrary time function $F(t)$, the response is given by the convolution integral of $F(t)$ and the Green's function $G(t)$. Equation (22.4) shows, in addition, that for $F(t) = 0$ and $\xi(0) = 0$, the displacement is given by

$$\xi(t) = \dot{\xi}(0)G(t) . \tag{22.14}$$

Therefore, we can see that the solution obtained with a Dirac delta force is proportional to the one obtained with an initial velocity $\dot{\xi}(0)$.

22.1.4 Harmonic Excitation

For harmonic excitation, $F(t) = F_\mathrm{M}\sin\Omega t$, of the oscillator in the underdamped case, (22.4) gives

$$\xi(t) = \frac{F_\mathrm{M}}{M}\frac{\left(\omega_0^2-\Omega^2\right)\sin\Omega t - 2\zeta_0\omega_0\Omega\cos\Omega t}{\left(\omega_0^2-\Omega^2\right)^2 + \left(2\zeta_0\omega_0\Omega\right)^2} + \alpha G(t) + \beta\dot{G}(t) , \tag{22.15}$$

where α and β are constants that depend on the initial conditions. The Green's function $G(t)$ and its time derivative are proportional to $\mathrm{e}^{-\zeta_0\omega_0 t}$ and become negligible for $\zeta_0\omega_0 t \gg 1$. With this assumption, the response to the forcing term at frequency Ω is given by the first term on the right-hand side of (22.15). This term can be written alternatively as

$$\xi(t) = A(\Omega)\sin\left[\Omega t - \Phi(\Omega)\right] \tag{22.16}$$

with

$$A(\Omega) = \frac{F_\mathrm{M}}{M}\frac{1}{\sqrt{\left(\omega_0^2-\Omega^2\right)^2 + (2\zeta_0\omega_0\Omega)^2}}$$

Amazon
EX1010 Page 908

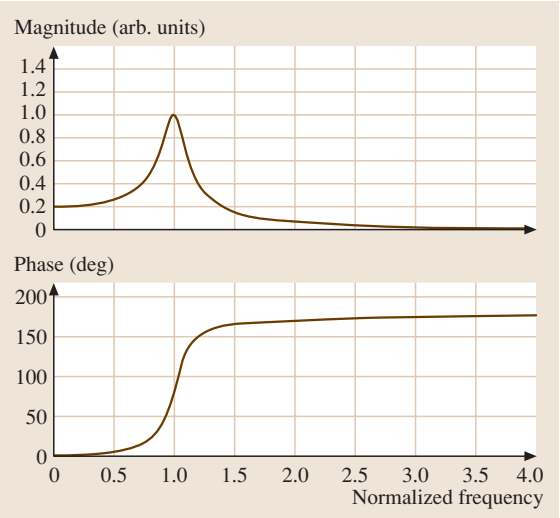


Fig. 22.2 Magnitude and phase of the mass displacement for the forced underdamped oscillator as a function of the normalized frequency Ω/ω_0

and

$$\tan \Phi(\Omega) = \frac{2\zeta_0\omega_0\Omega}{\omega_0^2 - \Omega^2} \,. \tag{22.17}$$

Figure 22.2 shows the variations of A and Φ with Ω in the underdamped case. The amplitude A reaches its maximum for frequency $\Omega = \omega_0\sqrt{1-2\zeta_0^2}$, which is very close to ω_0 for $\zeta_0 \ll 1$. The maximum is equal to $F_M/2M\zeta_0\omega_0\Omega$.

22.1.5 Energetic Approach

The instantaneous mechanical power $p_m(t)$ into the system is given by the scalar product of F and v, which yields

$$p_m = \frac{d}{dt}\left(\frac{1}{2}Mv^2 + \frac{1}{2}K\xi^2\right) + Rv^2 \,. \tag{22.18}$$

The terms on the right-hand side of (22.18) represent the kinetic energy of the mass M, the elastic energy of the spring K and the energy dissipated in the mechanical resistance R, respectively. In a number of applications, we are mostly interested in the time-averaged value of $p_m(t)$ rather than in details of its time evolution. In audio acoustics, for example, the human ear is sensitive to the sound level, which is correlated to the average value of the instantaneous acoustic power, after integration over a duration of nearly 50 ms. Therefore, after defining an integration duration T, whose appropriate selection is discussed later in this section, we can define the average mechanical power $\mathcal{P}_m(T)$ as

$$\begin{aligned}\mathcal{P}_m(T) &= \frac{1}{2T}\left[Mv^2(T) + K\xi^2(T) - Mv^2(0) - K\xi^2(0)\right] \\ &\quad + \frac{1}{T}\int_0^T Rv^2(t)\,dt \,.\end{aligned} \tag{22.19}$$

In a conservative system, the sum of the kinetic and elastic energy remains constant over time, so that the term between the square brackets in (22.19) is equal to zero. As a consequence, the average input power becomes:

$$\mathcal{P}_m(T) = \frac{1}{T}\int_0^T Rv^2(t)\,dt = \mathcal{P}_s(T) \,, \tag{22.20}$$

where $\mathcal{P}_s(T)$ represents the mean *structural* power dissipated in the mechanical resistance R.

22.1.6 Mechanical Power

A particular case of importance is the steady-state harmonic motion of the mechanical oscillator with angular frequency ω. Given an excitation force $F(t) = F_M \sin \omega t$, then, due to the assumed linearity of the system, the mass velocity is written $v(t) = V_M \sin(\omega t + \phi)$. Therefore, $\mathcal{P}_m(T)$ is given by

$$\mathcal{P}_m(T) = \frac{1}{T}\int_0^T F_M V_M \sin \omega t \sin(\omega t + \phi)\,dt \,. \tag{22.21}$$

Denoting the period of motion by $\tau = 2\pi/\omega$, we can write $T = n\tau + \tau_0$, where n is a positive integer. In this case, the mean power can be rewritten

$$\begin{aligned}\mathcal{P}_m(T) &= \frac{1}{2}F_M V_M \cos\phi + \frac{F_M V_M}{4(2\pi n + \tau_0\omega)} \\ &\quad \times [\sin\phi - \sin(2\omega\tau_0 + \phi)] \,.\end{aligned} \tag{22.22}$$

Comment. This equation (22.22) shows that the mean (or average) power $\mathcal{P}_m(T)$ is nearly equal to $1/2F_M V_M \cos\phi$ only if the average duration T contains a sufficiently large number n of periods. If T is equal to $n\tau$, then the previous result is strict. In what follows, it will be assumed that this condition is fulfilled, so that the dependence versus integration time T of the mean power terms will be suppressed. For a given force, the

Amazon
EX1010 Page 909

velocity amplitude V_M and phase angle ϕ are given by

$$V_M = \frac{F_M}{M} \frac{\omega}{\sqrt{\left(\omega^2 - \omega_0^2\right)^2 + 4\zeta_0^2\omega^2\omega_0^2}} , \quad (22.23)$$

$$\cos\phi = \frac{2\zeta_0\omega_0\omega}{\sqrt{\left(\omega^2 - \omega_0^2\right)^2 + 4\zeta_0^2\omega^2\omega_0^2}} , \quad (22.24)$$

and the mean power becomes:

$$\mathcal{P}_m = \frac{F_M^2}{2R} \frac{4\zeta_0^2\omega_0^2\omega^2}{\left(\omega^2 - \omega_0^2\right)^2 + 4\zeta_0^2\omega^2\omega_0^2} . \quad (22.25)$$

Equation (22.25) shows that the maximum of the dissipated power, and thus the maximum of the input power, is obtained for $\omega = \omega_0$, i. e. when the excitation frequency is equal to the eigenfrequency of the oscillator. In this case, we obtain:

$$\mathrm{Max}\left(\mathcal{P}_m\right) = \frac{F_M^2}{2R} . \quad (22.26)$$

Since F_M is known, in general, (22.26) can be used for estimating the mechanical resistance R.

Remark. Recall that (22.25) is only valid in the dynamic equilibrium, which does not correspond to many experimental (or numerical) situations where, for obvious causality reasons, the force is applied at a given instant of time, usually taken as origin. In this more realistic case, the force signal should be written as $F(t) = F_M H(t) \sin\omega t$, where $H(t)$ is the Heaviside function. In this case, the Laplace transform of the velocity is

$$V(s) = \frac{F_M}{M} \frac{s\omega}{\left(s^2 + \omega^2\right)\left(s^2 + 2\zeta_0\omega_0 s + \omega_0^2\right)} . \quad (22.27)$$

From which the velocity is derived

$$v(t) = \frac{F_M\omega}{M\sqrt{D(\omega)}} + A(\omega)\exp(-\zeta_0\omega_0 t)\times \sin\left[\omega_0\sqrt{1-\zeta_0^2}\, t + \psi(\omega)\right] , \quad (22.28)$$

where $D(\omega) = \left(\omega^2 - \omega_0^2\right)^2 + 4\zeta_0^2\omega^2\omega_0^2$. $A(\omega)$ and $\psi(\omega)$ are also functions of the excitation frequency whose exact expressions do not add significant matter to the present discussion. The first term in the expression of $v(t)$ corresponds to the steady-state regime. The important features of the second term are the following:

- It is non-negligible as long as the time is small compared to the decay time $(\zeta_0\omega_0)^{-1}$. For lightly damped structural modes, the decay time can be of the order of 0.1 ms or more. The second term cannot then be neglected during the first 0.5–1.0 s of the sound, if one wants to estimate the mean sound power correctly.
- When multiplying $v(t)$ by $F(t)$ and integrating over time, terms with frequencies $\omega + \omega_0\sqrt{1-\zeta_0^2}$ and $\left|\omega - \omega_0\sqrt{1-\zeta_0^2}\right|$ appear in the expression of $\mathcal{P}_m$. As a consequence, the mean power fluctuates at low frequency, which is another cause of difficulty for estimating its value properly.

22.1.7 Single-DOF Structural–Acoustic System

We now investigate the simple example of a mechanical oscillator acting as a piston at one end of an air-filled semi-infinite tube presenting an additional acoustical resistance $R_a = \rho c S$. The oscillator motion is now governed by the equation

$$F = M\frac{\mathrm{d}v}{\mathrm{d}t} + Rv + \int v\,\mathrm{d}t + R_a v . \quad (22.29)$$

The instantaneous input power is given by

$$p_m(t) = \frac{\mathrm{d}}{\mathrm{d}t}\left(\frac{1}{2}Mv^2 + \frac{1}{2}K\xi^2\right) + (R + R_a)v^2 . \quad (22.30)$$

The average input power becomes

$$\mathcal{P}_m(T) = \frac{1}{T}\int_0^T Rv^2(t)\,\mathrm{d}t + \frac{1}{T}\int_0^T R_a v^2(t)\,\mathrm{d}t = \mathcal{P}_s(T) + \mathcal{P}_a(T) , \quad (22.31)$$

where $\mathcal{P}_a(T)$ is the acoustic mean power radiated in the tube. The acoustical efficiency of the system is given by .

$$\eta = \frac{\mathcal{P}_a(T)}{\mathcal{P}_m(T)} = \frac{\mathcal{P}_a(T)}{\mathcal{P}_s(T) + \mathcal{P}_a(T)} = \frac{R_a}{R + R_a} \quad (22.32)$$

Some remarks can be formulated with regards to (22.32).

- The expression for the acoustical efficiency is independent of the integration time T.
- Though (22.32) appears simple in form, the experimental (or numerical) determination of the efficiency is generally not straightforward. R can be estimated through calculation of the mechanical power in vacuo $\mathcal{P}_{mo}(T)$.
- In the simple example discussed here, the acoustical resistance, and hence the acoustic power, is known.

Amazon
EX1010 Page 910

This does not include the case where the acoustic power is not known, and has to be estimated by measurements of the acoustic intensity in the fluid, for example.

Link Between Sound Power and Free-Vibration Decay Times

For a single-DOF system, an alternative method for estimating the sound power consists of estimating the decay times of free vibrations through experiments or numerical calculations. Let us take the example of the previously described oscillator loaded by the semi-infinite tube. We consider the case $F(t) = 0$, with the mass initially moved from equilibrium by a quantity $\xi(0) = \xi_0$ and released with zero velocity at $t = 0$. The equation of motion is written as

$$\frac{\mathrm{d}^2\xi}{\mathrm{d}t^2} + 2\zeta\omega_0\frac{\mathrm{d}\xi}{\mathrm{d}t} + \omega_0^2\xi = 0 \qquad (22.33)$$

with

$$\zeta = \frac{R + R_\mathrm{a}}{2M\omega_0} .$$

The Laplace transform of the displacement is given by

$$\xi(s) = \xi_0\frac{s + 2\zeta\omega_0}{s^2 + 2\zeta\omega_0 s + \omega_0^2} \qquad (22.34)$$

from which the time evolution of the mass displacement is obtained (assuming $\zeta < 1$)

$$\xi(t) = \exp(-\zeta\omega_0 t)\left[\cos\left(\omega_0\sqrt{1-\zeta^2}t\right) + \frac{\zeta}{\sqrt{1-\zeta^2}}\sin\left(\omega_0\sqrt{1-\zeta^2}t\right)\right] . \qquad (22.35)$$

Equation (22.35) shows that the *decay factor* α (equal to the inverse of the decay time) is equal to $\zeta\omega_0 = (R + R_\mathrm{a})/2M$. The same mathematical derivations applied to the oscillator in vacuo yields $\alpha_0 = \zeta_0\omega_0 = R/2M$. In conclusion, this shows that, for the 1-DOF system studied here, the acoustical efficiency can be estimated in the time domain by the expression

$$\eta = \frac{\alpha - \alpha_0}{\alpha} . \qquad (22.36)$$

22.1.8 Application: Accelerometer

Accelerometers are piezoelectric transducers which are widely used for vibration measurements. An accelerometer has a base, a piezoelectric crystal and a seismic mass (Fig. 22.3). It delivers an electric signal which is proportional to the compression force applied to the crystal. Such a device can be modeled by a 1-DOF oscillator equation. Let us denote by k the equivalent stiffness of the crystal, by m the seismic mass, and by $\omega_0 = \sqrt{k/m}$ the resonance frequency of the accelerometer. Internal damping is neglected here, for simplicity. For a sinusoidal excitation $A\sin\Omega t$ of the base, the compression force is [22.2]:

$$F \simeq -\frac{k\Omega^2}{\omega_0^2 - \Omega^2} A\sin\Omega t . \qquad (22.37)$$

Therefore, we can see that if $\Omega \ll \omega_0$, then the signal delivered by the accelerometer is proportional to the acceleration of the base. The frequency response curve of an accelerometer is flat below its resonance frequency, which gives the upper limit of its valid frequency range.

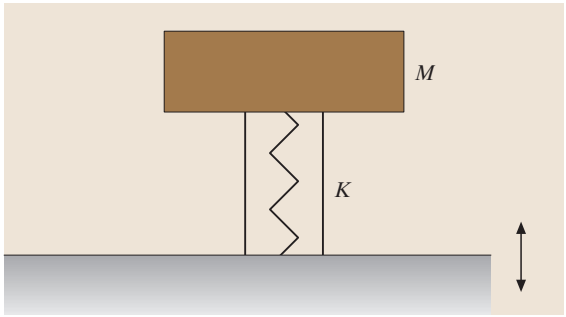


Fig. 22.3 Accelerometer

22.2 Discrete Systems

In a number of applications, real structures can be approximated by an assembly of discrete rigid substructures, which leads to enormous computational simplifications. In fact numerical modeling (finite elements, finite differences) is such an example where continuous structures are replaced by an equivalent set of discretely connected elements. In experimental techniques, such as modal analysis, measurements are taken at discrete positions on the structure under study, and thus the measurements are treated by methods applicable to discrete systems.

Amazon
EX1010 Page 911

22.2.1 Lagrange Equations

For a discrete system with n degrees of freedom, the kinetic energy E_k can be formulated as a function of the generalized coordinates q_n and velocities $\dot{q}_n$

$$E_\mathrm{k} = E_\mathrm{k}(q_1, q_2, \ldots, q_n, \dot{q}_1, \dot{q}_2, \ldots \dot{q}_n) = E_\mathrm{k}(q, \dot{q}) \tag{22.38}$$

Thus, given virtual vectors of displacements δq and velocities $\delta\dot{q}$, the variation of the kinetic energy is written

$$\delta E_\mathrm{k} = \sum_{k=1}^{n} \frac{\partial E_\mathrm{k}}{\partial q_k}\delta q_k + \frac{\partial E_\mathrm{k}}{\partial \dot{q}_k}\delta\dot{q}_k \,. \tag{22.39}$$

Remark. Recall that δq has to be kinematically compatible with the system, though not necessarily equal to a real displacement, so that the partial derivatives of T versus δq and $\delta\dot{q}$ are independent.

Applying Hamilton's principle, with $\delta q = 0$ at t_1 and t_2, we can write the minimization integral as

$$\int_{t_1}^{t_2} \left(\delta E_\mathrm{k} - \delta V + \delta W_\mathrm{nc}\right) \mathrm{d}t = 0 \tag{22.40}$$

where V is the potential energy of the system and W_nc is the energy of the nonconservative applied external forces. Through integration by parts, we can write

$$\begin{aligned}
&\int_{t_1}^{t_2} \frac{\partial E_\mathrm{k}}{\partial \dot{q}_k}\delta\dot{q}_k \,\mathrm{d}t \\
&= \left[\frac{\partial E_\mathrm{k}}{\partial \dot{q}_k}\delta q_k\right]_{t_1}^{t_2} - \int_{t_1}^{t_2} \frac{\mathrm{d}}{\mathrm{d}t}\left(\frac{\partial T}{\partial \dot{q}_k}\right)\delta q_k \,\mathrm{d}t \\
&= -\int_{t_1}^{t_2} \frac{\mathrm{d}}{\mathrm{d}t}\left(\frac{\partial E_\mathrm{k}}{\partial \dot{q}_k}\right)\delta q_k \,\mathrm{d}t \,.
\end{aligned} \tag{22.41}$$

Assuming that $V = V(q)$, which corresponds to a large class of problems in dynamics and vibrations,

$$\delta V = \sum_{k=1}^{n} \frac{\partial V}{\partial q_k}\delta q_k \,. \tag{22.42}$$

Finally, the virtual work δW_nc can be written as the scalar product of the vectors F of generalized forces and virtual displacement δq in the form $\delta W_\mathrm{nc} = \sum_{k=1}^{n} F_k \delta q_k$, so that (22.40) becomes

$$\sum_{k=1}^{n} \int_{t_1}^{t_2} \left[\frac{\partial E_\mathrm{k}}{\partial q_k} - \frac{\mathrm{d}}{\mathrm{d}t}\left(\frac{\partial E_\mathrm{k}}{\partial \dot{q}_k}\right) - \frac{\partial V}{\partial q_k} + F_k\right]\delta q_k \,\mathrm{d}t = 0 \,. \tag{22.43}$$

Since the integral in (22.43) must be equal to zero for any δq this implies, for each k

$$\frac{\mathrm{d}}{\mathrm{d}t}\left(\frac{\partial E_\mathrm{k}}{\partial \dot{q}_k}\right) - \frac{\partial E_\mathrm{k}}{\partial q_k} + \frac{\partial V}{\partial q_k} = F_k \,. \tag{22.44}$$

The set of n differential equations (22.44) are the Lagrange equations of the discrete system. This set yields the equations of motion in a very elegant and practical manner.

Small Displacements. Linearization

For small perturbations from equilibrium, we can write $q_k = Q_k + \varepsilon X_k$, where $\varepsilon \ll 1$. Assuming that Q is given by the Lagrange equations and that the generalized forces F are independent of q, a first-order approximation of (22.44), for each k, gives

$$\begin{aligned}
&\frac{\partial^2 E_\mathrm{k}}{\partial \dot{q}_k \partial \dot{q}_j}\ddot{X}_k + \\
&\left[\frac{\mathrm{d}}{\mathrm{d}t}\left(\frac{\partial^2 E_\mathrm{k}}{\partial \dot{q}_k \partial \dot{q}_j}\right) + \frac{\partial^2 E_\mathrm{k}}{\partial q_k \partial \dot{q}_j} - \frac{\partial^2 E_\mathrm{k}}{\partial \dot{q}_k \partial q_j}\right]\dot{X}_k + \\
&\left[\frac{\mathrm{d}}{\mathrm{d}t}\left(\frac{\partial^2 E_\mathrm{k}}{\partial q_k \partial \dot{q}_j}\right) + \frac{\partial^2 V}{\partial q_k \partial q_j} - \frac{\partial^2 E_\mathrm{k}}{\partial q_k \partial q_j}\right] X_k = 0 \,,
\end{aligned} \tag{22.45}$$

which becomes in matrix form

$$\mathbf{M}\ddot{\boldsymbol{X}} + \mathbf{C}\dot{\boldsymbol{X}} + \mathbf{K}\boldsymbol{X} = 0 \,. \tag{22.46}$$

1. Since the kinetic energy E_k is a positive quadratic form of the velocity, the mass matrix $\mathbf{M}$ is a symmetric positive operator.
2. The matrix $\mathbf{C}$ is a generalized damping matrix made up of three terms:
   - The first, with generic element $C_{kj1} = \frac{\mathrm{d}}{\mathrm{d}t}\left(\frac{\partial^2 E_\mathrm{k}}{\partial \dot{q}_k \partial \dot{q}_j}\right)$ is associated with the temporal variation of the mass matrix;
   - The two other terms $\frac{\partial^2 E_\mathrm{k}}{\partial q_k \partial \dot{q}_j} - \frac{\partial^2 E_\mathrm{k}}{\partial \dot{q}_k \partial q_j}$ relate to gyroscopic forces. This part of the matrix $\mathbf{C}$ is antisymmetric and does not lead to dissipation.
3. The stiffness matrix $\mathbf{K}$ also is a sum of three terms:
   - The first is associated with the time variation of the first gyroscopic term in $\mathbf{C}$;
   - The second is governed by the q dependence of V;
   - The third is governed by the q dependence of E_k.

In what follows, we restrict our attention to conservative systems where E_k is independent of q and where

Amazon
EX1010 Page 912

the mass matrix is taken to be constant with time. In this case, (22.46) becomes

$$\mathbf{M}\ddot{\boldsymbol{X}} + \mathbf{K}\boldsymbol{X} = 0 \tag{22.47}$$

with

$$\begin{cases} M_{kj} = M_{jk} = \dfrac{\partial^2 E_\mathrm{k}}{\partial \dot{q}_k \partial \dot{q}_j} \\ K_{kj} = K_{jk} = \dfrac{\partial^2 V}{\partial q_k \partial q_j} \end{cases} . \tag{22.48}$$

22.2.2 Eigenmodes and Eigenfrequencies

Natural modes (or eigenmodes) are the sinusoidal (or harmonic) solutions of (22.47) with frequency ω in the absence of a driving term. As a consequence, the natural modes are solutions of the equation

$$\left(-\omega^2\mathbf{M} + \mathbf{K}\right)\boldsymbol{X} = 0 \tag{22.49}$$

with roots (or eigenvalue, or eigenfrequency) ω_n solutions of the characteristic equation

$$\det\left(-\omega^2\mathbf{M} + \mathbf{K}\right) = 0\,. \tag{22.50}$$

The eigenvector $\boldsymbol{\Phi}_n$ associated to each eigenfrequency ω_n is given by

$$\left(-\omega_n^2\mathbf{M} + \mathbf{K}\right)\boldsymbol{\Phi}_n = 0\,. \tag{22.51}$$

$\boldsymbol{\Phi}_n$ is defined with an arbitrary multiplicative constant. The natural modes are defined by the set of eigenvalues ω_n and associated eigenvectors $\boldsymbol{\Phi}_n$. Spectral analysis theory shows that the $\boldsymbol{\Phi}_n$ form an $\mathbf{M}$ and $\mathbf{K}$ orthogonal basis set, so that

$${}^{\mathrm{t}}\boldsymbol{\Phi}_m\mathbf{M}\boldsymbol{\Phi}_n = 0$$

and

$${}^{\mathrm{t}}\boldsymbol{\Phi}_m\mathbf{K}\boldsymbol{\Phi}_n = 0 \quad \text{for} \quad m \neq n \tag{22.52}$$

The orthogonality properties of the eigenmodes mean that the inertial (stiffness) forces developed in a given mode do not affect the motion of the other modes. The modes are mechanically independent. As a consequence, it is possible to expand any motion onto the eigenmodes. Given a force distribution $\boldsymbol{F}$, the motion of the system is governed by the equation

$$\mathbf{M}\ddot{\boldsymbol{X}} + \mathbf{K}\boldsymbol{X} = \boldsymbol{F}\,. \tag{22.53}$$

The modal projection is written in the form:

$$\boldsymbol{X} = \sum_n \boldsymbol{\Phi}_n q_n(t)\,. \tag{22.54}$$

The functions $q_n(t)$ in (22.54) are the modal participation factors. Inserting (22.54) into (22.53) and, after taking the scalar product of both sides of the equation with an eigenfunction $\boldsymbol{\Phi}_m$, we find

$$\langle\boldsymbol{\Phi}_n, \mathbf{M}\boldsymbol{\Phi}_n\rangle\ddot{q}_n + \langle\boldsymbol{\Phi}_n, \mathbf{K}\boldsymbol{\Phi}_n\rangle q_n = \langle\boldsymbol{\Phi}_n, \boldsymbol{F}\rangle \tag{22.55}$$

where the notation $\langle\boldsymbol{A}, \boldsymbol{B}\rangle$ denotes the scalar product ${}^{\mathrm{t}}\boldsymbol{A}.\boldsymbol{B}$ between vectors the $\boldsymbol{A}$ and $\boldsymbol{B}$. Equation (22.55) shows that the generalized displacements are uncoupled. Each q_n is governed by a single-DOF oscillator differential equation. The quantity

$$m_n = \langle\boldsymbol{\Phi}_n, \mathbf{M}\boldsymbol{\Phi}_n\rangle \tag{22.56}$$

is the modal mass associated with the mode n. These coefficients are defined with an arbitrary multiplicative constant. Similarly,

$$\kappa_n = \langle\boldsymbol{\Phi}_n, \mathbf{K}\boldsymbol{\Phi}_n\rangle \tag{22.57}$$

is the modal stiffness, related to the modal mass through the relationship

$$\kappa_n = m_n\omega_n^2\,. \tag{22.58}$$

Finally, the quantity

$$f_n = \langle\boldsymbol{\Phi}_n, \boldsymbol{F}\rangle \tag{22.59}$$

is the projection of the nonconservative forces onto mode n. Each independent oscillator equation can then be rewritten as

$$\ddot{q}_n + \omega_n^2 q_n = \frac{f_n}{m_n}\,. \tag{22.60}$$

Remark. Since the eigenvectors are defined with arbitrary multiplicative constants C_n, (22.56) shows that the modal mass is proportional to C_n^2. In addition, (22.58) shows that f_n is also proportional to C_n. Therefore, through (22.60), q_n is proportional to C_n^{-1} and from (22.54), $\boldsymbol{X}$ is independent of C_n.

Normal Modes. The normal modes Ψ_n correspond to the case where the arbitrary constant is such that the modal masses become unity. In this case, we can write

$$\Psi_n = \frac{\Phi_n}{\sqrt{m_n}}\,. \tag{22.61}$$

Amazon
EX1010 Page 913

Consequently, (22.57) becomes

$$\langle \boldsymbol{\Psi}_n, \mathbf{K}\boldsymbol{\Psi}_n \rangle = \omega_n^2 \,. \tag{22.62}$$

22.2.3 Admittances

In general, a given structure vibrates as a result of the action of localized and distributed forces and moments. For both numerical and experimental reasons, one often has to work on a discrete representation of the structure. In practice, the geometry of the structure is represented by a mesh consisting of a number N of areas with dimensions smaller than the wavelengths under consideration. This results in having to consider the structure as an N-DOF system. At each point of the mesh, the motion is defined by three translation components plus three rotation components. Similarly, the action of the external medium on the structure can be reduced to three force components plus three moment components, here denoted by F_l. The translational and rotational velocity components V_k at each point are thus related to the forces and moments through a 6×6 admittance matrix, such that

$$\boldsymbol{V} = \mathbf{Y}\boldsymbol{F} \tag{22.63}$$

For each force component at a given point j on the structure, denoted $F_{j|l}$, a motion at another point i, denoted by $V_{i|k}$, can be generated. As a consequence one can define the transfer admittance

$$Y_{ij|kl} = \frac{V_{i|k}}{F_{j|l}} \quad \text{with} \quad 1 \le i, j \le N \quad \text{and} \quad 1 \le k, l \le 6 \,.$$

In summary, the transfer admittance matrix is defined by $6N\times6N$ coefficients such as $Y_{ij|kl}$.

Notation. In what follows, the indices (k, l) are omitted, for the sake of simplicity. The transfer admittances are written as Y_{ij}, which reduces to Y_{ii} (or, even to Y_i) in the case of a driving-point admittance. Attention here is mostly focused on translation, though the formalism remains valid for rotation.

The previous results obtained on modal decomposition are now used to investigate the frequency dependence of the admittances. Here, $X(x_i) \equiv X_i$ is one component of displacement at point x_i and $F(x_j) \equiv F_j$ is one force component at point x_j. The structure is subjected to a forced motion at frequency ω. We have

$$\left(\mathbf{K} - \omega^2\mathbf{M}\right) X_i = F_j \,, \tag{22.64}$$

where $X_i = \sum \Phi_n(x_i) q_n(t)$ and

$$\left(\omega_n^2 - \omega^2\right) q_n = \frac{f_n}{m_n} = \frac{{}^{\mathrm{t}}\Phi_n(x_j) F_j(\omega)}{m_n} \,. \tag{22.65}$$

For a structure discretized on N points, the displacement at point x_i is given by

$$X_i(\omega) = \sum_{n=1}^{N} \frac{\Phi_n(x_i)\, {}^{\mathrm{t}}\Phi_n(x_j)}{m_n\left(\omega_n^2 - \omega^2\right)} F_j(\omega) \,. \tag{22.66}$$

The complete set of functions $X_i(\omega)$ given in (22.66) is the operating deflexion shape (ODS) at frequency ω. The transfer admittance between points x_i and x_j is written

$$Y_{ij}(\omega) = \mathrm{i}\omega \sum_{n=1}^{N} \frac{\Phi_n(x_i)\, {}^{\mathrm{t}}\Phi_n(x_j)}{m_n\left(\omega_n^2 - \omega^2\right)} \,. \tag{22.67}$$

The driving-point admittance at point x_i becomes

$$Y_i(\omega) = \mathrm{i}\omega \sum_{n=1}^{N} \frac{[\Phi_n(x_i)]^2}{m_n\left(\omega_n^2 - \omega^2\right)} \tag{22.68}$$

Remark. To include damping, (22.67) can be written

$$Y_{ij}(\omega) = \mathrm{i}\omega \sum_{n=1}^{N} \frac{\Phi_n(x_i)\, {}^{\mathrm{t}}\Phi_n(x_j)}{m_n\left(\omega_n^2 + 2\mathrm{i}\zeta_n\omega_n\omega - \omega^2\right)} \,, \tag{22.69}$$

where ζ_n is a nondimensional damping factor. The physical origin of the damping terms will be presented in more detail in Sect. 22.6.1.

Frequency Analysis and Approximations

For weak damping, and low modal density, the modulus of $Y_{ij}(\omega)$ passes through maxima at frequencies close to the eigenfrequencies $\omega = \omega_n$ (Fig. 22.4).

- For $\omega \approx \omega_n$, the main term in $Y_{ij}(\omega)$ is equal to

$$\mathrm{i}\omega \frac{\Phi_n(x_i)\, {}^{\mathrm{t}}\Phi_n(x_j)}{m_n\left(\omega_n^2 - \omega^2\right)} \,. \tag{22.70}$$

- For $\omega \gg \omega_n$, the admittance becomes

$$Y_{ij} \approx \mathrm{i}\omega \sum_{l>n} \frac{\Phi_l(x_i)\, {}^{\mathrm{t}}\Phi_l(x_j)}{-m_l\omega^2} \approx \frac{1}{\mathrm{i}M\omega}$$

with

$$\frac{1}{M} = \sum_{l>n} \frac{\Phi_l(x_i)\, {}^{\mathrm{t}}\Phi_l(x_j)}{m_l} \tag{22.71}$$

It can be seen that the modes with a rank larger than a given mode n play the role of a mass M.

Amazon
EX1010 Page 914

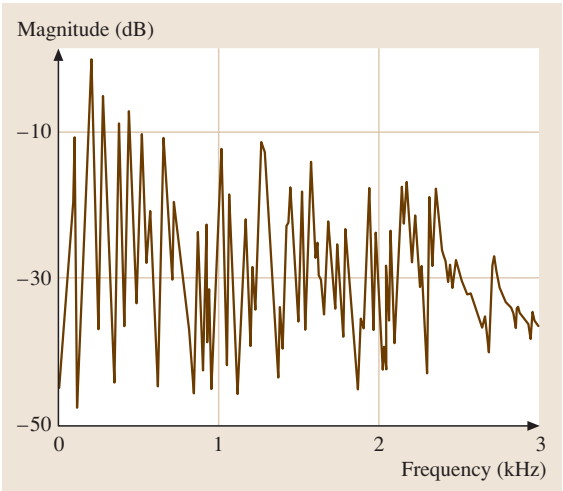


Fig. 22.4 Typical frequency dependence of an admittance modulus for a lightly damped structure. (After *Derveaux* et al. [22.3]

- Similarly, for modes with a rank smaller than n, we find

$$Y_{ij} \approx \mathrm{i}\omega \sum_{l<n} \frac{\Phi_l(x_i)\,{}^{\mathrm{t}}\Phi_l(x_j)}{m_l\omega_l^2} \approx \frac{\mathrm{i}\omega}{K}$$

with

$$\frac{1}{K} = \sum_{l<n} \frac{\Phi_l(x_i)\,{}^{\mathrm{t}}\Phi_l(x_j)}{m_l\omega_l^2} \,. \qquad (22.72)$$

Here, the contribution of the modes is equivalent to a stiffness K.

In summary, in the vicinity of a resonance of mode n, the transfer admittance can be written

$$Y_{ij}(\omega) \approx \mathrm{i}\omega \frac{\Phi_n(x_i)\,{}^{\mathrm{t}}\Phi_n(x_j)}{m_n\left(\omega_n^2-\omega^2\right)} + \frac{\mathrm{i}\omega}{K} + \frac{1}{\mathrm{i}M\omega} \,. \qquad (22.73)$$

22.2.4 Example: 2-DOF Plate–Cavity Coupling

To illustrate the previous concepts, a simple example of structural–acoustic coupling represented by a moving plate over a cavity with a hole is considered. This corresponds to a crude low-frequency model for stringed instruments or vented boxes [22.4]. V is the volume of the cavity, A_h is the section of the air piston of mass m_h and displacement x_h, and m_p is the mass of the plate with area A_p (Fig. 22.4). It is assumed that all points of the plate move in phase with the displacement x_p;

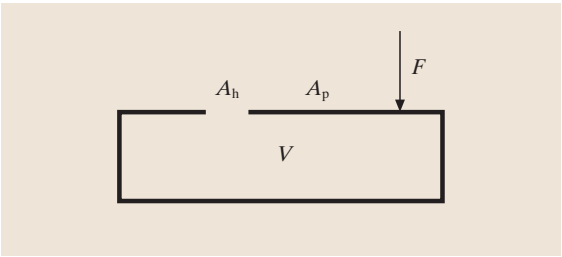


Fig. 22.5 Two-DOF plate–cavity coupling

k_p is the equivalent stiffness of the elastic plate and $\omega_{\mathrm{p},0} = \sqrt{k_\mathrm{p}/m_\mathrm{p}}$ denotes its eigenfrequency in the absence of coupling to the cavity. As the plate and piston are set in motion, the change of volume in the cavity is equal to $\Delta V = A_\mathrm{p}x_\mathrm{p} + A_\mathrm{h}x_\mathrm{h}$. Consequently, the pressure change in the cavity is $\Delta p = -\frac{\rho c^2 \Delta V}{V}$. F is the vertical external force applied to the plate, R_p and R_h are fluid damping coefficients. The equations that govern the motion of the coupled oscillators can be written

$$\begin{cases} m_\mathrm{p}\ddot{x_\mathrm{p}} = F - k_\mathrm{p}x_\mathrm{p} - R_\mathrm{p}\dot{x_\mathrm{p}} + A_\mathrm{p}\Delta p \,, \\ m_\mathrm{h}\ddot{x_\mathrm{h}} = A_\mathrm{h}\Delta p - R_\mathrm{h}\dot{x_\mathrm{h}} \end{cases} \,. \qquad (22.74)$$

Let us write $\mu = c^2\rho/V$. If the cavity is closed ($A_\mathrm{h} = 0$), then the eigenfrequency of the plate is given by $\omega_\mathrm{p} = \sqrt{\left(k_\mathrm{p} + \mu A_\mathrm{p}^2\right)/m_\mathrm{p}}$. If the stiffness k_p of the plate tends to zero, then the eigenfrequency of the plate coupled to the cavity becomes $\omega_\mathrm{a} = \sqrt{\mu A_\mathrm{p}^2/m_\mathrm{p}}$. Finally, if the plate is assumed to be completely rigid ($x_\mathrm{p} = 0$), then the eigenfrequency of the cavity–hole system (Helmholtz resonance) is $\omega_\mathrm{h} = \sqrt{\mu A_\mathrm{h}^2/m_\mathrm{h}}$. Solving (22.74) for a sinusoidal excitation $F\mathrm{e}^{\mathrm{i}\omega t}$, with $\gamma_\mathrm{p} = R_\mathrm{p}/m_\mathrm{p}$ and $\gamma_\mathrm{h} = R_\mathrm{h}/m_\mathrm{h}$, yields for the plate velocity u_p and air velocity u_h in the piston:

$$u_\mathrm{p} = \mathrm{i}\omega \frac{F}{m_\mathrm{p}} \frac{\left(\omega_\mathrm{h}^2 - \omega^2 + j\omega\gamma_\mathrm{h}\right)}{D} \qquad (22.75)$$

and

$$u_\mathrm{h} = -\mathrm{i}\omega \frac{F}{m_\mathrm{p}} \frac{A_\mathrm{p}}{A_\mathrm{h}} \frac{\omega_\mathrm{h}^2}{D} \qquad (22.76)$$

with

$$D = \left(\omega_\mathrm{p}^2 - \omega^2 + \mathrm{i}\omega\gamma_\mathrm{p}\right)\left(\omega_\mathrm{h}^2 - \omega^2 + \mathrm{i}\omega\gamma_\mathrm{h}\right) - \omega_\mathrm{ph}^4 \,, \qquad (22.77)$$

where

$$\omega_\mathrm{ph}^4 = \omega_\mathrm{h}^2\omega_\mathrm{a}^2 \,.$$

Amazon
EX1010 Page 915

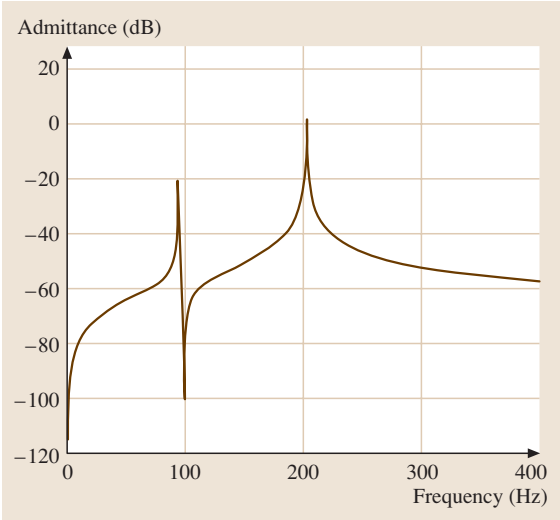


Fig. 22.6 Driving-point admittance of a plate loaded by a cavity. $A_p = 0.01\,\mathrm{m}^2$; $V = 0.1\,\mathrm{m}^3$; $f_h = 100\,\mathrm{Hz}$; $f_p = 200\,\mathrm{Hz}$; $\gamma_h = 1.0\,\mathrm{s}^{-1}$; $\gamma_p = 2.0\,\mathrm{s}^{-1}$; $m_p = 0.4\,\mathrm{kg}$; Admittance Y (in dB) $= 20\log|u_p/F|$

The eigenfrequencies of the coupled system correspond to the roots of the denominator D. Neglecting the influence of losses, these eigenfrequencies are solutions of the equation

$$\left(\omega_p^2 - \omega^2\right)\left(\omega_h^2 - \omega^2\right) - \omega_{ph}^4 = 0\,. \tag{22.78}$$

The solutions ω_+ and ω_- satisfy the relation

$$\omega_+^2 + \omega_-^2 = \omega_p^2 + \omega_h^2\,, \tag{22.79}$$

which shows that the difference between the eigenfrequencies increases due to the coupling between the plate and the Helmholtz resonator, compared to the uncoupled case. Figure 22.6 shows the modulus of the driving-point admittance $|u_p/F|$ of the plate, showing two maxima at ω_+ and ω_- and a zero at ω_h.

In stringed instruments and vented boxes, the main effect of the open cavity is to enhance the radiated sound in the low-frequency range, below the lowest resonance of the moving structure (the top plate or loudspeaker diaphragm).

22.2.5 Statistical Energy Analysis

The aim of statistical energy analysis (SEA) is to use power flows as a means for estimating the responses of complex systems. It is of particular interest for the analysis of coupled structures such as those encountered in the transportation industry. It is often used for the preliminary design of structures, or for identifying energy transmission paths [22.5].

One main advantage of SEA is that it usually leads to a substantial reduction of the number of degrees of freedom. The price to pay is that results are only given in terms of average and variance over frequency and space. It is particularly suitable when structural details are not known, or when measurements yield uncertainty in the modal parameters. SEA techniques focus on the analysis of energy levels in resonant modes of dynamical systems. Its main principle is based on the property that the average power flow between two coupled systems (or subsystems) is proportional to the difference in the average modal energies of each system. In order to illustrate this basic concept of SEA, the case of two coupled 1-DOF oscillators is summarized below. Detailed developments can be found in [22.6].

To consider a general case, it is assumed that both oscillators are coupled by means of a coupling spring with stiffness coefficient k_{12} and a gyroscopic constant B. The equations of motion of this system are given by

$$\begin{cases} m_1\dfrac{\mathrm{d}^2\xi_1}{\mathrm{d}t^2} + r_1\dfrac{\mathrm{d}\xi_1}{\mathrm{d}t} + s_1\xi_1 + B\dfrac{\mathrm{d}\xi_2}{\mathrm{d}t} + k_{12}\xi_2 = F_1\,, \\ m_2\dfrac{\mathrm{d}^2\xi_2}{\mathrm{d}t^2} + r_2\dfrac{\mathrm{d}\xi_2}{\mathrm{d}t} + s_2\xi_2 - B\dfrac{\mathrm{d}\xi_1}{\mathrm{d}t} + k_{12}\xi_1 = F_2\,, \end{cases} \tag{22.80}$$

where m_1 and m_2 are the masses of the oscillators, $r_1 = 2\delta_1 m_1$ and $r_2 = 2\delta_2 m_2$ are the mechanical resistances, $s_1 = k_1 - k_{12}$ and $s_2 = k_2 - k_{12}$ are stiffness coefficients, and F_1 and F_2 are the magnitudes of the forces applied to each mass. For a harmonic motion with frequency ω, the power flow between the oscillators is given by

$$P_{12} = \frac{1}{2}\,\mathrm{Re}\left(F_{12}v_2^*\right)\,, \tag{22.81}$$

where v_2^* is the complex conjugate of the velocity for the second oscillator and F_{12} is the force applied by oscillator 1 to oscillator 2. Using (22.80), the power flow at frequency ω is written [22.6]

$$P_{12} = \frac{\omega^2 s_{12}^2 + \omega^4 B^2}{m_1^2 m_2^2 |D(\omega)|^2}\left(m_2\delta_2|F_1|^2 - m_1\delta_1|F_2|^2\right)\,, \tag{22.82}$$

Amazon
EX1010 Page 916

where

$$D(\omega) = \omega^4 - 2\mathrm{i}\omega^3(\delta_1+\delta_2) - \omega^2\left(\omega_1^2+\omega_2^2+4\delta_1\delta_2+\frac{B^2}{m_1m_2}\right) + 2\mathrm{i}\omega\left(\delta_1\omega_2^2+\delta_2\omega_1^2\right) - \frac{k_{12}}{m_1m_2} + \omega_1^2\omega_2^2 \,. \tag{22.83}$$

In (22.83), ω_1 and ω_2 are the natural frequencies of the undamped uncoupled oscillators. It can be shown that (22.82) can be generalized to a broadband excitation with frequency bandwidth $\Delta\omega$. One basic property of SEA follows from the fact that P_{12} is proportional to the energy difference $W_1 - W_2$ of the oscillators. For a broadband excitation, these energies are given by

$$W_i = \frac{m_i}{2\Delta\omega}\int_{-\infty}^{+\infty} |v_i(\omega)|^2\,\mathrm{d}\omega \tag{22.84}$$

and the basic SEA equation becomes

$$P_{12} = \beta\left(W_1 - W_2\right)$$

give the rate at which energy is transferred from one subsystem to the other. The SEA theory can be used, for example, for predicting the vibration level of coupled

with

$$\beta = \frac{2}{m_1m_2}\,\frac{\left(\delta_1\omega_2^2+\delta_2\omega_1^2\right)B^2+\left(\delta_1+\delta_2\right)k_{12}^2}{\left(\omega_1^2-\omega_2^2\right)^2+2\left(\delta_1+\delta_2\right)\left(\delta_1\omega_2^2+\delta_2\omega_1^2\right)} \,. \tag{22.85}$$

Equation (22.85) shows that β is positive and depends on the parameters of the oscillators and on the coupling parameters B and k_{12}. This equation can be generalized to the coupling between any mode m_1 of a given subsystem with N_1 modes and a mode m_2 of another subsystem with N_2 modes. Considering a frequency band with central frequency ω_c, the generalization leads to the following expression for the power flow from subsystem 1 to subsystem 2

$$P_{12} = \omega_c\left(\eta_{12}W_1 - \eta_{21}W_2\right) \,, \tag{22.86}$$

where η_{12} and η_{21} are the coupling loss factors obtained through averaging of the parameters $\beta_{m_1m_2}$ analogous to that defined in (22.85)

$$\eta_{12} = \frac{N_2}{\omega_c}\langle\beta_{m_1m_2}\rangle_{N_1N_2} \quad\text{and}\quad \eta_{21} = \frac{N_1}{N_2}\eta_{12} \,. \tag{22.87}$$

$W_1 = N_1W_{m_1}$ and $W_2 = N_2W_{m_2}$ are the total modal energies in both subsystems, averaged over a frequency band, with the assumption that both energies are equally divided among the modes. The coupling loss factors plates over a large frequency range, where standard numerical methods, such as the finite-element method are too costly [22.6].

22.3 Strings and Membranes

Strings and membranes belong to that category of structures where the stiffness is due to external tension. This is sometimes called *geometrical* stiffness, in contrast with the *elastic* stiffness of most vibrating solids. In practice, strings and membranes also are made of elastic materials and, consequently, show more or less elastic stiffness due to their Young's moduli. This elastic stiffness will be neglected in the present section. The relative contributions of both stiffnesses will be discussed in Sect. 22.4 in the case of prestressed beams.

22.3.1 Equations of Motion

Consider a small element at a given point of Cartesian coordinates $\boldsymbol{x}$ on a stretched membrane of density $\rho(\boldsymbol{x})$. The membrane is assumed to be in equilibrium in the plane $\boldsymbol{e}_x, \boldsymbol{e}_y$ and subjected to a tension field $\tau(\boldsymbol{x})$ so that the resulting forces per unit length are (Fig. 22.7):

$$\begin{cases} \text{on both sides oriented in the } \boldsymbol{e}_x \text{ direction:} \\ \quad \boldsymbol{\tau}_x = \tau_{11}\boldsymbol{e}_x + \tau_{21}\boldsymbol{e}_y \,, \\ \text{on both sides oriented in the } \boldsymbol{e}_y \text{ direction:} \\ \quad \boldsymbol{\tau}_y = \tau_{12}\boldsymbol{e}_x + \tau_{22}\boldsymbol{e}_y \,, \end{cases} \tag{22.88}$$

where $\tau_{12} = \tau_{21}$ to ensure the moment equilibrium (reciprocity principle). In the general case, τ_{ij} are functions of the coordinates $\boldsymbol{x}$. The membrane is subjected to a small displacement in the direction $\boldsymbol{e}_z$ and released, so that its vertical motion $u(x, y, t)$ is governed by the balance between inertial forces and elastic forces due to tension. Gravity is neglected. After balance of forces on the four sides of the membrane element and projection on the vertical axis, with the assumption of small displace-

Amazon
EX1010 Page 917

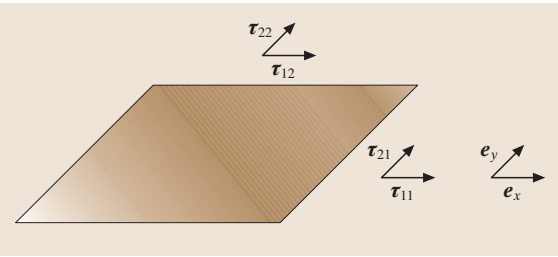


Fig. 22.7 Balance of forces on a membrane element

ments, one obtains the equation that governs the flexural motion of a nonuniformly stretched membrane:

$$\rho(\boldsymbol{x})h\ddot{u} = \frac{\partial}{\partial x}\left(\tau_{11}\frac{\partial u}{\partial x} + \tau_{12}\frac{\partial u}{\partial y}\right) + \frac{\partial}{\partial y}\left(\tau_{12}\frac{\partial u}{\partial x} + \tau_{22}\frac{\partial u}{\partial y}\right), \tag{22.89}$$

where h is the thickness. The tension field

$$\boldsymbol{\tau} = \begin{bmatrix} \tau_{11} & \tau_{12} \\ \tau_{12} & \tau_{22} \end{bmatrix} \tag{22.90}$$

is a symmetric tensor of order two, and

$$\mathbf{grad}\, u = \frac{\partial u}{\partial x}\boldsymbol{e}_x + \frac{\partial u}{\partial y}\boldsymbol{e}_y\,. \tag{22.91}$$

The previous equation can be written in the more compact form

$$\mathrm{div}\left(\boldsymbol{\tau}.\,\mathbf{grad}\, u\right) = \rho(\boldsymbol{x})h\ddot{u}\,, \tag{22.92}$$

where this last formulation has the advantage of being independent of the selected system of coordinates.

One-Dimensional (1-D) Approximation. Transverse Motion of Strings

Strings can be viewed as membranes where one dimension (the length) is much larger than the other two, so that a 1-D approximation is justified. Thus, rewriting (22.89) after integrating mass and tension along the axis $\boldsymbol{e}_y$, one obtains the equation of transverse motion for a string with nonuniform tension

$$\mu(x)\ddot{u} = \frac{\partial}{\partial x}\left[T(x)\frac{\partial u}{\partial x}\right], \tag{22.93}$$

where $\mu = \rho S$ is the linear mass density, S is the cross-sectional area and T is the tension.

Remark.

1. A similar equation can be obtained for the transverse motion $v(x, t)$ of the string in the direction $\boldsymbol{e}_y$. Therefore, two transverse motions polarized in orthogonal directions can exist on a string.
2. In the absence of coupling terms, u and v are independent. However, induced motion at the ends and/or nonlinear terms usually lead to coupling between these motions (Sect. 22.7).
3. Strings and membranes are also subjected to longitudinal motion. This motion is due to the variation of tension resulting from the variation in strain associated with the motion.

Homogeneous and Uniformly Stretched Strings and Membranes

For a uniformly stretched and homogeneous membrane, (22.92) reduces to

$$\tau\,\mathrm{div}\left(\mathbf{grad}\, u\right) = \tau\,\Delta u = \rho h\ddot{u}\,, \tag{22.94}$$

where the Laplacian is written in Cartesian coordinates as

$$\Delta u = \frac{\partial^2 u}{\partial x^2} + \frac{\partial^2 u}{\partial y^2} \tag{22.95}$$

For a string, we get the well-known wave equation

$$\mu\ddot{u} = T\frac{\partial^2 u}{\partial x^2}\,. \tag{22.96}$$

22.3.2 Heterogeneous String. Modal Approach

Extending the previous results to continuous structures shows that, in the linear regime, these structures have an infinite number of eigenmodes with similar properties of orthogonality with respect to mass and stiffness to those presented in Sect. 22.2 for discrete systems. In this case, the previously defined eigenvectors $\boldsymbol{\Phi}_n$ become continuous functions of the space coordinates $\Phi(\boldsymbol{x})$. To illustrate the modal approach for continuous systems, consider the case of an heterogeneous string (i. e., a nonuniformly stretched string with variable density), rigidly fixed at both ends and subjected to a force density $f(x, t)$:

$$\rho(x)S(x)\frac{\partial^2 y}{\partial t^2} - \frac{\partial}{\partial x}\left[T(x)\frac{\partial y}{\partial x}\right] = f(x,t)\,, \tag{22.97}$$

$\Phi_n(x)$ are the eigenfunctions of the string, which account for the boundary conditions. We seek solutions of the

Amazon
EX1010 Page 918

form

$$y(x,t) = \sum_n \Phi_n(x) q_n(t) \,. \tag{22.98}$$

Multiplying both sides of (22.97) by the eigenfunction $\Phi_m(x)$ and integrating over the length of the string yields

$$\begin{aligned} &\sum_n \ddot{q}_n(t) \int_0^L \Phi_n(x)\Phi_m(x)\rho(x)S(x)\,\mathrm{d}x \\ &- \sum_n q_n(t) \int_0^L \Phi_m(x) \frac{\mathrm{d}}{\mathrm{d}x}\left[T(x)\frac{\mathrm{d}\Phi_n(x)}{\mathrm{d}x}\right]\mathrm{d}x \\ &= \int_0^L \Phi_m(x) f(x,t)\,\mathrm{d}x \end{aligned} \tag{22.99}$$

which can be written in symbolic form as

$$\mathcal{M}\left(\ddot{y}, \Phi_m\right) + \mathcal{K}\left(y, \Phi_m\right) = \langle f, \Phi_m \rangle \,. \tag{22.100}$$

Equation (22.100) is general and can be applied to all conservative systems. $\mathcal{M}$ denotes the mass operator and $\mathcal{K}$ the stiffness operator.

Orthogonality Properties of the Eigenmodes

Each eigenmode $\Phi_n(x)$ is a solution of the equation

$$-\omega_n^2 \rho(x) S(x) \Phi_n(x) = \frac{\mathrm{d}}{\mathrm{d}x}\left[T(x)\frac{\mathrm{d}\Phi_n(x)}{\mathrm{d}x}\right] . \tag{22.101}$$

These eigenfunctions are orthogonal with respect to the mass

$$\int_0^L \Phi_n(x)\Phi_m(x)\rho(x)S(x)\,\mathrm{d}x = 0 \tag{22.102}$$

and orthogonal with respect to the stiffness

$$\int_0^L T(x)\frac{\mathrm{d}\Phi_m(x)}{\mathrm{d}x}\frac{\mathrm{d}\Phi_n(x)}{\mathrm{d}x}\,\mathrm{d}x = 0 \,. \tag{22.103}$$

Generalized Coordinates

Taking the orthogonality properties of the eigenmodes into account, we can write

$$-\frac{\mathrm{d}}{\mathrm{d}x}\left[T(x)\frac{\mathrm{d}\Phi}{\mathrm{d}x}\right] = \omega^2 \rho(x) S(x) \Phi(x) \tag{22.104}$$

so that (22.100) becomes:

$$\ddot{q}_n(t) + \omega_n^2 q_n(t) = \frac{f_n(t)}{m_n} \,, \tag{22.105}$$

where the modal mass is given by:

$$m_n = \int_0^L \Phi_n^2(x)\rho(x)S(x)\,\mathrm{d}x \tag{22.106}$$

with

$$f_n(t) = \int_0^L f(x,t)\Phi_n(x)\,\mathrm{d}x \,. \tag{22.107}$$

The equations that govern the generalized displacements are therefore formally identical to those obtained for discrete systems. For continuous systems, truncation of the theoretically infinite number of differential equations has to be performed. The truncation criteria are often determined by the frequency domain under consideration. For a lossless string of length L with perfect boundary conditions excited by a source term $f(x,t)$, the general solution can be written in the modal domain as

$$y(x,t) = \sum_n \Phi_n(x) q_n(t) \tag{22.108}$$

where

$$\ddot{q}_n(t) + \omega_n^2 q_n(t) = \frac{f_n(t)}{m_n}$$

with

$$f_n(t) = \langle f(x,t), \Phi_n(x) \rangle = \int_0^L \Phi_n(x) f(x,t)\,\mathrm{d}x \,.$$

Let us assume an initial shape $y(0,t)$ and an initial velocity $\dot{y}(0,t)$. The initial values of the $q_n(t)$ are thus given by

$$\begin{cases} q_n(0) = \dfrac{1}{m_n}\displaystyle\int_0^L \rho(x)S(x)y(0,t)\Phi_n(x)\,\mathrm{d}x \\ \text{and} \\ \dot{q}_n(0) = \dfrac{1}{m_n}\displaystyle\int_0^L \rho(x)S(x)\dot{y}(0,t)\Phi_n(x)\,\mathrm{d}x \end{cases} . \tag{22.109}$$

Amazon
EX1010 Page 919

Denoting the Laplace transform of $q_n(t)$ by $Q_n(s)$, we have

$$Q_n(s) = \frac{1}{s^2+\omega_n^2}\left[\frac{F_n(s)}{m_n} + sq_n(0) + \dot{q}_n(0)\right], \tag{22.110}$$

where $F_n(s)$ is the Laplace transform of $f_n(t)$. The first term of $Q_n(s)$ is a product of two transforms which, in the time domain, corresponds to a convolution. Using transform tables, we obtain

$$q_n(t) = \frac{1}{m_n\omega_n}\int_0^t f_n(\theta)\sin\omega_n(t-\theta)\,\mathrm{d}\theta + q_n(0)\cos\omega_n t + \dot{q}_n(0)\frac{\sin\omega_n t}{\omega_n}. \tag{22.111}$$

If $f_n(t)$ is a Dirac delta function of the form $f_{n0}\delta(t)$, the Laplace transform reduces to $F_n(s) = f_{n0}$ Equation (22.111) can then be written

$$q_n(t) = \frac{f_{n0}}{m_n}\frac{\sin\omega_n t}{\omega_n} + q_n(0)\cos\omega_n t + \dot{q}_n(0)\frac{\sin\omega_n t}{\omega_n}. \tag{22.112}$$

From the above impulse response for mode n of the string, we note the following:

1. There is an equivalence between $q_n(t)$ from the impulse source term and the initial velocity term. In other words, the motion of the string induced by an initial velocity profile is equivalent if the string is excited by a spatial distribution of Dirac delta function forces.
2. A source term localized at a given point x_0 can be written $f(x,t) = A\delta(x-x_0)\delta(t)$. In this case, $f_n(t) = \langle f(x,t), \Phi_n(x)\rangle = A\Phi_n(x_0)\delta(t)$. Therefore, the mode n will not be excited if the force is applied on a node of vibration.
3. The first term of the function $g_n(t) = \sin\omega_n t/m_n\omega_n$ is the Green's function of mode n.

String with a Finite Mass at One End

To present general results, the string is still assumed to be heterogeneous. The purpose of this section is to give the orthogonality properties of the modes for a heterogeneous string terminated by a finite mass M. The boundary conditions are

$$y(0,t) = 0 \quad \text{and} \quad -T(x)\frac{\partial y}{\partial x} = M\frac{\partial^2 y}{\partial t^2}, \quad \text{at} \quad x = L. \tag{22.113}$$

The eigenfunctions $\Phi(x)$ therefore have to satisfy

$$\begin{aligned} \rho(x)S(x)\omega^2\Phi(x) &= -\frac{\mathrm{d}}{\mathrm{d}x}\left[T(x)\frac{\mathrm{d}\Phi(x)}{\mathrm{d}x}\right] = 0, \\ \text{for} \quad & 0 < x < L \\ \text{with} \quad & \Phi(0) = 0 \\ \text{and} \quad & T(x)\mathrm{d}\Phi/\mathrm{d}x = \omega^2 M\Phi(x), \\ \text{at} \quad & x = L. \end{aligned}$$

For $n \neq m$, the orthogonality condition with respect to mass becomes

$$\int_0^L \rho(x)S(x)\Phi(x)\Phi_m(x)\,\mathrm{d}x + M\Phi_n(L)\Phi_m(L) = 0 \tag{22.114}$$

and the orthogonality condition with respect to stiffness remains

$$\int_0^L T(x)\frac{\mathrm{d}\Phi_n(x)}{\mathrm{d}x}\frac{\mathrm{d}\Phi_m(x)}{\mathrm{d}x}\,\mathrm{d}x = 0. \tag{22.115}$$

For a homogeneous string with uniform tension and constant diameter, these conditions reduce to

$$\int_0^L \Phi_n(x)\Phi_m(x)\,\mathrm{d}x = -\frac{M}{\rho S}\Phi_n(L)\Phi_m(L) \tag{22.116}$$

and

$$\int_0^L \frac{\mathrm{d}\Phi_n(x)}{\mathrm{d}x}\frac{\mathrm{d}\Phi_m(x)}{\mathrm{d}x}\,\mathrm{d}x = 0. \tag{22.117}$$

22.3.3 Ideal String

To solve initial-boundary problems in simple cases, we assume that the lossless string is homogeneous with density ρ, constant tension T and constant cross section S. In this case, the vertical displacement is given by the wave equation

$$\frac{1}{c^2}\frac{\partial^2 u}{\partial t^2} = \frac{\partial^2 u}{\partial x^2}, \tag{22.118}$$

where $c = \sqrt{T/\rho S}$ is the transverse wave velocity.

D'Alembert's Solution in the Time Domain

In order to show the correspondence between the wave and modal approaches, a time-domain method is used

Amazon
EX1010 Page 920

first to solve the wave equation (22.118) with initial conditions [22.7]

$$u(x,0)=f(x) \quad \text{and} \quad \frac{\partial u}{\partial t}(x,0)=g(x)\,. \tag{22.119}$$

Using the change of variables $\xi=x-ct$ and $\eta=x+ct$, we have

$$u(x,t)=U(\xi,\eta) \tag{22.120}$$

from (22.120), we obtain:

$$\begin{cases} \dfrac{\partial^2 u}{\partial t^2}=c^2\left(\dfrac{\partial^2 U}{\partial \xi^2}-2\dfrac{\partial^2 U}{\partial \xi\,\partial \eta}+\dfrac{\partial^2 U}{\partial \eta^2}\right) \\ \dfrac{\partial^2 u}{\partial x^2}=\dfrac{\partial^2 U}{\partial \xi^2}+2\dfrac{\partial^2 U}{\partial \xi\,\partial \eta}+\dfrac{\partial^2 U}{\partial \eta^2} \end{cases}. \tag{22.121}$$

Inserting (22.121) into (22.118) yields $\left(\partial^2 U\right)/\left(\partial\xi\,\partial\eta\right)=0$ which implies

$$u(x,t)=F(x-ct)+G(x+ct)\,, \tag{22.122}$$

where F and G are are two twice-differentiable functions. $F(x-ct)$ represents a travelling wave moving to the right (direction of increasing values for x), while $G(x+ct)$ is a travelling wave moving to the left. Using (22.119) implies that F and G must fulfill the conditions

$$\begin{cases} F(x)+G(x)=f(x) \\ -cF'(x)+cG'(x)=g(x) \end{cases}. \tag{22.123}$$

Solving (22.123) yields

$$\begin{cases} F(x) &= \dfrac{1}{2}f(x)-\dfrac{1}{2}\left[-F(0)+G(0)\right] \\ &\quad -\dfrac{1}{2c}\displaystyle\int_0^x g(s)\,\mathrm{d}s \\ G(x) &= \dfrac{1}{2}f(x)+\dfrac{1}{2}\left[-F(0)+G(0)\right] \\ &\quad +\dfrac{1}{2c}\displaystyle\int_0^x g(s)\,\mathrm{d}s \end{cases}. \tag{22.124}$$

Finally, the solution of the wave equation is written explicitly

$$u(x,t)=\frac{1}{2}\left[f(x-ct)+f(x+ct)\right]+\frac{1}{2c}\int_{x-ct}^{x+ct} g(s)\,\mathrm{d}s\,. \tag{22.125}$$

Semi-infinite String. For a semi-infinite string rigidly fixed at $x=0$, we have the boundary condition $u(0,t)=0$. This requires:

$$F(-ct)+G(ct)=0 \tag{22.126}$$

and, finally, with the appropriate change of variables

$$\begin{aligned} u(x,t) &= -G(x-ct)+G(x+ct) \\ &= F(x-ct)-F(-x-ct)\,. \end{aligned} \tag{22.127}$$

Equation (22.127) expresses the fact that, due to the fixed end at $x=0$, the left-traveling wave is reflected with a change of sign and becomes a right-traveling wave. The validity domain for (22.127) is $0\le x<+\infty$ and $t>0$.

String of Finite Length. In the case of an ideal string fixed at both ends, the wave approach can still be used, with the additional boundary condition $u(L,t)=0$, which yields

$$\begin{aligned} u(L,t) &= -G(L-ct)+G(L+ct) \\ &= F(L-ct)-F(-L-ct)=0\,. \end{aligned} \tag{22.128}$$

Equation (22.128) can be rewritten $F(z)=F(z-2L)$, which shows that F (and G) are now periodic functions with spatial period $2L$ or, equivalently, temporal period $2L/c$. The validity domain of (22.128) is now $0\le x\le L$ and $t>0$. Equations (22.126)–(22.128) can be used for step-by-step constructions of the string shape at successive instants of time.

String Fixed at Both Ends. Eigenmodes

Injecting a harmonic wave of the form $u(x,t)=\mathrm{e}^{\mathrm{i}(\omega t-kx)}$ in (22.118), we find the dispersion equation $D(\omega,k)$ that governs the relationship between frequency ω and wavenumber k. Here, we obtain

$$D(\omega,k)=\omega^2-c^2k^2=0\,. \tag{22.129}$$

This equation shows that the ratio between the frequency and wavenumber is constant, which is a characteristic property of a nondispersive medium. If we assume further that the string is rigidly fixed at both ends, the eigenmodes must satisfy the equation

$$\frac{\mathrm{d}^2\Phi(x)}{\mathrm{d}x^2}+\frac{\omega^2}{c^2}\Phi(x)=0 \tag{22.130}$$

with the boundary conditions $\Phi(0)=\Phi(L)=0$ from which we obtain

$$\Phi_n(x)=\sin k_n x\,. \tag{22.131}$$

Amazon
EX1010 Page 921

The only possible values for the wavenumber are given by the discrete series

$$k_n = n\pi/L \quad \text{so that} \quad \omega_n = n\pi c/L \,. \tag{22.132}$$

Using (22.106), the modal mass is $m_n = \rho SL/2 = M_s/2$, where M_s is the total mass of the string. Recall, however, that the ratio $m_n/M_s = 1/2$ is purely arbitrary since the modal masses are defined with an arbitrary multiplicative constant. The important result here is that all modal masses are equal and do not depend on the rank n of the mode.

Application: Plucked String. Modal Approach

The particular case where the string is released from an initial triangular shape at the origin of time without initial velocity is now examined. With the assumption of no stiffness, the initial profile of the string is given by

$$u(0,t) = \begin{cases} \dfrac{hx}{x_0} & \text{for } 0 \le x \le x_0 \\ \dfrac{h(L-x)}{L-x_0} & \text{for } x_0 \le x \le L \end{cases} . \tag{22.133}$$

The modal method consists of looking for solutions of the form

$$u(x,t) = \sum_n \Phi_n(x) q_n(t) \,. \tag{22.134}$$

At the origin of time, we can write

$$u(0,t) = \sum_n \Phi_n(x) q_n(0) \,. \tag{22.135}$$

The unknowns of the problem are the functions $q_n(0)$. Exploiting again the orthogonality properties of the eigenmodes, we find

$$q_n(0) = \frac{2hL^2}{n^2\pi^2 x_0(L-x_0)} \sin k_n x_0 \,. \tag{22.136}$$

The functions $q_n(t)$ are given by the oscillator equations

$$\ddot{q}_n + \omega_n^2 q_n = 0 \tag{22.137}$$

which, in the case of zero initial velocity, leads to $q_n(t) = q_n(0)\cos\omega_n t$. In summary, the transverse displacement of the string is given by

$$u(x,t) = \sum_n \frac{2hL^2}{n^2\pi^2 x_0(L-x_0)} \times \sin k_n x_0 \sin k_n x \cos\omega_n t \,. \tag{22.138}$$

Despite the simplicity of this example, a number of important issues can be derived from this result:

1. The eigenfrequencies are integer multiples of the fundamental $f_1 = c/2L$. The solution is periodic and the fundamental frequency is the inverse of the period of vibration.
2. The amplitudes of the modal components decrease as $1/n^2$ with the rank n of the modes.
3. Because the magnitude is proportional to $\sin k_n x_0$, a modal component n can be suppressed by selecting the plucking point $x_0 = pL/n$, where p is an integer $< n$.
4. The excitation point x_0 and observation point x can be interchanged in (22.138). This is an illustration of the reciprocity principle.

Moving End

To a first approximation, a vibrating string radiates as a dipole. Because of its small diameter compared to the acoustic wavelength, it is a poor radiator. If significant sound is to be radiated, one end of the string must be coupled to a component with a considerable vibrating area (plate, shell, etc.). In Sect. 22.3.2, the general properties of a heterogeneous string attached to a mass were obtained. In this section, the simple example of an ideal string coupled to a spring will be considered to illustrate the influence of such coupling on the eigenmodes, eigenfrequencies and modal masses. We consider a string fixed at point $x = 0$ to a spring of stiffness K_0. The boundary condition at this end is then

$$T\left(\frac{\partial u}{\partial x}\right)_{x=0} = K_0\, u(0,t) \,. \tag{22.139}$$

The string is rigidly fixed at the other end, so that $u(L,t) = 0$. We look for solutions of the form $u(x,t) = \Phi(x)\cos\omega t$. Following (22.118), the eigenfunctions $\Phi(x)$ must satisfy the equation

$$\frac{\mathrm{d}^2\Phi}{\mathrm{d}x^2} + k^2\Phi = 0 \tag{22.140}$$

and the boundary conditions. Thus, we derive the equation for the eigenvalues k_n

$$\tan(k_n L) = -\frac{k_n T}{K_0} \quad \text{with} \quad k_n > 0 \,. \tag{22.141}$$

The graphical representation of (22.141) shows that the k_n are no longer integer multiples of k_1 (Fig. 22.8). As a consequence, the free vibration of the string is no longer periodic. Note that the spring decreases the eigenfrequencies relative to those of a perfectly rigid end.

The eigenfunctions become

$$\Phi_n(x) = \sin k_n x + \frac{k_n T}{K_0}\cos k_n x = \frac{\sin k_n(L-x)}{\cos k_n L} \tag{22.142}$$

Amazon
EX1010 Page 922

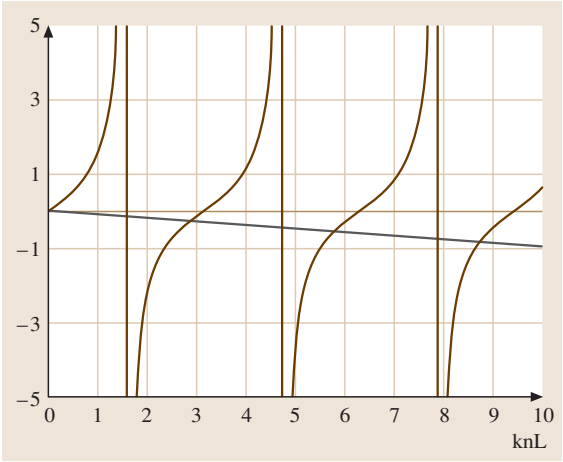


Fig. 22.8 Graphical resolution of the eigenvalue problem for a string attached to a spring (22.141)

from which the initial values $q_n(0)$ and the modal masses can be derived. We obtain:

$$m_n = \int_0^L \rho S \left(\sin k_n x + \frac{k_n T}{K_0} \cos k_n x \right)^2 \mathrm{d}x$$
$$= \frac{M_\mathrm{s}}{2} \left[1 + \left(\frac{k_n T}{K_0} \right)^2 \right] . \qquad (22.143)$$

Equation (22.143) shows here that the modal masses increase with the rank n of the mode. In the case of a mass termination, a similar procedure would lead to the eigenvalue equation

$$\tan(k_n L) = \frac{\rho S}{M_0 k_n} . \qquad (22.144)$$

Here, the inertial load at the end leads to an increase of the eigenfrequencies.

Application to Stringed Instruments. In plucked and struck strings instruments (guitar, piano, harp, etc.), the main part of the sound is due to the free regime of vibration, and the spectrum is composed of the eigenfrequencies of the vibrating system. Previous considerations show that the coupling between the strings and the radiating body (top plate, soundboard) alters the frequencies, compared to the perfect harmonic case. Though this alteration is usually relatively small, it has the consequence that the waveform is not perfectly periodic anymore. This might have in turn some perceptual effects on the produced sound. See the chapter on musical acoustics (Chap. 15) in this Handbook for more details.

22.3.4 Circular Membrane in Vacuo

Membranes are used in percussion instruments, microphones, loudspeakers and wall resonators. Because of their small thickness, the influence of air loading cannot be neglected in most applications. However, we limit ourselves here by solving the equation for transverse vibrations of a homogeneous membrane in vacuo. Fluid-loading effects on structures are discussed in later sections. From (22.94) the membrane equation, in circular geometry, is

$$\sigma \frac{\partial^2 u}{\partial t^2} = \tau \Delta u = \tau \left(\frac{\partial^2 u}{\partial r^2} + \frac{1}{r} \frac{\partial u}{\partial r} + \frac{1}{r^2} \frac{\partial^2 u}{\partial \theta^2} \right) , \qquad (22.145)$$

where $\sigma = \rho h$. Equation (22.145) can be solved by using the method of separation of variables [22.8]. For zero displacement at the edge, $z(r = a, \theta, t) = 0$, and neglecting losses, the expansion of the displacement on the eigenmodes can be expressed as

$$u(r, \theta, t) = \sum_{m=1}^{\infty} \left[\sum_{n=0}^{\infty} U_{nm}(r, \theta) \times \left(A_{nm} \cos \omega t + B_{nm} \sin \omega t \right) + \sum_{n=1}^{\infty} \tilde{U}_{nm}(r, \theta) \times \left(\tilde{A}_{nm} \cos \omega t + \tilde{B}_{nm} \sin \omega t \right) \right] . \qquad (22.146)$$

In (22.146), the eigenfunctions are

$$U_{nm}(r, \theta) = J_n(\beta_{nm} r) \cos n\theta$$

and

$$\tilde{U}_{nm}(r, \theta) = J_n(\beta_{nm} r) \sin n\theta , \qquad (22.147)$$

where J_n is the order-n Bessel function of the first kind [22.9]. The indices n and m refer to the number of nodal lines and to the number of nodal circles, respectively (Fig. 22.9).

The fixed edge corresponds to one nodal circle. The symmetrical modes are those where there are no nodal diameters. In this case, the eigenfunctions are of the form $J_n(\beta_{0m} r)$. All other modes can be viewed as *pairs of modes* with the same eigenfrequency and the same dependence versus r. They only differ by an angle of $\pi/2n$. The discrete values β_{mn} of the wavenumbers are derived from the boundary condition at the edge, such that

$$J_n(\beta a) = 0 . \qquad (22.148)$$

Amazon
EX1010 Page 923